The Dissertation Committee for Irina Stoilova Marinova
certifies that this is the approved version of the following dissertation:

The Properties of Barred Disks in the Field and Dense Environments: Implications for Galaxy Evolution

Committee:

Shardha Jogee, Supervisor

Neal Evans

Karl Gebhardt

Gary Hill

John Kormendy

Isaac Shlosman

The Properties of Barred Disks in the Field and Dense Environments: Implications for Galaxy Evolution

by

Irina Stoilova Marinova, B.S.; M.A.

DISSERTATION

Presented to the Faculty of the Graduate School of

The University of Texas at Austin

in Partial Fulfillment

of the Requirements

for the Degree of

DOCTOR OF PHILOSOPHY

THE UNIVERSITY OF TEXAS AT AUSTIN

August 2011

Acknowledgments

There are many people in my life without whose help this work would have been impossible. I would like to acknowledge the guidance and support of my advisor, Prof. Shardha Jogee. Thank you for sharing your knowledge, expertise, and time, which were invaluable to my success in graduate school. In addition, I would like to thank my research committee, Neal Evans, Karl Gebhardt, Gary Hill, John Kormendy, and Isaac Shlosman, for their insightful input during seminars, committee meetings, and while writing this thesis.

While graduate school was sometimes challenging and stressful, I met plenty of close friends whom I could always count on to get me through the tough times. In particular, Amanda, Miranda, Athena, John, Julie, Randi, Sean, Theresa - it was great having you guys to talk to about such diverse topics ranging from science, to pregnancy, to running, to cave exploration. My time here would not have been the same without you!

Finally, I am eternally grateful to all of my family for supporting me in every way through this journey. First and foremost, I must thank my husband, Josh, who assumed household and baby duties without complaint and made this thesis possible. Thank you for always being there for me, believing in me, and keeping me (mostly) sane. Thank you for always being there to listen, to keep me grounded, and to remind me about what is most important in my

life. I would also like to thank my parents, Stoil and Lilia, who helped spark and nurture my interest in science. Thank you to my grandparents, Stanka and Marin, who traveled a long way from home to take care of their great-granddaughter Kalina while I worked on the last chapters of my thesis. Also, a big thank you to my sister Michelle, who gave up her summer vacation to pitch in with baby care, and to my sister-in law Amanda, who was a great help in the week leading up to my PhD defense.

The Properties of Barred Disks in the Field and Dense Environments: Implications for Galaxy Evolution

Publication No. _____

Irina Stoilova Marinova, Ph.D.
The University of Texas at Austin, 2011

Supervisor: Shardha Jogee

Stellar bars are the most important internal drivers of the evolution of disk galaxies because they efficiently redistribute mass and angular momentum in the baryonic and dark matter components of galaxies. Mounting evidence suggests that mechanisms other than major mergers of galaxies, such as minor mergers, gas accretion, and bar-driven secular processes, play an important role in galaxy evolution since a redshift $z \sim 2$. In order to characterize the evolution of barred disks, this thesis presents one of the most comprehensive studies of barred galaxies in the field at low redshifts, and also as a function of environment across galaxy clusters of different densities. This work improves significantly on earlier studies by using quantitative methods to characterize bars, analyzing high-quality data from some of the largest disk galaxy samples to date, and using results across a range of Hubble types and environments to test different theoretical models for the evolution of disk galaxies. Our main results are summarized below: (1) Studies done as a part of this thesis have

quantitatively shown for the first time that the optical bar fraction in $z \sim 0$ field galaxies is a sensitive and non-monotonic function of host galaxy properties, such as the luminosity, stellar mass, and bulge-to-disk ratio. We find that at $z \sim 0$, the bar fraction increases significantly from galaxies of intermediate mass and Hubble types (Sb) toward those of lower mass and late Hubble types (Sd-Sm). The behavior from intermediate to early Hubble types is more uncertain. These results, which have been subsequently confirmed by independent studies, set constraints for theoretical models and in particular underline the importance for bar growth of angular momentum exchange between the bar, disk, bulge, and dark matter halo, as well as the possible triggering of bars by external satellites and interactions with the dark matter. Furthermore, our results at optical and near-infrared wavelengths on the fraction and sizes of bars at $z \sim 0$ provide the zero-redshift anchor point for studies of bars at higher redshifts with current and future space missions (e.g., ACS, WFC3, JWST), and allow us to assess the systematic effects in such studies. (2) Although cluster environments are unique laboratories for investigating the evolution of barred disks, only sparse and disparate results have emerged from early studies. In this thesis, we study barred disks in clusters using high-quality data from the Hubble Space Telescope Advanced Camera for Surveys for the moderately-rich cluster Abell 901/902 (characterized by a galaxy number density $n \sim 1{,}000$ gal Mpc^{-3}) at $z \sim 0.165$, and of the Coma cluster at $z \sim 0.02$, the densest cluster ($n \sim 10{,}000$ gal Mpc^{-3}) in the nearby Universe. We find that the optical bar fraction for bright, early Hubble type disk galaxies does

not show a statistically significant variation (within the error bars of ± 10 to 12%) as a function of galaxy environment within the Abell 901/902 cluster, as well as between the Abell 901/902 cluster and the field. Similarly, the optical bar fraction for bright S0 galaxies shows no statistically significant variation (within the error bars of ±10%) between the Virgo, Abell 901/902, and core of the Coma clusters, even though these environments span over an order of magnitude in galaxy number density ($n \sim 300$ to 10,000 gal Mpc^{-3}). We suggest that the S0 bar fraction is not greatly enhanced in denser environments, such as the core of Coma, due to the predominance of high speed encounters over slow ones, the tidal heating of S0 disks, and the low gas content of S0s in rich clusters.

Table of Contents

List of Tables

List of Figures

Chapter 1

Introduction

In the 1920's, Edwin Hubble greatly expanded the known universe by showing the first definitive evidence that the 'spiral nebulae' were separate and distant from the Milky Way, and in fact galaxies in their own right (e.g., Hubble, 1926, 1929). One of the first ways to accumulate and organize knowledge about these objects was through morphological classification. The ultimate aim of such a classification system was, of course, to understand something about the underlying physics (e.g., mechanisms for formation and evolution), through which galaxies with similar characteristics emerge. To this day, the most widely used classification system is based on the one first put forth by Hubble (1936). In his early morphological classification, Hubble not only recognized the fundamental difference between elliptical galaxies and those with disks, but also recognized two families of spirals: barred and unbarred (Fig. 1.1).

It is interesting that unbarred and barred galaxies of the same Hubble stage are split into *parallel* sequences (Fig. 1.1). This reflects the fact that it is not apparently obvious why one galaxy should be barred, while another galaxy with the same physical properties should be unbarred. In addition, it begs the

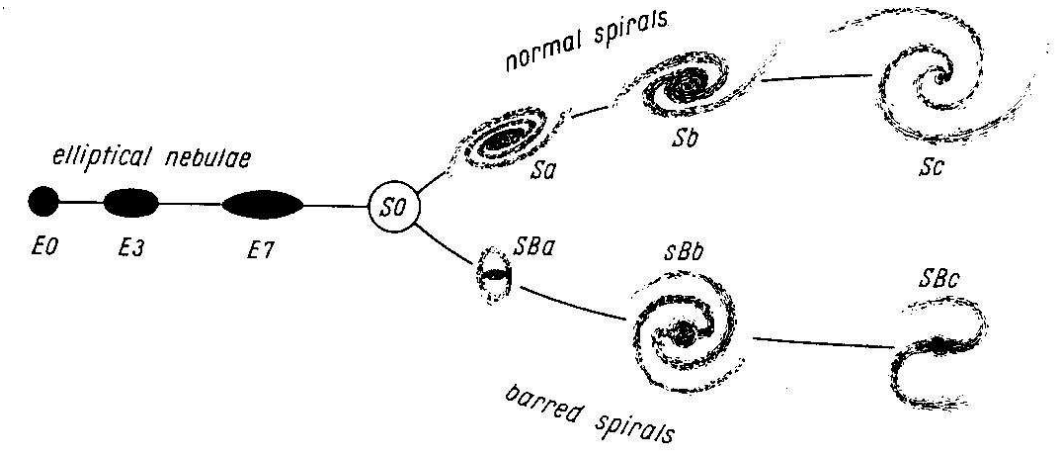

Figure 1.1 Hubble tuning fork diagram, showing the distinction between ellipticals and disks, as well as barred and unbarred galaxies.

questions: How frequent are bars among disk galaxies of different Hubble types in the present-day? How does this vary as a function of environment density, in the field, in groups, and in rich clusters? Does the fraction of barred disks change at early epochs? How do bars form in galaxies and what conditions are necessary for bar formation? What is the interplay between the bar and other components of galaxies such as the bulge, gas and stars in the disk, and the dark matter (DM) halo? What role do bars play in terms of driving the internal, secular evolution in galaxies (e.g., triggering starbursts, fueling active galactic nuclei or AGN, etc.)? How does all of the above change as a function of redshift and environment?

1.1 Stellar bars: definition and nomenclature

Observationally, stellar bars are defined as an elongated component in the plane of the galaxy disk, that passes through the galaxy center (see Fig. 1.2). In galaxies where gas and dust are present, offset dust lanes can be seen toward the leading edges of the bar. Theoretical studies reveal that the bar can be described as a density wave, supported by families of periodic and non-periodic stellar orbits, such as the '$x1'$ orbits, forming the main backbone of the bar (Contopoulos & Papayannopoulos, 1980), the '$x2'$ orbits, perpendicular to the bar major axis, and the stars on non-periodic orbits that are trapped around these periodic orbits. Resonances exist at the locations where the dominating orbits switch from one family to another, such as the inner Lindblad resonance (ILR), located where the dominant orbits switch from '$x2'$ in the central regions of the bar, to '$x1'$ orbits.

Due to the fact that the bar is a non-axisymmetric feature in the galaxy disk, it can drive radial inflows of gas. This occurs because the gas is dissipative, and therefore its response is phase-shifted from that of the stars. As the gas enters the density enhancement of the bar, it shocks toward the leading edges of the bar. This causes the gas to lose angular momentum and therefore its rotational support. In addition, due to the offset between gas and stars, the bar exerts a torque on the gas. The direction of this torque switches sign (inward or outward) along the bar at the resonances, but it is inward between the ILR and corotation, resulting in bar-driven radial inflows of gas.

Thus, quantifying the amount of radial inflow that a bar is able to drive

would be a good way to characterize the bar strength. However, this is very difficult to do observationally. Instead, several other ways are used to determine the strength of the bar observationally, which are indirectly related to the total torque the bar exerts on the gas. Bar strength is commonly characterized through visual classification by assigning the classes 'SB' - strongly barred, and 'SAB' - weakly barred. The criteria used to differentiate between a strong bar (SB) and a weak bar (SAB) are not always uniform, but for the most part, the main characteristic considered is the ellipticity (e) of the bar, defined as:

$$e = 1 - b/a. \tag{1.1}$$

Here, b is the minor axis length of the bar, and a is the length of the major axis. The quantity b/a is the axis ratio. Higher ellipticity bars are visually classified as SB, or strong. Fatter, or lower ellipticity bars, are generally visually classified as SAB. Figure 1.2 shows an example of the SB galaxy NGC 7479 (left), and the SAB galaxy NGC 1637 (right).

Using quantitative methods such as ellipse-fitting, the bar strength is also characterized by the bar ellipticity e, which is then defined as the peak ellipticity in the radial profile of ellipticity (Chapter 2, 3, 4, and Appendix 1). Other methods, such as the $Q_{\rm b}$ method, characterize bar strength by measuring the torque of the bar, but only at one point along the bar. These methods are further discussed in Appendix 1.

We note that some galaxies have very weakly non-axisymmetric disk components known as ovals (Kormendy & Norman, 1979; Kormendy, 1982a;

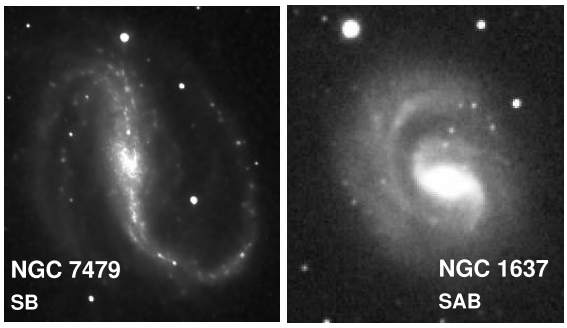

Figure 1.2 Examples of two barred spirals in the local Universe. NGC 7479 (left) is strongly-barred (SB), while NGC 1637 (right) has a bar that appears fatter, and is visually classified as weakly-barred (SAB). Images are from the Ohio State University Bright Galaxy Survey (OSUBGS; Eskridge et al., 2002).

Kormendy & Kennicutt, 2004), which contain much more of the disk mass than the bar, but are much less elongated (axis ratios of $\sim$0.8). The study of oval disks is beyond the scope of this thesis, as we focus on stronger non-axisymmetric features (i.e., stellar bars) and not ovals for several reasons. Firstly, from a conceptual point of view, the the efficiency with which ovals drive gas inflow and galaxy evolution is as yet undemonstrated both observationally and theoretically, while bars are established as important drivers. The inflow rate driven by a bar depends both on the shocks driven by the bar and the gravitational torque it exerts. While one may argue that a low ellipticity oval disk may contain more mass than a bar, and as such can exert large gravitational torques, ovals do not drive shocks in simulations. The orbital structure of ovals and bars may in fact be quite different. Secondly, separating the effect of oval disks and bars is quite difficult, given that many galaxies described to have strong oval distortions (e.g., Kormendy & Kennicutt, 2004) also host a

stellar bar (e.g., NGC 2903, NGC 1068, NGC 5248). Even NGC 4736, which is often described as a prototypical unbarred oval galaxy (e.g., Kormendy & Kennicutt, 2004) hosts a bar in the near infrared (Moellenhoff et al., 1995). While these galaxies show evidence of evolution from gas inflows in their inner few kiloparsec, much of this appears to be tied to the primary stellar bar. It thus seems sensible as a first step to focus on stellar bars. Thirdly from a practical point of view, bar detection can be performed consistently and robustly across different samples and is therefore easily reproducible because stellar bars have strong non-axisymmetries with high ellipticities ($e > 0.25$). This is not the case for oval disks (with $e \sim 0.15$). Finally, it should be noted that features such as bars and ovals, or bars and lenses can coexist in the same galaxy, and are thus not mutually exclusive.

1.2 Importance of stellar bars for galaxy evolution

Over the next several decades following Hubble's classification, studies used visual classification to tabulate the number of galaxies with bars in the local universe and to connect bars with other morphological components often seen in barred galaxies. de Vaucouleurs & de Vaucouleurs (1964) expanded the Hubble classification system to include features such as inner and outer rings, inner spirals, and lenses (also see Kormendy, 1977). Kormendy (1979) explored the frequencies and apparent properties of these morphological components, and recognized the impact that bars have on the galaxy disk, likely driving its internal, secular evolution by redistributing gas and stars. This idea

is corroborated by numerous subsequent observational studies of barred galaxies showing that significant gas streaming motions are present along the bar (Burbidge et al., 1962; de Vaucouleurs & de Vaucouleurs, 1963; Quillen et al., 1995; Regan et al., 1997; Mundell & Shone, 1999; Jogee, 1999; Knapen et al., 2000; Zurita et al., 2004). Barred galaxies show increased central gas concentrations (Sakamoto et al., 1999), as well as central starbursts and star-forming rings (Elmegreen & Elmegreen, 1980; van Albada & Roberts, 1981; Ball et al., 1985; Lord et al., 1987; Scoville et al., 1988; Kenney et al., 1991; Martin & Roy, 1995; Knapen et al., 1995; Martin & Friedli, 1997; Koribalski et al., 1996; Huang et al., 1996; Jogee, 1999; Jogee et al., 1999; Weiner et al., 2001; Regan & Teuben, 2003; Jogee et al., 2005; Sheth et al., 2005; Knapen et al., 2006; Peeples & Martini, 2006; Hao et al., 2009). Hunt & Malkan (1999), Hao et al. (2009), and Laurikainen et al. (2004a) find that starburst galaxies have a higher incidence of bars compared to non-starbursts. Higher bar fractions have also been reported in Seyfert galaxies compared to non-active galaxies (Knapen et al., 2000; Laine et al., 2002; Laurikainen et al., 2004a, also see Jogee, 2006 and references therein), but interestingly the bars in Seyfert hosts are weaker (lower e) than those in non-active galaxies (Shlosman et al., 2000). On the other hand, Hao et al. (2009) finds similar bar fractions for galaxies hosting active galactic nuclei (AGN) and non-active galaxies. For several galaxies, bar driven inflows in the range of 1 to 4 $M_{\odot}$ yr^{-1} have been inferred from observations and modeling (Quillen et al., 1995; Regan et al., 1997; Laine et al., 1998). Finally, metallicity gradients are shallower in barred than un-

barred galaxies (Vila-Costas & Edmunds, 1992; Zaritsky et al., 1994; Martin & Roy, 1994; Ellison et al., 2011), providing indirect evidence that the bar redistributes material within the galaxy disk. Combined, these results point to bars as an efficient internal driver of secular evolution in galaxies (also see Kormendy, 1993; Jogee, 1999; Kormendy & Kennicutt, 2004).

Concurrently, theoretical studies complemented the observational results by exploring in detail the physical significance of bars and reproducing morphological features observed in barred galaxies. For example, early simulations showed that rings usually form at the resonances, where gas is funneled by the bar and trapped (e.g., Combes & Gerin, 1985; Athanassoula & Bosma, 1985; Shlosman et al., 1989; Sellwood & Wilkinson, 1993; Heller & Shlosman, 1996). Athanassoula (1992b) successfully reproduced the morphology of dust lanes observed on the leading edges of bars in spirals and showed that the lanes occur at shock loci. Boxy and peanut-shaped bulges observed in about 20–45% of edge-on galaxies (Shaw, 1987; Kuijken & Merrifield, 1995; Lütticke et al., 2000; Kormendy & Kennicutt, 2004) were found to be related to bars as the result of the bar being observed end-on (Combes & Sanders, 1981; Athanassoula & Misiriotis, 2002; Athanassoula, 2005; Bureau & Athanassoula, 2005) or caused by the bar vertical buckling instability or resonant heating in a bar observed edge-on (Combes & Sanders, 1981; Pfenniger & Friedli, 1991; Sellwood & Wilkinson, 1993; Berentzen et al., 1998; Athanassoula & Misiriotis, 2002; Athanassoula, 2005; Bureau & Athanassoula, 2005; Martinez-Valpuesta et al., 2006). Studies used simulations to explore the connection between bars,

central starbursts, and AGN from the theoretical perspective. They find possible mechanisms for fueling AGN in disk galaxies, which include bar-driven gas transport to the central few kiloparsec where subsequently the gas may be funneled to even smaller radii (perhaps reaching the supermassive black hole, SMBH) through nuclear bars, nuclear spirals, dynamical friction, and viscous torques (Shlosman et al., 1989; Heller & Shlosman, 1994; Heller et al., 2001; Shlosman & Heller, 2002; Englmaier & Shlosman, 2004; Jogee, 2006). Numerous theoretical studies explored the dynamics of the bar pattern, characterized the orbits of stars and gas influenced by the bar potential, and showed that the bar evolves through the transfer of angular momentum to the outer disk and/or DM halo (e.g., Miller & Smith, 1979; Sellwood, 1981; Athanassoula et al., 1983; Weinberg, 1985; Sparke & Sellwood, 1987; Contopoulos & Grosbol, 1989; Athanassoula, 1992b,a; Pfenniger & Friedli, 1991; Shlosman & Noguchi, 1993; Berentzen et al., 1998; Debattista & Sellwood, 1998; Heller et al., 2001; Martinez-Valpuesta & Shlosman, 2004; Martinez-Valpuesta et al., 2006; Debattista et al., 2006; Sellwood & Debattista, 2006; Berentzen et al., 2007; Villa-Vargas et al., 2009, 2010), thus efficiently redistributing material in the galaxy disk and driving its evolution.

The importance of internal structures such as stellar bars for the evolution of galaxy disks becomes even more clear in light of recent studies, suggesting that since $z \sim 1$, major mergers among massive galaxies are not very frequent (e.g., Bell et al., 2006; Jogee et al., 2009; López-Sanjuan et al., 2010; Weinzirl et al., 2009) and have not contributed significantly to the cosmic star

formation rate (SFR) density (e.g., Bell et al., 2005; Wolf et al., 2005a; Jogee et al., 2009; Robaina et al., 2009), to the building of bulges in massive spirals (Weinzirl et al., 2009; Kormendy & Fisher, 2008; Laurikainen et al., 2007), and to the build-up of early-type E/S0/Sa galaxies (López-Sanjuan et al., 2010). Other processes, such as minor mergers (Jogee et al., 2009; Weinzirl et al., 2009; López-Sanjuan et al., 2010), smooth accretion, or internal secular processes such as those driven by stellar bars (Laurikainen et al., 2007; Kormendy & Fisher, 2008; Weinzirl et al., 2009) are now increasingly invoked.

1.3 Goals and overview

In this work we conduct some of the most extensive studies of barred disks as a function of environment density at low redshifts ($z < 0.2$). In addition, we establish an anchor for intermediate- and high-redshift studies as well as studies at various environment densities. Our results offer constraints on models of the formation and evolution of bars and their host disks.

This thesis improves significantly on work done to date for barred galaxies in three important ways. Firstly, we use quantitative methods to identify and characterize bars, thereby allowing objective comparisons across different redshifts and environments. Furthermore, we compare the results obtained using different methods (e.g., ellipse fits, visual classification, bulge-disk-bar decomposition) and characterize the limitations of each method (see Chapter 4 in particular). Secondly, we analyze some of the largest galaxy samples studied to date, using deep, high-resolution datasets obtained through large

surveys of galaxies conducted with the Hubble Space Telescope (HST) Advanced Camera for Surveys (ACS), such as the STAGES Abell 901/902 survey (Chapter 3) or the Coma HST Treasury survey (Chapter 4). Third, we use the broad results obtained across galaxies of different Hubble types and across a wide range of environments to test different theoretical paradigms for the evolution of bars and their host disks. The main components of the thesis are outlined below.

1.3.1 Methods used for bar identification

The methods we use to identify disks and bars are outlined in Chapters 2 to 4, which describe three different studies focusing on galaxies at different epochs and environments, using data at optical and NIR wavelengths. In addition, we have summarized the essential methods and concepts for bar identification in Appendix 1.

1.3.2 Establishing an anchor at $z \sim 0$: the quantitative bar fraction and properties in the local Universe

Ironically, the motivation for comprehensive, quantitative studies of the fraction of barred disks in the local universe (such as the one we undertake in Chapter 2), arose from the need for a quantitative comparison point for studies of barred disks at intermediate redshift (Elmegreen et al., 2004; Jogee et al., 2004; Sheth et al., 2008), only recently made possible by ACS on the HST.

Even with the substantial and detailed body of work on barred galaxies

in the local universe described in the preceding paragraphs, at the time that studies began exploring the fraction of barred disk at intermediate redshifts (Abraham et al., 1999; Jogee et al., 2004; Elmegreen et al., 2004), there still did not exist a large *quantitative* study establishing the optical bar fraction for field galaxies in the local universe, which could serve as a quantitative comparison 'zero point' for the results out to $z \sim 1$, as well as for studies in more dense environments at various redshifts. Establishing such a quantitative 'zero point' for the bar fraction and properties in the local universe was one of the goals of our study in Chapter 2 (MJ07). A second goal was to explore the redshift-dependent systematic effects that impact the observed optical bar fraction at intermediate redshifts. In MJ07, we provide this zero-point in both the optical B band and the NIR H band using ellipse fitting in a sample of disk (S0–Im) galaxies, but where *most* galaxies are of intermediate Hubble types Sb–Sc. In addition, we present quantitative distributions of bar ellipticity $e_{\rm bar}$ and bar semi-major axis length $a_{\rm bar}$ in the local universe, and outline the constraints and redshift-dependent systematic effects that these place on observations of bars at intermediate redshifts with the ACS and future space missions such as the James Webb Space Telescope (JWST).

We also study how the visual classifications in the RC3 compare to characterizing bars with ellipse fits. We find that the RC3 visual bar types (SB and SAB) should be used with caution. Many galaxies with RC3 bar type SAB are unbarred, and the bar types SB and SAB have a significant overlap in $e_{\rm bar}$ (Fig. 2.15).

In MJ07, we cannot robustly constrain whether the bar fraction varies with Hubble type, as most galaxies in our sample have a narrow range in Hubble type (Sb–Sc), and we are limited by low number statistics at very early (e.g., S0–Sa) and very late (e.g., Scd–Im) Hubble types. The first quantitative study large enough to probe the variation of the bar fraction with host galaxy properties was Barazza, Jogee, & Marinova (2008, hereafter BJM08). Using an SDSS sample drawn from over 3000 galaxies at $z = 0.01$–0.03, in BJM08 we found the dramatic result that the optical bar fraction increases by a factor of ~ 1.75 from galaxies that have prominent bulges to disk-dominated galaxies (as characterized by $r_{\rm e}/R_{24}$). An important thing to note, is that in BJM08, disk galaxies are selected via a color cut in $B - V$, resulting in a sample of blue, mostly late-type systems, with $M_{\rm r} = -18.5$ – -22. The results from BJM08 show that it is vitally important to understand the effects of sample selection when drawing conclusions about the bar fraction and properties, or comparing these across different samples. In addition, in BJM08 we show that the bar fraction averaged over a range of Hubble types (or galaxy masses, etc.) may not tell the whole story. Due to the fact that many galaxy properties vary simultaneously with Hubble type, subsequent studies now isolate the dependence of the bar fraction on mass, B/T, and other galaxy properties. Our results are in agreement with subsequent studies (Marinova et al. 2009, hereafter M09, Aguerri et al., 2009; Laurikainen et al., 2009; Nair & Abraham, 2010b), which confirm that the dependence of the bar fraction on galaxy properties is complex and non-monotonic (see Chapters 4 and 5). In Chapter 5,

we discuss in detail what these trends can tell us about bar formation and evolution in the context of results from theoretical studies.

1.3.3 Barred galaxies in dense environments

Another area of opportunity in terms of piecing together the complex co-evolution of bars and their host disks, is studying the properties of barred galaxies in environments of different densities. Cluster environments provide a unique laboratory for bar studies due to the multitude of environmental processes acting on cluster galaxies, caused by the high galaxy number density, large galaxy velocity dispersions, and the presence of the intra-cluster medium (ICM). These conditions lead to fast, impulsive tidal encounters (the cumulative effect of which is known as galaxy harassment; Moore et al., 1996), ram pressure stripping of diffuse gas (Gunn & Gott, 1972; Larson et al., 1980; Quilis et al., 2000; Balogh et al., 2000), and the influence of the tidal forces from the cluster potential as a whole (Gnedin, 2003). Therefore, by studying the properties of bars and disks in clusters and comparing them to those in the field, we can hope to glean insights into what factors are important in the formation of bars and their subsequent evolution.

Until recently, there existed only a handful of studies exploring this issue. The most comprehensive early study was that of Kumai et al. (1986), which used visual classifications of Uppsala General Catalog galaxies in the field and cluster environments, as well as binary pairs. Among other things, Kumai et al. (1986) found that the fraction of barred galaxies for all morpho-

logical sub-types is independent of environment, while there is an excess of early-type barred galaxies in pairs. The latter result on binary pairs has also been confirmed by Elmegreen et al. (1990) and Varela et al. (2004). Interestingly, Thompson (1981) reports that the frequency of barred S0 galaxies is higher in the Coma cluster core than in the outer regions, but the results are compromised by uncertainty in cluster membership and the use of lower quality B-band photographic plates. In contrast, Andersen (1996) reports no difference in the distribution of barred and unbarred S0s between the core and outer regions in Virgo. In light of the importance of pinning down the effects of environment on the evolution of barred disks, the disparate and sparse results of early studies, as well as the newly-discovered dependence of the bar fraction and properties on those of the host disk, we undertake some of the most comprehensive, quantitative studies of bars as a function of environment density in Chapters 3 and 4 (M09; Marinova et al. 2011, hereafter M11), using the highest-resolution data available.

In Chapter 3 (M09), we investigate the properties of barred disks in the *HST* ACS survey of the Abell 901/902 cluster system at $z \sim 0.165$. In Chapter 4 (M11), we focus specifically on S0 galaxies in the dense central regions of the Coma cluster core ($z \sim 0.02$), using the *HST* ACS treasury survey of Coma. We show that the bar fraction for bright ($M_{\rm V} \lesssim -20$) early-type disk galaxies (e.g., S0–Sab) does not show a strong variation (within the errors) between field and cluster environments (for matched samples; M09). We also find that the bar fraction in matched samples of bright ($M_{\rm V} \lesssim -18$) S0s does

not show a statistically significant variation over a wide range of environment density, as characterized by the galaxy number density n, ranging from Virgo ($n \sim 300$ gal Mpc^{-3}) to the Coma cluster core ($n \sim 10{,}000$ gal Mpc^{-3}). Our results are supported by concurrent and subsequent studies, who also find no difference in the bar fraction as a function of environment density (van den Bergh, 2002; Aguerri et al., 2009; Barazza et al., 2009; Cameron et al., 2010), although we note that the situation can be quite different for pairs of galaxies and galaxy groups (Chapter 4). In Chapter 5, we discuss the implications of these results.

1.3.4 Constraints on theory of bar formation and evolution

While it has been well established by theoretical studies that bars grow and evolve through angular momentum exchange with the disk and DM halo, exactly how bars form in real galaxies is still largely a mystery. In one scenario, the bar forms spontaneously in a disk with favorable conditions (i.e., one that is dynamically cold), and the bar instability is maintained and amplified via the swing amplification mechanism (e.g., Binney & Tremaine, 1987). Alternatively, the bar can be triggered externally, either by tidal interactions with other galaxies (Noguchi, 1988; Mihos & Hernquist, 1996; Gerin et al., 1990; Aguerri & González-García, 2009), or through interactions with an asymmetrical DM halo, or the DM substructure surrounding the galaxy (Heller et al., 2007; Romano-Díaz et al., 2008; Dubinski & Chakrabarty, 2009). Important factors influencing the bar include the host galaxy stellar mass, DM frac-

tion, and concentration, the triaxiality of the DM halo in which it lies (e.g., Berentzen et al., 2006), the amount of angular momentum that the DM halo can absorb (e.g., Athanassoula, 2003; Martinez-Valpuesta et al., 2006), the central mass concentrations (CMCs) present in the inner few hundred parsecs (e.g., Shen & Sellwood, 2004; Athanassoula, 2005; Martinez-Valpuesta et al., 2006; Debattista et al., 2006; Berentzen et al., 2007; Villa-Vargas et al., 2010), and the distribution and amount of gas in the disk (e.g, Roberts, 1969; Shlosman & Noguchi, 1993; Berentzen et al., 1998; Bournaud & Combes, 2002; Bournaud et al., 2005; Debattista et al., 2006; Berentzen et al., 2007; Villa-Vargas et al., 2010).

What do theoretical studies have to say about the robustness and lifetime of bars? Early studies suggested that an existing bar could be easily destroyed by a moderate CMC (Hasan & Norman, 1990; Hasan et al., 1993). However, more recent work shows that this is not the case (e.g., Athanassoula, 2005; Shen & Sellwood, 2004; Martinez-Valpuesta et al., 2006; Debattista et al., 2006). The types of very massive, dense CMC's (CMC-to-disk mass ratios of $> 10\%$) necessary to destroy a bar do not exist in present-day galaxies (Shen & Sellwood, 2004; Athanassoula, 2005, Chapter 2).

The gas content of disks also influences the robustness and evolution of the bar. While a gas-rich disk is generally more dynamically cold and more susceptible to bar formation, in the case of extremely gas-rich disks, the gas can become clumpy and actually act to heat the disk, making it less bar unstable (e.g., Shlosman & Noguchi, 1993). However, in the simulations of bar-driven

gas inflow by Bournaud et al. (2005) the bar can be destroyed even with a gas mass fraction that is as low as 5% to 7%. Such gass mass fractions are frequently seen in present-day disks. In these simulations, the bar is destroyed by gaining angular momentum from the gas inflowing along the bar. However, these results are starkly different than those from most simulations to date, which show that gas inflows in present-day galaxies do not readily destroy bars (Debattista et al., 2006; Curir et al., 2006; Berentzen et al., 2007). In fact, bar destruction through the shedding of angular momentum from inflowing gas to the bar has been tested in Berentzen et al. (2007), who find that this has little effect on the robustness of the bar. The different results may be due to the fact that Bournaud et al. (2005) adopt rigid halos in their studies instead of live massive halos with high DM fraction.

Constraining these theoretical predictions on the formation and evolution of bars requires observationally determining how the bar fraction varies as a function of host galaxy properties (e.g., B/T, mass, Hubble type, DM fraction, age) over a range of environment densities. We provide such constraints in Chapters 2, 3, and 4 of this thesis. In addition, we tie in our results at low redshifts with those of recent studies at intermediate redshift in Chapter 5.

In the last chapter (Chapter 5), we summarize the results of this thesis in the context of the current state of the field. We synthesize the main existing observational results and discuss the constraints they provide for theoretical studies. Based on this we speculate on the implications of our results for bar formation and evolution, as well as the overall evolution of galaxy disks.

Finally, we explore outstanding issues that are currently at the forefront of the field.

Chapter 2

Characterizing Bars at $z \sim 0$ in the optical and NIR: Implications for the Evolution of Barred Disks with Redshift[0]

2.1 Introduction

Stellar bars are recognized as the most important internal factor that redistributes the angular momentum of the baryonic and dark matter components of disk galaxies (e.g., Weinberg, 1985; Debattista & Sellwood, 1998, 2000; Athanassoula, 2002; Berentzen et al., 2006), thereby driving their dynamical and secular evolution. Bars efficiently drive gas from the outer disk to the central few hundred parsecs and are observed to feed central starbursts in local galaxies (Elmegreen, 1994; Knapen et al., 1995; Hunt & Malkan, 1999; Jogee, 1999; Jogee et al., 2005). It remains a matter of contention whether large-scale bars relate to AGN activity in galaxies, given the reduction by several orders of magnitude needed in the specific angular momentum of gas before it can feed a central black hole, and conflicting observational results (see review by Jogee 2006 and references therein; also Mulchaey & Regan, 1997; Knapen et al., 2000; Laine et al., 2002; Laurikainen et al., 2004b). In

[0]A significant part of this chapter was originally published in the Astrophysical Journal by Irina Marinova as lead author. Reproduced by permission of the AAS.

several galaxies, bar-driven gas inflows appear intimately tied to the formation of disky, high v/σ stellar components in the inner kpc, or 'pseudobulges' (Kormendy, 1993; Jogee, 1999; Kormendy & Kennicutt, 2004; Jogee et al., 2005; Athanassoula, 2005). Furthermore, the orbital structure of bars can lead to the observed peanut-shaped and boxy bulges in inclined galaxies (Combes et al., 1990; Pfenniger & Norman, 1990; Bureau & Athanassoula, 2005; Athanassoula, 2005; Martinez-Valpuesta et al., 2006; Debattista et al., 2006).

Earlier *Hubble Space Telescope* (*HST*) studies at optical wavelengths (e.g., Abraham et al., 1999) reported a paucity of stellar bars and a sharply declining optical bar fraction at intermediate redshifts $z > 0.5$. Studies at near-infrared (NIR) wavelengths also found a low bar fraction, but the authors rightly concluded that the large effective point spread functions (PSFs) of the NIR camera only allowed the detection of large bars whose semi-major axes exceeded $0.9''$, corresponding to 7.2 kpc[1] at $z \sim 1.0$ (Sheth et al., 2003). Recent works based on large optical surveys have now demonstrated the abundance of bars at intermediate redshifts $z \sim 0.2$–1.0, corresponding to lookback times of 3–8 Gyr (Elmegreen et al., 2004; Jogee et al., 2004; Zheng et al., 2005; Sheth et al., 2008). The fundamental issue of how robust bars are, and the associated implications for bar-driven evolution in disks over the last 10 Gyr, remains open (e.g., Jogee et al., 2004; Shen & Sellwood, 2004; Athanassoula, 2005; Bournaud et al., 2005; Berentzen et al., 2006; Berentzen & Shlosman,

[1]We assume in this paper a flat cosmology with $\Omega_M = 1 - \Omega_\Lambda = 0.3$ and H_0 =70 km s^{-1} Mpc^{-1}.

2006; Martinez-Valpuesta et al., 2006; Debattista et al., 2006).

In order to put bars in a cosmological context, it now behooves us to characterize the frequency and impact of bars by applying the *same quantitative* methods to large samples at $z \sim 0$ and at higher redshifts. Spurred by these considerations, we characterize in this paper the frequency and structural properties of bars in the local Universe at optical and NIR wavelengths, by ellipse-fitting the B and H images of the OSU Bright Spiral Galaxy Survey (OSUBSGS; Eskridge et al., 2002) of 180 spirals. The first goal of this study is to provide *quantitative* characterizations of the bar fraction $f_{\rm bar}$ (defined as the fraction of disk galaxies that are barred) and structural properties (sizes, ellipticities, etc.) of bars at $z \sim 0$, as a function of wavelength, Hubble types, and host galaxy properties. Furthermore, with the advent of high redshift *HST* surveys, such as the Tadpole field (Tran et al., 2003), the Galaxy Evolution from Morphology and SEDs (GEMS; Rix et al., 2004), the Great Observatories Origins Deep Survey (GOODS; Giavalisco et al., 2004), and COSMOS (Scoville et al., 2007), which trace bars in the rest-frame optical band out to $z \sim 1$, it becomes increasingly important to provide a reference baseline for bars at $z \sim 0$ in the optical band. Thus, a second goal of our study is to provide *a rest-frame optical* $z \sim 0$ point for bars based on ellipse fits, in order to directly compare with studies of intermediate-redshift bars (Jogee et al., 2004; Elmegreen et al., 2004; Zheng et al., 2005; Sheth et al., 2008) that also use ellipse fits. In particular, we use in this paper the same procedure of ellipse fits (§ 2.3.1) and the same quantitative characterizations (§2.3.3) of bars that were

applied by Jogee et al. (2004) to bars at intermediate redshifts ($z \sim 0.2$–1.0) in the GEMS survey.

Several studies have used the OSUBSGS to gauge bars in the local Universe (e.g., Eskridge et al., 2000; Block et al., 2002; Whyte et al., 2002; Buta et al., 2005), but they differ significantly from our study and cannot meet our two goals. Eskridge et al. (2000) visually classified bars in the H band, and in the B band, they used the Third Reference Catalog of Bright Galaxies (de Vaucouleurs et al., 1991, hereafter RC3) visual bar classes. Such visual classifications form an invaluable first step, but by definition, are subjective and difficult to compare with results from other studies. Block et al. (2002) and later Buta et al. (2005) applied the gravitational torque $Q_{\rm b}$ method, based on Fourier amplitudes, to H-band images of 163 and 147 OSUBSGS galaxies, respectively. This quantitative method is less subjective than visual classification, but the results of Block et al. (2002) and Buta et al. (2005) cannot be compared to intermediate redshift studies for two reasons. First, the latter studies were based on the *HST* Advanced Camera for Surveys (ACS) data and trace the rest-frame optical properties of bars, while Block et al. (2002) and Buta et al. (2005) deal with the rest-frame NIR. Second, it is non-trivial to derive $Q_{\rm b}$ for intermediate-redshift galaxies because of resolution and signal-to-noise limitations. Whyte et al. (2002) fitted ellipses to B-band images of only 89 of the 180 OSUBSGS galaxies, and do not provide a distribution of bar properties as a function of Hubble type. Our present study complements these existing studies by ellipse fitting B-band and H-band images of all 180

OSUBSGS galaxies, and performing a comprehensive, statistically significant analysis of barred galaxies in the local Universe. It complements the ongoing analysis (BJM08) of local bars based on a sample of 5000 galaxies in the Sloan Digitized Sky Survey (SDSS).

The outline of this paper is as follows. §2.2 discusses the sample selection based on the OSUBSGS survey (Eskridge et al., 2002). §2.3 describes the ellipse-fitting method, the criteria used for identifying bars, and deprojection of images and profiles to face-on. In §2.4.1–2.4.4, we present results on the bar fraction at $z \sim 0$, its dependence on Hubble type, the distribution of bar sizes and strengths as characterized by ellipse-fitting, and the variation of bar properties along the Hubble sequence. Results are presented both before and after deprojection to face-on. In §2.4.5, we present a first-order comparison of the bar fraction and properties at $z \sim 0$ from OSUBSGS to those derived at $z \sim 0.2$–1.0 or lookback times of 3–8 Gyr from GEMS (Jogee et al., 2004) and the Tadpole field (Elmegreen et al., 2004). In §2.4.6, we discuss the constraints set by our results for theoretical models addressing the robustness of bars, and the assembly of the Hubble sequence over cosmological times. §2.5 presents the summary and conclusions.

2.2 Data and Sample

The OSUBSGS targets local spiral galaxies that are taken from the RC3 catalog and chosen to represent the bright disk galaxy population in the local universe (Eskridge et al., 2002). The galaxies are selected using the following

criteria: RC3 type of S0/a or later, ($0 \leq$ T ≤ 9), $M_B < 12$, $D_{25} < 6'.5$, and $-80^\circ < \delta < +50^\circ$ (Eskridge et al., 2002), and are imaged in the B, V, R, H, J, and K bands. The B and H images of 182 OSUBSGS galaxies are available as part of a public data release (Eskridge et al., 2002). Our starting sample (sample S1) consists of the afore-mentioned 182 OSUBSGS galaxies with B and/or H images. After discarding galaxies (2 galaxies or 1% of sample S1) that do not have images in both the B and H bands, we are left with sample S2 of 180 galaxies imaged in both bands. This constitutes the sample of galaxies to which we fitted ellipses in order to characterize bars and disks, as outlined in §2.3.

2.3 Method for Characterizing Bars and Disks

We adopt the widely used procedure of characterizing bars and disks in galaxies via ellipse fits (e.g., Wozniak et al., 1995; Friedli et al., 1996; Regan et al., 1997; Mulchaey & Regan, 1997; Jogee, 1999; Jogee et al., 2002a,b, 2004; Knapen et al., 2000; Laine et al., 2002; Sheth et al., 2003; Elmegreen et al., 2004), as described in detail in §2.3.1. Our analysis procedure is schematically illustrated in Figure 2.1 and described in sections 2.3.1 to 2.3.4.

2.3.1 Ellipse Fitting

We start with the sample S2 of 180 galaxies imaged in both the B and H bands (Fig. 2.1). We first remove stars from the B- and H-band images of each galaxy by replacing them with the average of the sky background using

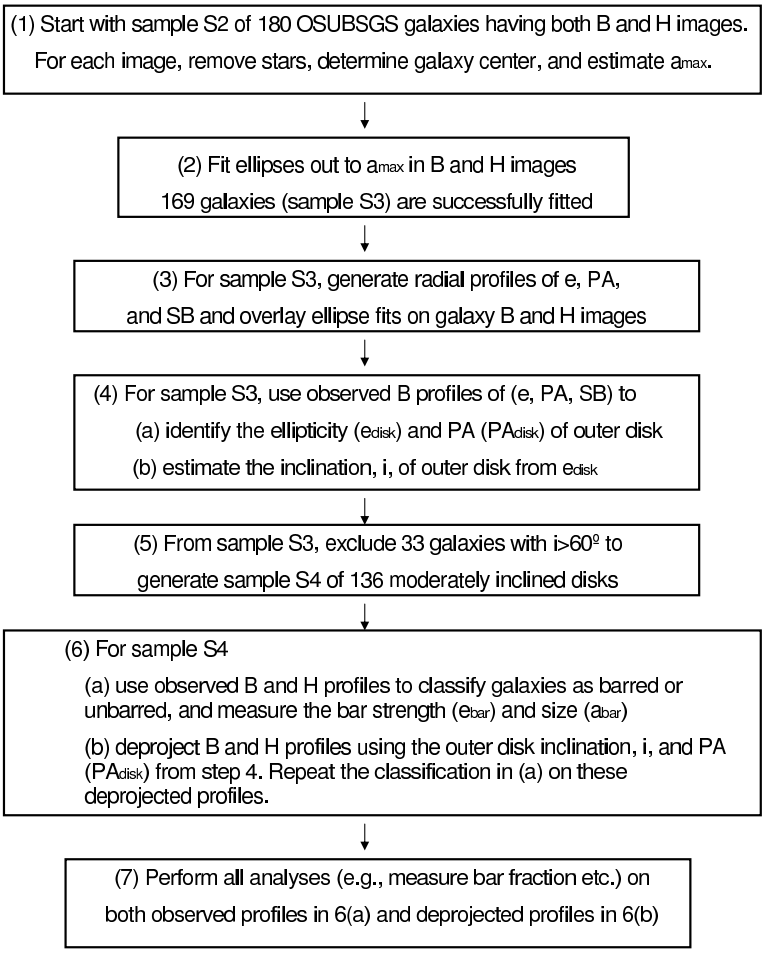

Figure 2.1 Analysis steps for characterizing bars and disks at $z \sim 0$ from OSUBSGS.

a circular aperture. We then find the center of the galaxy using the IRAF routine 'imcenter'. We determine a maximum galaxy semi-major axis length ($a_{\rm max}$) out to which ellipses will be fitted in each image by finding out where the galaxy isophotes reach the sky level.

We then use the standard IRAF task 'ellipse' to fit ellipses to each image out to $a_{\rm max}$. We employ an iterative wrapper developed by Jogee et al. (2004) to run 'ellipse' up to to 300 times for each object in order to get a good fit across the whole galaxy. A successful fit is one where the routine is able to fit a ellipse at each radial increment from the center until it reaches $a_{\rm max}$. When using the iraf task 'ellipse' for ellipse fits, the goodness of the best fit is measured by four harmonic amplitudes (A3, A4, B3, B4), which describe by how much the actual isophote differs from the best-fitting ellipse (e.g., Jedrzejewski, 1987). We have inspected plots of these residuals for representative strongly and weakly barred galaxies (e.g., NGC 4314, NGC 613, NGC 1187, NGC 0210, NGC 1300, NGC 7479, NGC 5701, NGC 4643, NGC 4548, NGC 4450, NGC 3681, NGC 3275, NGC 1703, and NGC 1358). We find that the A3 and B3 residuals are small, typically on the order of a few percent. Values for the A4 and B4 residuals typically range from 2% to 10%, and do not exceed 15%.

From the final fit for each galaxy, we generate radial profiles of surface brightness (SB), ellipticity (e), and position angle (PA). The fitted ellipses are over-plotted onto the galaxy images to generate overlays. Examples of the radial plots and overlays are shown in Figures 2.2, 2.4, and 2.5. For each

galaxy, an interactive visualization tool (Jogee et al., 2004) is used to display both the radial profile and the overlays in order to perform an extra inspection of the fits.

Of the 180 galaxies in sample S2, 179 (99%) and 169 (94%) were successfully fitted in the H and B band, respectively. Of the 11 galaxies that could not be fitted in the B band, five had strong morphological distortions and seem to be interacting; one had a very bright, saturated star with leakage; and five had no clearly defined center. The latter five galaxies were all of later Hubble type (Sbc and Sc), and had very flat or irregular surface brightness profiles in the B band. Further analyses to characterize inclined, unbarred, and barred disks in §2.3.2 were then restricted to the sample S3 of 169 galaxies with successful fits in both the B and H bands (Fig. 2.1).

2.3.2 Identifying and excluding highly inclined spirals

For sample S3, we use the B-band images, rather than the H-band images, to identify and characterize the outer disk because the former are deeper and trace the disk farther out. From the radial profiles generated by ellipse-fitting the B-band image, we measure the ellipticity ($e_{\rm disk}$) and PA ($\rm PA_{disk}$) of the outer disk. The outer disk inclination, i, is derived from $e_{\rm disk}$ using $\cos(i) = (1 - e_{\rm disk})$. Of the 169 galaxies in sample S3, we find 33 (20%) galaxies with disk inclination $i > 60^{\circ}$ and classify them as 'inclined'. They are listed in the lower part of Table 2.5. Figure 2.2 shows an example of the B-band radial profile and ellipse overlays for an inclined galaxy.

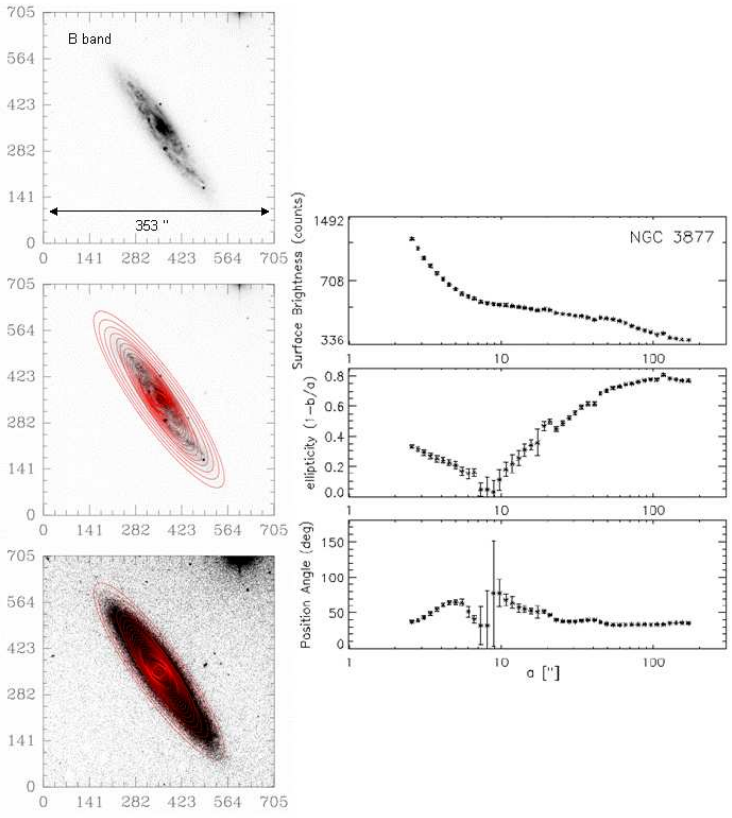

Figure 2.2 **Left:** Ellipse fits on the B-band image of NGC 3877, where the middle and bottom panels show grayscale stretches chosen to emphasize the inner and outer regions of the galaxy, respectively. **Right:** The radial profiles of surface brightness (SB), ellipticity (e), and position angle (PA). The profiles show evidence for some structure in the inner regions, but at $a > 100''$, the e settles to a high value of 0.8, while the PA also settles to a constant value (the signature of an inclined disk with $i > 60°$).

We only use the final sample S4 (Fig. 2.1) of 136 moderately inclined ($i < 60°$) spirals to further characterize the properties of bars (e.g., size, ellipticity, frequency) and disks in §2.3.3–2.3.4. Such an inclination cutoff is routinely applied in morphological studies because projection effects make it very difficult to reliably trace structural features in a galaxy that is close to edge-on. The exclusion of highly inclined galaxies does not bias the distribution of Hubble types, as shown in Figure 2.3a, where the Hubble types of samples S3 and S4 are compared. The absolute V-band magnitudes ($M_{\rm V}$) of both sample S3 and S4 cover the range -18 to -23, with most galaxies lying in the range $M_{\rm V} \sim$ -20 to -22 (Fig. 2.3b).

2.3.3 Characterizing bars and disks before deprojection

In §2.3.4, we use the *deprojected* radial profiles of (SB, e, PA) to characterize the intrinsic properties of bars and disks in sample S4. However, we also decide to first perform the analysis on the *observed* radial profiles *before* deprojecting them to face-on. There are several reasons for this dual approach of deriving bar properties both before and after deprojection. First, it is useful to have bar properties (e.g., frequency, strength as characterized by ellipse-fitting, size) prior to deprojection to compare directly to studies at intermediate redshifts (Jogee et al., 2004; Elmegreen et al., 2004; Zheng et al., 2005), where deprojection is not done for several reasons, including the difficulty in accurately measuring the PA of the line of nodes and the inclination of the outer disk in noisy images of distant galaxies. Second, by having bar

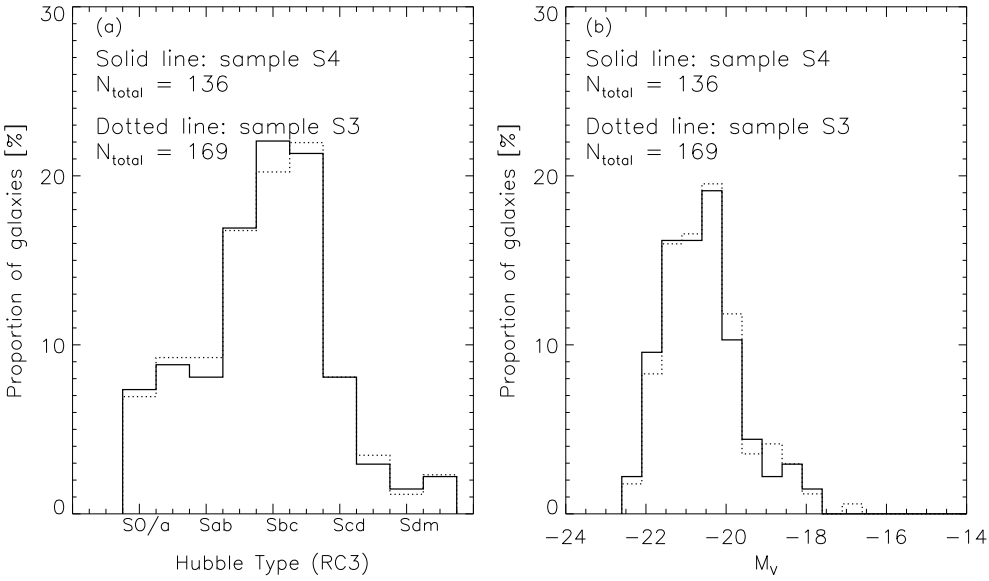

Figure 2.3 **Left:** The distributions of RC3 Hubble types are shown for the sample S4 (solid line) of 169 galaxies that include inclined systems, and for the sample S3 (dotted line) produced by excluding 33 galaxies with high inclination ($i > 60°$). This exclusion does not significantly affect the Hubble type distribution of the sample. **Right:** The distributions of absolute V-band magnitudes for sample S4 (solid line) and S3 (dotted line) are similar as well.

properties both before and after deprojection, we are able to assess whether deprojection makes a substantial difference to the statistical distributions of bar properties. A large difference would raise concerns for intermediate redshift studies or even for large nearby studies where deprojection is often not carried out.

For sample S4, we use the observed radial profiles of (SB, e, PA) and the ellipse overlays to classify galaxies as 'unbarred' (Fig. 2.4) or 'barred' (Fig. 2.5), according to the following quantitative criteria. A galaxy is classified as barred if the radial variation of ellipticity and PA follows the behavior that is expected based on the dominant orbits of a barred potential. Specifically the following conditions must be satisfied before a galaxy is deemed to be barred: (1) The ellipticity, e, increases steadily to a global maximum, $e_{\rm bar}$, greater than 0.25, while the PA value remains constant (within 10°). This criterion is based on the fact that the main bar-supporting orbits, namely the 'x_1' family of orbits, can be modeled by concentric ellipses with a constant PA as a function of radius in the bar region (Athanassoula, 1992a). The requirement that the PA must remain constant in the bar region is important for excluding other spurious elliptical features that may mimic a bar signature in their ellipticity profile. (2) Then, at the transition from the bar to the disk region, the ellipticity, e, must drop by at least 0.1, and the PA usually changes. This criterion is justified by the fact that we expect a transition from the highly eccentric x_1 orbits near the bar end to the more circular orbits in the disk. We also note that the drop in ellipticity by 0.1 at the transition from bar to disk has been

shown to work well in identifying bars (e.g., Knapen et al., 2000; Laine et al., 2002; Jogee et al., 2002a,b, 2004).

What are the limitations of criteria (1) and (2) in identifying bars? We note that the 'constant PA' criterion that we use to identify bars may cause us to miss some weak bars at optical wavelengths due to the following reason. In weak bars, the shock loci and corresponding dust lanes on the leading edge of the bar are curved (Athanassoula, 1992b). In optical images of weak bars, these curved dust lanes may cause the PA to twist or vary slightly along the bar, thereby preventing the 'constant PA' criterion from being met. In the case of very strong bars, the 'constant PA' criterion is a good one and isophotal twist is not an issue, because such bars have strong shocks and straight dust lanes along their leading edges (Athanassoula, 1992b). In order to gauge how many bars we might be missing because of the 'constant PA' criterion, we identify galaxies that show a PA twist accompanied by an ellipticity maximum. It turns out that only a small fraction ($\sim 7\%$) of galaxies show this effect.

We also note that criterion (1) requires the peak ellipticity (e_{bar}) over the PA plateau to be greater than 0.25 before we call a feature a bar. We picked 0.25 for the practical reason that structures with lower ellipticities are quite round and not always readily distinguishable from disks. Nonetheless, one may be tempted to ask whether we would find more bars if this arbitrary limit of 0.25 were to be lowered, and whether there is a population of low-ellipticity (e.g., $e_{\rm bar} \sim 0.10$–0.25) bars that we might miss. We investigated this question using the OSUBSGS sample, and find that there is no increase in the number

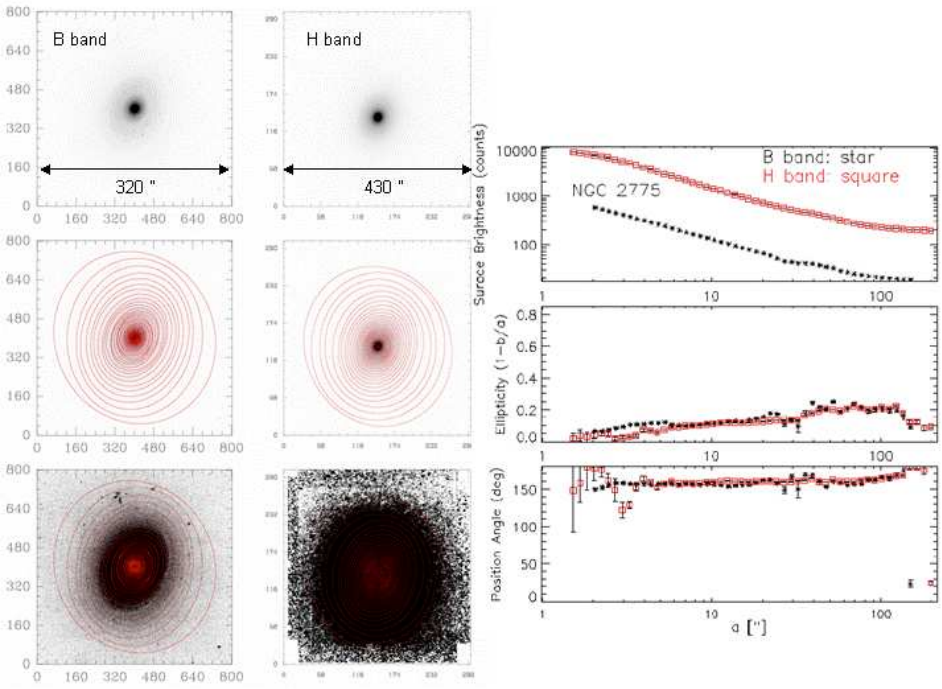

Figure 2.4 **Left and middle panels:** Ellipse-fits overlayed on the B- and H-band images of the unbarred galaxy NGC 2775. The scales of the B and H images are shown in the top image panels for each band. $1''$ corresponds to 86 pc at the galaxy distance of 17 Mpc. Within each panel, there are three images with different greyscale stretches that are chosen to emphasize the inner (middle image) and outer (bottom image) regions of the galaxy. Note that ellipses are fitted out to the sky level in the image. **Right panel:** This shows the radial profiles of (SB, e, and PA) for the B (stars) and H (squares) bands, derived from the ellipse fits prior to deprojection. The profiles do not show any characteristic bar signatures, such as a smooth rise in e to a maximum above 0.25, concurrent with a PA plateau. The e remains below 0.25 across the galaxy. There is no signature of large-scale structure, such as spiral arms or a bar.

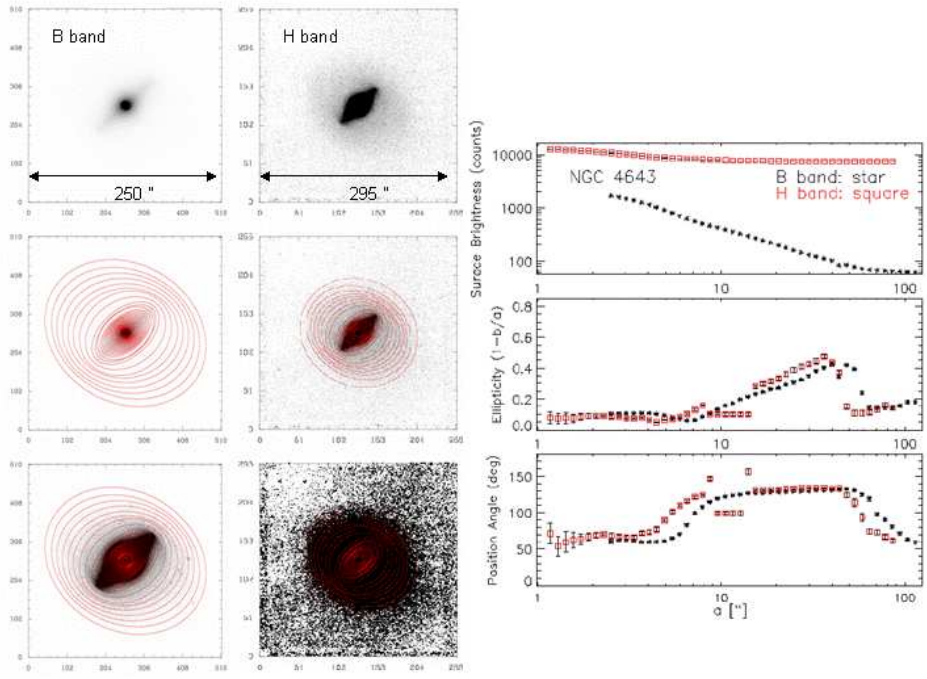

Figure 2.5 **Left and middle panels:** Ellipse-fits overlayed on the B- and H-band images of the barred galaxy NGC 4643. The scales of the B and H images are shown in the top image panels for each band. $1''$ corresponds to 130 pc at the galaxy distance of 26 Mpc. Within each panel, there are three images with different greyscale stretches that are chosen to emphasize the inner (middle image) and outer (bottom image) regions of the galaxy. Note that ellipses are fitted out to the sky level in the image. **Right panel:** This shows the radial profiles of (SB, e, and PA) for the B (stars) and H (squares) bands, derived from the ellipse fits and prior to deprojection. The profiles show a clear bar signature. Between $15''$ and $40''$, the e rises smoothly to a global maximum of 0.5, while the PA remains roughly constant. The e then drops to ~ 0.1, and the PA changes at the transition from the bar to the disk region.

of bars if the limiting value for $e_{\rm bar}$ in criterion (1) were to be lowered from 0.25 to 0.10. The reason for this becomes clear later, in Figure 2.13, which shows that the number of bars already starts to drop rapidly for ellipticities below 0.40, such that by the time we reach $e_{\rm bar}$ of 0.25, we are already probing the tail end of bar distributions.

In addition to classifying galaxies as 'barred' and 'unbarred', we also use the radial profiles to derive the structural properties of the bar and disk. Specifically, for all galaxies, we measure the ellipticity, PA, and semi-major axis of the outer disk ($e_{\rm disk}$, $\rm PA_{disk}$, $a_{\rm disk}$). For galaxies classified as 'barred', we also measure the maximum ellipticity (e_{bar}), the PA, and the semi-major axis of the bar. We will discuss in §2.4.3 how the maximum bar ellipticity ($e_{\rm bar}$) constrains the bar strength. Here, we discuss the question of how to locate the end of the bar in order to measure the bar semi-major axis. There has been some discussion in the literature as to whether the bar end should be defined as the radius ($a_{\rm bar}$) where the bar ellipticity is a maximum, or as the radius where the PA changes abruptly at the transition from the bar to the disk. From a theoretical perspective, several early simulations (e.g., Athanassoula, 1992a; O'Neill & Dubinski, 2003) show that the definition of bar length based on 'peak ellipticity' can underestimate the true extent of the bar. Recently, Martinez-Valpuesta et al. (2006) have performed a systematic study of the radius ($a_{\rm bar}$) of maximum bar ellipticity and the bar length. They show that there is a very good correspondence between two independent methods to determine the bar size: ellipse fitting and orbital analysis. The orbital analysis

has involved finding the largest (Jacobi) energy x_1 orbit in the bar that is still stable. The ellipse fitting becomes better if the size of the bar is given by the radius where the ellipticity declines by 15% from its maximal value.

In his empirical study of bar sizes using ellipse fits, Erwin (2005) argues that using the PA signature to define the bar size provides an upper limit, and that the two measures of bar length are very well correlated. However, he finds that it is harder to unambiguously measure the bar size from the PA criterion and that the definition of bar size based on peak ellipticity is more readily applied consistently to a large number of different galaxy morphologies Erwin (2005). In this study, we have adopted the first approach. We use the semi major axis ($a_{\rm bar}$) where the maximum bar ellipticity occurs as a measure of the bar length. We caution that this may underestimate the bar length in some galaxies. However, a visual comparison of $a_{\rm bar}$ with the images of our galaxies suggests that $a_{\rm bar}$ does a reasonable job in most cases.

2.3.4 Characterizing bars and disks after deprojection

For sample S4, we use the inclination, i, and the PA of the outer disk (determined in §2.3.2) to *analytically* deproject the observed H and B band radial profiles of (e, PA) to face-on. We perform the analytical deprojection using a code developed by Laine et al. (2002) and used previously in Laine et al. (2002) and Jogee et al. (2002a,b). It should be noted that the deprojection formula used in the code only strictly applies to infinitesimally thin structures, and may be inaccurate near the galaxy center in the vicinity of the bulge.

However, it is a reasonable approximation in the region of interest where large-scale bars reside. Figure 2.6 shows an example of the deprojected radial profiles of NGC 4548 in the B and H bands overlaid on the observed profiles.

We note that the process of analytically deprojecting the radial *profiles* to face-on after ellipse-fitting the observed (i.e, un-deprojected) images is analogous to the process of first deprojecting the observed *images* to face-on, and then ellipse-fitting the deprojected images in order to generate face-on radial *profiles*. The two methods should yield the same results unless the images are very noisy. We verified this expectation with the following steps. (1) We deproject the *images* of several galaxies using the Multichannel Image Reconstruction, Image Analysis and Display (MIRIAD) routine 'deproject'. The routine takes as input the observed image, the galaxy center, the inclination i and PA of the outer disk, and outputs the deprojected image; (2) We then fit ellipses to these deprojected images using the procedure outlined in §2.3.1, and generate face-on radial profiles of SB, e, and PA; (3) These face-on radial profiles generated from the deprojected images, are compared with the deprojected radial profiles derived analytically from the the observed profile. There is good agreement in all cases, showing that we are not noise limited.

This is illustrated in Figure 2.7 for the B band image of NGC 4548. The observed and deprojected images are shown in the left panel. In the right panel, three radial profiles are plotted: the observed radial profile derived by fitting ellipses to the observed image is plotted as stars; the deprojected radial profile derived analytically from the observed profile is plotted as squares; and

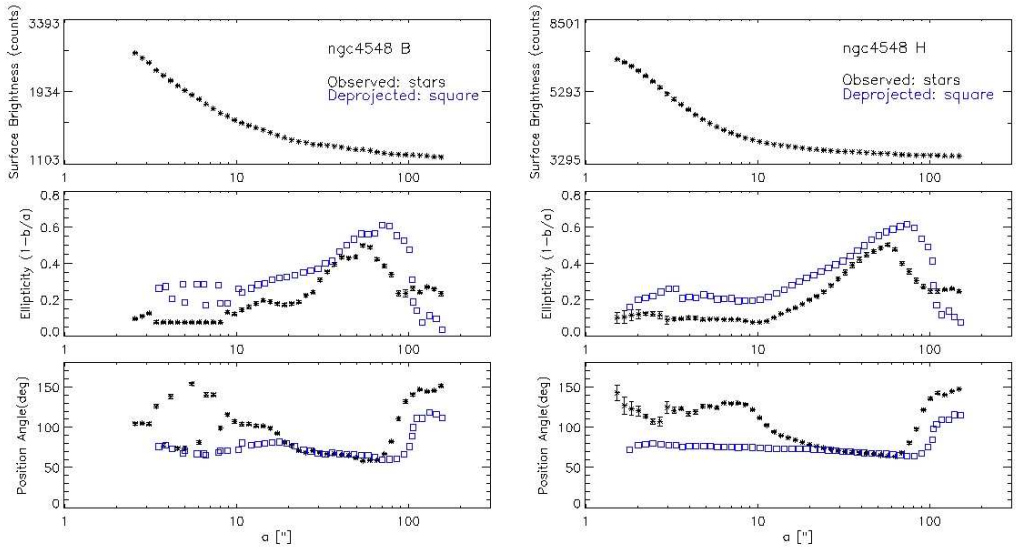

Figure 2.6 For galaxies in sample S4, we use the inclination i and the PA of the outer disk (from §2.3.2) to analytically deproject the observed H- and B-band radial profiles of (e, PA) to face-on. The case for NGC 4548 is illustrated here. The left panel shows the observed (stars) and deprojected (squares) radial profiles in the B band. The right panel shows the observed and deprojected radial profiles in the H band. After deprojection, as expected, the outer disk e is nearly zero in the B band. Note also that the bar size is slightly different and the bar appears somewhat stronger in both bands after deprojection.

the face-on radial profile derived by fitting ellipses to the deprojected image is plotted as triangles. There is good agreement between the squares and the triangles.

The deprojected profiles provide an accurate characterization of the 'intrinsic' or face-on properties of disks and bars. For all galaxies in S4, we therefore use the analytically deprojected B and H radial profiles to classify galaxies as 'barred' or 'unbarred', according to the criteria outlined in §2.3.3. We also re-measure the bar ellipticity (e_{bar}), semi-major axis (a_{bar}), and disk size $a_{\rm disk}$ from the deprojected radial profile. In the rest of this paper, many of these deprojected quantities will be compared to those derived before deprojection (§2.3.3) in order to gauge the impact of deprojection.

2.4 Results and Discussions

2.4.1 The optical and NIR bar fraction at $z \sim 0$

Table 2.5 and Figure 2.8 show the bar fraction (defined as the fraction of spiral galaxies that are barred) for the B and H bands, both before (§2.3.3) and after deprojection (§2.3.4). The results are based on sample S4 of 136 moderately inclined ($i < 60°$) spirals (§2.3.2). The sample is dominated by galaxies with $M_{\rm V} \sim$ -20 to -22. We find a deprojected bar fraction of 60% in the H band and a lower fraction of 44% in the B-band images, which likely miss bars obscured by dust and star formation. Our results that 60% of spirals are barred in the infrared confirms the preponderance of bars among spirals in the local Universe.

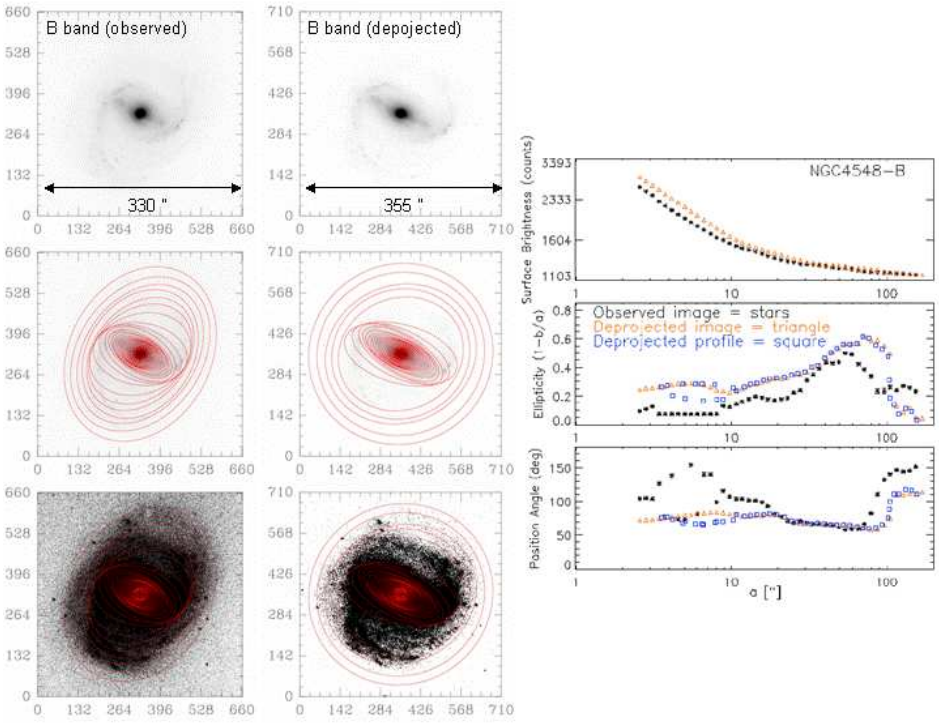

Figure 2.7 For the B-band image of NGC 4548, this figure compares the face-on radial profiles of e and PA generated via two different methods. In the first method, ellipses are fitted to the observed image (left panel) to generate the observed radial profile (plotted as stars in the right panel), which is then analytically deprojected to produce the face-on profile (plotted as squares in the right panel). In the second method, the observed image is deprojected with MIRIAD and the resulting deprojected image (middle panel) is fitted with ellipses to generate the second face-on profile (plotted as triangles in the right panel). Note the good agreement between the squares and triangles.

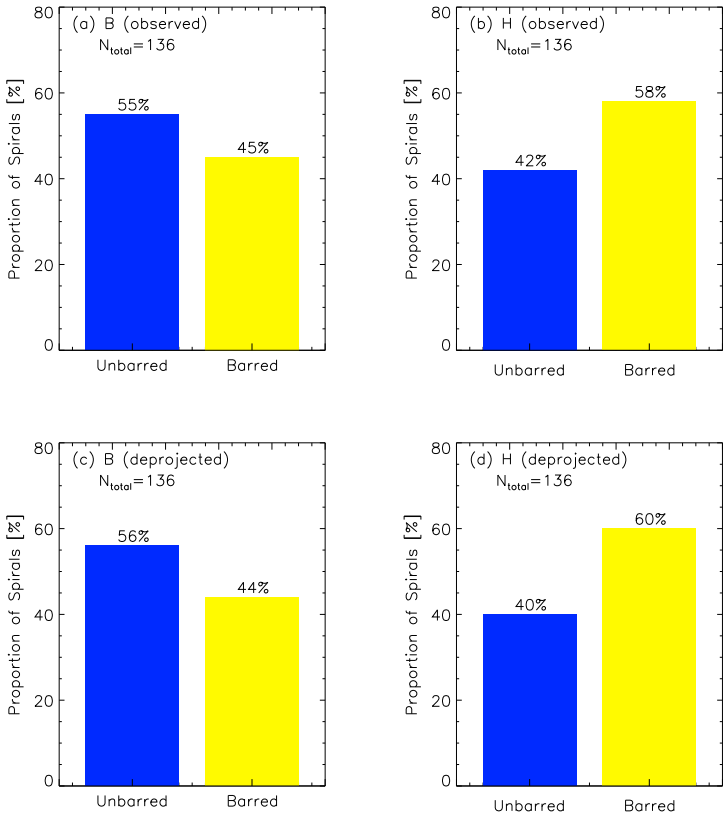

Figure 2.8 We show the fraction of spirals that are barred in the B and H bands, based on ellipse fits of 136 moderately inclined galaxies (sample S4), followed by quantitative characterization of the resulting radial profiles of (e, SB, PA). Top row: The observed bar fraction before deprojection is 45% in the B band (left) and 58% in the H band (right). Bottom row: The deprojected bar fraction is 44% in the B band (left) and 60% in the H band (right).

Our deprojected H-band bar fraction of 60% is consistent within a margin of 12% with the results of Eskridge et al. (2000), who visually inspected the OSUBSGS H-band images and reported an overall H-band bar fraction of 72%, with 56% of spirals hosting 'strong' bars and 16% hosting 'weak' bars. Why is there a 12% deviation? The Eskridge et al. (2000) paper does not give 'barred' or 'unbarred' classifications for individual galaxies, so we can not make a case by case comparison with that study. However, in a subsequent paper, Eskridge et al. (2002) give visual classifications of individual galaxies as barred or unbarred, and classify barred systems as 'SB' (strongly barred) and 'SAB' (weakly barred). We find that our classifications as barred or unbarred disagree on 25 galaxies in the B band ($\sim$ 18% of sample S4), and 23 galaxies in the H band ($\sim$ 17% of sample S4). Of the galaxies in the B band and H band where we differ, we find that the majority (15 of the 25 galaxies in the B band, and 11 of the 23 galaxies in the H band) are classified as 'SAB' (weakly barred) by Eskridge et al. (2002). We conclude that, as might be intuitively expected, the differences between visual and quantitative classifications of bars are strongest for systems that visually appear as 'weakly barred'.

How does our study compare with other quantitative studies? We find that our reported H-band bar fraction of 60% agrees with that of Laurikainen et al. (2004b), who used Fourier modes and the $Q_{\rm b}$ method for 158 galaxies in the OSUBSGS sample and 22 2MASS galaxies. Laurikainen et al. (2004b) find a NIR bar fraction of 62% for galaxies with $i < 60^{\circ}$. We present a more detailed comparison of our bar ellipticity and fraction with other studies in

§2.4.3.

Another important result is that deprojection does not make any significant changes to the global bar fraction, when dealing with the fairly large OSUBSGS sample. As shown by Table 2.5 and Figure 2.8, the B- and H-band bar fractions are 45% and 58% before deprojection, and change by only a factor of 0.97 and 1.03, respectively, after deprojection. We suggest several reasons for the small impact of projection effects. First, this study uses only moderately inclined ($i < 60°$) galaxies where projection effects are less severe than in highly inclined systems. Second, projection effects produce large changes in the morphology of a galaxy only when the disk inclination, i, is significant *and* the difference in PA between the bar and the disk major axes is close to 90°. From a statistical point of view, these two conditions are unlikely to occur simultaneously in a dominant fraction of the sample. These arguments are supported by Figures 2.9a and 2.9b, which show that the galaxy classes assigned prior to deprojection are in no way biased by the galaxy inclination, i: both barred and unbarred galaxies span a similar range in i. Furthermore, even the bar ellipticity $e_{\rm bar}$ measured before deprojection is uncorrelated with i (Figs. 2.9c and 2.9d).

The fact that the bar fraction in large samples is similar before and after deprojection is encouraging for large studies of bars at intermediate redshift (e.g., Jogee et al., 2004; Elmegreen et al., 2004; Zheng et al., 2005), where deprojection is not done because of the difficulty in accurately measuring the PA of the line of nodes and the inclination of the outer disk in noisy images

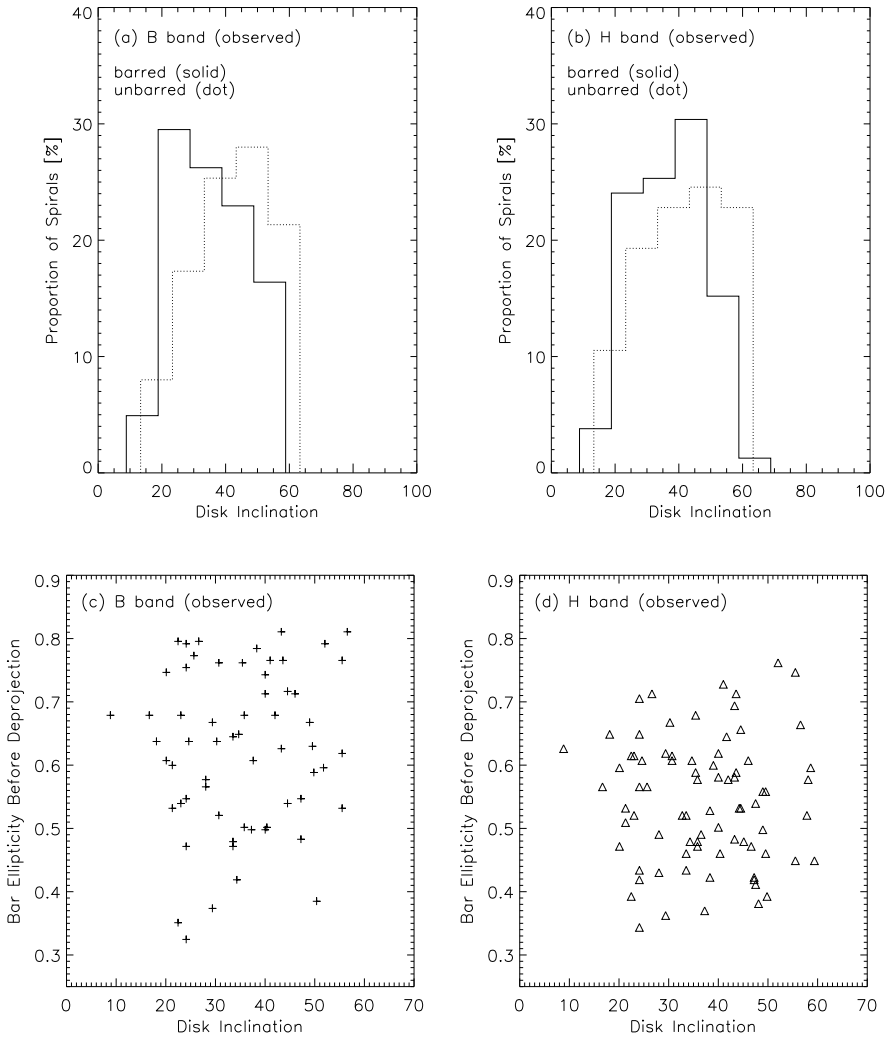

Figure 2.9 The distributions of inclination i for galaxies that were classified as 'barred' or 'unbarred', prior to deprojection, **(a)** in the B band and **(b)** H band. Note that there is no correlation with i. The measured bar ellipticity $e_{\rm bar}$ is shown **(c)** in the B band and **(d)** H band, prior to deprojection, are plotted against the galaxy inclination i. Note that there is no correlation between $e_{\rm bar}$ and i.

of distant galaxies.

2.4.2 Sizes of bars and disks at $z \sim 0$

As outlined in §2.3.1, we use the semi major axis $a_{\rm bar}$, where the bar ellipticity is a maximum, as a measure of the bar length. We caution that this may underestimate the bar length in some galaxies. However, a visual comparison of $a_{\rm bar}$ with the images of our galaxies suggests that $a_{\rm bar}$ does a reasonable job in most cases.

The distributions of bar sizes or semi-major axes ($a_{\rm bar}$) before and after deprojection are shown for the B and H bands in Figure 2.10. Some bars do appear larger after deprojection, but from a statistical point of view, deprojection does not have a substantial effect on the bar size distribution. For example, the mean bar size in the H band before deprojection is 3.4 kpc and after deprojection it is 4.0 kpc. Sizes of large-scale bars in the local Universe lie in the range $\sim$ 1 to 14 kpc, with most (68% in B and 76% in H) bars having $a_{\rm bar} \leq 5$ kpc, and $\sim$ 50% of them clustering with $a_{\rm bar}$ in the range 2 to 5 kpc. If such a distribution of bar sizes is present at a redshift $z \sim 1$, where $1''$ corresponds to 8.0 kpc, then only observations with angular resolutions superior to $0\farcs3$ can adequately resolve the majority of bars. This is relevant for assessing the relative effectiveness of current NIR capabilities, such as NICMOS, and those of future planned missions, such as WFC3, in detecting high redshift bars in the NIR band over wide fields.

In Figure 2.11, we plot the bar size versus the disk size before and after

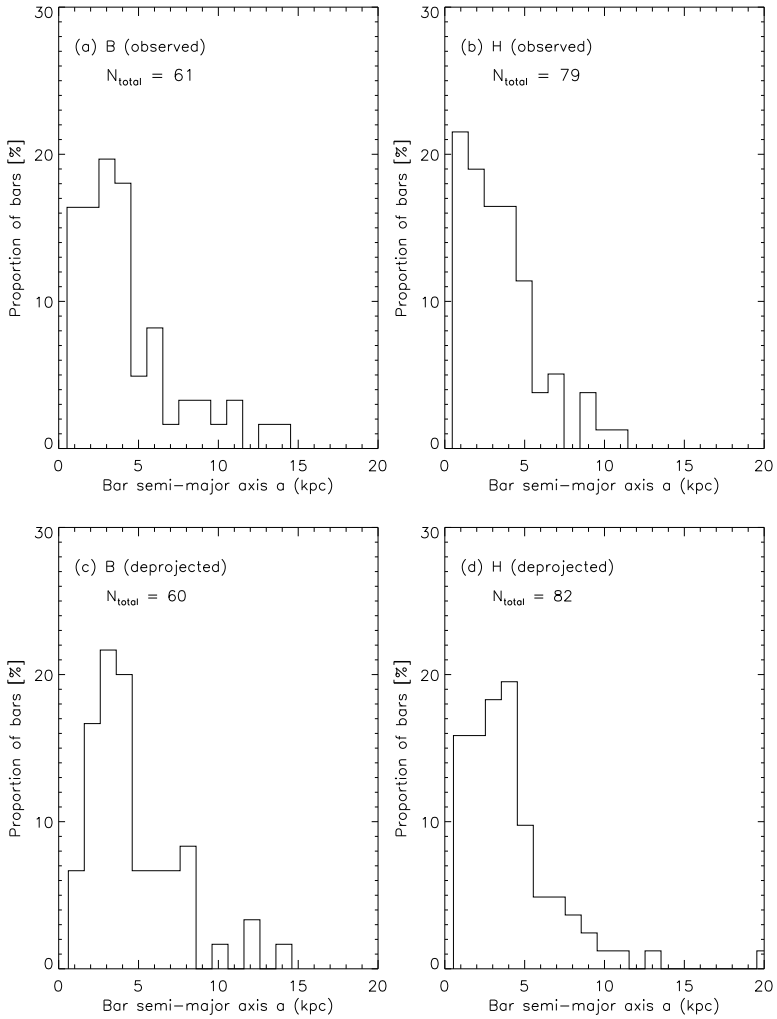

Figure 2.10 The distributions of bar semi-major axes ($a_{\rm bar}$) before (top row) and after (bottom row) deprojection are shown, for the B (left) and H (right) bands. Most (68% in B and 76% in H) bars have $a_{\rm bar} \leq 5$ kpc, and $\sim 50\%$ of them cluster in the range 2 to 5 kpc. Deprojection makes several bars appear somewhat larger, but does not otherwise produce a large change in the overall shape of the distributions.

deprojection. The bar size is measured from the H band, whose low extinction enables more accurate measurement than in the optical. The disk is measured from the B-band image, which is deeper than the H band and traces the disk further out (§2.3.2). Both before and after deprojection, we find that bar and disk sizes are correlated with an average slope of ~ 0.9, albeit with a large scatter of several kpc in bar size at a given disk size.

Figure 2.12 shows the observed bar semi-major axis distribution normalized to R_{25} (the radius in arcseconds of the isophote, where the surface brightness equals 25 mag arcsec^{-2}) of the disk. R_{25} values are obtained from the Nearby Bright Galaxies Catalogue (Tully, 1988, hereafter NBG), except for NGC 6753, 6782, 5078, 6907, 7814, and ESO 142-19, which are from the RC3. The ratio ($a_{\rm bar}/R_{25}$) lies primarily in the range 0.1 to 0.5 in both the H and B bands (Fig. 2.12). Only a minority of galaxies have larger values out to 0.95.

These results are consistent with several smaller earlier studies. Laine et al. (2002) find that the sizes of primary bars correlate with the host galaxy sizes and the ($a_{\rm bar}/R_{25}$) ratio lies primarily in the range 0.1 to 0.5. Menéndez-Delmestre et al. (2007) find an average ($a_{\rm bar}/R_{25}$) ratio of 0.35, on the basis of ellipse fits of 134 2MASS galaxies. In his study of bar lengths, based on ellipse fits of R-band images of 65 local early-type S0-Sab galaxies, Erwin (2005) finds a similar mean ($a_{\rm bar}/R_{25}$) ratio of 0.38 and reports a correlation between bar size and disk size.

What do these results imply? From a theoretical standpoint, the size

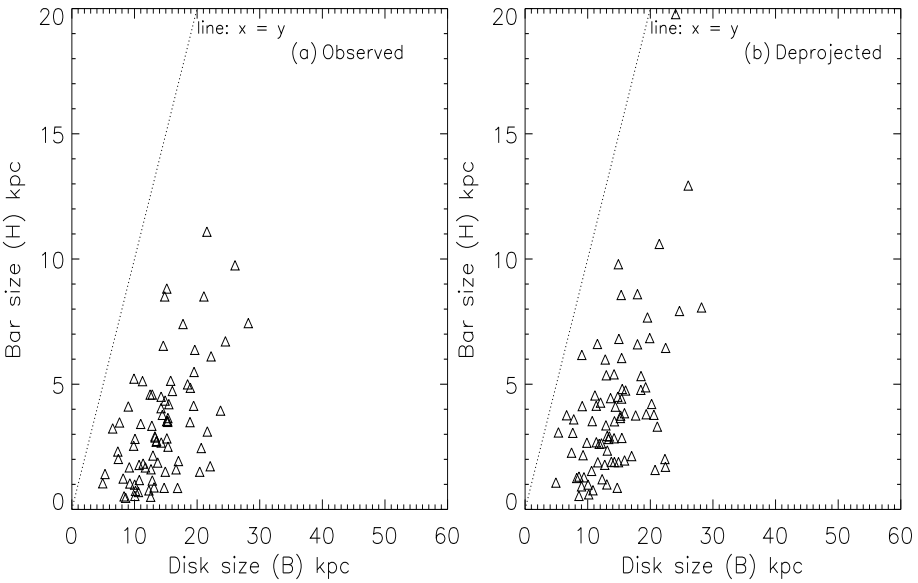

Figure 2.11 The bar semi-major axis in the H band is plotted versus the disk size before (left panel) and after (right panel) deprojection. The disk size is measured in the B-band image which is deeper than the H band and traces the disk further out. The deprojected bar and disk sizes are correlated with an average slope of ~ 0.9. However, there is a large scatter of several kpc in bar size at a given disk size. For comparison, the dotted line has slope of 1.

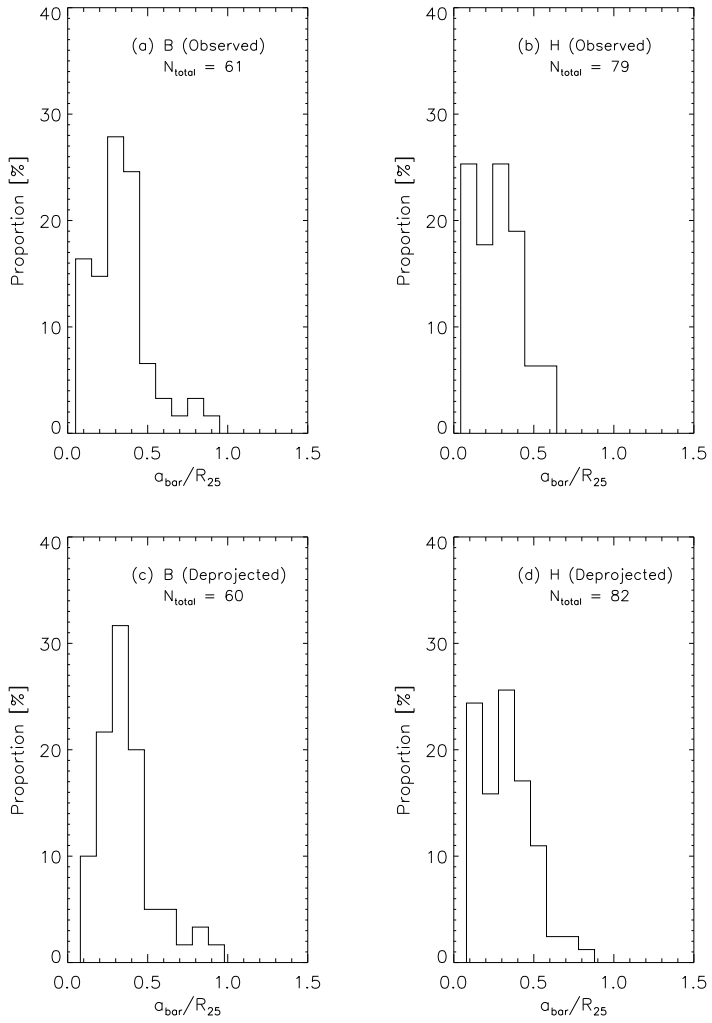

Figure 2.12 The ratio of the bar semi-major axis ($a_{\rm bar}$) to the isophotal radius (R_{25}) where the B-band surface brightness is 25 mag arcsec^{-2} is shown before (top row) and after (bottom row) deprojection. In the left panels, the bar size ($a_{\rm bar}$) is determined from the B-band image and in the right panels from the H-band image. We find that the ratio ($a_{\rm bar}/R_{25}$) is always below 1.0, and lies primarily in the range 0.2 to 0.4 in both H and B bands.

of the bar ($a_{\rm bar}$) depends on the concentration of matter in the disk and the distribution of resonant material that can absorb angular momentum from the bar (Athanassoula, 2003). Furthermore, the prevalence of chaotic orbits between the 4:1 and the corotation resonance (CR) would naturally lead bars to end somewhere between the two resonances. If bars end very near the CR as is found observationally (e.g., Merrifield & Kuijken, 1995; Debattista et al., 2002; Aguerri et al., 2003), then our result that ($a_{\rm bar}/R_{25}$) is generally well below 1.0 suggests that the CR of disk galaxies lies well inside their R_{25} radius. Furthermore, the correlation between bar and disk sizes and the narrow range in ($a_{\rm bar}/R_{25}$) suggests that the growths of the bar and disk may be intimately tied.

2.4.3 Distribution of bar strengths as characterized by $e_{\rm bar}$ at $z \sim 0$

The term 'bar strength' is not well defined in the literature. Various measures of bar strength are used and each measure has some benefits and trade-offs. These measures include the $Q_{\rm b}$ method (Block et al., 2002; Buta et al., 2003, 2005), the maximum ellipticity of the bar, bar/interbar contrasts, Fourier decomposition techniques (Elmegreen & Elmegreen, 1985; Elmegreen et al., 1996), and visual estimates of strength (e.g., Martin, 1995; Eskridge et al., 2000, 2002) gauged via eyeball inspection of images.

The $Q_{\rm b}$ method Block et al. (2002); Buta et al. (2003, 2005) directly measures the gravitational torque exerted by the bar, but it measures the torque at only one point along the bar. The $Q_{\rm b}$ method depends on the scale

height of the disk and the ability to derive a reliable model for the potential using images. It is hard to apply this method to a large number of intermediate redshift galaxies due to resolution and signal-to-noise limitations. In the bar/interbar contrast method used by Elmegreen & Elmegreen (1985) and Elmegreen et al. (1996), the bar strength is characterized by the ratio of the peak surface brightness in the bar region to the minimum surface brightness in the interbar region. The Fourier decomposition method also used by Elmegreen & Elmegreen (1985) and Elmegreen et al. (1996) is similar to the $Q_{\rm b}$ method. It characterizes bar strength by measuring the relative amplitudes of the Fourier components of the bar. The maximum amplitude of the m=2 mode determines the strength of a bar.

In studies where ellipse fits are used to characterize bars, the maximum ellipticity of the bar ($e_{\rm bar}$) is used as a measure of bar strength (e.g., Athanassoula, 1992a; Martin, 1995; Wozniak et al., 1995; Jogee, 1999; Jogee et al., 2002a,b; Knapen et al., 2000; Laine et al., 2002). One advantage of this approach is that the bar ellipticity can be estimated without making any assumptions about the mass to light ratio of the galaxy or its scale height. It can also be applied to local galaxies as well as galaxies out to intermediate redshifts ($z \sim 0.2$–1.0; Jogee et al., 2004; Elmegreen et al., 2004). There are also several theoretical reasons that support the use of the maximum bar ellipticity as a measure of bar strength. Shen & Sellwood (2004) compare bar strength in N-body simulations, as characterized by the $m = 2$ Fourier components and the peak ellipticity. They find that the ellipticity is very well

correlated to bar strength estimator A, where A is the relative amplitude of the bisymmetric ($m = 2$) Fourier component of the mass density averaged over a certain inner radial range where the bar dominates. In addition, from an observational standpoint, Laurikainen et al. (2002) find that, on average, the gravitational torque, $Q_{\rm b}$, and $e_{\rm bar}$ are correlated for $e_{\rm bar} \leq 0.6$. For higher $e_{\rm bar}$ values, the relation appears to flatten out although the small number of galaxies precludes a firm conclusion.

Nonetheless, if we deem that a measure of bar strength should give an indication of the gas inflow rate that a bar drives via gravitational torques, then the maximum ellipticity of the bar ($e_{\rm bar}$) is only a *partial* measure of the bar strength. Both the mass and shape of the bar influence the magnitude of the gravitational torque at each point along the bar. The peak bar ellipticity describes the shape of the bar, but does not directly measure its mass or luminosity. While bearing this caveat in mind, we use the maximum bar ellipticity $e_{\rm bar}$ as a partial measure of the bar strength in this study.

Figure 2.13 shows the observed and deprojected distributions of bar strength as characterized by $e_{\rm bar}$ from ellipse-fits in the B (Figs. 2.13a,c) and H bands (Figs. 2.13b,d). It is striking that only a very small proportion (7% in B; 10% in H) of bars are very weak with $0.25 \leq e_{\rm bar} \leq 0.40$, while the majority of bars (70% in B; 71% in H) have moderate to high strengths as characterized by $e_{\rm bar}$, with $0.50 \leq e_{\rm bar} \leq 0.75$. This point is further illustrated in Figure 2.14, which is a generalized plot of the fraction of disks with 'strong' and 'weak' bars. It shows how the fraction of spiral galaxies that host bars with

ellipticities ($e_{\rm bar} > e_1$) changes as we vary e_1. As we increase e_1 from 0.35 to 0.45, 0.55, and 0.75, the deprojected bar fraction in the B band falls from 43% to 39%, 34%, and 7%, respectively. Correspondingly, the bar fraction in the H band falls from 59% to 47%, 30%, and 1%, respectively. The flattening of the curve around $e_1 \sim 0.40$ shows that the majority of bars have $e_{\rm bar}$ above this value. This has implications for theoretical models that address the robustness of bars, and we refer the reader to §2.4.6 for a discussion.

How do our results on bar strength as characterized by the maximum bar ellipticity $e_{\rm bar}$ from ellipse-fitting compare with those of Buta et al. (2005) who use the $Q_{\rm b}$ parameter? At first glance, the results may seem contradictory: they conclude that 40% of the galaxies in the OSUBSGS H band have 'weakly barred' or unbarred states ($Q_{\rm b} \leq 0.1$), whereas we find that only 6% of galaxies have 'weak' bars with $0.25 \leq e_{\rm bar} \leq 0.4$ in the H band after deprojection. However, it should be noted that Buta et al. (2005) group unbarred and weakly barred galaxies together. Their cited fraction of 40% for weak and unbarred states is, in fact, fully consistent with the fraction (46%) that we find when we group together unbarred galaxies (40%) and 'weakly barred' galaxies (6%).

How do the bar classes and bar strengths from ellipse-fits, as derived by our quantitative method (§2.3.3), compare with the RC3 bar classes based on visual inspection of optical B images? The three RC3 visual bar classes, 'A', 'AB', and 'B' denote 'unbarred', 'weakly barred', and 'strongly barred' disks, respectively. Of the 42, 47, and 46 galaxies in our sample that have an RC3 bar class of 'A', 'B', and 'AB', respectively, our quantitative characterization

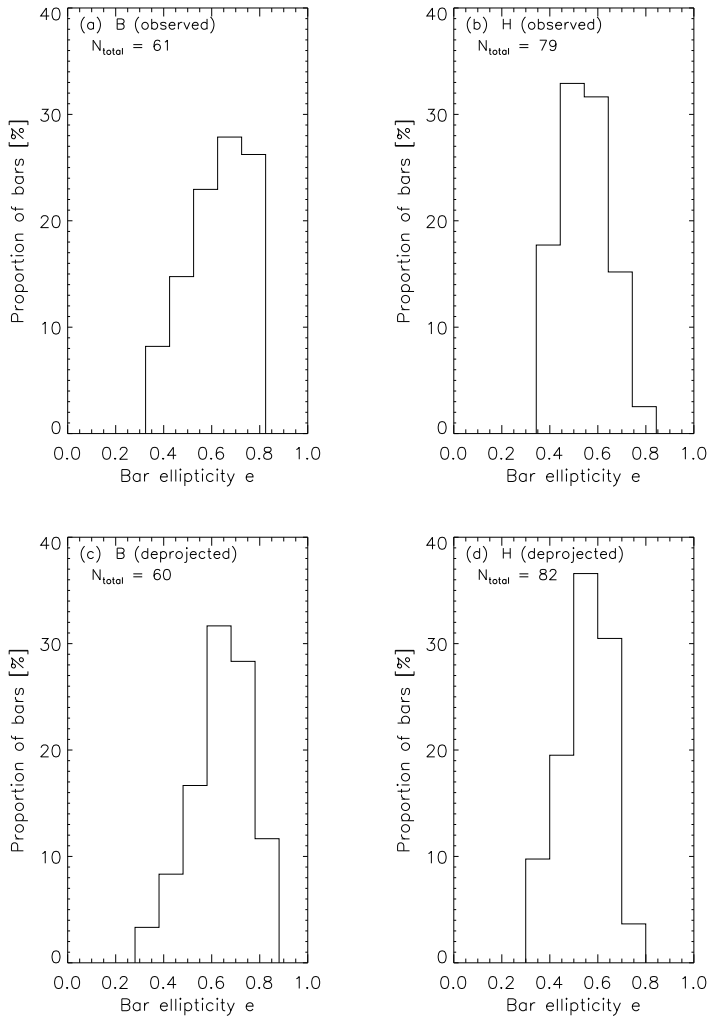

Figure 2.13 The distributions of bar strengths (as characterized by $e_{\rm bar}$ from ellipse-fitting) before (top row) and after (bottom row) deprojection, in the B (left) and H (right) bands are shown. It is striking that only a tiny fraction (7% in B; 10% in H) of bars are very weak with $e_{\rm bar}$ between 0.25–0.40, while the majority of bars (70% in B; 71% in H) seem to have moderate to high ellipticities, with $e_{\rm bar}$ between 0.50 to 0.75. Furthermore, we find no evidence for bimodality in the distribution of bar strength as characterized by $e_{\rm bar}$ in the B or H bands.

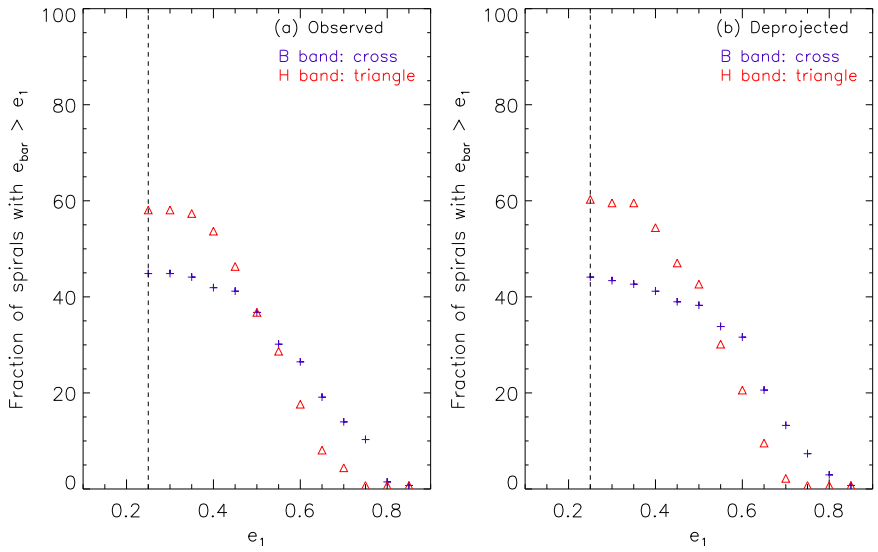

Figure 2.14 A generalized plot of the fraction of disks with 'strong' and 'weak' bars is shown **(a)** before and **(b)** after deprojection. The bar strength is characterized by $e_{\rm bar}$ from ellipse-fitting. The y-axis shows the fraction of spiral galaxies that host bars whose strength $e_{\rm bar}$ exceeds a value e_1 in the B (cross) and H (triangle) bands. Along the the x-axis, e_1 is varied. The flattening of the curve around $e_1 \sim 0.45$ reflects the paucity of very weak (low ellipticity) bars with $0.25 \geq e_{\rm bar} \leq 0.40$, while the steep fall in the curve for e_1 in the range 0.50–0.75 shows the preponderance of 'strong' (high ellipticity) bars.

(§2.3.3) shows that 5%, 85%, and 41% host bars in B-band images and 19%, 87%, and 65% host bars in H-band images. Clearly, only a small fraction (41% or 19/46) of galaxies with RC3 bar class 'AB' qualify as barred in B-band images, according to our quantitative criteria (§2.3.3). We visually inspected the remaining 27 galaxies that fail to qualify in order to investigate why they do not. We found that for 17 of them, we could not identify a bar feature in the B-band image, even by eye. For the remaining 10, we could visually see a somewhat elongated feature, but it does not satisfy the ellipticity and PA criteria outlined in §2.3.3. Another interesting point highlighted by Figure 2.15 is that while the mean bar strength (as characterized by $e_{\rm bar}$) is higher for RC3 visual class 'B' than for class 'AB', the two classes have significant overlap in the range $e_{\rm bar} \sim 0.5$–0.7. Thus, RC3 bar types should be used with caution and may be misleading.

It is also noteworthy that Figure 2.13 shows no evidence for bimodality in the distribution of bar strength, as characterized by $e_{\rm bar}$ from ellipse fits, in the B or H bands, in agreement with Buta et al. (2005). What about the bimodality claimed in earlier studies by Abraham & Merrifield (2000) and Whyte et al. (2002)? Both of these studies used the parameter $f_{\rm bar}$ to characterize the ellipticity of the most elliptical feature of a galaxy, and measure $f_{\rm bar}$ for both barred and unbarred galaxies. They report no bimodality in $f_{\rm bar}$ among barred galaxies, which is consistent with our findings that $e_{\rm bar}$ shows no bimodality among barred galaxies. The only bimodality that they report in $f_{\rm bar}$ is between barred and unbarred galaxies. It is unclear how robust

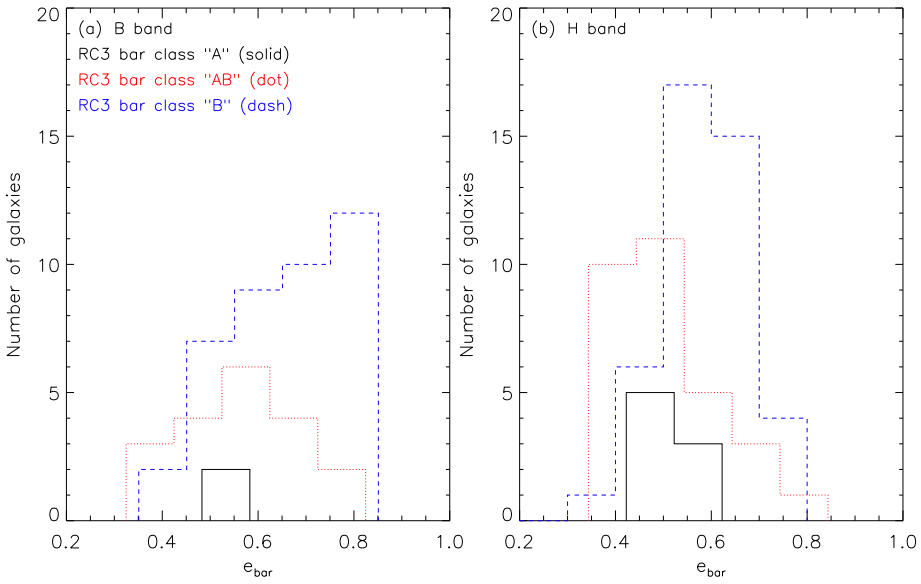

Figure 2.15 This figure shows the RC3 visual bar classes for all those galaxies in sample S4 that we classified as barred based on ellipse fits (§2.3.3 and §2.3.4). The x-axis shows the bar strength as characterized by $e_{\rm bar}$ from ellipse-fitting in the B (left panel) and H (right panel) bands, prior to deprojection. The three RC3 visual bar classes are based on visual inspection of optical images and classes 'A' (solid line), 'AB' (dotted line), and 'B' (dashed line) denote 'unbarred', 'weakly barred', and 'strongly barred' disks, respectively. In the B band, we find that 5%, 41%, and 85%, respectively, of the sample galaxies with RC3 visual classes of 'A', 'AB', and 'B', host bars. In the H band, the corresponding numbers are 19%, 65%, and 87%, respectively. Thus, many galaxies that are classified as unbarred in RC3 turn out to be barred and vice-versa. The mean bar ellipticity $e_{\rm bar}$ is higher for RC3 visual class "B" than for class "AB", but the two classes have significant overlap in the range $e_{\rm bar} \sim 0.5$–0.7.

this bimodality is since Whyte et al. (2002) report a bimodality that is much weaker than the one seen by Abraham & Merrifield (2000). The authors assigned this weakening to the larger sample size used by Whyte et al. (2002). At any rate, we cannot make any direct comparison with their bimodality results involving unbarred galaxies, since we measure $e_{\rm bar}$ in barred galaxies, but not in unbarred galaxies. The reason for this selective measurement is rooted in our rigorous approach for identifying a bar. In the study of Abraham & Merrifield (2000) and Whyte et al. (2002), a bar is simply considered as the innermost feature whose isophote has the highest ellipticity. In contrast, we use a rigorous approach for identifying a bar: we call a feature a bar only if its radial variation of ellipticity and PA follows the behavior expected based on the dominant orbits of a barred potential, as outlined in §2.3.3. We measure the maximum bar ellipticity $e_{\rm bar}$ only for those features that qualify as a bar.

2.4.4 Bar fraction and ellipticity as a function of Hubble type at $z \sim 0$

Figure 2.16 shows how the fraction of barred disks varies across different Hubble types in sample S4. The Hubble types are taken from RC3 and the bins represent S0, Sa/Sab, Sb/Sbc, Sc/Sd, and Sd/Sm. We first note that the bar fraction in different RC3 Hubble types does not change significantly after deprojection, whether in the B (Fig. 2.16a vs. 2.16d) or H (Fig. 2.16b vs. 2.16e) band images. This is again encouraging for large studies of bars at intermediate redshift (e.g., Jogee et al., 2004; Elmegreen et al., 2004; Zheng et al., 2005), where deprojection is not done for the reasons outlined in §2.4.1.

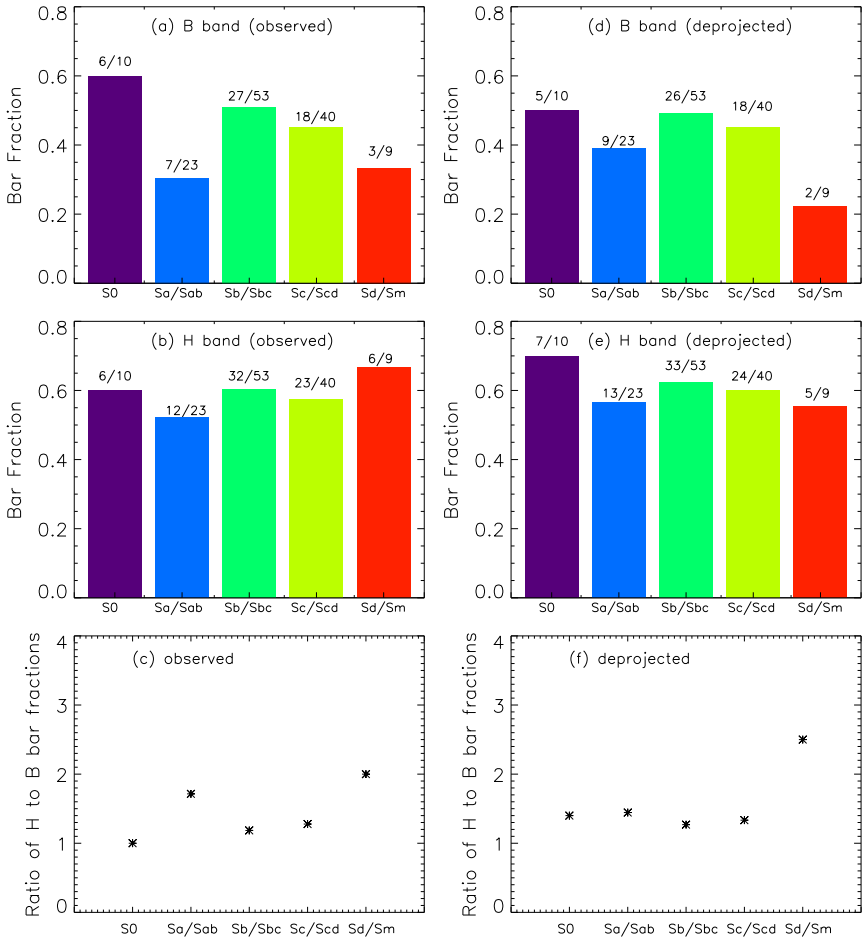

Figure 2.16 The bar fractions in the B band (top row) and H band (middle row) are shown as a function of RC3 Hubble types, before (left) and after (right) deprojection. The bar fraction is shown above each bin The number of galaxies are small for S0 and Sd/Sm types and robust number statistics only apply to RC3 Hubble types Sa to Scd: we find that the H-band bar fraction remains at $\sim 60\%$ across RC3 Hubble types Sa to Scd. The bottom row shows the ratio of the H-band bar fraction to the B-band bar fraction before (left) and after (right) deprojection. In the B band, we find that the bar fraction is lower with respect to the H band by ~ 1.2–1.5 for S0s to Scs, and by ~ 2.5 for Sds/Sms. This is likely due to extinction, especially in the dusty, gas-rich late type (Scd–Sm) galaxies.

In the B band, we find that the bar fraction is lower with respect to the H band by $\sim$ 1.2–1.5 in Sas to Scs, and by $\sim$ 2.5 in Sds/Sms (Fig. 2.16c,f). This is consistent with higher obscuration in dusty, gas-rich late types. Eskridge et al. (2000) also find that the increase in bar fraction from the B to H band is most significant for late-type galaxies.

How does the bar fraction vary across RC3 Hubble types? The number of galaxies involved are too small in the S0 and Sd/Sm bins for robust number statistics and we therefore restrict our analysis to types Sa to Scd. We conclude that the H-band bar fraction (Fig. 2.16e) remains $\sim$ 60% across RC3 Hubble types Sa to Scd. Our quantitative result based on 136 galaxies is consistent with the results based on ellipse fits of a much smaller sample (58 galaxies) by Knapen et al. (2000), as well as with the qualitative results of Eskridge et al. (2000), who also report a constant NIR bar fraction as a function of RC3 Hubble types, based on visual inspection. The large H-band bar fraction of $\sim$ 60% across different Hubble types implies that bars are ubiquitous in spirals across the entire Hubble sequence. Further implications are discussed in §2.4.6.

How does the bar strength, as characterized by $e_{\rm bar}$ from ellipse-fitting, vary as a function of RC3 Hubble type? In the H band, the bar strength $e_{\rm bar}$ lies in the range 0.35–0.80, and shows no systematic variation across Hubble types Sa to Scd, either before (Fig. 2.17a) or after (Fig. 2.17b) deprojection. We note, however, that Buta et al. (2005) and Laurikainen et al. (2004b) find that the $Q_{\rm b}$ and $Q_{\rm g}$ parameters tend to have lower values toward earlier-type

galaxies. In order to understand this discrepancy, we first note that the $Q_{\rm b}$ and $Q_{\rm g}$ parameters measure the bar strength relative to the axisymmetric components, such as the disk and bulge. The lower $Q_{\rm b}$ and $Q_{\rm g}$ values in early type galaxies could reflect the fact that such galaxies have stronger axisymmetric components, which make the relative strength of the bar lower, even if the bar was as strong or stronger intrinsically than those in later-type galaxies.

2.4.5 Comparison of optical properties of bars at $z \sim 0$ and at $z \sim 0.2$–1.0

Studies of bars at $z \sim 0.2$–1.0 (lookback times of 3–8 Gyr) based on *HST* ACS observations in the Tadpole field (Elmegreen et al., 2004), the GEMS and GOODS fields (Jogee et al., 2004), and COSMOS surveys (Sheth et al., 2008) trace bars in the *rest-frame optical*. The reddest ACS filter F850LP has a pivot wavelength of 9103 Å, while the value for the F814W filter is 8064 Å. Over the redshift range $z \sim 0.2$–1.0, the rest-frame wavelength traced by the F850LP filter ranges from 7586 Å to 4550 Å, which corresponds to the *rest-frame optical* R/I to V/B bands. In order to avoid the pernicious effects of bandpass shifting, it is essential that ACS studies of bars at $z \sim 0.2$–1.0 compare their rest-frame optical results to the optical bar fraction at $z \sim 0$, rather than to the NIR bar fraction at $z \sim 0$. If they use the the NIR $z \sim 0$ point, it can lead to flawed conclusions, as the NIR $z \sim 0$ bar fraction ($60\% \pm 6\%$) is significantly larger than the optical $z \sim 0$ bar fraction ($44\% \pm 6\%$), as reported in §2.4.1. We therefore use the OSUBSGS optical bar fraction at $z \sim 0$ in the discussion below.

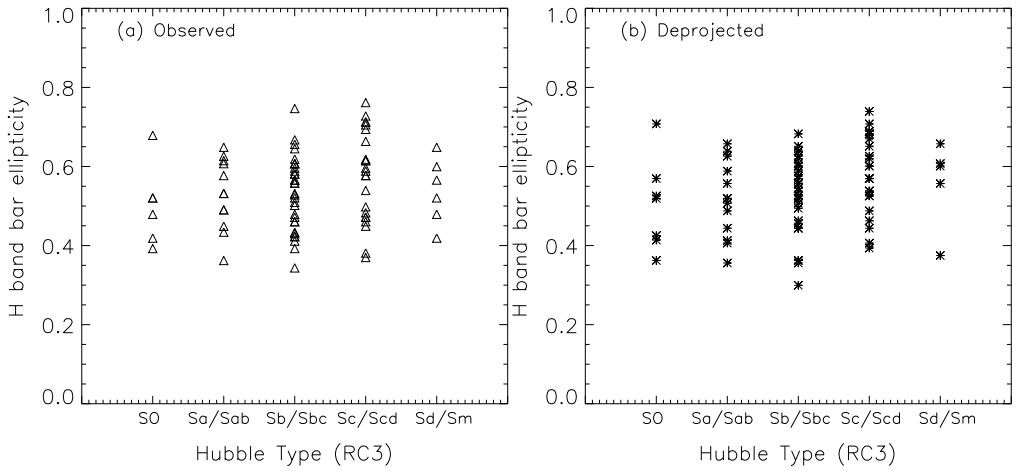

Figure 2.17 The bar strength as characterized by the bar ellipticity $e_{\rm bar}$ in the H band is plotted as a function of Hubble types before (left panel) and after (right panel) deprojection. The Hubble types are from RC3 and are binned as in Figure 2.16. Before deprojection, the number of galaxies in each Hubble type bin is: S0 = 6, Sa/Sab = 12, Sb/Sbc = 32, Sc/Scd = 23, Sd/Sm =6. After deprojection, the corresponding numbers are S0 = 7, Sa/Sab = 13, Sb/Sbc = 33, Sc/Scd = 24, Sd/Sm = 5. The number of galaxies are small for S0s and Sd/Sm types and robust number statistics only apply to RC3 Hubble types Sa to Scd. The bar ellipticity $e_{\rm bar}$ lies in the range 0.35–0.80, and shows no systematic variation across Hubble types Sa to Scd, either before or after deprojection.

In the study of bars at $z \sim 0.2$–1.0, Jogee et al. (2004) ellipse fitted a sample of 1590 galaxies at $z \sim 0.2$–1.0, drawn from 25% of the GEMS survey area. Then they applied essential cutoffs in absolute magnitude, bar size, and bar ellipticity in order to ensure a complete sample, high spatial resolution, and reliable bar identification out to $z \sim 1$. In particular, in order to ensure that the sample of spiral galaxies is fairly complete out to $z \sim 0.9$, an absolute magnitude cutoff of $M_{\rm V} < -19.3$ had to be applied. Secondly, at $z > 0.5$ (where $1''$ corresponds to scales > 6.2 kpc), the study could not efficiently resolve very small bars with semi-major axes $a < 1.5$ kpc, in agreement with Lisker et al. (2006a). Thus, a cutoff of $a_{\rm bar} \geq 1.5$ kpc is implicitly applied. Finally, the study only considered bars with moderate ellipticity $e_{\rm bar} \geq 0.4$ because at intermediate redshifts, it becomes difficult to unambiguously identify and characterize bars with lower ellipticities. This is not a dramatic cutoff as most bars have $e_{\rm bar} \geq 0.4$ (Fig. 2.13). After applying these cutoffs in absolute magnitude ($M_{\rm V}$ <-19.3), bar size ($a_{\rm bar} \geq 1.5$ kpc), and bar ellipticity ($e_{\rm bar} \geq 0.4$), Jogee et al. (2004) find a rest-frame optical bar fraction of $f_{\rm optical2} \sim 30\% \pm 6\%$ $z \sim 0.2$–1.0. A constant and similar optical bar fraction (23% to 40%) out to $z \sim 1$ is also reported by Elmegreen et al. (2004).

In order to get a valid optical bar fraction for comparison at $z \sim 0$, we must apply the exact same cutoffs to the OSUBSGS optical data. We start with observed bar properties prior to deprojection from OSUBSGS because no deprojection was applied in any of the intermediate redshift studies (Jogee et al., 2004; Elmegreen et al., 2004; Zheng et al., 2005). With a cutoff of

$M_{\rm V}$ <-19.3, the optical B-band bar fraction at $z \sim 0$ drops from 45% (61/136) to 43% (45/104). Applying a further cutoff of $a_{\rm bar} \geq 1.5$ kpc makes it drop to 36% (37/104). Finally, a third cutoff of $e_{\rm bar} \geq 0.4$ reduces the optical B-band bar fraction to 34% (35/104).

Thus, after the same cutoffs in absolute magnitude ($M_{\rm V}$ <-19.3), bar size ($a_{\rm bar} \geq 1.5$ kpc), and bar ellipticity ($e_{\rm bar} \geq 0.4$) are applied, a very good agreement ensues between the GEMS optical bar fraction at $z \sim 0.2$–1.0 ($f_{\rm optical2} \sim 30\% \pm 6\%$) and the OSUBSGS optical B-band bar fraction at $z \sim 0$ ($f_{\rm optical3} \sim 34\% \pm 6\%$). This agreement strongly suggests that the optical bar fraction in bright disks does not decline strongly with redshift. Such a decline would cause $f_{\rm optical2} \ll f_{\rm optical3}$ because the observed bar fraction would be lowered both by the intrinsic decline, and by systematic effects at intermediate redshifts, such as cosmological dimming, the loss of spatial resolution, and lower signal-to-noise.

However, our finding allows for models where the optical bar fraction is either constant, or rises with redshift. In the latter class of models, one can arrive at comparable values of $f_{\rm optical2}$ and $f_{\rm optical3}$ only if the intrinsic increase in bar fraction with redshift produced by the model is compensated for by the 'loss' of bars due to systematic effects, such as cosmological dimming, and low signal-to-noise.

2.4.6 Constraints on the robustness and evolution of bars

The robustness and lifetime of bars define some of the most fundamental issues in the evolution of bars, their impact on disk galaxies (§2.1) and the assembly of the Hubble sequence. In general terms, the evolution of a bar depends on the exchange of angular momentum between the stars in the bar and the other components of a galaxy, namely, the dark matter (DM) halo and the baryons (gas and stars) in the bulge and disk. Important factors influencing the bar include the triaxiality of the DM halo in which it lies (Berentzen et al., 2006); the amount of angular momentum that the DM halo can absorb (Athanassoula, 2003); the central mass concentrations (CMCs) present in the inner few hundred pc (e.g., Shen & Sellwood, 2004; Athanassoula, 2005; Martinez-Valpuesta et al., 2006; Debattista et al., 2006); and the distribution and amount of gas in the disk (e.g, Shlosman & Noguchi, 1993; Bournaud & Combes, 2002; Bournaud et al., 2005; Debattista et al., 2006; Berentzen et al., 2007). In this section, we compare our empirical results to different simulations in order to constrain theoretical scenarios. We note, however, that most simulations do not yet fully incorporate the effects of star formation and feedback, which can impact the evolution of the disk in important ways.

Dubinski (1994) showed that the triaxiality of DM halos is diluted by baryonic dissipation. Recent simulations by Berentzen et al. (2006) find that bars embedded in triaxial non-rotating DM halos can only survive if the inner halo ellipticity is washed out. Otherwise, the interaction between the bar and the DM halo induces chaotic orbits and destroys the bar. In the present

paper, our findings that the majority (60%) of spirals are barred in the infrared (§2.4.1), and that these bars have primarily moderate to high strengths, as characterized by the maximum bar ellipticity $e_{\rm bar}$ ($0.50 \leq e_{\rm bar} \leq 0.80$; §2.4.3), suggest that DM halos of most present-day spirals are close to axisymmetric, with a maximum equatorial axial ratio of ~ 0.9 in potential. These limits may change slightly if one allows the DM halo to have a figure of rotation. These results are consistent with Kazantzidis et al. (2004), who find that in the very early stages of disk formation, the settling of the dissipative baryonic component within a triaxial halo strongly dilutes the triaxiality to such values. Berentzen & Shlosman (2006) also report that a growing disk is responsible for washing out the halo prolateness (in the disk plane) and for diluting its flatness over a period of time comparable to the disk growth.

The CMC typically refers to the mass present within the inner hundred or few hundred pc. A large or more centrally concentrated CMC can weaken a bar amplitude by changing the orbital structure of a barred potential and inducing chaotic orbits. Most recent simulations (e.g., Athanassoula, 2005; Shen & Sellwood, 2004; Martinez-Valpuesta et al., 2006; Debattista et al., 2006) find that bars are more robust than previously thought: in order to produce any significant reduction in bar strength, the ratio $X_{\rm CMC} \sim (M_{\rm CMC}/M_{\rm disk})$, where $M_{\rm CMC}$ is the mass of the CMC in the inner few hundred pc, and $M_{\rm disk}$ is the disk mass, must be very large, at least 10%. Such large values are only of academic interest and are not realized in present-day galaxies, as we discuss below.

In present-day galaxies, the components that contribute to the CMC in the inner few hundred pc consist of super-massive black holes (SMBHs) central dense stellar clusters, gaseous concentrations, and the inner parts of bulges. SMBHs have typical masses in the range 10^6–10^9 $M_\odot$ and tend to scale as 0.001 of the bulge mass; gaseous concentrations range from 10^7–10^9 $M_\odot$ in the central 500 to 1000 pc radius (e.g., Jogee et al., 2005); and central dense stellar clusters typically have masses in the range 10^6–10^8 $M_\odot$. These components typically lead to $X_{\rm CMC}$ values that are much lower than 10%. This suggests that CMCs that exist in present-day galaxies are not large enough to produce any significant reduction in bar strength. Our results are consistent with these expectations and with simulations that support robust bars. We found that the majority ($\sim$ 71%–80%) of bars have moderate to high strengths, as characterized by $e_{\rm bar}$ from ellipse-fitting ($0.50 \leq e_{\rm bar} \leq 0.80$). We also found that the bar fraction ($\sim$ 60%) and mean bar strength, as characterized by ellipse fits ($e_{\rm bar} \sim 0.5$), is relatively constant across RC3 Hubble types Sa to Scd (§2.4.4), although the latter encompasses a wide range of gas mass fractions, CMC masses, and CMC components.

Gas can affect the formation and evolution of a bar in different ways, depending on its distribution and clumpiness. In the case of an unbarred disk, the accretion of cold gas makes the disk more massive, dynamically colder, and therefore more bar unstable (e.g., Bournaud & Combes, 2002). However, in the case of very gas-rich disks, the gas can become clumpy, and the effect of dynamical friction on massive gas clumps at low radii can heat the disk

and prevent it from forming the bar (e.g., Shlosman & Noguchi, 1993). In the case of a disk that is already barred, the bar exerts gravitational torques that drive gas located outside the corotation resonance (CR) outward, and drive gas located between the CR and inner Lindblad resonance (ILR) inward. Most simulations to date (e.g., Debattista et al., 2006; Curir et al., 2006; Berentzen et al., 2007) show that gas inflows in present-day galaxies do not readily destroy bars. For instance, simulations (e.g., Debattista et al., 2006), can only destroy the bar when there are large gas inflows that build a very massive, soft CMC, of order 20% of the mass of the total baryonic (gas and stars) disk. Furthermore, the simulations also suggest that gas which sinks into the center can become bar supporting if it forms stars. As discussed above, CMCs as large as 10% or 20% are not realized in present-day galaxies and the simulations therefore imply that gas inflows in present-day galaxies do not readily destroy bars. In the very early Universe, if extreme gas inflows and extreme CMCs are realized, the evolution of bars might be different.

We note that simulations of bar-driven gas inflow by Bournaud et al. (2005) yield widely different predictions from those discussed above. The simulations of Bournaud et al. (2005) appear to destroy a bar even with a gas mass fraction (GMF) that is as low as 5% to 7%. Here, the GMF is defined as the ratio of gas mass to the total mass of the stellar disk. A GMF of order 5% is easily met in present-day galaxies and these simulations would suggest, therefore, that strong bars in present-day galaxies are easily destroyed by bar-driven gas inflows (Bournaud et al., 2005). There is clearly a stark

difference between the predictions of these simulations and the ones outlined in the previous paragraph. Part of the reason why the simulations yield such different results might lie in the way the DM halo is modeled and the assumed ratio of DM halo mass to disk mass. The DM halo is live and dominates over the disk mass in Debattista et al. (2006), while it is rigid and less massive than the disk in Bournaud et al. (2005).

What do our observational results suggest? We found that at $z \sim 0$, only a small fraction ($\sim$ 7%–10%) of bars are very weak ($0.25 \leq e_{\rm bar} \leq 0.40$), while the majority ($\sim$ 71%–80%) of bars have moderate to high strengths (as characterized by the maximum bar ellipticity $e_{\rm bar}$), with $0.50 \leq e_{\rm bar} \leq 0.80$. We also do not see any sign of bimodality in bar strength, as characterized by $e_{\rm bar}$ from ellipse fits. Finally, we found that the bar fraction ($\sim$ 60%) and mean bar ellipticity ($e_{\rm bar} \sim 0.5$) is relatively constant across RC3 Hubble types Sa to Scd (§2.4.4), despite the wide variation in GMFs. Our results are easily reconciled with scenarios where bars in present-day moderately gas-rich galaxies remain strong under the effect of bar-driven gas inflows. Our results do not necessarily rule out models where bars are easily destroyed by bar-driven gas inflows. They do, however, imply that if such an easy destruction occurs, then there must be a very efficient mechanism that not only regenerates bars on a short timescale (e.g., Block et al., 2002; Bournaud & Combes, 2002), but is also very well tuned to the bar destruction rate so that it can reproduce the observed constant optical bar fraction in bright galaxies over the last 8 Gyr (Jogee et al., 2004; Elmegreen et al., 2004, §2.4.5).

2.5 Summary and Conclusions

With the advent of high redshift *HST* surveys, such as the Tadpole Field, GEMS, GOODS, and COSMOS, which trace bars in the rest-frame optical band out to $z \sim 1$, it becomes increasingly important to provide a reference baseline for bars at $z \sim 0$ in the optical band. Motivated by these considerations, we characterize the frequency and structural properties of bars at $z \sim 0$ in the optical and NIR bands, by ellipse-fitting the B and H images of 180 spirals in the OSUBSGS (Eskridge et al., 2002), and applying quantitative criteria in order to identify and characterize bars. We determine the inclination of the outer disk and exclude highly inclined ($i > 60^\circ$) galaxies to derive a sample S4 of 136 moderately inclined spirals. For this sample, we derive bar properties both before and after deprojection to face-on. Our study complements existing work on OSUBSGS based on Fourier amplitudes (Block et al., 2002; Buta et al., 2005) and visual classification (Eskridge et al., 2000), and it can be compared with studies (Jogee et al., 2004; Elmegreen et al., 2004; Zheng et al., 2005) of intermediate redshift ($z \sim 0.2$–1.0) bars employing the same ellipse-fitting methodology. Our results are summarized below.

(1) The optical and NIR bar fraction at $z \sim 0$: For our sample, which is dominated by galaxies with $M_{\rm V} \sim$ -20 to -22, we find a deprojected bar fraction at $z \sim 0$ of $f_{\rm NIR1} \sim 60\% \pm 6\%$ in the near-infrared H band, and $f_{\rm optical1} \sim 44\% \pm 6\%$ in the optical B-band images. The latter likely miss bars obscured by dust and star formation. Deprojection does not make any significant changes to the global B- and H- band bar fractions, which are 45%

and 58% before deprojection, and change by only a factor of 0.97 and 1.03, respectively, after deprojection. This is encouraging for large studies of bars at intermediate redshift (e.g., Jogee et al. 2004, Elmegreen et al. 2004, Zheng et al. 2005), where deprojection is not performed.

(2) Comparison of optical properties of bars at $z \sim 0$ and at intermediate redshifts: Studies of bars at $z \sim 0.2$–1.0 (lookback times of 3–8 Gyr) based on *HST* ACS observations in the Tadpole field, the GEMS and GOODS fields, and COSMOS surveys trace bars in the *rest-frame optical*. R/I to V/B bands (7586 Å to 4550 Å). Therefore, in order to avoid the pernicious effects of bandpass shifting, it is essential that ACS studies of bars at $z \sim 0.2$–1.0 compare their rest-frame optical results to the optical bar fraction at $z \sim 0$, rather than to the significantly higher NIR bar fraction at $z \sim 0$.

Furthermore, at $z \sim 0.2$–1.0, it is essential to apply cutoffs in absolute magnitude, bar size, and bar ellipticity in order to ensure a complete sample, adequate spatial resolution, and reliable bar identification. After applying cutoffs in absolute magnitude ($M_{\rm V}$ <-19.3), bar size ($a_{\rm bar} \geq 1.5$ kpc), and bar ellipticity ($e_{\rm bar} \geq 0.4$), Jogee et al. (2004) found a rest-frame optical bar fraction of $f_{\rm optical2} \sim 30\% \pm 6\%$ at $z \sim 0.2$–1.0. A constant and similar optical bar fraction (23% to 40%) out to $z \sim 1$ is also reported by Elmegreen et al. (2004). In order to derive the equivalent optical bar fraction for comparison at $z \sim 0$, we applied the exact same cutoffs to the OSUBSGS optical data. With a cut off of $M_{\rm V}$ <-19.3, the optical bar fraction $z \sim 0$ drops from 45% (61/136) to 43%. Applying a further cutoff of $a_{\rm bar} \geq 1.5$ kpc makes it drop to 36%. Finally,

a third cutoff of $e_{\rm bar} \geq 0.4$ reduces optical B-band bar fraction at $z \sim 0$ to $f_{\rm optical3} \sim 34\% \pm 6\%$. The result that $f_{\rm optical2}$ is comparable to $f_{\rm optical3}$ rules out scenarios where the *optical* bar fraction in *bright* disks declines strongly with redshift. It allows for models where the optical bar fraction is either constant, or rises with redshift.

(3) Distribution of bar strengths $z \sim 0$ as characterized by ellipse-fitting: In this study, we use the maximum bar ellipticity $e_{\rm bar}$ from ellipse-fits as a partial measure of the bar strength. Only a very small proportion (7% in B; 10% in H) of bars are very weak as characterized by $e_{\rm bar}$ from ellipse fits ($0.25 \leq e_{\rm bar} \leq 0.40$), while the majority of bars (70% in B; 71% in H) have moderate to high ellipticities ($0.50 \leq e_{\rm bar} \leq 0.75$). We find no evidence for bimodality in the distribution of bar strength, as characterized by $e_{\rm bar}$ in the B or H bands, in agreement with Buta et al. (2005).

(4) Bar fraction and strength, as characterized by ellipse-fitting, as a function of RC3 Hubble type at $z \sim 0$: The deprojected bar fraction is 60% in H and 44% in B, confirming the ubiquity of local bars. In the B band, the bar fraction is lower with respect to the H band by ~ 1.2–1.5 for Hubble types S0s to Scs, and by ~ 2.5 for Sds/Sms. This is consistent with the higher obscuration in dusty, gas-rich late types. The bar fraction and bar strength, as characterized by $e_{\rm bar}$, in the H band shows no systematic variation across Hubble types Sa to Scd.

(5) Comparison with RC3 visual bar classes: Of the 42, 47, and 46 galaxies in our sample that have an RC3 visual bar class of 'A' (unbarred),

'B' (strongly barred), and 'AB' (weakly barred), respectively, our quantitative characterization (§2.3.3) shows that 5%, 85%, and 41% host bars in B-band images and 19%, 87%, and 65% host bars in H-band images. Thus, quantitative characterization of bars differs significantly from RC3 bar classes for the RC3 bar class 'AB'. Furthermore, the mean bar strength, as characterized by the maximum bar ellipticity $e_{\rm bar}$, is higher for RC3 visual class 'B' than for class 'AB', but the two classes have significant overlap in the range $e_{\rm bar} \sim 0.5$–0.7. Thus, RC3 bar types should be used with caution and may be misleading.

(6) Sizes of bars and disks at $z \sim 0$: The sizes or semi-major axes $a_{\rm bar}$ of large-scale bars in the local Universe lie in the range $\sim$ 1 to 14 kpc, with the majority of bars (68% in B and 76% in H) having $a_{\rm bar} \leq 5$ kpc. Bar and disk sizes are correlated with an average slope of ~ 0.9, albeit with a large scatter of several kpc in bar size at a given disk size. The ratio $(a_{\rm bar}/R_{25})$ lies primarily in the range 0.1 to 0.5, with only a minority of galaxies having larger values out to 0.95. The correlation between bar and disk sizes, and the narrow range in $a_{\rm bar}/R_{25}$ suggests that the growths of the bar and disk may be intimately tied. The fact that $(a_{\rm bar}/R_{25})$ is generally well below 1.0 suggests that the CR of disk galaxies lies well inside their R_{25} radius, assuming that bars end near the CR.

(7) Constraints on the robustness of bars: Our findings that the majority (60%) of spirals are barred in the infrared and that most ($\sim$ 71%–80%) of these bars have primarily moderate to high ellipticities ($0.50 \leq e_{\rm bar} \leq 0.80$)

suggest that DM halos of present-day spirals have at most a mild triaxiality, with a maximum equatorial axis ratio $b/a \sim 0.9$ in the potential. We also found that the bar fraction and mean bar strength (as characterized by the maximum bar ellipticity $e_{\rm bar}$) are relatively constant across Hubble types Sa to Scd, and there is no bimodality in $e_{\rm bar}$. Taken together, our results are easily reconciled with scenarios where bars in present-day galaxies are relatively robust against the range in gas mass fractions, gas inflows, and CMC components present across Hubble types Sa to Scd. Our results do not necessarily rule out models where bars are easily destroyed by bar-driven gas inflows. They do, however, imply that if such an easy destruction occurs, then there must be a very efficient mechanism that not only regenerates bars on a short timescale, but is also very well tuned to the bar destruction rate so that it can reproduce the observed constant optical bar fraction in bright galaxies over the last 8 Gyr.

Table 2.1. Global Properties of sample S3 (169 galaxies) with ellipse fits in B and H

Galaxy Name	Hubble Type (RC3)	Bar Type (RC3)	D (Mpc)	D_{25} (')	$B_{\rm T}$ (mag)	$M_{\rm V}$ (mag)	$L_{\rm IR}$ (log($L_\odot$))	$L_{\rm B}$ (log($L_\odot$))
(1)	(2)	(3)	(4)	(5)	(6)	(7)	(8)	(9)
Moderately inclined galaxies (N=136)								
IC 0239	SAB(rs)cd	AB	14.2	5.4	11.8	-19.66	-	9.81
IC 4444	SAB(rs)bc	AB	26.9	1.4	12	-20.79	10.53	10.33
IC 5325	SAB(rs)bc	AB	18.1	2.7	11.83	-20.02	-	9.83
NGC 0157	SAB(rs)bc	AB	20.9	3	11	-21.19	10.52	10.53
NGC 0210	SAB(s)b	AB	20.3	4.9	11.6	-20.65	-	10.22
NGC 0278	SAB(rs)b	AB	11.8	2.7	11.47	-19.53	10.03	10.04
NGC 0289	SAB(rs)bc	AB	19.4	8.3	11.72	-20.45	10.03	10.17
NGC 0428	SAB(s)m	AB	14.9	4.6	11.91	-19.4	-	9.85
NGC 0488	SA(r)b	A	29.3	5.4	11.15	-22.05	-	10.74
NGC 0685	SAB(r)c	AB	15.2	3.9	11.95	-19.42	-	9.8
NGC 0864	SAB(rs)c	AB	20	4.4	11.4	-20.66	-	10.27
NGC 1042	SAB(rs)cd	AB	16.7	4.4	11.56	-20.09	-	10.16
NGC 1058	SA(rs)c	A	9.1	3.6	11.82	-18.6	-	9.34
NGC 1073	SB(rs)c	B	15.2	5	11.47	-19.94	-	9.97
NGC 1084	SA(s)c	A	17.1	3.4	11.31	-20.43	10.54	10.3
NGC 1087	SAB(rs)c	AB	19	3.7	11.46	-20.45	10.26	10.28
NGC 1187	SB(r)c	B	16.3	5.4	11.34	-20.28	10.18	10.1
NGC 1241	SB(rs)b	B	26.6	3.6	11.99	-20.98	-	10.12
NGC 1300	SB(rs)bc	B	18.8	6.8	11.11	-20.94	-	10.36
NGC 1302	(R)SB(r)0	B	20	3.8	11.6	-20.8	-	10.24
NGC 1309	SA(s)bc	A	26	2.8	11.97	-20.54	10.24	10.26
NGC 1317	SAB(r)a	AB	16.9	3.1	11.91	-20.12	-	9.87
NGC 1350	(R')SB(r)ab	B	16.9	5	11.16	-20.85	-	10.18
NGC 1371	SAB(rs)a	AB	17.1	6.8	11.57	-20.49	-	10.08
NGC 1385	SB(s)cd	B	17.5	4.6	11.45	-20.28	10.18	10.1
NGC 1493	SB(r)cd	B	11.3	3.9	11.78	-19	-	9.58
NGC 1559	SB(s)cd	B	14.3	3.3	11	-20.13	10.21	10.24
NGC 1617	SB(s)a	B	13.4	4	11.38	-20.2	-	10.08
NGC 1637	SAB(rs)c	AB	8.9	5.1	11.47	-18.92	9.46	9.52
NGC 1703	SB(r)b	B	17.4	3.5	11.9	-19.86	-	-
NGC 1792	SA(rs)bc	A	13.6	6.1	10.87	-20.48	10.33	10.24
NGC 1832	SB(r)bc	B	23.5	2.6	11.96	-20.53	10.28	10.26
NGC 2139	SAB(rs)cd	AB	22.4	2.9	11.99	-20.12	10.16	10.16
NGC 2196	(R')SA(s)a	A	28.8	2.9	11.82	-21.29	-	10.46
NGC 2566	(R')SB(rs)ab pec	B	21.1	4.3	11.83	-20.6	10.6	-
NGC 2775	SA(r)ab	A	17	4.6	11.03	-21.02	-	10.24
NGC 2964	SAB(r)bc	AB	21.9	3	11.99	-20.39	10.36	10.15
NGC 3166	SAB(rs)0	AB	22	3.2	11.32	-21.32	9.94	10.28
NGC 3169	SA(s)a pec	A	19.7	5	11.08	-21.24	10.18	10.37
NGC 3223	SA(s)b	A	38.1	3.6	11.79	-21.93	-	10.88
NGC 3227	SAB(s)a pec	AB	20.6	5.9	11.1	-21.29	10.13	10.26
NGC 3261	SB(rs)b	B	33.4	3.9	12	-	-	10.64

Table 2.1 (cont'd)

Galaxy Name (1)	Hubble Type (RC3) (2)	Bar Type (RC3) (3)	D (Mpc) (4)	D_{25} (') (5)	B_T (mag) (6)	M_V (mag) (7)	L_{IR} (log($L_\odot$)) (8)	L_B (log($L_\odot$)) (9)
NGC 3275	SB(r)ab	B	42.4	2.8	11.8	-	-	10.61
NGC 3423	SA(s)cd	A	10.9	4	11.59	-19.05	-	9.66
NGC 3504	(R)SAB(s)ab	AB	26.5	2.6	11.82	-20.99	10.72	10.34
NGC 3507	SB(s)b	B	19.8	3.2	11.73	-	-	10.23
NGC 3513	SB(rs)c	B	17	3.2	11.93	-19.65	-	9.98
NGC 3583	SB(s)b	B	34	2.6	11.9	-	10.54	10.61
NGC 3593	SA(s)0	A	5.5	4.8	11.86	-17.78	9.22	9
NGC 3596	SAB(rs)c	AB	23	4.1	11.95	-	-	10.32
NGC 3646	Ring	-	55.8	3.9	11.78	-22.6	-	-
NGC 3681	SAB(r)bc	AB	24.2	2.9	11.9	-20.73	-	10.06
NGC 3684	SA(rs)bc	A	23.4	2.9	12	-20.47	-	10.07
NGC 3686	SB(s)bc	B	23.5	2.9	11.89	-20.54	-	10.17
NGC 3726	SAB(r)c	AB	17	5.5	10.91	-20.73	9.78	10.33
NGC 3810	SA(rs)c	A	16.9	3.8	11.35	-20.37	10.12	10.24
NGC 3885	SA(s)0	A	27.8	2.9	11.89	-21.28	10.27	10.29
NGC 3887	SB(r)bc	B	19.3	3.4	11.41	-	9.8	10.16
NGC 3893	SAB(rs)c	AB	17	4.3	11.16	-	10.2	10.3
NGC 3938	SA(s)c	A	17	4.9	10.9	-20.77	9.93	10.3
NGC 3949	SA(s)bc	AB	17	2.8	11.54	-20.06	9.87	10.16
NGC 4027	SB(s)dm	B	25.6	3.3	11.66	-20.92	10.36	10.41
NGC 4030	SA(s)bc	A	25.9	4	11.42	-	10.64	10.3
NGC 4051	SAB(rs)bc	AB	17	5.4	10.83	-20.97	9.9	10.29
NGC 4123	SB(r)c	B	16.5	4.6	11.98	-19.71	9.76	10.29
NGC 4136	SAB(r)c	AB	9.7	4	11.69	-	-	9.48
NGC 4145	SAB(rs)d	AB	20.7	5.9	11.78	-20.31	-	10.28
NGC 4151	(R')SAB(rs)ab	AB	20.3	6.3	11.5	-20.77	10.2	10.38
NGC 4212	SAc	A	16.8	2.3	11.83	-19.97	9.82	10.02
NGC 4242	SAB(s)dm	AB	7.5	5.2	11.37	-18.55	-	9.36
NGC 4254	SA(s)c	A	16.8	5	10.44	-	10.54	10.53
NGC 4303	SAB(rs)bc	AB	15.2	5.9	10.18	-21.26	10.51	10.48
NGC 4314	SB(rs)a	B	9.7	4.2	11.43	-19.35	-	9.65
NGC 4394	(R)SB(r)b	B	16.8	3.4	11.73	-20.25	-	9.99
NGC 4414	SA(rs)c	A	9.7	4.5	10.96	-19.81	10.56	9.84
NGC 4450	SA(s)ab	A	16.8	5	10.9	-21.05	-	10.34
NGC 4457	(R)SAB(s)0	AB	17.4	3.2	11.76	-20.29	-	10.01
NGC 4487	SAB(rs)cd	AB	19.9	3.9	11.63	-	-	10.27
NGC 4496	SB(rs)m	B	13.1	3.7	11.94	-19.17	-	9.8
NGC 4504	SA(s)bc	A	19.5	3.3	11.89	-	-	10.17
NGC 4548	SB(rs)b	B	16.8	5	10.96	-20.98	-	10.3
NGC 4571	SA(r)d	A	16.8	3.6	11.82	-19.82	-	9.94
NGC 4579	SAB(rs)b	AB	16.8	5.4	10.48	-21.47	9.87	10.46
NGC 4580	SAB(rs)a pec	AB	25.6	2.5	11.83	-	-	9.97
NGC 4593	(R)SB(rs)b	B	39.5	3.3	11.67	-	-	10.82
NGC 4618	SB(rs)m	B	7.3	3.1	11.22	-18.54	-	9.44
NGC 4643	SB(rs)0	B	25.7	2.9	11.72	-21.29	-	10.39

Table 2.1 (cont'd)

Galaxy Name (1)	Hubble Type (RC3) (2)	Bar Type (RC3) (3)	D (Mpc) (4)	D_{25} (') (5)	$B_{\rm T}$ (mag) (6)	$M_{\rm V}$ (mag) (7)	$L_{\rm IR}$ ($\log(L_\odot)$) (8)	$L_{\rm B}$ ($\log(L_\odot)$) (9)
NGC 4647	SAB(rs)c	AB	16.8	2.8	11.94	-19.84	9.81	9.93
NGC 4651	SA(rs)c	A	16.8	3.6	11.39	-20.31	9.72	10.22
NGC 4665	SB(s)0	B	17.9	4.2	10.5	-	-	9.94
NGC 4689	SA(rs)bc	A	16.8	3.7	11.6	-20.18	-	10.04
NGC 4691	(R)SB(s)0 pec	B	22.5	3.5	11.66	-20.68	10.32	10.24
NGC 4698	SA(s)ab	A	16.8	3.3	11.46	-20.58	-	10.22
NGC 4699	SAB(rs)b	AB	25.7	3.1	10.41	-22.53	10.12	10.89
NGC 4775	SA(s)d	A	26.6	2.3	11.67	-	-	10.32
NGC 4900	SB(rs)c	B	17.3	2.5	11.9	-19.82	9.73	9.83
NGC 4902	SB(r)b	B	39.2	2.6	11.61	-22.05	-	10.65
NGC 4930	SB(rs)b	B	35	5.4	12	-21.62	-	-
NGC 4939	SA(s)bc	A	44.3	5.6	11.9	-21.97	-	11.16
NGC 4941	(R)SAB(r)ab	AB	6.4	4.2	11.9	-17.97	-	9.12
NGC 4995	SAB(rs)b	AB	28	2.3	12	-21.11	-	10.4
NGC 5005	SAB(rs)bc	AB	21.3	5.6	10.61	-21.83	10.46	10.7
NGC 5054	SA(s)bc	A	27.3	4.6	11.67	-21.27	10.46	10.66
NGC 5085	SA(s)c	A	28.9	3.9	11.96	-	-	10.48
NGC 5101	(R)SB(rs)0	B	27.4	5.4	11.63	-21.54	-	10.57
NGC 5121	(R')SA(s)a	A	22.1	2.2	11.51	-21.16	-	10.08
NGC 5247	SA(s)bc	A	22.2	4.6	10.5	-21.77	10.32	10.57
NGC 5334	SB(rs)c	B	24.7	4.2	11.99	-	-	10.06
NGC 5371	SAB(rs)bc	AB	37.8	4.2	11.32	-22.27	10.67	10.82
NGC 5427	SA(s)c pec	A	38.1	2.3	11.93	-21.54	10.8	10.57
NGC 5483	SA(s)c	A	24.7	4.6	11.93	-	10.05	10.3
NGC 5676	SA(rs)bc	A	34.5	4	11.87	-21.5	10.63	10.77
NGC 5701	(R)SB(rs)0	B	26.1	4.2	11.76	-21.2	-	10.33
NGC 5713	SAB(rs)bc pec	AB	30.4	3.1	11.84	-21.21	10.72	10.43
NGC 5850	SB(r)b	B	28.5	4.6	11.54	-21.52	-	10.47
NGC 5921	SB(r)bc	B	25.2	4.9	11.49	-21.18	-	10.46
NGC 5962	SA(r)c	A	31.8	2.8	11.98	-21.17	10.55	10.46
NGC 6215	SA(s)c	A	20.5	1.9	12	-20.1	10.54	10.53
NGC 6300	SB(rs)b	B	14.3	5.2	10.98	-20.58	10.09	10.32
NGC 6384	SAB(r)bc	AB	26.6	6.3	11.14	-21.7	-	10.72
NGC 6753	(R)SA(r)b	A	40.9	2.5	11.97	-21.92	10.89	-
NGC 6782	(R)SAB(r)a	AB	50.8	2.2	11.84	-	-	-
NGC 6902	SA(r)b	A	35.7	6.8	11.64	-21.83	-	10.33
NGC 6907	SB(s)bc	B	43	3.3	11.9	-21.96	11.03	-
NGC 7083	SA(s)bc	A	38.7	3.2	11.87	-21.72	10.45	10.73
NGC 7205	SA(s)bc	A	20.5	3.2	11.55	-20.61	10.07	10.3
NGC 7213	SA(s)a	A	22	2.1	11.01	-21.59	-	10.34
NGC 7217	(R)SA(r)ab	A	16	3.6	11.02	-20.9	9.9	10.34
NGC 7412	SB(s)b	B	21.1	4.3	11.88	-20.27	-	10.12
NGC 7418	SAB(rs)cd	AB	17.8	3.6	11.65	-	10.01	9.96
NGC 7479	SB(s)c	B	32.4	3.9	11.6	-21.7	10.79	10.64
NGC 7552	(R')SB(s)ab	B	19.5	3.5	11.25	-20.88	11.03	10.25

Table 2.1 (cont'd)

Galaxy Name (1)	Hubble Type (RC3) (2)	Bar Type (RC3) (3)	D (Mpc) (4)	D_{25} (') (5)	$B_{\rm T}$ (mag) (6)	$M_{\rm V}$ (mag) (7)	$L_{\rm IR}$ ($\log(L_\odot)$) (8)	$L_{\rm B}$ ($\log(L_\odot)$) (9)
NGC 7713	SB(r)d	B	8.2	4.6	11.51	-18.38	-	9.58
NGC 7723	SB(r)b	B	23.7	3.9	11.94	-20.66	-	10.31
NGC 7727	SAB(s)a pec	AB	23.3	3.3	11.5	-21.25	-	10.34
NGC 7741	SB(s)cd	B	12.3	4.1	11.84	-19.14	-	9.7
Highly inclined galaxies with $i > 60°$ (N=33)								
IC 4402	SA(s)b sp	A	22.9	5	12	-20.24	10.05	-
IC 5052	SBd sp	B	6.7	5	11.16	-18.6	-	9.28
NGC 0625	SB(s)m sp	B	3.9	5	11.91	-16.61	8.57	8.73
NGC 0779	SAB(r)b	AB	17.3	4.4	11.95	-20.03	-	10.2
NGC 0908	SA(s)c	A	17.8	6.1	10.83	-21.07	10.27	10.51
NGC 1003	SA(s)cd	A	10.7	6.3	12	-18.7	-	9.64
NGC 1421	SAB(rs)bc	AB	25.5	3.5	11.95	-20.61	10.25	10.64
NGC 1808	(R)SAB(s)a	AB	10.8	7.6	10.74	-20.24	10.71	10
NGC 1964	SAB(s)b	AB	20	6.1	11.58	-20.7	10.09	10.37
NGC 2090	SA(rs)c	A	10.2	6.8	11.99	-18.84	-	9.61
NGC 2280	SA(s)cd	A	23.2	6.8	10.9	-21.53	10.13	10.6
NGC 3511	SA(s)c	A	15.5	6.8	11.53	-19.99	9.82	10.25
NGC 3675	SA(s)b	A	12.8	5.8	11	-	9.92	10.13
NGC 3705	SAB(r)ab	AB	17	4.6	11.86	-20.08	-	10.25
NGC 3877	SA(s)c	A	17	5.1	11.79	-20.16	9.89	10.29
NGC 4062	SA(s)c	A	9.7	4.5	11.9	-18.79	-	9.5
NGC 4100	(P)SA(rs)bc	A	17	5.1	11.89	-19.99	10.04	10.25
NGC 4293	(R)SB(s)0	B	17	6.3	11.26	-20.79	-	10.21
NGC 4388	SA(s)b	A	16.8	5.6	11.76	-20.11	10	10.16
NGC 4448	SB(r)ab	B	9.7	3.8	12	-18.86	-	9.56
NGC 4527	SAB(s)bc	AB	13.5	6.3	11.38	-20.13	10.42	10.08
NGC 4654	SAB(rs)cd	AB	16.8	4.8	11.1	-20.63	10.1	10.32
NGC 4666	SABc	AB	14.1	4.2	11.49	-20.01	10.36	10.1
NGC 4772	SA(s)a	A	16.3	2.8	11.96	-20.02	-	9.7
NGC 4818	SAB(rs)ab pec	AB	21.5	3.4	12	-20.55	9.75	10.46
NGC 4856	SB(s)0	B	21.1	3.8	11.49	-21.12	-	10.3
NGC 5078	SA(s)a sp	A	27.1	4	12	-21.2	10.5	-
NGC 5161	SA(s)c	A	33.5	6.1	12	-21.42	-	10.64
NGC 5448	(R)SAB(r)a	AB	32.6	4	11.93	-	-	10.47
NGC 7184	SB(r)c	B	34.1	6.1	11.65	-21.81	-	10.73
NGC 7582	(R')SB(s)ab	B	17.6	4.5	11.37	-20.61	10.87	10.26
NGC 7606	SA(s)b	A	28.9	5.2	11.51	-21.55	-	10.7
NGC 7814	SA(s)ab: sp	AB	16	5.5	11.56	-20.45	-	10.18

Note. — Columns are : (1) Galaxy name; (2) Hubble type from RC3; (3) RC3 bar type, which is based on visual inspection of optical images and runs as 'B'='strongly barred', 'AB'='weakly barred', and 'A'='unbarred'; (4) Distance in Mpc. Most values are from the NBG (Tully 1988), which assumes a Hubble constant of 75 km s^{-1} Mpc^{-1}. Exceptions are NGC 6753, NGC 6782, NGC 5078, NGC 6907, NGC 7814, and ESO 142-19, for which distances from RC3 are used; (5) D_{25} in arcminutes, the diameter of the isophote where the B band surface brightness is 25 magnitude $arcsecond^{-2}$. Values are from the NBG, except for NGC 6753, NGC 6782, NGC 5078, NGC 6907, NGC 7814, and ESO 142-19 where RC3 data are used; (6) $B_{\rm T}$, the total blue magnitude from RC3; (7) $M_{\rm V}$, the absolute V magnitude from RC3; (8) $L_{\rm IR}$, the global IR luminosity (8 – 1000 μm) in units of $\log(L_\odot)$, from the IRAS Revised Bright Galaxy Sample (Sanders et al. 2003); (9) $L_{\rm B}$, the global blue luminosity in units of $\log(L_\odot)$, from the RC3.

Table 2.2. Bar statistics from sample S4 (136 galaxies)

Band	Unbarred	Barred
B (observed)	75 = 55%	61 = 45%
H (observed)	57 = 42%	79 = 58%
B (deprojected)	76 = 56%	60 = 44%
H (deprojected)	54 = 40%	82 = 60%

Note. — Columns are : (1) Band (observed or deprojected); (2) Number and fraction of galaxies classified as unbarred; (3) Number and fraction of galaxies classified as barred.

Table 2.3. Structural properties of sample S4 (136 galaxies) in the B and H bands

Galaxy Name	i (°)	$PA_{\rm disk}$	class (B)	$e_{\rm bar}$ (B)	$a_{\rm bar}$ (B) (kpc)	class (H)	$e_{\rm bar}$ (H)	$a_{\rm bar}$ (H) (kpc)
(1)	(2)	(3)	(4)	(5)	(6)	(7)	(8)	(9)
IC 0239	37	171	u	-	-		-	-
IC 4444	36	77	u	-	-	u	-	-
IC 5325	38	34	u	-	-	b	0.5	1.5
NGC 0157	41	43	u	-	-	u	-	-
NGC 0210	49	160	b	0.6	12.3	b	0.4	9.7
NGC 0278	25	161	u	-	-	u	-	-
NGC 0289	35	162	u	-	-	b	0.6	2.1
NGC 0428	47	109	u	-	-	u	-	-
NGC 0488	38	6	u	-	-	u	-	-
NGC 0685	35	95	b	0.6	2.0	b	0.6	1.2
NGC 0864	43	31	b	0.7	4.2	b	0.6	3.5
NGC 1042	40	173	b	0.6	4.6	b	0.6	4.4
NGC 1058	13	79	u	-	-	u	-	-
NGC 1073	24	174	b	0.7	4.2	b	0.7	4.5
NGC 1084	39	58	u	-	-	b	0.4	6.1
NGC 1087	52	4	u	-	-	u	-	-
NGC 1187	30	130	b	0.7	3.5	b	0.5	2.9
NGC 1241	55	151	b	0.6	3.8	b	0.6	4.1
NGC 1300	55	102	b	0.6	8.4	b	0.5	8.5
NGC 1302	22	13	b	0.3	2.9	b	0.3	2.9
NGC 1309	21	64	u	-	-	u	-	-
NGC 1317	29	171	b	0.4	0.6	b	0.4	0.6
NGC 1350	58	2	u	-	-	b	0.5	6.8
NGC 1371	24	81	u	-	-	b	0.4	1.9
NGC 1385	47	24	b	0.8	2.0	b	0.6	1.7
NGC 1493	21	90	u	-	-	b	0.5	1.2
NGC 1559	56	61	b	0.8	1.7	b	0.5	0.9
NGC 1617	58	109	u	-	-	u	-	-
NGC 1637	35	31	b	0.5	1.2	b	0.4	1.0
NGC 1703	30	134	u	-	-	b	0.3	1.3
NGC 1792	50	139	u	-	-	b	0.5	4.2
NGC 1832	48	11	b	0.6	2.5	b	0.4	2.2
NGC 2139	36	154	u	-	-	u	-	-
NGC 2196	45	57	u	-	-	u	-	-
NGC 2566	24	59	b	0.6	4.9	b	0.5	4.7
NGC 2775	24	24	u	-	-	u	-	-
NGC 2964	49	95	b	0.6	2.6	b	0.5	2.6
NGC 3166	56	77	u	-	-	b	0.5	3.8
NGC 3169	55	58	u	-	-	u	-	-
NGC 3223	47	117	u	-	-	u	-	-
NGC 3227	55	151	u	-	-	u	-	-
NGC 3261	28	59	b	0.5	5.4	b	0.4	3.7
NGC 3275	21	150	b	0.6	7.6	b	0.5	6.6
NGC 3423	39	35	u	-	-	u	-	-
NGC 3504	8	79	b	0.6	3.8	b	0.6	4.1

Table 2.3 (cont'd)

Galaxy Name	i (°)	$PA_{\rm disk}$	class (B)	$e_{\rm bar}$ (B)	$a_{\rm bar}$ (B) (kpc)	class (H)	$e_{\rm bar}$ (H)	$a_{\rm bar}$ (H) (kpc)
(1)	(2)	(3)	(4)	(5)	(6)	(7)	(8)	(9)
NGC 3507	21	67	b	0.5	2.9	b	0.5	2.6
NGC 3513	43	63	b	0.8	2.7	b	0.7	2.1
NGC 3583	39	134	u	-	-	b	0.5	4.4
NGC 3593	57	86	u	-	-	u	-	-
NGC 3596	32	81	u	-	-	u	-	-
NGC 3646	56	56	u	-	-	u	-	-
NGC 3681	24	132	b	0.3	1.1	b	0.3	0.9
NGC 3684	47	127	u	-	-	u	-	-
NGC 3686	33	18	b	0.7	2.7	b	0.5	2.6
NGC 3726	52	13	b	0.7	4.0	b	0.6	3.8
NGC 3810	45	17	u	-	-	u	-	-
NGC 3885	58	114	u	-	-	u	-	-
NGC 3887	44	13	b	0.6	3.7	b	0.5	3.3
NGC 3893	48	10	u	-	-	b	0.5	6.0
NGC 3938	30	13	u	-	-	u	-	-
NGC 3949	16	143	u	-	-	u	-	-
NGC 4027	38	176	u	-	-	b	0.6	1.2
NGC 4030	43	21	u	-	-	u	-	-
NGC 4051	30	116	b	0.6	4.2	b	0.6	4.8
NGC 4123	43	121	b	0.6	10.5	b	0.6	4.2
NGC 4136	20	51	b	0.6	1.7	b	0.4	0.7
NGC 4145	57	98	b	0.6	1.4	b	0.5	1.7
NGC 4151	36	2	u	-	-	b	0.5	7.9
NGC 4212	43	72	u	-	-	b	0.4	2.8
NGC 4242	45	22	u	-	-	b	0.3	3.0
NGC 4254	24	59	u	-	-	u	-	-
NGC 4303	30	144	b	0.7	3.3	b	0.5	4.5
NGC 4314	18	38	b	0.6	3.2	b	0.6	3.7
NGC 4394	24	109	b	0.5	4.0	b	0.5	3.6
NGC 4414	44	166	u	-	-	u	-	-
NGC 4450	44	174	b	0.4	3.8	b	0.4	3.6
NGC 4457	25	86	u	-	-	u	-	-
NGC 4487	48	72	u	-	-	b	0.3	1.0
NGC 4496	24	65	b	0.7	2.1	b	0.6	0.8
NGC 4504	55	147	u	-	-	u	-	-
NGC 4548	40	154	b	0.6	6.2	b	0.6	5.9
NGC 4571	33	36	u	-	-	u	-	-
NGC 4579	35	95	b	0.4	3.9	b	0.4	3.7
NGC 4580	43	161	b	0.6	4.3	b	0.3	1.9
NGC 4593	43	105	b	0.6	13.6	b	0.6	12.9
NGC 4618	25	178	u	-	-	b	0.6	0.5
NGC 4643	34	56	b	0.5	7.1	b	0.5	5.4
NGC 4647	50	121	b	0.6	2.5	u	-	-
NGC 4651	49	71	u	-	-	u	-	-
NGC 4665	33	17	b	0.3	3.8	b	0.4	4.1

Table 2.3 (cont'd)

Galaxy Name	i (°)	$PA_{\rm disk}$	class (B)	$e_{\rm bar}$ (B)	$a_{\rm bar}$ (B) (kpc)	class (H)	$e_{\rm bar}$ (H)	$a_{\rm bar}$ (H) (kpc)
(1)	(2)	(3)	(4)	(5)	(6)	(7)	(8)	(9)
NGC 4689	44	173	u	-	-	u	-	-
NGC 4691	34	27	u	-	-	b	0.7	2.01
NGC 4698	59	174	u	-	-	b	0.5	2.6
NGC 4699	33	34	b	0.3	1.7	b	0.3	1.5
NGC 4775	18	47	u	-	-	u	-	-
NGC 4900	22	113	b	0.8	5.4	b	0.6	1.8
NGC 4902	16	102	b	0.6	6.8	b	0.5	4.7
NGC 4930	40	52	b	0.5	8.1	b	0.4	8.0
NGC 4939	53	6	u	-	-	u	-	-
NGC 4941	58	13	u	-	-	u	-	-
NGC 4995	47	93	b	0.6	6.3	b	0.5	3.7
NGC 5005	59	59	u	-	-	u	-	-
NGC 5054	52	159	u	-	-	u	-	-
NGC 5085	32	56	u	-	-	u	-	-
NGC 5101	23	65	b	0.5	7.3	b	0.5	6.8
NGC 5121	48	57	u	-	-	u	-	-
NGC 5247	36	36	u	-	-	u	-	-
NGC 5334	41	11	b	0.6	3.0	b	0.5	1.8
NGC 5371	40	31	b	0.5	6.5	b	0.4	19.7
NGC 5427	38	11	u	-	-	b	0.5	4.8
NGC 5483	34	50	u	-	-	u	-	-
NGC 5676	59	50	u	-	-	u	-	-
NGC 5701	24	43	b	0.4	5.8	b	0.4	5.3
NGC 5713	32	1	u	-	-	b	0.6	3.5
NGC 5850	29	178	b	0.7	12.1	b	0.6	10.6
NGC 5921	46	130	b	0.7	8.5	b	0.6	7.6
NGC 5962	42	109	u	-	-	u	-	-
NGC 6215	44	43	u	-	-	b	0.5	1.8
NGC 6300	38	109	b	0.7	3.0	b	0.5	2.8
NGC 6384	55	27	u	-	-	u	-	-
NGC 6753	30	25	u	-	-	u	-	-
NGC 6782	28	36	b	0.5	6.7	b	0.4	6.4
NGC 6902	22	162	u	-	-	b	0.3	3.3
NGC 6907	51	65	u	-	-	u	-	-
NGC 7083	54	8	u	-	-	u	-	-
NGC 7205	58	65	u	-	-	u	-	-
NGC 7213	18	179	u	-	-	u	-	-
NGC 7217	30	136	u	-	-	u	-	-
NGC 7412	52	74	b	0.6	1.8	b	0.6	6.6
NGC 7418	27	91	b	0.7	2.6	b	0.6	2.8
NGC 7479	41	33	b	0.7	8.0	b	0.6	8.6
NGC 7552	23	33	b	0.7	2.0	b	0.6	5.3
NGC 7713	59	166	u	-	-	u	-	-
NGC 7723	34	38	b	0.6	3.2	b	0.5	2.3
NGC 7727	16	64	u	-	-	u	-	-

Table 2.3 (cont'd)

Galaxy Name	i ($^\circ$)	$PA_{\rm disk}$	class (B)	$e_{\rm bar}$ (B)	$a_{\rm bar}$ (B) (kpc)	class (H)	$e_{\rm bar}$ (H)	$a_{\rm bar}$ (H) (kpc)
(1)	(2)	(3)	(4)	(5)	(6)	(7)	(8)	(9)
NGC 7741	40	167	b	0.7	3.2	b	0.6	3.0

Note. — Columns are : (1) Galaxy name; (2) Outer disk inclination i, calculated from B band ellipse fits before deprojection; (3) Outer disk PA, calculated from B band ellipse fits before deprojection; (4) B band classification as unbarred (u) or barred (b) from ellipse fits after deprojection; (5) Bar strength, as characterized by $e_{\rm bar}$, of large-scale bar in B band after deprojection; (6) Bar semi-major axis $a_{\rm bar}$ in kpc of large-scale bar in B band after deprojection; (7) H band classification as unbarred (u) or barred (b) from ellipse fits after deprojection; (8) Bar strength, as characterized by $e_{\rm bar}$, of large-scale bar in H band after deprojection; (9) Bar semi-major axis $a_{\rm bar}$ in kpc of large-scale bar in H band after deprojection.

Chapter 3

Barred Galaxies in the Abell 901/2 Supercluster with STAGES[0]

3.1 Introduction

Stellar bars are one of the most important internal drivers of disk galaxy evolution. For field galaxies in the local Universe, bars are known to be the most efficient way to redistribute material in the galaxy disk (Combes & Sanders, 1981; Weinberg, 1985; Debattista & Sellwood, 1998, 2000; Athanassoula, 2002). Bars channel gas into the central regions of galaxies, where powerful starbursts can ignite (Schwarz, 1981; Shlosman et al., 1989; Kormendy & Kennicutt, 2004; Jogee, 1999; Jogee et al., 2005; Sheth et al., 2005), building central disky structures known as 'pseudobulges' (Kormendy, 1982b, 1993; Jogee, 1999; Jogee et al., 2005; Fisher, 2006; Weinzirl et al., 2009). Peanut/boxy bulges in inclined galaxies are thought to be associated with bending instabilities and vertical resonances in bars (e.g., Combes & Sanders, 1981; Combes et al., 1990; Pfenniger & Norman, 1990; Athanassoula, 2005;

[0]A significant part of this chapter was originally published in the Astrophysical Journal by Irina Marinova as lead author. Reproduced by permission of the AAS.

Martinez-Valpuesta et al., 2006).

As early as 1963, de Vaucouleurs used visual classification on photographic plates to find that approximately 30% of nearby galaxies appear strongly barred in the optical band, with the fraction increasing to approximately 60% if very weak bars are considered. Quantitative studies for the optical bar fraction at $z \sim 0$ yield a mean value of 45% to 52% with a typical uncertainty of +8% from ellipse-fits (MJ07; BJM08; Aguerri et al. 2009, hereafter A09) and $\sim 47\%$ from bulge-disk-bar decomposition (Reese et al. 2007). The lower value from these quantitative methods compared to the 60% value from de Vaucouleurs (1963) stems from the fact that many weak bars (with RC3 class 'AB') are obscured by dust and star formation (SF), caused by the presence of curved shocks/dust lanes (e.g., Athanassoula 1992) on the leading edges of the bar. Many such bars may fail to meet rigorous quantitative criteria for characterizing bars via ellipse-fit or bulge-disk-bar decomposition, but their presence can sometimes be guessed via visual inspection (see MJ07 for detailed discussion). In the near infra-red (NIR), where obscuration by dust and SF is minimized, different quantitative methods, such as ellipse-fit (Menendez-Delmestre et al. 2007; MJ07), bulge-disk-bar decomposition (Weinzirl et al. 2009) and Fourier decomposition (Laurikainen et al. 2004) all yield a NIR bar fraction of $\sim 60\%$ for bright nearby samples.

The above values of the bar fraction at $z \sim 0$ refer to the globally-averaged value over a wide range of Hubble types and luminosities. Several studies have performed more detailed explorations to look at how bars relate

to the properties of the host spiral galaxies. Recent studies based on SDSS (BJM08; A09) using ellipse-fits report that the optical bar fraction rises in spiral galaxies which appear to be disk-dominated, quasi-bulgeless, or have a morphology suggestive of a low bulge-to-disk ratio. A similar trend was observed by Odewahn (1996) using visual classes: he found that the optical fraction of strong bars in disk galaxies rises from Sc galaxies towards later types. Similar results are found in the near-infrared by Weinzirl et al. (2009) using 2D bulge-disk-bar decomposition on nearby bright spiral galaxies.

Recently, studies performed at intermediate redshifts with the Advanced Camera for Surveys (ACS) on the Hubble Space Telescope (HST) have allowed bars to be probed at earlier epochs. Several studies have shown that the optical fraction of strong ($e > 0.4$) or prominent bars is $\sim 30\%$ on average over $z \sim 0.2$–1 (Elmegreen et al. 2004; Jogee et al. 2004; Zheng et al. 2005). In particular, Jogee et al. (2004) find that the optical fraction of strong bars does not show an order of magnitude decline, but only varies from 36%±6% over $z \sim 0.2$–0.7 to 24%±4% over $z \sim 0.7$ to 1.0. A much larger study finds a variation in the optical fraction of strong bars from 27%±1% to 12%±1% for $z \sim 0.2$–0.84 (Sheth et al. 2008). Interpretations differ on whether the observed decline is simply due to systematic effects, such as loss of resolution and rising obscuration with redshift (Jogee et al. 2004; MJ07; BJM08), or whether it reflects an intrinsic decline (Sheth et al. 2008) in the true bar fraction.

While bars have been studied extensively in the field, little is known about the fraction of bars and their properties in dense environments. The

presence of bars is particularly useful to identify galaxies with disks in clusters (§ 3.4.1), where other disk signatures, such as spiral arms, may be absent due to ram pressure stripping. Furthermore, we can use galaxy clusters as a lab to test our theories of bar formation and evolution. The fraction of barred galaxies in a cluster depends on the epoch of bar formation, the robustness of bars, the interplay between cluster environmental processes (harassment, tidal interactions, ram pressure stripping), and the evolutionary history of clusters.

The detailed process of bar formation is not yet known, but simulations suggest that a cold disk, with low velocity dispersion, σ, favors the formation of spontaneous disk instabilities (e.g., Toomre, 1964; Jog & Solomon, 1984). External triggers, such as tidal interactions, can also induce bars in a dynamically cold disk (e.g., Noguchi, 1987; Elmegreen et al., 1990, 1991; Hernquist & Mihos, 1995). Thus, cluster processes can have competing effects on bar formation. While frequent tidal interactions can induce stellar bars, they may also heat the disks and thereby make them less susceptible to bar formation. Dubinski et al. (2008) explored these effects by modeling the interaction of a hundred DM satellites on M31. They found that while the satellites did not have a large heating effect on the disk, encounters close to the galaxy center could produce strong non-axisymmetric instabilities such as stellar bars. However, in dense clusters, disk galaxies that are deprived of their cold gas through ram-pressure stripping may be too dynamically hot to form bars. Recently van den Bosch et al. (2008) have shown that low-mass satellite cluster galaxies may be more affected by gas strangulation, which may in turn make

them less favorable to bar formation. It is also important to note that if bars cannot be easily dissolved once formed (see § 3.5), then in scenarios where clusters grow by accretion of field galaxies, existing bars in accreted galaxies may not be much impacted by subsequent cluster processes.

There have been only a handful of observational studies that have explored the impact of environment on barred disks. Recently, A09 studied the effects of environment in field and intermediate density regions on barred galaxies using $\sim$ 3000 galaxies at $0.01 \leq z \leq 0.04$ from SDSS-DR5, and found that the bar fraction and properties were not correlated to galaxy environment. Bars were identified using ellipse fits. However, they excluded interacting galaxies from their study. Barazza et al. (2009) study the impact of environment on bars in disk galaxies using $\sim$ 2000 galaxies at intermediate redshift ($z \sim 0.4$–1) from the ESO Distant Clusters Survey (EDisCS; White et al., 2005). van den Bergh (2002) found no difference between the bar fraction in the field and in clusters using a uniform sample of 930 galaxies from the Shapley-Ames catalog, in a study where bar classifications were performed through visual inspection of optical images. He therefore concluded that the bar fraction depends solely on host-galaxy properties. It should be noted that for this study, the environment assignments were largely qualitative, made by inspecting the region around the galaxy on the image, and looking at luminosities and radial velocities of surrounding galaxies. Varela et al. (2004) found that the bar fraction is almost twice as high in galaxies that are interacting, compared to isolated galaxies. Their study relied on redshifts from the CfA

survey and morphological classifications from LEDA and NED. The results of Varela et al. (2004) confirm previous studies (e.g., Elmegreen et al., 1990), who find a higher number of barred galaxies in binary systems.

We are now in a position to make further progress in this largely unexplored aspect of galaxy evolution with the STAGES panchromatic dataset (§ 3.2), which includes: a 0.5×0.5 square degree HST ACS mosaic in F606W of the A901/2 supercluster, spectrophotometric redshifts from COMBO-17, coverage with $XMM-Newton$, $GALEX$, and $Spitzer$, as well as dark matter maps. In § 3.3, we outline the techniques for characterizing bars and disks. It should be noted that traditionally the bar fraction $f_{\rm bar-opt}$ is defined as the fraction of *disk galaxies* that are barred. Hence calculation of $f_{\rm bar-opt}$ requires disk galaxies to be reliably identified. We use the term 'disk galaxies' to describe all galaxies with an outer disk component (e.g., S0-Sm), which may or may not be accompanied by a central bulge. In this paper, we draw attention to the fact that many automated methods commonly used to identify disks in the field may fail in clusters. Motivated by this, we explore different ways of identifying disks (e.g., color cut, Sérsic cut, visual classification) in § 3.4.1, and explore the effect on $f_{\rm bar-opt}$. We determine the frequency of bars as a function of host disk properties (§ 3.4.3, 3.4.4, 3.4.5), and as a function of cluster radius, galaxy number density, ICM density, and DM density (§ 3.4.6). The comparison of our results to those from field studies is given in § 3.4.7. In § 3.5, we discuss the implications of our results for the evolution of bars and disks in dense environments. In § 3.6, we give the summary and conclusions.

3.2 Data and Sample Selection

The Abell 901/902 supercluster consists of three galaxy clusters and a group at $z \sim 0.165$, with an average separation of 1 Mpc. The properties of this system are described in detail in Gray et al. (2002). The STAGES survey (Gray et al., 2009) covers a 0.5×0.5 square degree field centered on the supercluster, consisting of an 80-tile mosaic with the HST ACS F606W. This ACS filter corresponds closely to the optical B band. The ACS point spread function (PSF) of $0.1''$ corresponds to ~ 282 pc at $z \sim 0.165$[1]. Spectro-photometric redshifts are available for all galaxies from COMBO-17 (Wolf et al., 2004, 2005b) where the photo-z accuracy of the sample used in this paper is $\delta z/(1+z) \sim 0.01$. The multi-wavelength dataset includes X-ray maps of the ICM density from $XMM-Newton$, UV from $GALEX$, $Spitzer$ 24μ coverage, and dark matter maps from weak lensing (Heymans et al., 2008). Total star formation rates (SFRs) derived from UV and $Spitzer$ 24μ luminosities (Bell et al., 2005), as well as stellar masses (Borch et al., 2006) are also available for this field.

Cluster galaxies are selected using photometric redshifts (see Gray et al. 2009 for a detailed description). This provides a sample of 1990 cluster galaxies. For this paper, we focus on galaxies brighter than $M_{\rm V} \leq -18$. We choose this cutoff, because it tends to separate well the regimes where normal and dwarf galaxies dominate on the luminosity functions of clusters (Binggeli

[1]We assume in this paper a flat cosmology with $\Omega_M = 1 - \Omega_\Lambda = 0.3$ and H_0 =70 km s^{-1} Mpc^{-1}.

et al., 1988). We do not consider dwarf galaxies in this study for two reasons. Firstly, our resolution of ~ 282 pc may be insufficient in many cases to reliably identify morphological structures such as bars in smaller dwarf galaxies. Secondly, the contamination of the sample by field galaxies at magnitudes fainter than $M_{\rm V} = -18$ becomes significant. This leaves us with a sample of 785 bright ($M_{\rm V} \leq -18$), cluster galaxies. The field contamination for this sample is estimated to be $\sim 10\%$, from the space density of field galaxies using the same absolute magnitude cut (Wolf et al., 2005b).

3.3 Methodology

3.3.1 Methods for Selection of Disk Galaxies

In all studies conducted to date (e.g., de Vaucouleurs & de Vaucouleurs, 1963; Sellwood & Wilkinson, 1993; Eskridge et al., 2000; Knapen et al., 2000; Mulchaey & Regan, 1997; Jogee et al., 2004; Laurikainen et al., 2004b; Elmegreen et al., 2004; Zheng et al., 2005; Buta et al., 2005; Marinova & Jogee, 2007; Menéndez-Delmestre et al., 2007; Barazza et al., 2008; Sheth et al., 2008), the bar fraction, $f_{\rm bar}$ has been defined as the number of barred *disk* galaxies divided by the total number of *disk* galaxies:

$$f_{\rm bar} = \frac{N_{\rm barred}}{N_{\rm disk}} = \frac{N_{\rm barred}}{N_{\rm barred} + N_{\rm unbarred}}. \tag{3.1}$$

Note that in the above studies, as well as in this paper, we use the term 'disk galaxies' to describe all galaxies with a significant outer disk component (e.g., systems typically labeled as S0-Sm), which may or may not be accompanied

by a central bulge. The bar fraction is only quoted with disk galaxies in mind, because bars are believed to be related to an $m = 2$ instability in the disk component of galaxies. Furthermore, if the bar fraction were calculated over *all* galaxies, changes in the morphological distribution between disk and spheroidal (e.g., E) galaxies would influence the bar fraction and make it hard to compare across different samples. In the local Universe, for nearby galaxies, catalogs like the RC3 (de Vaucouleurs et al., 1991) contain visual classifications of galaxy morphology, making it possible to select a sample of disk galaxies for bar studies. In large surveys such as the SDSS and GEMS, two quantitative methods have been used to pick out disk galaxies: (1) using a blue-cloud color cut in color-magnitude space (Jogee et al., 2004, BJM08) and (2) using a Sérsic index, n, from a single component fit to isolate a sample of disk-dominated galaxies (Jogee et al., 2004; Bell et al., 2004; Barden et al., 2005; Ravindranath et al., 2004). In the color cut method, only blue cloud galaxies are selected on a $U - V$ color-magnitude diagram. The Sérsic cut method involves selecting only galaxies with Sérsic index $n < 2.5$. This is motivated by the fact that a pure disk has a Sérsic index of 1, while a deVaucouleurs profile typically used to describe a spheroid has a Sérsic index of 4. Note that in Bell et al. (2004), Barden et al. (2005), and Ravindranath et al. (2004), the goal was to broadly separate early-type (E/S0/Sa) galaxies, from late-type disk-dominated galaxies (Sb-Sm). However, because bars can occur in all types of disk galaxies from S0-Sm, we would like to explore how well such Sérsic and color cuts work in our cluster sample at separating spheroidal galaxies (Es) from disk galaxies

as defined above (e.g., S0-Sm).

Using a blue-cloud or Sérsic cut to pick out disk-dominated galaxies works fairly well at isolating a disk-galaxy sample in the field. However, these methods can grossly fail in a cluster environment, where the galaxy populations are different than those in the field. Gas stripping of spirals could quench their star formation and make them look redder. These galaxies might then be missed by a color cut. On the other hand, the prevalence of bulge-dominated S0-type disk galaxies in clusters Dressler (1980) could be missed by a Sérsic cut. For this reason, we use a third method to pick out disk galaxies: visual classification.

We visually classify the whole sample and put galaxies into different groups according to the galaxy morphology (§ 3.3.3). A galaxy is identified as a disk galaxy if it exhibits the dynamical signatures of disk instabilities such as a stellar bar and spiral arms. In the absence of such structure, disks are picked by an identifiable break between the bulge and disk component either in the image itself and/or looking for a break between a steep inner profile and a slowly declining outer profile in an estimation of the brightness profile with the Smithsonian Astrophysical Observatory visualization tool *DS*9. Three classifiers (I.M., A.H., S.J.) completed a training set of several hundred galaxies, and two classifiers (A.H. & I.M.) classified the full cluster sample, with the third classifier performing random checks. Subsequently, uncertain cases were reviewed by all three classifiers. In our bright cluster galaxy sample of 785 galaxies, 750 of them could be classified into visual classes as described

above. The remaining galaxies were either too messy to classify, too compact to classify, or unclassifiable for other reasons, such as noise or edge effects. We could not reach agreement on 4% of cases regarding whether a galaxy was a pure bulge or contained a disk component.

From the three different methods of disk selection (visual, Sérsic cut, blue-cloud cut) we obtain 625, 485, and 353 disk galaxies, respectively. Detailed results from the different methods of disk selection are presented in § 3.4.1.

3.3.2 Characterization of Bars

We use the standard IRAF task 'ellipse' to fit ellipses to the galaxy isophotes out to $a_{\rm max}$, where $a_{\rm max}$ is the radius at which the surface brightness reaches sky level. This method of ellipse fitting has been widely used to identify and characterize bars (e.g., Wozniak et al. 1995; Friedli et al. 1996; Regan et al. 1997; Jogee et al. 1999, 2002a, 2002b, 2004; Knapen et al. 2000; Laine et al. 2002; Sheth et al. 2003; Elmegreen et al. 2004; MJ07; Menéndez-Delmestre et al. 2007). We employ an iterative adaptive wrapper, developed by Jogee et al. (2004), which runs the task 'ellipse' up to a maximum number of N iterations. Each iteration uses the previous fit to produce an improved guess for the isophote parameters. N is typically set to 300, but for most objects we obtain a good fit in only a few iterations. A good fit is one where an ellipse is able to be fitted at every radial increment out to $a_{\rm max}$. As described in detail in Jedrzejewski (1987), the goodness of the ellipse fits is character-

ized by the harmonic amplitudes A3, B3, A4, and B4. The amplitudes of these components signify how well the shape of the actual isophote is approximated by the fitted ellipses Jedrzejewski (e.g., 1987). For this sample, we find typical amplitudes of 0–15% in the bar region. The advantages and limitations of the ellipse-fitting method are further discussed in detail in MJ07, where the statistical effects of deprojection are also addressed. We were able to successfully fit 97% of the visually identified disk sample of 625 galaxies. The galaxies where 'ellipse' fails generally do not have a regularly decreasing surface brightness profile, which is necessary to define the center for the fitting routine.

We overlay the fitted ellipses onto the galaxy images and plot the radial profiles of surface brightness (SB), ellipticity (e), and position angle (PA). We use both the overlays and radial profiles to classify the disk galaxies as 'inclined', 'barred' or 'unbarred' using an interactive classification tool and quantitative criteria (Jogee et al. 2004). The three classes are described below. We also extract quantitative parameters from the radial profiles, such as the size, ellipticity, and PA of both the disk and bar.

Disk galaxies classified as 'inclined' have an outermost isophote with $e > 0.5$, corresponding to $i > 60°$. Because it is difficult to identify morphological structures in such highly inclined disk galaxies, we do not attempt to classify them as 'barred' or 'unbarred'. After discarding highly inclined disk galaxies (226 or 36%) and those with visually-identified poor fits (32 or 5%), we are left with 350 moderately inclined ($i < 60°$), bright ($M_{\rm V} \leq -18$), cluster disk galaxies. The luminosity and color distributions of the total sam-

ple of 785 bright, cluster galaxies, the visually-identified disk galaxy sample (N= 625), and the moderately-inclined, ellipse-fitted sample of 350 disk galaxies are over-plotted in Figure 3.1a and b. The figure shows that no significant bias is introduced on $M_{\rm V}$ and color by restricting the sample to moderately inclined disk galaxies.

For galaxies with moderate inclinations ($i < 60^{\circ}$), we classify a galaxy as barred if: (1) the e rises smoothly to a global maximum, $e_{\rm bar} > 0.25$, while the PA remains relatively constant (within 20°), and (2) the e then drops by at least 0.1 and the PA changes at the transition between the bar and disk region. These criteria have been shown to work well in identifying barred galaxies (e.g., Knapen et al. 2000; Jogee et al. 2002a,b, 2004; Laine et al. 2002). An example of the overlays and radial profiles of a barred cluster galaxy are shown in Figure 3.2. The semi-major axis of the bar $a_{\rm bar}$ is taken as the radius where the ellipticity reaches a global maximum ($e_{\rm bar}$). The disk semi-major axis length $a_{\rm disk}$ and ellipticity $e_{\rm disk}$ are measured from the radius of the last fitted isophote.

The moderately inclined galaxies, which do not satisfy the bar criteria are classified as unbarred. This category includes clearly unbarred cases, as well as cases, which we denote as 'PA twist'. The latter are systems where all the bar criteria are satisfied, except for the criterion of constant PA in the bar region: rather than being constant within 20°, the PA of the high ellipticity feature may twist slightly more than this limit. Some of these 'PA twist' systems may actually be barred galaxies where the effects of dust and

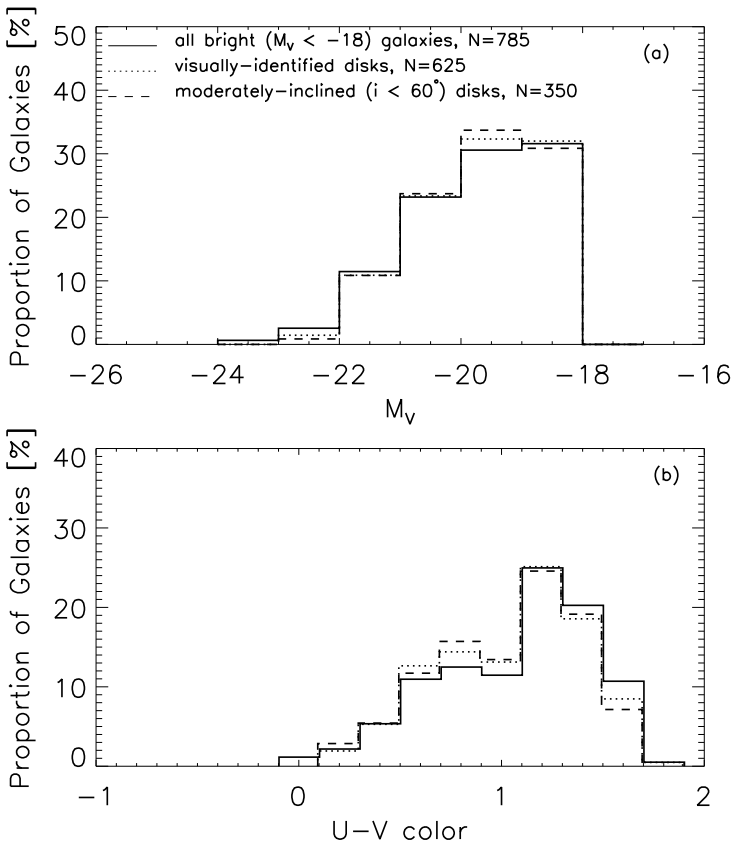

Figure 3.1 (a) The solid line shows the histogram of absolute magnitude $M_{\rm V}$ of our total cluster sample of 785 bright ($M_{\rm V} \leq -18$) galaxies. Most galaxies have $-20 \leq M_{\rm V} \leq -18$. The dotted line shows the $M_{\rm V}$ distribution of galaxies visually classified as disks. The dashed line shows the $M_{\rm V}$ distribution of the final ellipse-fitted disk sample, after excluding highly inclined ($i > 60°$), and poorly fitted galaxies. (b) Rest-frame $U - V$ color distribution of the whole cluster galaxy sample (solid line), visually-identified disk sample (dotted line), and ellipse-fitted, moderately-inclined disk sample (dashed line). Excluding highly inclined disk galaxies does not have a significant effect on the absolute $M_{\rm V}$ magnitude, or rest-frame $U - V$ color distributions.

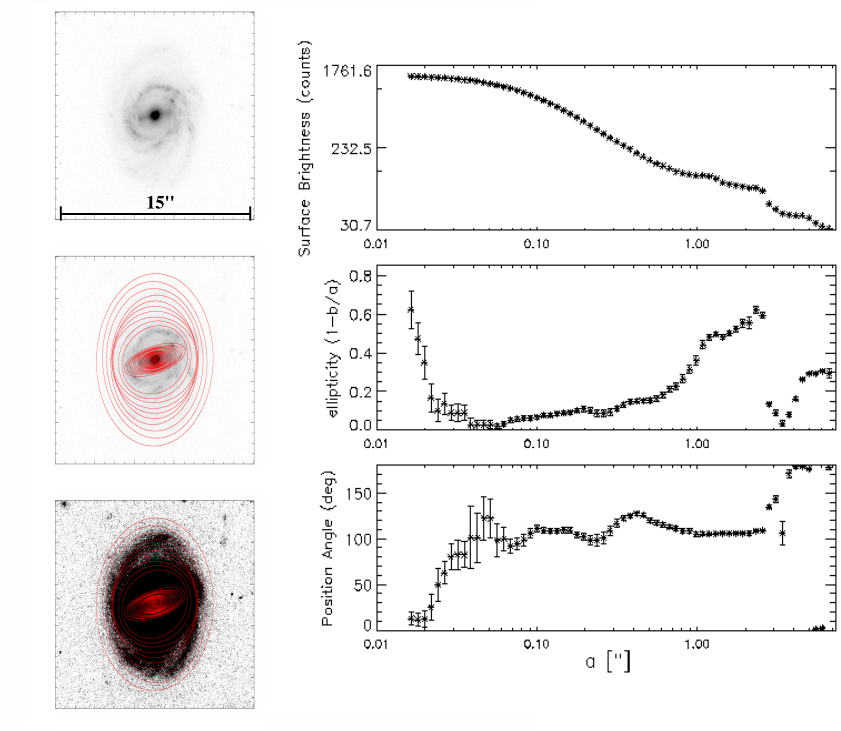

Figure 3.2 *Left*: Ellipse fit overlays on the F606W image of a barred cluster galaxy. In the middle and bottom panels, the contrast is adjusted to show the inner regions and outer disk regions, respectively. *Right*: Radial profiles of the surface brightness (SB), ellipticity e, and position angle (PA). The bar signature is evident in the smooth rise of the e to a global maximum, while the PA remains relatively constant in the bar region. The e then drops and the PA changes, indicating the transition to the disk region. See § 3.3.2 for details.

SF can cause the PA to vary more than it would in a near-IR image. This effect is more likely to happen with weak bars, where the dust lanes along the leading edges of the bar are curved, producing a 'twisting' in the PA radial profile (Athanassoula, 1992b). Such weak bars are also associated with SF along their leading edge. Among the unbarred galaxies, we have 36 cases of 'PA twist'. We use this number as an estimate of the number of barred galaxies we might be classifying as unbarred in the optical images, and fold it into the error bar (upper limit) for the optical bar fraction.

Another effect we have to address is whether we can detect bars in the smaller/fainter disk systems. We consider in the following analysis only disk galaxies, which we define as galaxies with an outer disk component (e.g., S0-Sm) that may or may not be accompanied by a central bulge (see § 3.3.1). As discussed in § 3.2, our resolution is $\sim$ 280 pc. With ellipse-fitting, at least 2.5 PSF elements are necessary to detect a bar. This means that the lower limit on the bar radius ($a_{\rm bar}$) that we can reliably detect is $\sim$ 700 pc. It was already noted by Kormendy (1979) that the sizes of bars correlate with galaxy luminosity, and late-type, fainter galaxies host smaller bars. Erwin (2004, 2005) found that primary bars in galaxies later than Sbc can have radius $a_{\rm bar}$ as small as 500 pc. Thus, in order to avoid missing small bars in late-type, faint galaxies, we make a cut in galaxy semi-major axis $a_{\rm disk} = 3$ kpc in addition to our magnitude cut of $M_{\rm V} = -18$. We choose the value of $a_{\rm disk} = 3$ kpc as a conservative cut, according to the following analysis. In our cluster sample, for visually identified disk galaxies (§ 3.3.1), we find that $a_{\rm disk}$ and R_{25} correlate

with a mean ratio of $R_{25}/a_{\rm disk} = 0.87$ (Fig. 3.3a), where R_{25} is calculated for the cluster sample from the absolute $M_{\rm B}$ magnitude according to

$$log(\frac{R_{25}}{kpc}) = -0.249 \times M_{\rm B} - 4.00, \tag{3.2}$$

from Schneider (2006). In MJ07 we find that most bars have ratios $a_{\rm bar}/R_{25}$ =0.2–0.4, where R_{25} is the isophotal radius at which the B-band surface brightness reaches 25 mag arcsec^{-2}. Assuming a median $a_{\rm bar}/R_{25} \sim 0.3$, it follows that in order to ensure that we are looking at galaxies that host bars larger than 700 pc, we need to select galaxies with $R_{25} \times 0.3 \sim 700$ pc, or $R_{25} \sim 2300$ pc. Using the mean $R_{25}/a_{\rm disk} = 0.87$ for our sample, this yields a galaxy semi-major axis $a_{\rm disk}$ of ~ 2.7 kpc. There are only 10 disk galaxies that are eliminated by this cut. Figures 3.3b and 3.3c show the correlation of $a_{\rm bar}$ and $a_{\rm disk}$ with $M_{\rm V}$, showing only galaxies visually classified as disks. The dashed line in panel 3.3b at 0.7 kpc represents the limit in $a_{\rm bar}$ at which we can reliably identify all bars. The dashed line in panel 3.3c at 3 kpc indicates the cut in $a_{\rm disk}$.

In addition to quantitatively identifying and characterizing bars using ellipse fitting, we also visually classify all galaxies in the sample. The identification of bars through visual inspection provides an independent check for the detection of bars through ellipse-fits. The visual bar classification agrees with the ellipse fits for over 90% of cases. For the cases where a bar is found through visual classification, but not through ellipse-fitting, it is because dust and gas mask the bar signature, making the PA twist. We conservatively take

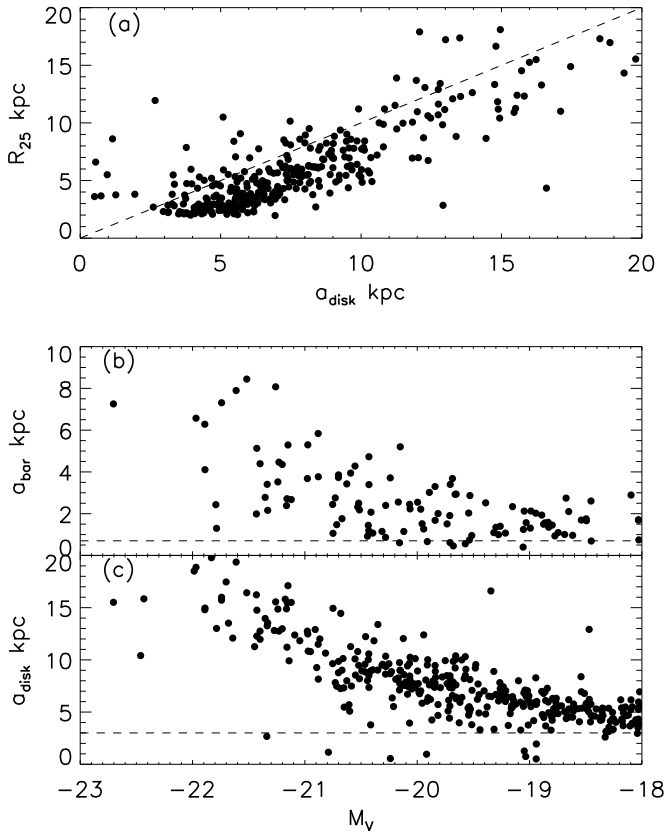

Figure 3.3 *(a)*: The semi-major axes $a_{\rm disk}$ of galaxies visually classified as disks (§ 3.3.1) correlate with the isophotal radius R_{25} where the B-band surface brightness reaches 25 mag arcsec^{-2}. The mean ratio of $R_{25}/a_{\rm disk} = 0.87$. The dashed line shows a slope of 1. *(b)*: The relationship between bar semi-major axis length $a_{\rm bar}$ and $M_{\rm V}$ absolute magnitude. The dashed line shows the limit of $a_{\rm bar} \sim$ 700 pc for reliable bar detection and characterization using ellipse-fit. *(c)*: The relationship between disk semi-major axis length $a_{\rm disk}$ and absolute magnitude $M_{\rm V}$. For the bright $M_{\rm V} \leq -18$ sample, we only select disks with $a_{\rm disk} \geq 3$ kpc in order to ensure that the bars of interest typically have $a_{\rm bar} \geq 700$ pc and can be reliably detected. See § 3.3.2 for details.

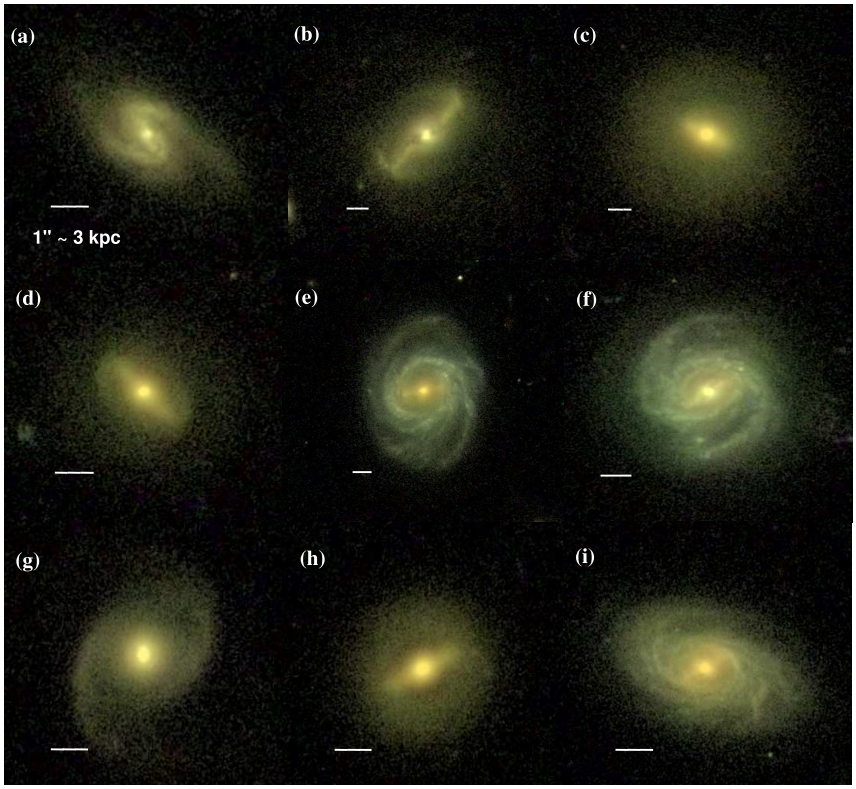

Figure 3.4 Examples of representative bright ($M_{\rm V} \leq -18$) barred galaxies identified through ellipse-fitting in the A901/902 supercluster. The white line in each panel shows the scale of $1'' \sim 3$ kpc.

the upper error bar in the optical bar fraction as the sum in quadrature of the binomial term and the error of +10% caused by isophotal twists. Note that the error from missed bars due to isophotal twisting can only make the bar fraction higher. Representative barred galaxies from the cluster sample are shown in Figure 3.4.

3.3.3 Visual Classification of Secondary Morphological Parameters

For our cluster sample, we visually classify secondary morphological parameters such as the prominence of the bulge and the presence of gas and dust.

Since we are only interested in studying large-scale bars that extend well beyond the bulge region of the galaxy, the prominence of the bulge is not key for determining the bar fraction. It is interesting, however, for studying and interpreting correlations between bar and host disk properties (see § 3.4.3–3.4.5). Our goal is not to finely measure the bulge-to-total light (B/T) ratio in galaxies, but to identify galaxies with extreme B/T, such as systems that appear nearly bulgeless and likely have very low B/T, and those with prominent bulges, suggestive of high B/T. We thus classify galaxies into three broad groups: 'pure bulge' (Fig. 3.5a,b), 'pure disk' (Fig. 3.5g–j), and 'bulge+disk' (Fig. 3.5c–f). 'Pure disk' galaxies are those where no central spheroidal component is seen. Conversely, a galaxy is classified as a 'pure bulge' if its morphology is spheroidal and there is no break in the brightness profile, indicative of the transition between the bulge-dominated and disk-dominated region. In addition, 'pure bulge' galaxies do not exhibit disk features such as spiral arms or stellar bars. In our cluster sample of bright galaxies, we find that 23%±12% of galaxies are visually classified as 'pure disk', 60%±10% are classified as 'bulge+disk', and 17%±1% were classified as 'pure bulge.' The values quoted are from the classifications of I.M. and the percent errors indicate the sum in quadrature of the dispersion between classifiers and the binomial term

of the statistical error. The disagreement is due to the inherent difficulty in separating ellipticals from disk galaxies, when the disk is smooth and has no unambiguous disk signature, such as a bar or a spiral arm.

Seven members of the STAGES team performed an independent visual classification of the sample using the standard Hubble Type system. The agreement between our classifications and theirs on whether a particular galaxy is a disk galaxy was 70%. If their sample of visually selected disks is used for the analysis in § 3.4, our results on the optical bar fraction do not change. Note that the standard Hubble type system is not optimal for our study. Principally, this is because Hubble types assume a correlation between the prominence of the bulge and the smoothness of the galaxy disk/spiral arms. While this correlation holds fairly well for field galaxies, it can break down in clusters, where there can be galaxies with large bulge-to-disk ratios but fairly smooth disks (Koopmann & Kenney, 1998). We discuss this in more detail below.

In Table 3.1, we show the breakdown of morphological classes as a function of projected distance to the nearest cluster center for galaxies with $M_{\rm V} \leq -18$. We take the core radius to be at 0.25 Mpc, because the number density of galaxies shows a sharp break at this radius (Heiderman et al. 2008). The outer region is defined as lying between the core radius at R = 0.25 Mpc and the virial radius of the cluster, $\rm R_{vir}$ = 1.2 Mpc (Heymans et al. 2008). Beyond the virial radius is the outskirt region.

We also visually classify galaxies into those with a clumpy or smooth

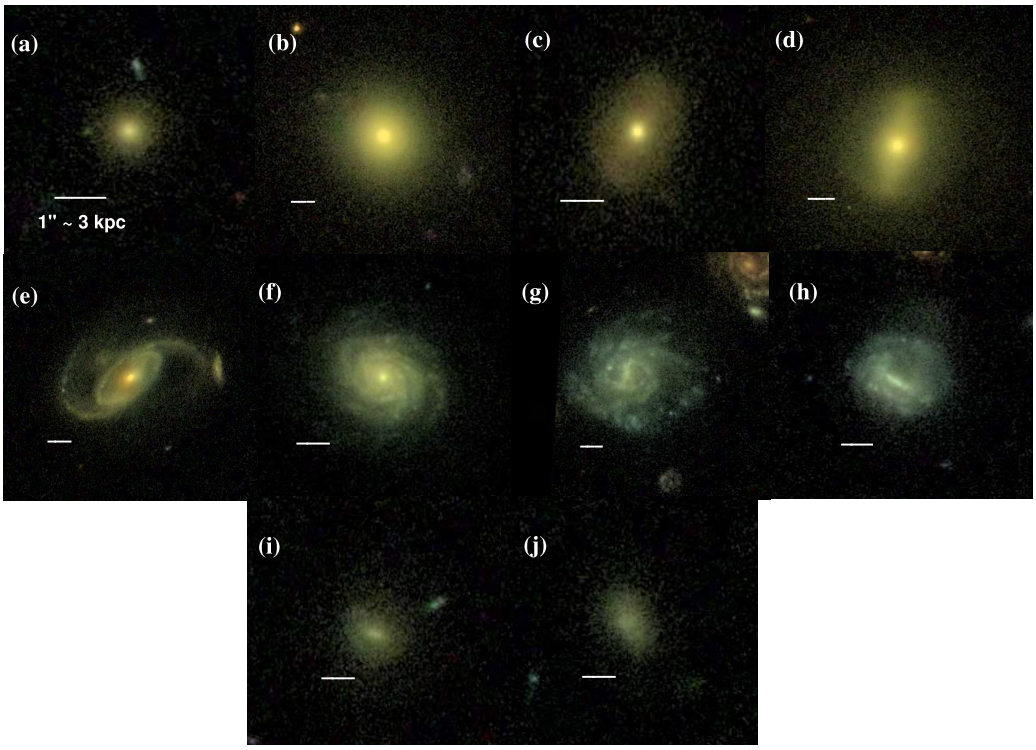

Figure 3.5 Examples of the visual classification of secondary morphological properties (§ 3.3.3) for the bright ($M_V \leq -18$), moderately inclined ($i < 60°$) sample. The white line in each panel shows the scale of $1'' \sim 3$ kpc. Galaxies are grouped according to the visual prominence of the bulge into three groups: 'pure bulge' (a,b), 'bulge+disk' (c–f), and 'pure disk' (g–j). Note that it is difficult to visually separate the classes 'pure bulge' and 'bulge+disk' (e.g., b vs. c) when the galaxy appears smooth and shows no disk signatures such as bars or spiral arms.

disk, motivated by the following considerations. Firstly, the presence of gas, dust, and star formation along the bar can prevent its detection in optical images, particularly for weak bars. In weak bars, the dust lanes are curved because of weaker shocks (Athanassoula, 1992b). In addition, weaker shocks can induce star formation along the bar, while strong shocks are accompanied by straight dust lanes and tend to suppress star formation along the bar (e.g., Elmegreen, 1979; Das & Jog, 1995; Laine et al., 1999; Jogee et al., 2005). The curved dust lanes and star formation regions in weak bars produce a pattern that causes fitted ellipses to have varying PA along the bar, and to sometimes fail to satisfy the criterion of a flat PA plateau along the bar (§ 3.3.2). In very gas/dust-rich galaxies, even strong bars can be masked by dust and star formation. These effects make it more difficult to identify bars at optical wavelengths (e.g., Block et al., 1994). Several studies (Eskridge et al. 2000; Laurikainen et al. 2004; MJ07) show that, because of obscuration by gas, dust, and star formation regions in the optical, the bar fraction is higher in the infrared (IR) band by a factor of ~ 1.3 for galaxies at $z \sim 0$. In cluster environments, the correction factor for bar obscuration is unknown.

Secondly, it is useful to explore the relationship between clumpiness, the visual prominence of the bulge, and bars in cluster environments, where the situation might well differ from the field. In the field, along the traditional Hubble Sequence, on average the visual prominence of bulge and the tightness of the spiral arms increase from Sd to Sa, while the clumpiness of the spiral arms decreases. In field galaxies, there is a wide range of B/T for each Hubble

type, with low B/T galaxies being present across S0 to Sc (Laurikainen et al. 2007; Weinzirl et al. 2009; Graham & Worley 2008), but the average B/T tends to fall in later Hubble types (Laurikainen et al., 2007; Weinzirl et al., 2009; Graham & Worley, 2008). In clusters, where a number of processes, such as ram-pressure stripping or galaxy harassment can alter the gas content of galaxies, the relationship between B/T and gas/SF content or clumpiness of the disk may break down. For example, in the Virgo cluster, the central concentration of galaxies does not correlate with their star formation properties, as it does in the field (Koopmann & Kenney 1998). Wolf et al. (2009) discuss the effect of these issues with respect to the Hubble type classifications performed by the STAGES team.

Motivated by these considerations, we attempt to visually characterize the presence of gas and dust in galaxies. The degree of 'clumpiness' in a galaxy is used as a rough proxy for estimation of the presence of gas and dust. We allocate galaxies into two broad classes: (1) 'smooth' galaxies that show no patchy obscuration by gas and dust or (2) 'clumpy' galaxies that have a lot of patchiness indicative of the presence of gas and dust. We find that 73%±2% (551/750) of the bright galaxies in our supercluster sample appear mostly smooth (contain little or no gas and dust), while 27%±2% (199/750) of the bright galaxies appear clumpy (contain some gas and dust). The fractions quoted are from the classifications of I.M. and the percent errors indicate the sum in quadrature of the dispersion between classifiers and the binomial term of the statistical error. Examples of 'smooth' galaxies are shown in Fig. 3.5,

panels a–d and i–j. 'Clumpy' galaxies are shown in panels e–h of Figure 3.5.

3.4 Results

3.4.1 Selection of Disk Galaxies in Clusters

How well do the Sérsic and blue-cloud cut methods pick out disk galaxies when compared to visual classification? Out of the 762 ellipse-fitted galaxies, 608 are visually classified as disks. This number is reduced to 573 if only galaxies with $a_{\rm disk} > 3$ kpc are considered.

Figure 3.6 compares the disk galaxies identified through the three different methods: visual classification, blue-cloud color cut, and a Sérsic cut. In this paper, the color cut is made using $U - V$ color. Panel (a) shows where the visually-identified disk galaxies lie in the rest-frame $U - V$ vs. $M_{\rm V}$ plane. Moderately-inclined, $i < 60°$, barred galaxies are shown as green points, where the bars are identified through ellipse-fitting. Even though we did not identify bars with ellipse-fits for highly inclined galaxies with $i > 60°$, and do not consider inclined systems in the rest of the study, bars were noted in such systems during the visual classification (cyan points). Unbarred galaxies with visually-identified spiral arms (all inclinations) are shown in pink. The black points show galaxies identified as disks with visual classification for all inclinations, but without a bar or spiral arms. The solid line separates the red sample from the blue cloud galaxies, using the equation

$$U - V = (1.48 - 0.4 \times 0.165 - 0.08 \times (M_{\rm V} + 20.0)) - 0.25, \qquad (3.3)$$

derived for the STAGES sample by Wolf et al. (2005b), where $M_{\rm V}$ is the V absolute magnitude and $U-V$ is the rest-frame color. Panel (b) shows where visually identified disk galaxies lie in the $U-V$ color vs. Sérsic index n plane. Symbols are the same as in panel (a). The solid line shows the cutoff of $n = 2.5$, which is supposed to separate disk galaxies and spheroids.

The technique of identifying disk galaxies as those with a Sérsic index $n < 2.5$ (Fig. 3.6b) picks out 69%±2% (396/573) of galaxies visually selected as disks. The error bars represent the statistical error. The Sérsic cut method will pick up many of the red disks that the color cut misses, however the Sérsic cut method might miss some early-type disk galaxies with very prominent bulges or very clumpy galaxies with bright star formation regions in their outer disks. In addition, the presence of an AGN will drive the Sérsic index to high values. Figure 3.7a shows examples of visually-identified disk galaxies missed by the Sérsic cut.

Our analysis suggests that the Sérsic cut misses $31\% \pm 2\%$ of visually-identified disks. How robust is this number? We consider the possibility that some galaxies visually classified as disk galaxies ('pure disk' or 'bulge+disk') may in fact be misclassified ellipticals. This is most likely to happen when the disk is smooth and has no unambiguous disk signature, such as a bar or a spiral arm. As stated in § 3.3.3, it is difficult to separate a 'pure bulge' galaxy from an unbarred, smooth 'bulge+disk' (e.g., S0) without spiral arms. In addition, unbarred 'pure disk' galaxies without spiral arms that appear mostly smooth could also be misclassified ellipticals. As a firm lower limit to the number

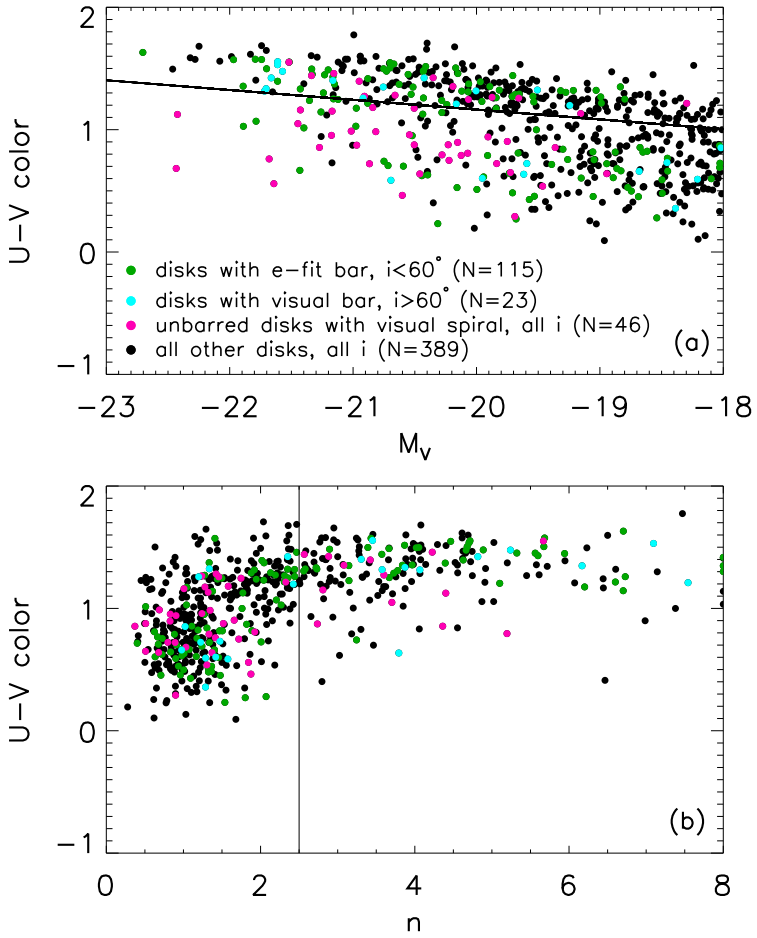

Figure 3.6 This figure compares the disk galaxies identified through three different methods: visual classification, blue-cloud color cut, and a Sérsic cut for the bright ($M_{\rm V} \leq -18$) sample with $a_{\rm disk} > 3$ kpc. Panel (a) shows where the visually-identified disk galaxies lie in the rest-frame $U-V$ vs. $M_{\rm V}$ plane. Moderately-inclined, $i < 60°$, barred galaxies are shown as green points, where the bars are identified through ellipse-fitting. Bars in highly inclined galaxies ($i > 60°$), identified during visual classification are shown as cyan points. Unbarred disk galaxies with visually-identified spiral arms (all inclinations) are shown in pink. The black points show galaxies identified as disks with visual classification for all inclinations, but without a bar or spiral arms. The solid line separates the red sample from the blue cloud galaxies. Panel (b) shows where visually identified disk galaxies lie in the Sérsic index n vs. $M_{\rm V}$ plane. Colors are the same as in panel (a). The solid line shows the cutoff of $n = 2.5$, which is supposed to separate disk galaxies and spheroids.

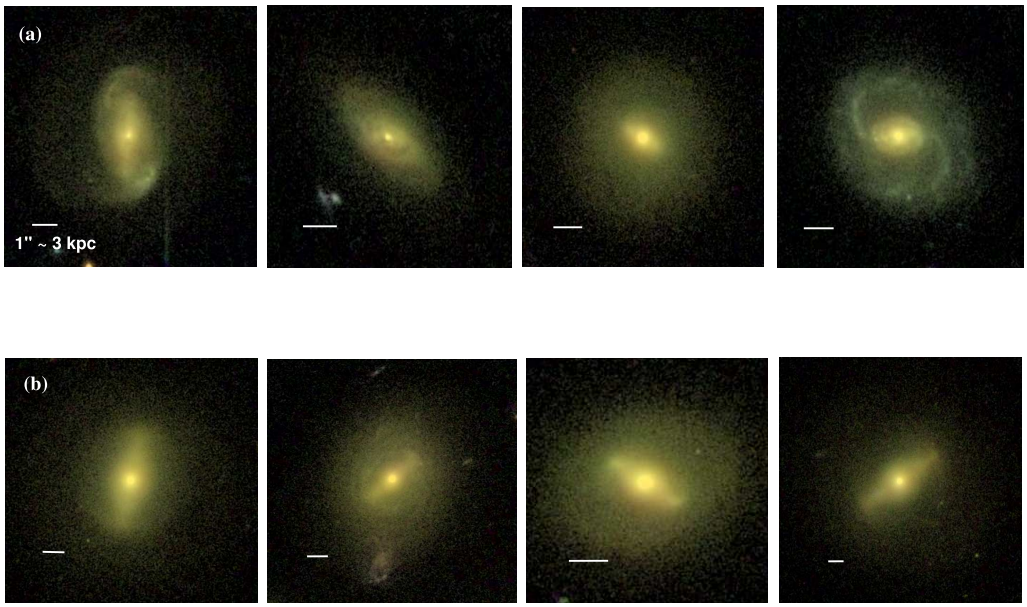

Figure 3.7 Examples of bright ($M_{\rm V} \leq -18$), moderately inclined ($i < 60°$), visually-identified disk galaxies, which are missed by a Sérsic cut with $n \leq 2.5$ (a), or by a blue-cloud cut (b). The white line in each panel shows the scale of $1'' \sim 3$ kpc.

of visually-identified disk galaxies missed by the Sérsic cut we consider disk galaxies ('pure disk' or 'bulge+disk') that have a clear disk signature such as a bar and/or spiral arms. This sets a firm lower limit on the number of disk galaxies that are missed by a Sérsic cut. We find that at least 25% (67/267) of the galaxies with $n > 2.5$ display unambiguous disk signatures. Thus, in summary, we estimate that 25% to 31% of visually-identified disk galaxies (e.g., S0-Sm) are missed by taking a Sérsic cut ($n < 2.5$).

The technique of selecting blue cloud galaxies picks out out $49\% \pm 2\%$ (279/573) of the visually-identified disk galaxies. The 294 galaxies missed are in the red sample and the large number of these galaxies is consistent with the high number of red disks in a cluster environment. Figure 3.7b shows some examples of visually-identified disk galaxies in the red sample, which would be missed if a blue-cloud color cut is used to pick out disks.

It is interesting to look at the composition of the red sample in more detail. The 294 visually-identified disks make up 75% of the total population of 390 red sample galaxies. Galaxies classified as 'pure bulge' (e.g., E's) make up 25% (96/390). Out of the galaxies visually identified as disks in the red sample, 95% (279/294) are classified as 'bulge+disk' and only 5% (15/279) are classified as 'pure disk' with no visible bulge component.

The large proportion of the red sample consisting of visually identified disk galaxies (e.g., S0-Sm) may seem surprising if one typically thinks of the red sample as made up mostly of ellipticals. However, Wolf et al. (2009) have shown that the red sample in the cluster contains both galaxies on the red

sequence and also dusty red disk galaxies which do not lie on the sequence. Again, we set a firm lower limit to the disk galaxies in the red sample, by considering disk galaxies ('pure disk' or 'bulge+disk') that have a clear disk signature such as a bar and/or spiral arms. This gives a robust lower limit of 22% (84/390) of galaxies in the red sample that are disks. Thus, in summary, our results suggest that 22% to 75% of the red sample is made up of disks, with the large range primarily caused by the difficulty in differentiating red, featureless S0-type galaxies from spheroidals (see Figure 3.5). A significant fraction of dusty, red disk galaxies in the supercluster sample is also found by Wolf et al. (2009), where the properties of these galaxies are discussed in detail.

In summary, we have explored how three commonly used methods for selecting disk galaxies in the field, namely, visual classification, a single component Sérsic cut ($n \leq 2.5$), and a blue-cloud cut, fare in the A901/902 cluster environment. We found that the Sérsic cut and blue-cloud cut methods suffer from serious limitations, and miss 31% and 51% , respectively, of visually-identified disks, particularly the many red, bulge-dominated disk galaxies in clusters. In cluster environments, the latter two methods are not well suited to reliably picking disk galaxies. Thus, unless otherwise stated, we use the visual classifications to define a disk galaxy sample in the remaining analysis.

3.4.2 Global Optical Bar Fraction

The optical fraction of barred galaxies *among all galaxies* brighter than $M_{\rm V} = -18$, is $25\%^{+10\%}_{-2\%}$. However, this number is not very useful as changes in this number can reflect a change in the disk fraction, as well as the fraction of disks that host bars. Furthermore, stellar bars are $m = 2$ instabilities that occur only in disks, and insights into their formation and evolution can be best gleaned by inspecting the fraction of disks that are barred at different epochs and in different environments.

As mentioned in § 3.3.1, this has motivated the definition of the bar fraction as the fraction of disks that are barred as given by Equation 3.1. All studies of bars to date (e.g., deVaucouleurs 1963; Sellwood & Wilkinson 1993; Eskridge et al. 2000; Knapen et al. 2000; Mulchaey & Regan 1997; Jogee et al. 2004; Laurikainen et al. 2004; Elmegreen et al. 2004; Zheng et al. 2005; Buta et al. 2005; MJ07; Menéndez-Delmestre et al. 2007; BJM08; Sheth et al. 2008) have adopted this definition and thus provide complementary comparison points for our studies.

For the STAGES cluster, we use visual classification to define a disk galaxy sample (see § 3.3.1 and § 3.4.1) and calculate the optical bar fraction $f_{\rm bar-opt}$. We find $f_{\rm bar-opt} = 34\%^{+10\%}_{-3\%}$. This value is similar to the optical bar fraction $f_{\rm bar-opt-EDisCS} \sim$25% found for galaxies brighter than $M_{\rm V} = -19$ in intermediate-redshift ($z \sim 0.4$–1.0) clusters by Barazza et al. (2009).

For completeness, we also calculate the bar fraction using a blue-cloud

color cut and Sérsic cut to select disk galaxies. The results are shown in Table 3.2 for bright ($M_{\rm V} \leq -18$) galaxies, and in Table 3.3 for galaxies with $\rm M_*/M_\odot > 10^9$. Although the three disk selection methods pick very different number of disks (Tables 3.2, 3.3, and § 3.4.1), they yield a similar optical bar fraction $f_{\rm bar-opt}$ in the range of 29–34%, This result means that the optical bar fraction in blue galaxies picked out by the color cut and that in low Sérsic index galaxies, is similar to the total average bar fraction found through selecting disk galaxies by visual classification (Tables 3.2 and 3.3).

3.4.3 Optical Bar Fraction as a Function of the Prominence of the Bulge

We explore the relationship between the optical bar fraction and host galaxy properties, such as the prominence of the bulge.

While we did not perform a structural bulge+disk+bar decomposition to accurately characterize B/T (e.g., Laurikainen et al. 2007, Weinzirl et al. 2009), we can use the three broad visually-classified groups of galaxies: 'bulge+disk', 'pure disk', and 'pure bulge'.

We plot the optical fraction of bars as a function of morphological class in Figure 3.8a. Here the morphological classes have been grouped by the visual prominence of the bulge. Galaxies with a 'bulge+disk' component are in the first bin, while 'pure disk' galaxies are in the second bin. We find that $f_{\rm bar-opt}$ increases from $29\%^{+10\%}_{-3\%}$ in 'B+D' galaxies to $49\%^{+12\%}_{-6\%}$ in 'pure disk' galaxies, suggesting that the optical bar fraction rises in spiral galaxies, which are disk-

dominated and have very low bulge-to-disk ratios. This result is also shown in Table 3.4

This result is further suggested by Figure 3.8b, which shows the optical bar fraction as a function of central concentration in the host galaxy, as characterized by the effective radius normalized to the disk radius, $r_{\rm e}/a_{disk}$. The effective radius $r_{\rm e}$ is calculated from single-component Sérsic fits (Gray et al., 2009). The disk semi-major axis a_{disk} comes from the semi-major axis of the outermost ellipse fitted to each galaxy, where the isophotes reach sky level (see § 3.3.2). The optical bar fraction clearly increases with decreasing central concentration, from $15\%^{+11\%}_{-4\%}$ in galaxies with high concentration ($r_{\rm e}/a_{disk}$=0.15), to $50\%^{+13\%}_{-9\%}$ in galaxies with low concentration ($r_{\rm e}/a_{disk}$=0.75). We note that the optical bar fraction does not show a similar correlation with Sérsic index n for this sample, as there is a large scatter of n within each morphological class. In addition, the relationship of the optical bar fraction with $r_{\rm e}/a_{disk}$ in Figure 3.8b can be compared with previous studies (BJM08), which show a similar trend in the field.

At this point, it is important to ask whether the trend of a higher $f_{\rm bar-opt}$ in disk galaxies with no significant bulge component is real, or due to systematic effects which cause us to miss primary bars in galaxies with prominent bulges. In this paper, we are considering large-scale primary bars, which by definition lie outside the bulge region. If the bar is strong and/or extended well beyond the bulge region, it is unlikely that the ellipse-fit method and quantitative criteria described in § 3.3.2 would miss the bar. On the other

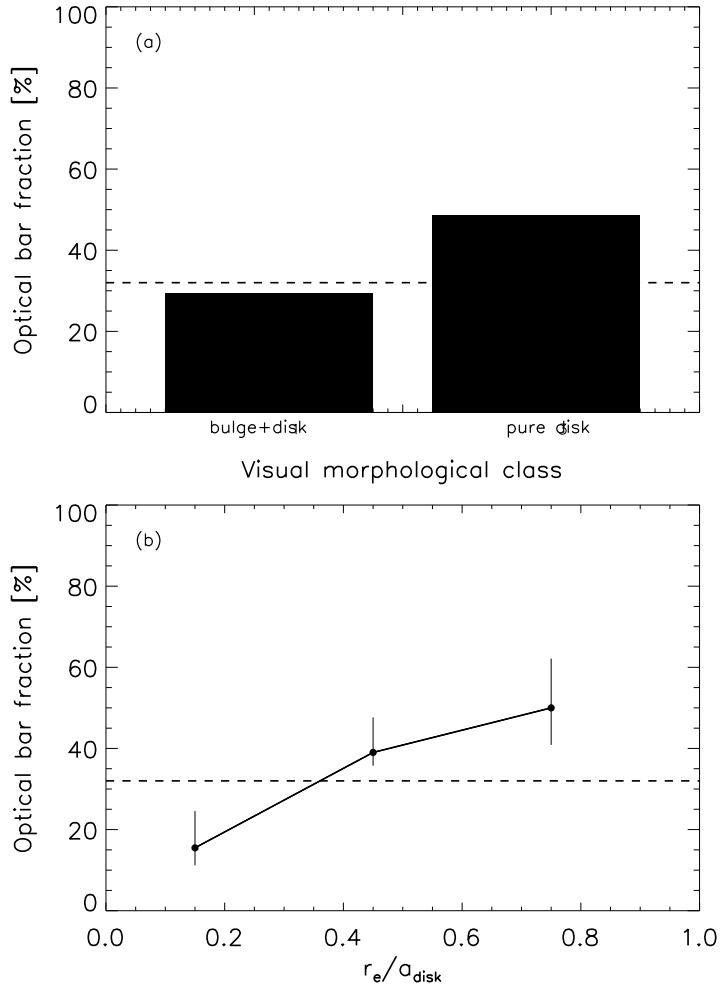

Figure 3.8 *(a)* The optical bar fraction as a function of visual morphological class. The total bar fraction ($34\%^{+10\%}_{-3\%}$) based on disk galaxies of all morphological types using visual disk selection is shown as the horizontal dashed line in both panels. The first bin contains galaxies classified as 'bulge+disk', while the second bin contains galaxies classified as 'pure disk'. The bar fraction shows a rise from $29\%^{+10\%}_{-3\%}$ to $49\%^{+12\%}_{-6\%}$ from galaxies classified as 'bulge+disk' to 'pure disk'. *(b)* The optical bar fraction as a function of central galaxy concentration, as characterized by the effective radius normalized to the disk radius, $r_{\rm e}/a_{\rm disk}$. Only bins with significant number statistics are shown. The bar fraction increases from $15\%^{+11\%}_{-4\%}$ in galaxies with high concentration ($r_{\rm e}/a_{\rm disk} \sim 0.15$), to $50\%^{+14\%}_{-9\%}$ in galaxies with low concentration ($r_{\rm e}/a_{\rm disk} \sim 0.75$).

hand, if the bar is only slightly larger than the bulge, one may face cases where the ellipse-fit method might miss the bar. Furthermore, if the bar is intrinsically weak (i.e. of low ellipticity), then the dilution effect of the large bulge may cause the measured ellipticity of the weak bar to fall below the cutoff value (0.25) where it would be considered a bar. We tested and assessed these effects in several ways described below.

Firstly, we note that studies using a method different from ellipse fitting, namely 2D bulge-disk-bar decomposition on nearby galaxies, also show that galaxies with a larger bulge-to-total ratio (B/T) host a lower proportion of bars than galaxies of lower B/T (Weinzirl et al. 2009). For disk galaxies with $M_{\rm B} < -19$, the bar fraction increases from 31%±13% in spirals with $B/T \geq 0.4$, to 68%±4% in spirals with $B/T \leq 0.2$ (see their Table 8 and § 5.6). Of course, one could argue that 2D bulge-disk-bar decomposition is also more likely to miss the bar component, when the bar contains a much smaller fraction of the light than the bulge. We therefore performed a second test. In addition to using ellipse-fitting to detect bars, we also visually inspect all galaxies as an extra check. We expect that we would see most short bars in galaxies with large bulges via visual classification. We only find two such cases. This small number is not enough to make up for the large drop in $f_{\rm bar-opt}$ toward bulge-dominated galaxies.

We also performed a third test. If the trend of a lower $f_{\rm bar-opt}$ in bulge-dominated galaxies was due to the fact that a prominent bulge causes us to systematically miss bars with low ellipticity around 0.25, then we would not

expect the trend to persist if we only include strong (high ellipticity) bars. We tested this by recomputing the optical bar fraction in pure disks and B+D systems after applying a lower limit cutoff 0.4 and 0.5 on the bar ellipticity. In both cases, we find that the trend of a higher $f_{\rm bar-opt}$ in disk galaxies without prominent bulges remains. We conclude that the latter trend is likely real, and will explore theoretical scenarios that could account for it in § 3.5

We also note that the rise in the optical bar fraction as a function of the prominence of the bulge or central concentration of the host galaxy is in agreement with BJM08, which found that the optical bar fraction in pure disk galaxies is a factor of ~ 2 higher than in disk galaxies with prominent bulges, for an SDSS sample of $M_{\rm V} \leq -18.6$ blue-cloud galaxies and redshift range $0.01 \geq z \geq 0.03$. This result is confirmed by A09, who find that the optical bar fraction increases from 29% in S0 galaxies, to 54% in late-type (Sc-Sd) systems, using SDSS galaxies at $0.01 \leq z \leq 0.04$.

3.4.4 Optical Bar Fraction as a Function of Host Luminosity

In Figure 3.9a-c we show the optical bar fraction as a function of host galaxy rest-frame magnitude $M_{\rm V}$. The optical bar fraction is calculated for all three methods of disk selection (color cut, Sérsic cut, and visual classification). For all three methods of disk selection, the optical bar fraction shows a decrease from $\sim 60\%^{+14\%}_{-10\%}$ at $M_{\rm V} = -21.5$ to $\sim 20\%^{+11\%}_{-4\%}$ at $M_{\rm V} = -18.5$.

This result may seem counter-intuitive given the fact that we find a lower optical bar fraction in bulge-dominated galaxies, and we might expect

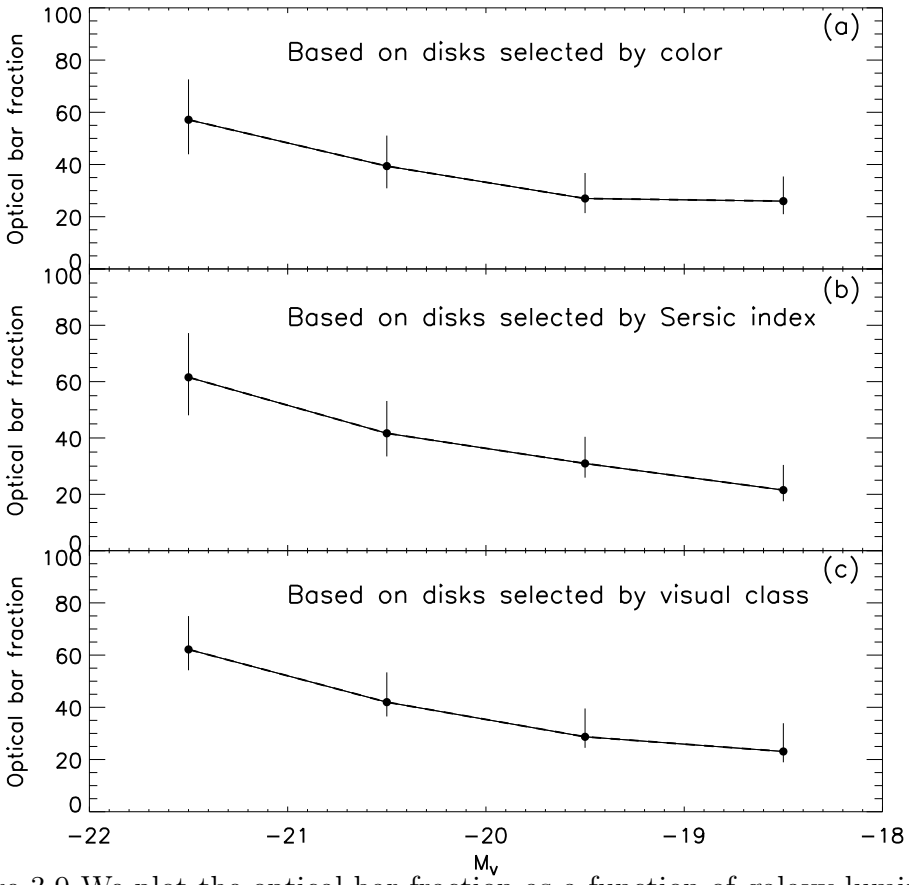

Figure 3.9 We plot the optical bar fraction as a function of galaxy luminosity $M_{\rm V}$ for the three methods of disk selection: *(a)* a blue-cloud color cut; *(b)* a Sérsic ($n \leq 2.5$) cut; *(c)* visual classification. For all three methods of disk selection, the optical bar fraction shows a decrease from $\sim 60\%^{+14\%}_{-10\%}$ at $M_{\rm V} \sim -21.5$ to $\sim 20\%^{+11\%}_{-4\%}$ at $M_{\rm V} = -18.5$.

such systems to be on average brighter. However, Table 3.5 explains why we find the opposite result. This table shows how the optical bar fraction varies as a function of morphological class and absolute magnitude. Here the morphological classes refer to the four visually-classified disk morphological classes: 'bulge+disk smooth', 'bulge+disk clumpy', 'pure disk smooth', and 'pure disk clumpy'. Table 3.5 shows that the optical bar fraction is higher at brighter $M_{\rm V}$ *for any given morphological class.* Therefore, when all of the visual morphological classes are grouped together and $f_{\rm bar-opt}$ is calculated as a function of $M_{\rm V}$ in Fig. 3.9c, the optical bar fraction is higher for brighter magnitudes.

This result is consistent with the findings of Barazza et al. (2009) for cluster galaxies at intermediate redshifts ($z \sim 0.4$–1). This study also finds that, although brighter, early Hubble type galaxies host fewer bars than fainter, late-type galaxies, within a given Hubble type, brighter galaxies on average have a higher optical bar fraction.

3.4.5 Optical Bar Fraction as a Function of Host Color

We find no significant difference in the optical bar fraction in disks on the red sequence and blue cloud. When disks are selected through visual classification, the optical bar fraction on the red sequence is $f_{\rm bar-RS} \sim 34\%^{+11\%}_{-4\%}$ and on the blue cloud, it is $f_{\rm bar-BC} \sim 34\%^{+11\%}_{-4\%}$. This can be easily seen by inspection of Fig. 3.6. The identical values for the blue cloud and red sequence explain in part why the global optical bar fraction $f_{\rm bar-opt}$ based on visual

selection of disks, is similar to the one obtained by selecting disks via a blue cloud cut.

Taking a global average of the optical bar fraction across the blue cloud and red sequence may not reveal the dependence of the optical bar fraction solely on color because the relative number of bright to faint galaxies is different on the blue cloud and red sequence, with the red sequence having more bright galaxies (Fig. 3.6). As already shown in § 3.4.4, the bright systems have a higher optical bar fraction than fainter galaxies, since the optical bar fraction rises at higher luminosities for each given morphological type (Table 3.5). Therefore, we expand the exploration of the optical bar fraction by looking at the breakdown of the optical bar fraction as a function of rest-frame $U-V$ and $M_{\rm V}$ (Table 3.6), as well as $U-V$ and visual morphological class (Table 3.7).

In Table 3.6, we find that most bright galaxies are red with $U-V$ color >1 and $f_{\rm bar-opt}$ of 44%–69% at $M_{\rm V}=-20$ to -22. Table 3.7 shows that for 'bulge+disk' galaxies that are red ($U-V>1$) galaxies classified as 'clumpy' have the highest bar fraction of 76%. Blue pure disk galaxies have an optical bar fraction of $\sim 50\%$.

3.4.6 Optical Bar Fraction as Function of Kappa, Σ_{10}, ICM density, and Distance to Nearest Cluster Center

How does the local environment affect the optical bar fraction, and where do barred galaxies live with respect to the density peaks in the A901/902 cluster environment? In this section, we make a first step in exploring these

questions using four traces of local environment density: the line-of-sight projected surface mass density κ (Heymans et al. 2008), the local galaxy number density Σ_{10} (Wolf et al., 2005b; Gilmour et al., 2007), the ICM density as characterized by the X-ray emission from hot intra-cluster gas in counts, and the projected distance to the nearest cluster center. We calculate Σ_{10} by finding the radius enclosing the ten nearest neighbors to a galaxy. This is used to calculate a galaxy number density, quoted in $(Mpc/h)^{-2}$. Maps of κ for the Abell 901/902 field are constructed by Heymans et al. (2008) through an analysis of weak gravitational lensing, which is sensitive to the line-of-sight projected surface mass density.

Figure 3.10 shows the variation of the three measures of local environment density (κ, Σ_{10}, and ICM density) with distance to the nearest cluster center. It is evident from all three tracers, that local density decreases with increasing distance from the nearest cluster center. The core, outer region, and outskirt of the clusters are defined in § 3.3.3. One caveat in this analysis is that the quantities used are projected quantities.

Figure 3.11 shows the variation of the optical bar fraction function of: (a) distance from nearest cluster center, (b) $\log \Sigma_{10}$, (c) κ, and (d) ICM density. We find that between the core and the virial radius of the cluster ($R \sim 0.25$ to 1.2 Mpc), the optical bar fraction $f_{\mathrm{bar-opt}}$ does not depend strongly on the local environment density tracers (κ, Σ_{10}, and ICM density), and varies at most by a factor of ~ 1.3, allowed by the error bars.

Within the core region, the small number statistics and projection ef-

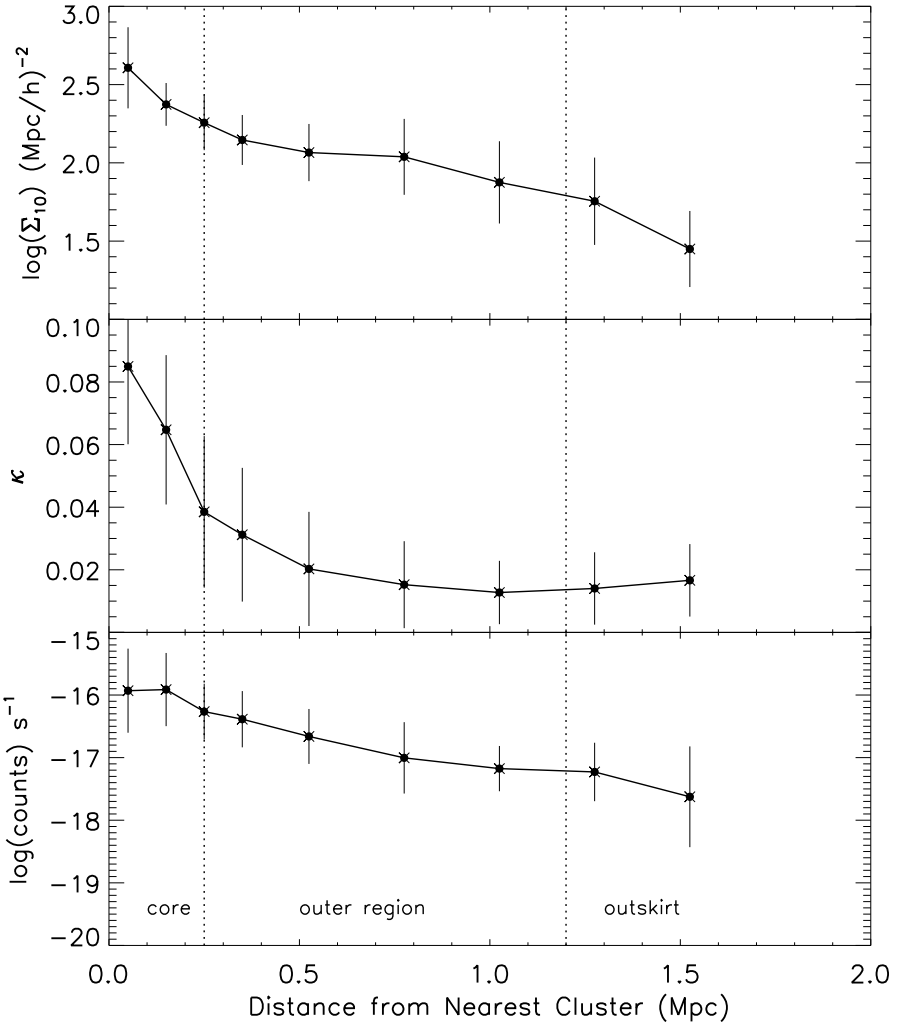

Figure 3.10 We plot the variation of the three measures of environment density (κ, Σ_{10}, ICM density) as a function of distance to the nearest cluster center. All three measures show a decrease in density as a function of cluster-centric distance. The vertical dashed lines denote the core radius at 0.25 Mpc and the virial radius at 1.2 Mpc. The error bars show the statistical Poisson errors in each bin.

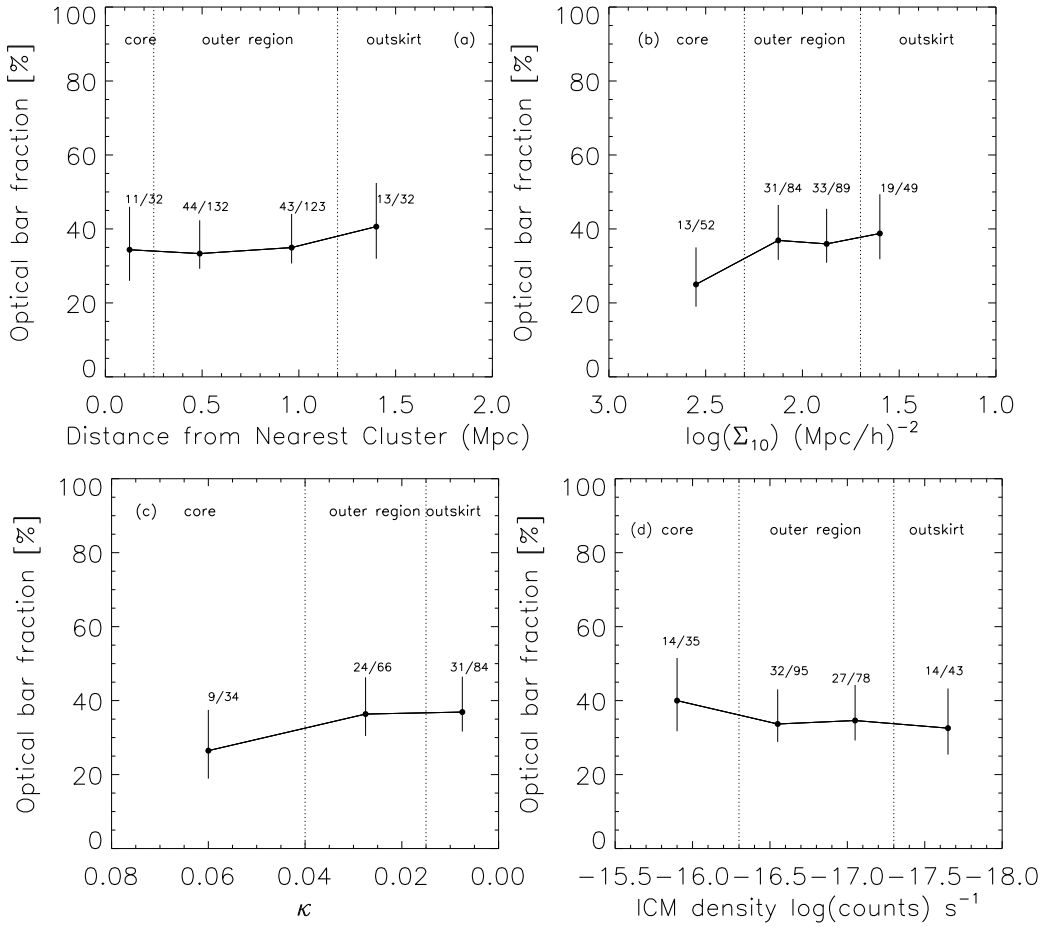

Figure 3.11 The fraction of barred galaxies a function of: (a) distance from nearest cluster center, (b) logΣ_{10}, (c) κ, and (d) ICM density. Bar classifications are from ellipse fits and disks are identified by visual classification. The vertical dashed lines denote the core radius at 0.25 Mpc and the virial radius at 1.2 Mpc. We find that between the core and the virial radius of the cluster ($R \sim 0.25$ to 1.2 Mpc), the optical bar fraction $f_{\rm bar-opt}$ does not depend strongly on the local environment density tracers (κ, Σ_{10}, and ICM density), and varies at most by a factor of ~ 1.3, allowed by the error bars.

fects make it hard to draw a robust conclusion on the detailed variation of the optical bar fraction. In fact, the detailed behavior seen as we move from the outer region to the cluster core varies according to which indicator is used: $f_{\rm bar-opt}$ shows no change when using projected radius (Fig. 3.11a), dips by a factor of ≤ 1.5 when using Σ_{10} (Fig. 3.11b), or κ (Fig. 3.11c), and rises by a factor of ≤ 1.2 when using the ICM density (Fig. 3.11d). Given the small number statistics, projection effects, and the fact that different indicators suggest different trends in the cluster core, we can only say that inside the cluster core, we do not find evidence for a variation stronger than a factor of 1.5 in the optical bar fraction $f_{\rm bar-opt}$ as a function of any of the three environmental indicators in Fig. 3.11.

How do our results compare to other studies? The recent study of bars in field and intermediate density regions by A09 reports no variation of the optical bar fraction with Σ_5, where Σ_5 varies between -3 and 2. On the other hand, several previous studies have found an enhanced optical bar fraction toward cluster centers (Barazza et al. 2009; Thompson 1981; Andersen 1996). We discuss the implication of the results from our study as as well as these other works in § 3.5.

3.4.7 Comparison of the Optical Bar Fraction in the A901/902 Clusters and the Field

To further explore the impact of environment on the evolution of bars and disk galaxies, it would be desirable to compare the properties of disk

galaxies in cluster and field samples, which are at similar redshifts and are analyzed in a similar way. We do not have a field sample at the same redshift as that of the A901/902 supercluster ($z \sim 0.165$), and therefore resort to an approximate comparison only, bearing in mind the caveats.

We compare the results on bars and disks from the STAGES sample to those from studies of nearby galaxies by MJ07 and A09. In these studies, bars are identified and characterized through ellipse-fits, as for our STAGES study. The sample of MJ07 is based on moderately inclined galaxies in the Ohio State University Bright Spiral Galaxy Survey (OSUBSGS; Eskridge et al. 2002), which contains galaxies of RC3 type S0/a or later, ($0 \leq$ T ≤ 9), $M_B < 12$, $D_{25} < 6'.5$, and $-80^\circ < \delta < +50^\circ$. This sample is dominated by early to intermediate-type (Sab-Sc) galaxies, in the range $M_{\rm V} = -20$ to -22. The galaxies are local field spirals, and strongly interacting galaxies are not included in the MJ07 analysis.

The sample of A09 is based on the Sloan Digital Sky Survey (SDSS; Abazajian et al., 2004) within the redshift range $z \sim 0.01$–0.04 and with $M_{\rm r} > -20$. Hubble types for galaxies in this sample are based on the location of the galaxy in the concentration-σ plane, calibrated with visual classification. Bars are identified through ellipse-fitting, and environment density is estimated from the projected local galaxy density (Σ_5). The densities considered in the A09 sample range from the field to intermediate densities comparable to those in the outer regions and outskirts of our clusters (Σ_5 from -3 to 2).

Before we compare the results obtained for bars in the cluster with those

from the field studies, we compare the properties (e.g., absolute magnitude, color) of the underlying galaxy populations in the field and cluster samples. In Figure 3.12a–b, we compare the distributions of $M_{\rm V}$ absolute magnitude and rest-frame $U-V$ color for the STAGES cluster, OSUBSGS, and SDSS field samples. The SDSS data are from A09. The OSU sample is brighter, and is dominated by galaxies in the range $M_{\rm V}=-20$ to -22, while the STAGES sample is dominated by galaxies in the range $M_{\rm V}=-18$ to -20. The SDSS sample spans a narrow range in $M_{\rm V}=-19.5$ to -22. The STAGES and OSU samples have a similar range in $U-V$ color, although the OSU sample has a slightly higher proportion of bluer galaxies.

We have shown that the optical bar fraction is a strong function of galaxy morphology and luminosity. It is therefore important to compare not only the global optical bar fraction, averaged over all galaxy types for a given magnitude cut, but also to compare galaxies of different morphological types, namely spiral galaxies with prominent bulges and spiral galaxies that appear as pure bulgeless disks. The latter galaxies are also of particular interest as they present a potential challenge to hierarchical ΛCDM models.

Table 3.8 shows the detailed comparison of the optical bar fraction between field and cluster galaxies. The global optical bar fraction averaged over all galaxy types in the samples, as well as the optical bar fraction for galaxies classified as 'bulge+disk' (B+D) is shown. In the STAGES sample, we do not have sufficient number statistics for pure-disk galaxies with $M\leq-20$, therefore comparisons are shown only for early-type (B+D) galaxies.

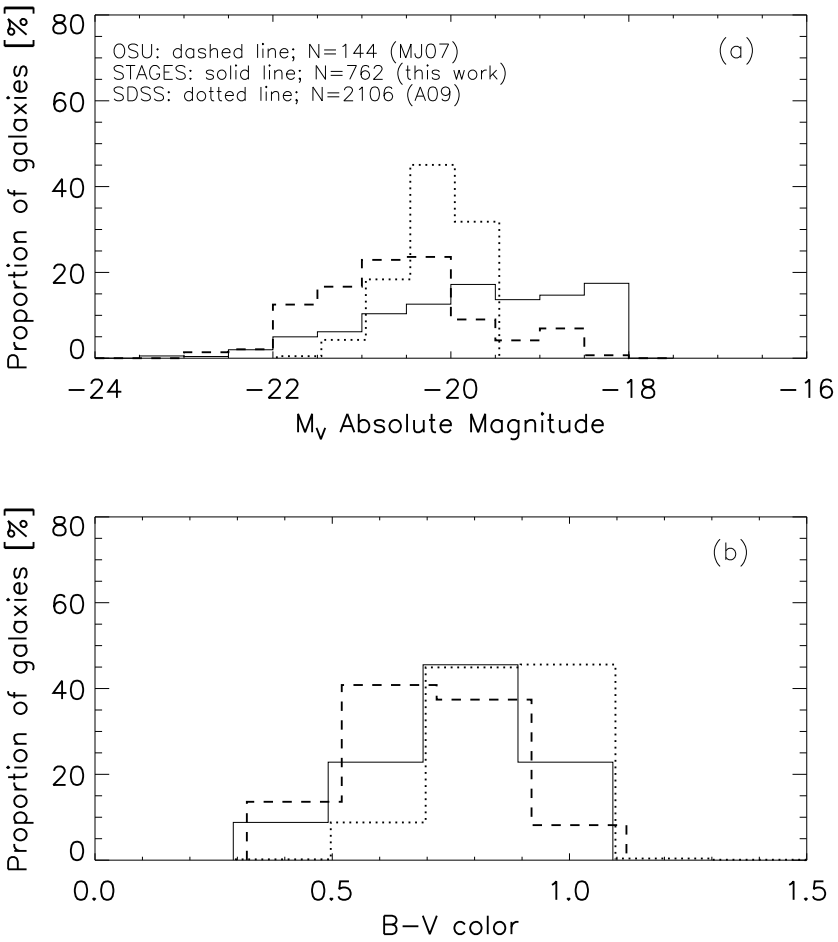

Figure 3.12 The absolute magnitude $M_{\rm V}$ *(a)* and rest-frame $U-V$ color *(b)* distributions are shown for the OSUBSGS (dashed line), STAGES (solid line), and SDSS (dotted line) samples. The SDSS data are from A09. The OUSBSGS data are from MJ07. The OSUBSGS sample is brighter and somewhat bluer than the STAGES sample. The SDSS sample spans a much narrower range in $M_{\rm V}$, with no galaxies fainter than -19.5.

The upper error bar on the optical bar fraction quoted for this study and MJ07, is the sum in quadrature of the error in the bar fraction from isophotal twists (§ 3.3.2) and the statistical error. Note that including isophotal twists into the optical bar fraction can only make the optical bar fraction higher. Therefore, the lower error bars quoted represent only the statistical error.

When comparing bright galaxies in STAGES with the OSU field survey (part A in Table 3.8), we find that the average global optical bar fraction, as well as the optical bar fraction for galaxies with B+D is slightly higher. However, the difference is not significant within the error margins. When comparing bright galaxies in STAGES with the SDSS field survey (part B in Table 3.8), we find that $f_{\rm bar-opt}$ for the STAGES cluster sample is higher than the field by a factor of ~ 1.3.

In summary, for bright, early Hubble types, the optical bar fraction in the Abell 901/2 clusters is comparable within a factor of ~ 1.3 to that of field galaxies at lower redshifts ($z < 0.04$).

3.4.8 Bar Strength Distribution in the A901/902 Clusters and the Field

Since we have found that the optical bar fraction is a strong function of $M_{\rm V}$, for the following analysis, we focus on galaxies brighter than $M_{\rm V} = -20$ in all samples. Figure 3.13a–b shows the peak ellipticity $e_{\rm bar}$ distributions for the STAGES and OSUBSGS samples, respectively. In panel (a) the pink and green lines show the $e_{\rm bar}$ distributions for galaxies classified as 'bulge+disk'

and 'pure disk', respectively. In panel (b) the distributions are split into bulge-dominated galaxies (S0-Sbc; pink) and (Sc-Sm; green).

We find that in both the cluster and field, the highest ellipticity bars lie in disk-dominated galaxies, although number statistics for this group are low in both samples, for galaxies brighter than $M_{\rm V} = -20$. In the A901/902 cluster system at $z = 0.165$, $e_{\rm bar}$ peaks at lower values ($e_{\rm bar} \sim 0.5$) than in lower-redshift field OSUBSGS galaxies ($e_{\rm bar} \sim 0.7$).

The result of lower $e_{\rm bar}$ in STAGES compared to OSU could be caused by more bulge-dominated hosts in STAGES than OSU. Bars in galaxies with large bulges can appear weaker (i.e., rounder). This effect has been observed in the STAGES sample, as well as in SDSS by BJMO8, and could be an artifact due to the apparent dilution of the ellipticity of the bar isophotes by the bulge. If it is not an artifact, it is possible that a massive bulge can affect the actual bar supporting orbits and cause the bar to become rounder. The same result is seen using $Q_{\rm g}$ (the maximum gravitational torque induced by the bar normalized to the axisymmetric component) for characterizing bar strength (Laurikainen et al. 2007).

However when measuring the Fourier amplitude of the bar to characterize bar strength, early-type galaxies appear to host stronger bars (e.g., Laurikainen et al. 2007). The bar-to-total mass ratio also increases toward early-type galaxies, although with large scatter, as measured from 2D bulge-disk-bar decomposition (Weinzirl et al. 2009).

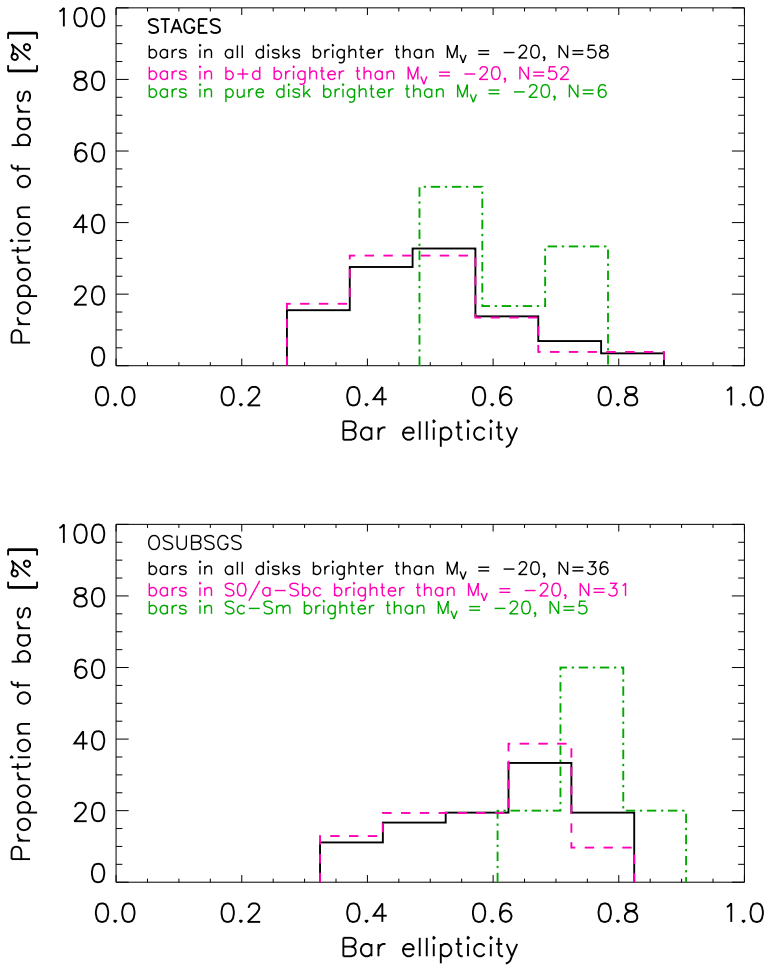

Figure 3.13 (a) Distribution of bar peak ellipticity $e_{\rm bar}$ for galaxies brighter than $M_{\rm V} = -20$ in the STAGES sample. The solid black line shows the ellipticity distribution for all bars. The pink and green lines show the ellipticity distributions for bars in galaxies visually classified as 'bulge+disk' and 'pure disk', respectively. In the STAGES sample, bars in galaxies classified as 'bulge+disk' appear rounder than those in 'pure disk' galaxies. (b) Distribution of bar peak ellipticity $e_{\rm bar}$ for galaxies brighter than $M_{\rm V} = -20$ in the OSUBSGS sample. The pink and green lines show the ellipticity distributions for bulge-dominated (S0-Sbc) and disk-dominated (Sc-Sm) galaxies, respectively. For both the STAGES and OSU samples, the strongest (highest ellipticity) bars are found in disk-dominated, late-type galaxies.

3.5 Discussion

We can use clusters as a laboratory for learning about the interplay between internal and external drivers of galaxy evolution. Bars are the most efficient internal drivers of galaxy evolution, however it is still an open question what makes one galaxy more susceptible to bar formation than another, and how bars evolve as a function of epoch and environment. The situation is complex because, in principle, the fraction of barred galaxies in a cluster depends on the epoch of bar formation, the robustness of bars, the interplay between cluster environmental processes (harassment, tidal interactions, ram pressure stripping), and the evolutionary history of clusters.

The relationship between the bar and the properties of its host galaxy, such as the Hubble type or bulge-to-total (B/T) ratio has been explored in several studies (e.g., Odewahn 1996; BJM08; A09; Weinzirl et al. 2009; Laurikainen et al. 2009), focusing mainly on field galaxies. We first discuss results reported to date on how the bar fraction varies from intermediate to late Hubble types (Sbc to Sd or Sm). The early study by Odewahn (1996) found that the optical fraction of strong bars rises from intermediate to late Hubble types (e.g., from Sbc to Sm). The study by BJM08, where the sample of disk galaxies was dominated by galaxies of intermediate to late Hubble types, also found that the optical bar fraction rises in galaxies that tend to be disk-dominated and devoid of a bulge. Similarly, in the study by Weinzirl et al. (2009), the near-IR bar fraction was found to be larger toward systems of low bulge-to-total (B/T) ratios. Thus, the trend of a higher bar fraction in disk-dominated

systems is reported by at least three studies. Our results in the study of A901/902 (see below) are also in agreement with this trend.

As we go from intermediate to early Hubble types, (e.g., from Sbc to S0/a to S0), two recent studies seem to agree that the bar fraction is much lower in S0 than among galaxies of type Sbc to S0/a. Laurikainen et al. (2009) report that the NIR bar fraction first rises in going from spirals (Sa-Scd) to S0/a, and then falls sharply among S0 galaxies. The study by A09, based on SDSS galaxies, finds an optical bar fraction of 29% in S0, compared to 55% in early type (S0/a-Sb), and 54% in intermediate-to-late type (Sbc-Sm). Thus, they confirm that the bar fraction drops sharply among S0s, but unlike Laurikainen et al. (2009), they do not find evidence for an increase from Sbc to S0/a.

In summary, when considering all the studies to date (Odewahn 1996; BJM08; Weinzirl et al. 2009; Laurikainen et al. 2009; A09) it appears that *the bar fraction is highest in late type Sd-Sm disk-dominated galaxies* and *lowest among S0*, while conflicting results exist on how the bar fraction varies from S0/a to Sc.

How do our results in the A901/902 supercluster compare to the above results in the field? We have found that the optical bar fraction $f_{\rm bar-opt}$ in the A901/902 cluster system depends on *both* the bulge-to-disk ratio and the luminosity (§ 3.4.3 and 3.4.4). We do not have quantitative measures of bulge-to-total (B/T) ratios in order to classify galaxies into Hubble types, but we separate spirals into two broad classes: those with 'bulge+disk' and those that

are 'pure disks'. We then found that at a given luminosity, $f_{\rm bar-opt}$ is higher among galaxies, which are 'pure disks', without a significant bulge component, as compared to those with a bulge. In § 3.4.3, we explored whether this trend could be artificially caused by systematic effects whereby a more prominent bulge might cause us to systematically miss primary bars. We concluded that this was unlikely, and that the trend of a higher $f_{\rm bar-opt}$ in galaxies without a bulge, as opposed to those with bulges, is a robust one. This trend is in agreement with the above-described results from earlier studies (e.g., Odewahn 1996; BJM08; Weinzirl et al. 2009).

In addition, we have found a new hitherto unappreciated dependence of the bar fraction on luminosity. Specifically, we find that for a given visual morphological class, $f_{\rm bar-opt}$ rises at higher absolute magnitude. A concurrent study by Barazza et al. (2009) similarly report that for cluster and field galaxies at $z = 0.4 - 0.8$ with early Hubble types S0-Sb, the bar fraction rises for brighter galaxies. *Our results thus suggest that the relationship between bar fraction and bulge-to-disk ratio may not be a monotonic one, and may depend on other factors, such as the gas content or luminosity.*

How do our results and those reported from other studies fit within theoretical scenarios of bar formation? Let us first consider the trend of a higher $f_{\rm bar-opt}$ in galaxies classified as 'pure disk'. In one theoretical scenario, it has been suggested that bars can form and be maintained through the swing amplification of gravitational instabilities (e.g., Toomre, 1981; Binney & Tremaine, 1987) in dynamically cold disks. The presence of a significant

amount of cold gas in the disk lowers the Toomre Q parameter, favoring the onset on gravitational instabilities. Typically $Q < 1.5$ is needed for efficiently maintaining the swing amplifier. Such bars are less likely to grow in galaxies where a prominent bulge leads to an inner Lindblad resonance (ILR), which cuts off the feedback loop for swing amplification (by preventing stellar spiral density waves from going through the center of the galaxy). The existence of an ILR requires not only the presence of a bulge, but requires a large B/T in order to produce a large enough density contrast between the inner and outer regions of the disk. Therefore, in this scenario, it is expected that galaxies with a large gas mass fraction and/or with no ILR are more likely to host bars than galaxies, which are gas-poor and have ILRs, for instance, due to a prominent bulge.

Our result in A901/902, and the results in the field by BJM08, whereby the bar fraction is higher in galaxies with pure disks than in galaxies with bulges, seem broadly consistent with this scenario. We also note that the drop in bar fraction among S0s (Laurikainen et al. 2009; A09) is also consistent with this framework, since S0s have prominent bulges, likely host ILRs, and have a low gas mass fraction. One would like to know whether it is the B/T ratio or the gas fraction that primarily control the bar fraction. For field galaxies where the pure disk spirals (Sd) have both a low B/T and a large gas fraction, it is difficult to disentangle these two factors. However, the fact that we see a higher $f_{\rm bar-opt}$ among pure disks in *clusters* suggests that the gas content of the disk is less relevant, since cluster galaxies can be stripped of their gas

by various cluster processes (e.g., Balogh et al. 2000; Quilis et al. 2000). For the A901/902 cluster system, we find that 73%±2% of galaxies appear smooth (i.e., contain little or no patchiness caused by dust/gas).

However, the above scenario where bars are formed and maintained through the swing amplification of gravitational instabilities cannot fully explain the full range of observational results to date. For instance, our result that within a given morphological class, $f_{\rm bar-opt}$ rises at higher luminosity requires us to consider other theoretical aspects of bar evolution, such as the effect of the DM halo. Studies have found that the DM fraction rises for lower luminosity systems, although with large scatter (Persic et al., 1996; Kassin et al., 2006). The interplay between a DM halo and the disk can influence both the formation and subsequent growth of a bar. In early simulations with rigid DM halos, the halo acts as a dynamically hot component and thus tends to make an embedded *unbarred* disk more stable against bar formation. We note that such earlier simulations (e.g., Ostriker & Peebles, 1973), using rigid rather than live DM halos, may have exaggerated the inhibition of the bar. In more recent simulations, live halos are used to represent a more realistic view of real galaxies and bar evolution. Debattista & Sellwood (2000) find that in simulations with live halos, bars form readily and are difficult to destroy. A massive live halo has the effect of braking the bar through dynamical friction, where the amount of braking depends on the DM halo-to-disk mass ratio within the region of the disk. Athanassoula (2002, 2003) finds that the distribution of the halo mass is the most influential factor dictating the evolu-

tion of the bar. Bars in more halo-dominated simulations develop more slowly than bars embedded in disks that are massive compared to the halo in the inner regions. However, although the bars grow more slowly, they tend to become stronger because the live DM halo acts a sink for angular momentum transferred out by the bar.

In the context of these simulations, one would expect bars to form and grow more slowly in galaxies with higher DM fraction, namely in fainter galaxies. Our results are consistent with some aspects of this scenario. Our results of a higher $f_{\rm bar-opt}$ among brighter galaxies may be related to the faster and more efficient growth of bars in brighter galaxies with lower DM fraction. However, another prediction of these simulations is that bars in brighter galaxies with lower DM fraction would, in the end, be weaker. We do not find statistical evidence of a change in $e_{\rm bar}$ with luminosity. The mean $e_{\rm bar} = 0.6$ for galaxies fainter than $M_{\rm V} = -20$, compared to the mean $e_{\rm bar} = 0.5$ for galaxies brighter than $M_{\rm V} = -20$. This change in the mean $e_{\rm bar}$ by a factor of 1.2 is within the statistical error.

How does the frequency and evolution of bars differ in different environments? In § 3.4.6, we found that between the core and the virial radius of the cluster ($R \sim 0.25$ to 1.2 Mpc) at intermediate densities ($\log(\Sigma_{10}) = 1.7$ to 2.3), the optical bar fraction $f_{\rm bar-opt}$ does not depend strongly on the local environment density tracers (κ, Σ_{10}, and ICM density), and varies at most by a factor of ~ 1.3, allowed by the error bars. These results agree with those of A09 for intermediate densities. A09 find no dependence of the optical bar

fraction on local environment density, over a wide range of $\log(\Sigma_5) = -2$ to 3. The average galaxy number density in A09 is lower than our sample, and is comparable to the environments present in the outer region of our cluster sample (Fig. 3.11), where we also find no dependence of the bar fraction with Σ_{10}. Recently, Romano-Díaz et al. (2008) used theoretical models to study the formation of bars in a cosmological context. Their results suggest that interaction with the halo sub-structure induces bars. Because this substructure is present in all environments, these models imply a similar bar fraction across a large range of environment densities, which is consistent with our results.

Inside the cluster core at the highest densities, our data do not yield conclusive results for several reasons. Firstly, the number statistics are very limited, and at best, within the caveats of limited number statistics, we can say that $f_{\rm bar-opt}$ does not show evidence for a variation larger than a factor of 1.5 toward the core as a function of the environmental indicators (§ 3.4.6). Secondly, the detailed behavior seen as we move from the outer region to the cluster core varies according to which indicator is used: $f_{\rm bar-opt}$ shows no change when using projected radius (Fig. 3.11a), dips by a factor of ≤ 1.5 when using Σ_{10} (Fig. 3.11b), or κ (Fig. 3.11c), and rises by a factor of ≤ 1.2 when using the ICM density (Fig. 3.11d).

Some early studies looked at the optical bar fraction toward the centers of local clusters (Thompson 1981; Andersen 1996). These studies use visual classification of Coma and Virgo galaxies, respectively. Both studies use the velocity distributions of cluster galaxies to argue that the fraction of barred

galaxies is enhanced toward the cluster cores. Thompson (1981) finds that bars occur twice as often in the core compared to the outskirt region of the Coma cluster, while Andersen does not quote specific numbers. A recent study by Barazza et al. (2009) using ellipse-fitting on a sample dominated by galaxies with $M_{\rm V} = -20$ to -22 at intermediate redshifts $z \sim 0.4$–1, finds a rise in the optical bar fraction of a factor of ~ 2 in cluster cores. However they caution that this result may be affected by low number statistics.

Although, we cannot make a conclusive statement about the behavior of the bar fraction in the core region based on our data, we can speculate on what effects are at play in the cluster cores that might affect the bar fraction and trends found in previous studies. The possibility raised by previous studies (Thompson 1981; Andersen 1996; Barazza et al. 2009) that the optical bar fraction in the cluster core is higher (or not significantly lower) from that in the outer region of the cluster may at first seem puzzling because bulge-dominated galaxies are generally prevalent in cluster cores. Given our results of a lower optical bar fraction in bulge-dominated galaxies (§ 3.4.3), one might naively expect a sharp drop in the optical bar fraction toward the cluster cores. The fact that such a drop is not seen, suggests that other processes in the core tend to enhance the bar fraction, thereby countering the drop. We discuss two such processes below.

In the cluster core, the galaxy collision and interaction timescale is very short because of the high galaxy number density (n) and the large galaxy

velocity dispersion ($\sigma_{\rm gal}$):

$$t_{\rm coll} = \frac{1}{n\sigma_{\rm gal}A}, \tag{3.4}$$

where A is the collision cross-section. Heiderman et al. (2009) calculate $t_{\rm coll}$ for the core, outer region, and outskirt of the Abell 901/902 system. They find that $t_{\rm coll}$ in the cluster cores is $\sim$ 0.7 Gyr, compared to $\sim$ 10 Gyr and $\sim$ 200 Gyr in the outer region and outskirts, respectively. Thus, galaxy tidal interactions are expected to be frequent in the A901/902 cluster cores. This can lead to the tidal triggering of bars in sufficiently cold disks and would tend to raise the optical bar fraction in cluster cores.

Another additional factor favoring bar formation in cluster cores is that the frequent tidal interactions are unlikely to develop into galaxy mergers or into strong galaxy interactions associated with large tidal heating because the galaxy velocity dispersion is large (700 to 1000 km/s for the A901/902 system; Gray et al. in prep.). The latter type of mergers or interactions tend to lead to strong tidal damage and heating of the disk and could destroy the bars. The results of Heiderman et al. (2009) are consistent with this scenario: they find that in the A901/902 clusters, the galaxy mergers and strongly interacting galaxies (those with strong morphological distortions) are rare and tend to be located outside the cluster core, in the outer region between the core and virial radius. This supports the idea that the large galaxy velocity dispersion in cluster cores are not conducive to mergers and violent interactions. In effect, the core environment may well provide many frequent weak, non-destructive tidal interactions (harassment), which favor the triggering of bars in cold disks.

In such a case, the *trend of a lower bar fraction from a population of galaxies with high B/T in the core, may be counteracted by the opposite tendency for core environmental processes (e.g., harassment) to favor bar formation*[2].

It is also interesting in this context to note that higher bar fractions have been reported for binary pairs of galaxies (e.g., Elmegreen et al. 1990; Varela et al. 2004). Elmegreen et al. (1990) find a similar bar fraction in field and groups ($\sim 30\%$), and a higher fraction in galaxy pairs ($\sim 50\%$), but only for early Hubble types. Their study is based on visual classifications from a number of different field, group, and binary samples of nearby galaxies. Binary pairs vary in separation, but all have projected separation distances < 180 kpc. Varela et al. (2004) also find that the optical bar fraction in binary pairs is twice as high as in isolated galaxies, again only for early Hubble types. This is consistent with the idea that weak interactions may enhance the bar fraction.

3.6 Summary and Conclusions

We have used the STAGES $HSTACS$ survey of the Abell 901/902 supercluster in F606W at z$\sim$0.165 to study the properties of barred and unbarred disks in a dense environment. Ellipse-fitting was used to identify and charac-

[2]One way to further test the hypothesis that tidal triggering of bars via harassment is important toward the core would be to look at how the optical bar fraction for systems with a fixed narrow range of B/T varies within the cluster. Unfortunately, in the core, we do not have enough number statistics for pure disk systems ($B/D \sim 0$) and no quantitative measure of B/T to split the class of 'bulge+disk' systems into sub-classes with narrow ranges of B/T. We find no conclusive trend of the bar fraction with density within the clusters for the broad class of 'bulge+disk' systems.

terize the properties of bars in our sample. Visual classification was used to characterize secondary morphological parameters such as the prominence of the bulge, clumpiness, and spiral arms. Galaxies were grouped into the broad classes: 'pure bulge', 'bulge+disk', and 'pure disk'. In addition, the galaxies were classified as either 'clumpy' or 'smooth'. We find the following results:

1. *Disk selection in clusters:* To identify the optical bar fraction $f_{\rm bar-opt}$, three common methods of disk selection were used and compared: visual classification, $U-V$ color cut, and Sérsic cut. We find 625, 485, and 353 disk galaxies, respectively, via visual classification, a Sérsic cut ($n \leq 2.5$), and a blue-cloud cut (Table 3.2). A color cut misses 51%±2% of visually-identified disk galaxies. A Sérsic cut misses 31%±2% of visually-identified disk galaxies with $n > 2.5$. Therefore, a blind application of a color cut or Sérsic cut would miss many of the red galaxies with prominent bulges that are prevalent in a cluster environment.

2. *Global optical bar fraction:* For moderately inclined galaxies ($i < 60°$), we find that the three methods of disk selection (visual, color cut, Sérsic cut), we obtain a similar optical bar fraction $f_{\rm bar-opt}$ of $34\%^{+10\%}_{-3\%}$, $31\%^{+10\%}_{-3\%}$, and $30\%^{+10\%}_{-3\%}$, respectively (Table 3.2).

3. *Optical bar fraction as a function of morphology and luminosity:*

   We explore $f_{\rm bar-opt}$ as a function of host galaxy properties and find that it rises in spiral galaxies, which are less bulge-dominated and/or are brighter. The optical bar fraction is a factor of ~ 1.8 higher in

galaxies classified as 'pure disk' compared to galaxies visually classified as 'bulge+disk' (Table 3.4). *Within a given M_V bin, $f_{bar-opt}$ is higher in visually-selected disk galaxies that have no bulge as opposed to those with bulges.* Furthermore, we find that for a given visual morphological class, $f_{bar-opt}$ rises at higher absolute magnitudes (Fig. 3.9 and Table 3.5). When the normalized effective radius r_e/a_{disk} is used to trace central galaxy concentration, the bar fraction is ~ 2.7 times higher in galaxies with the lowest central concentration ($r_e/a_{disk} = 0.75$) compared to the galaxies with the highest central concentration ($r_e/a_{disk} = 0.15$; Fig. 3.8).

4. *Optical bar fraction as a function of κ, Σ_{10}, ICM density, and distance from nearest cluster center:* Between the core and the virial radius of the cluster ($R \sim 0.25$ to 1.2 Mpc) at intermediate densities ($\log(\Sigma_{10})= 1.7$ to 2.3), the optical bar fraction does not appear to depend strongly on the local environment density tracers (κ, Σ_{10}, and ICM density), and varies at most by a factor of ~ 1.3 (Fig. 3.11. Inside the cluster core, within the caveats of limited number statistics, $f_{bar-opt}$ does not show evidence for a variation larger than a factor of 1.5 as a function of the three environmental indicators. Overall, our results suggest that the optical bar fraction is not strongly dependent on environment at intermediate densities (e.g., $\log(\Sigma_{10})= 1.7$ to 2.3).

5. *Comparison to field studies:* We compare in Table 3.8 our results to those for field samples, specifically MJ07 (OSUBSGS) and A09 (SDSS), where

Table 3.1. Galaxy Morphology as a Function of Distance from Cluster Centers

	Whole cluster sample (1)	Core $R < R_{core}$ (2)	Outer region $R_{core} < R < R_{virial}$ (3)	Outskirt $R > R_{virial}$ (4)
N_{all}	750	81	556	113
N_{bulge}	125	26	88	11
N_{disk}	625	55	468	102
N_{disk} (bulge+disk)	452	46	334	72
N_{disk} (pure disk)	173	9	134	30
N_{bulge}/N_{all}	0.17	0.32	0.16	0.10
N_{disk}/N_{all}	0.83	0.68	0.84	0.90
$N_{bulge+disk}/N_{all}$	0.60	0.57	0.60	0.64
$N_{pure\ disk}/N_{all}$	0.23	0.11	0.24	0.27

Note. — The numbers shown are for the 750 bright ($M_V \leq -18$) galaxies, which we were able to classify into three broad groups: 'pure bulge', 'bulge+disk', and 'pure disk', as outlined in § 3.3.3. The relative numbers in each group are shown for the whole cluster (column 1) and different regions within the custer (columns 2, 3, and 4). The core radius $R_{core} = 0.25$ Mpc and the virial radius $R_{virial} = 1.2$ Mpc.

bar identification and characterization was done through ellipse-fitting. We find that for bright early Hubble types the optical bar fraction in the Abell 901/2 clusters is comparable within a factor of 1.3 to that of field galaxies at lower redshifts ($z < 0.04$).

6. *Bar strength distribution in cluster and field:* We find that in both the cluster and field, the highest ellipticity bars lie in disk-dominated galaxies.

Table 3.2. Optical Bar Fraction from Different Methods to Identify Disk Galaxies Among $M_V \leq -18$, $i < 60°$ Systems

Method (1)	N_{disk} (2)	N_{barred} (3)	$f_{bar,opt}$ (4)
Visual	340	115	$34\%^{+10\%}_{-3\%}$
Color	189	58	$31\%^{+10\%}_{-3\%}$
Sérsic	241	72	$30\%^{+10\%}_{-3\%}$

Note. — All optical bar fractions are for galaxies with $M_V \leq -18$, $i < 60°$, and $a_{disk} > 3$ kpc. Columns are: (1) Method for selecting disk galaxies. See § 3.3.1 and § 3.4.1 for details; (2) Number of moderately inclined disk galaxies, N_{disk}; (3) Number of barred disk galaxies, N_{barred}. Bars are detected through ellipse fitting; (4) Optical bar fraction, $f_{bar-opt}$, defined as in Eq. 1. The upper error bar on the optical bar fraction is the sum in quadrature of the error in the bar fraction from isophotal twists (§ 3.3.2) and the statistical error. Note that including isophotal twists into the optical bar fraction can only make the optical bar fraction higher. Therefore, the lower error bars quoted represent only the statistical error.

Table 3.3. Optical Bar Fraction from Different Methods to Identify Disk Galaxies Among $M_*/M_\odot \geq 10^9$, $i < 60°$ Systems

Method (1)	N_{disk} (2)	N_{bar} (3)	$f_{bar,opt}$ (4)
Visual	389	128	$33\%^{+10\%}_{-2\%}$
Color	208	69	$33\%^{+10\%}_{-3\%}$
Sérsic	290	85	$29\%^{+10\%}_{-3\%}$

Note. — All optical bar fractions are for galaxies with $M_*/M_\odot > 10^9$, $i < 60°$, and $a_{disk} > 3$ kpc. Columns are: (1) Method for selecting disk galaxies. See § 3.3.1 and § 3.4.1 for details; (2) Number of moderately inclined disk galaxies, N_{disk}; (3) Number of barred disk galaxies, N_{barred}. Bars are detected through ellipse fitting; (4) Optical bar fraction, $f_{bar-opt}$, defined as in Eq. 1. The upper error bar on the optical bar fraction is the sum in quadrature of the error in the bar fraction from isophotal twists (§ 3.3.2) and the statistical error. Note that including isophotal twists into the optical bar fraction can only make the optical bar fraction higher. Therefore, the lower error bars quoted represent only the statistical error.

Table 3.4. Optical Bar Fraction as a Function of Visually Classified Secondary Morphological Parameters

Morphology (1)	N_{all} (2)	N_{disk} (3)	N_{bar} (4)	$f_{bar,opt}$ (5)
Pure bulge	105	—	—	—
B+D	110^a+131^b+21^c	262	77	$29\%^{+10\%}_{-3\%}$
Pure disk	78	78	38	$49\%^{+12\%}_{-6\%}$
Clumpy	105	105	47	$45\%^{+11\%}_{-5\%}$
Smooth	340	235	68	$29\%^{+10\%}_{-3\%}$

Note. — All values are for galaxies with $M_V \leq -18$, $i < 60°$, and $a_{max} > 3$ kpc. Columns are : (1) Morphological parameters from visual classification (a - number of 'bulge+disk' galaxies with bar/spiral arm; b - number of 'bulge+disk' galaxies without bar/spiral; c - number of bulge+disk galaxies without bar and no spiral arm class); (2) Total number of galaxies in class; (3) Number of moderately inclined *disk* galaxies in class; (4) Number of barred disk galaxies, where bars are from ellipse fitting; (5) Optical bar fraction calculated as in Eq. 1. The upper error bar on the optical bar fraction is the sum in quadrature of the error in the bar fraction from isophotal twists (§ 3.3.2) and the statistical error. Note that including isophotal twists into the optical bar fraction can only make the optical bar fraction higher. Therefore, the lower error bars quoted represent only the statistical error.

Table 3.5. Optical Bar Fraction as a Function of Host Absolute Magnitude and Morphological Class

$M_{\rm V}$ range	Bulge+Disk Smooth	Bulge+Disk Clumpy	Pure Disk Smooth	Pure Disk Clumpy
$-18 \geq M_{\rm V} > -19$	10%±4% (6/58)	40%±22% (2/5)	46%±10% (11/24)	29%±11% (5/17)
$-19 \geq M_{\rm V} > -20$	20%±5% (14/71)	18%±9% (3/17)	57%±19% (4/7)	60%±11% (12/20)
$-20 \geq M_{\rm V} > -21$	42%±7% (22/53)	35%±11% (7/20)	—	63%±17% (5/8)
$-21 \geq M_{\rm V} > -22$	53%±11% (10/19)	75%±11% (12/16)	—	—

Note. — We show the variation of $f_{\rm bar-opt}$ as a function of absolute magnitude and morphological class for visually-identified, moderately inclined disk galaxies with $a_{\rm disk} > 3$ kpc. The numbers in parentheses give the values $N_{barred}/(N_{barred} + N_{unbarred})$ in each bin. Values are only shown for bins containing more than two galaxies. The error presented is the statistical error in each bin.

Table 3.6. Optical Bar Fraction as a Function of $U - V$ Color and Absolute Magnitude

	$-18 \geq M_{\rm V} > -19$	$-19 \geq M_{\rm V} > -20$	$-20 \geq M_{\rm V} > -21$	$-21 \geq M_{\rm V} > -22$
$U - V < 1$	31%±6% (20/65)	34%±7% (17/50)	36%±10% (8/22)	20%±18% (1/5)
$U - V > 1$	10%±5% (4/39)	25%±5% (16/65)	44%±6% (26/59)	69%±8% (22/32)

Note. — We show the variation of $f_{\rm bar-opt}$ as a function of rest-frame $U - V$ color and absolute magnitude for visually-identified, moderately inclined disk galaxies with $a_{\rm disk} > 3$ kpc. The numbers in parentheses give the values $N_{barred}/(N_{barred} + N_{unbarred})$ in each bin. Values are only shown for bins containing more than two galaxies. The error presented is the statistical error in each bin.

Table 3.7. Optical Bar Fraction as a Function of $U-V$ Color and Morphological Class

	Bulge+Disk Smooth	Bulge+Disk Clumpy	Pure Disk Smooth	Pure Disk Clumpy
$U-V<1$	6%±4% (2/33)	21%±7% (8/38)	52%±10% (14/27)	49%±7% (22/45)
$U-V>1$	30%±4% (51/170)	76%±9% (16/21)	20%±18% (1/5)	—

Note. — We show the variation of $f_{\mathrm{bar-opt}}$ as a function of rest-frame $U-V$ color and morphological class for visually-identified, moderately inclined disk galaxies with $a_{\mathrm{disk}} > 3$ kpc. The numbers in parentheses give the values $N_{barred}/(N_{barred}+N_{unbarred})$ in each bin. Values are only shown for bins containing more than two galaxies. The error presented is the statistical error in each bin.

Table 3.8. Comparison of local optical bar fraction in field and clusters

A) Bright galaxies split into morphological types		
Reference	MJ07	this work
Magnitude range	$M_V \leq -20$	$M_V \leq -20$
Environment	OSUBSGS (mostly field)	Abell 901/902 (cluster)
Redshift	~ 0	0.165
$f^1_{\rm bar,opt}$	All types[2]: $40\%^{+8\%}_{-5\%}$ (36/90)	All types: $48\%^{+11\%}_{-5\%}$ (58/121)
	S0-Sbc[2]: $41\%^{+10\%}_{-6\%}$ (31/71)	B+D: $47\%^{+11\%}_{-5\%}$ (52/111)

B) Bright galaxies split into morphological types		
Reference	A09	this work
Magnitude range	$M_V \leq -20.5$	$M_V \leq -20.5$
Environment	SDSS (field + interm. density)	Abell 901/902 (cluster)
Redshift	0.01-0.04	0.165
$f_{\rm bar,opt}$	All types: 48% (337/699)	All types[3]: $57\%^{+12\%}_{-6\%}$ (41/72)
	S0 to Sbc: 41% (196/474)	B+D [3]: $56\%^{+12\%}_{-6\%}$ (39/68)

Note. — (1): The fractions quoted for this study are for galaxies with $i < 60^\circ$ and $a_{\rm disk} > 3$ kpc. (2): The upper error bar on the optical bar fraction quoted for this study and MJ07 is the sum in quadrature of the error in the bar fraction from isophotal twists (§ 3.3.2) and the statistical error. Note that including isophotal twists into the optical bar fraction can only make the optical bar fraction higher. Therefore, the lower error bars quoted represent only the statistical error.
(3): The OSUBSGS sample of moderately inclined galaxies in MJ07 is dominated by early-to-intermediate Hubble types (S0-Sbc; 71) galaxies mostly S0/a to Sbc. The number of late Hubble type (Sc-Sm; 18) galaxies is too low to yield robust number statistics for the late types. We thus only show $f_{\rm bar,opt}$ for the early-to-intermediate Hubble types.
(4): In the STAGES sample, there are only 5 pure disk galaxies with magnitudes $M_V \leq -20.5$, while most pure disk galaxies have $M_V \geq -20$ (see Table 3.5). For this reason, we only show the bright-galaxy comparison for early-type (B+D) galaxies.

Chapter 4

The HST/ACS Coma Cluster Survey. VIII. Barred Disk Galaxies in the Core of the Coma Cluster[0]

4.1 Introduction

Mounting evidence suggests that at $z \sim 1$, major mergers among massive galaxies are not very frequent (e.g., Bell et al., 2006; Jogee et al., 2009; Robaina et al., 2009; Weinzirl et al., 2009) and have not contributed significantly to the cosmic star formation rate (SFR) density (e.g., Bell et al. 2005; Wolf et al. 2005; Jogee et al. 2009; Robaina et al. 2009) or to the building of bulges in massive spirals (Weinzirl et al., 2009; Kormendy & Fisher, 2008; Laurikainen et al., 2007) since $z < 1$. Other processes, such as minor mergers (Jogee et al., 2009; Weinzirl et al., 2009), or internal secular processes (Laurikainen et al. 2007; Kormendy & Fisher 2008) are increasingly invoked.

The most efficient internal driver of evolution in disk galaxies are stellar bars. They effectively redistribute angular momentum in the disk and DM halo, and drive large gas inflows to the central regions of galaxies. The resulting central dense gas concentrations ignite powerful starbursts (Schwarz 1981;

[0]A significant part of this chapter has been submitted for publication to the Astrophysical Journal by Irina Marinova as lead author. Reproduced by permission of the AAS.

Sakamoto 1999; Jogee 1999; Jogee et al. 2005; Sheth et al. 2005). In this way, bars are thought to build disky central components known as pseudobulges (Hohl, 1975; Kormendy, 1979; Combes & Sanders, 1981; Combes et al., 1990; Kormendy, 1993; Jogee, 1999; Jogee et al., 2005).

We describe below some of the recent progress made in exploring the bar fraction (defined as the fraction of disk galaxies hosting a large-scale bar) in terms of methodology, dependence on Hubble type, redshift, and environment. For a long time, statistics on the optical bar fraction in the local universe came from visual classification of the galaxies in the RC3 (deVaucouleurs et al. 1991). In the RC3, over all disk galaxies (S0–Im), the visual optical bar fraction is $\sim$ 30% for strong bars (SB), and $\sim$ 30% for weak bars (SAB), giving $\sim$ 60% overall. The RC3 optical bar fraction suffers from two limitations: firstly, it denotes the optical bar fraction averaged over a broad range of Hubble types, and secondly, it is based on visual classification to identify and characterize bars, thus giving no quantitative measurements of their properties (such as size, shape, strength). In fact, the former limitation has persisted in many recent studies which focus on the average bar fraction over disks of all Hubble types (Eskridge et al. 2000; Knapen et al. 2000; Hunt & Malkan 1999; Mulchaey & Regan 1997; Laine et al. 2002; Laurikainen et al. 2004; Block et al. 2004; although see Odewahn 1996).

Recent studies have made important headway on both fronts. Firstly, quantitative methods such as ellipse fitting (e.g., Wozniak et al. 1995, Friedli et al. 1996; Regan et al. 1997; Mulchaey & Regan 1997; Jogee et al. 1999, 2002,

2004; Knapen et al. 2000; Laine et al. 2002; Sheth et al. 2003, 2008; Elmegreen et al. 2004; Menéndez-Delmestre et al. 2007; MJ07; Aguerri et al. 2009), and bulge-bar-disk decomposition (e.g., Laurikainen et al., 2005; Reese et al., 2007; Weinzirl et al., 2009; Gadotti, 2011)

are being used to reduce the level of subjectivity. Secondly, evidence is mounting that the bar fraction varies across galaxies of different Hubble types (BJM08; Aguerri et al. 2009; M09) and depends non-monotonically on the host galaxy properties, such as bulge-to-total ratio (B/T), luminosity, stellar mass, and color, at a range of redshifts and environments (M09; Barazza et al., 2009; Weinzirl et al., 2009; Laurikainen et al., 2009; Nair & Abraham, 2010b; Cameron et al., 2010; Gadotti, 2011).

Most of the results described above have focused on field galaxies at low redshifts, while much less is known about barred disks at higher redshifts (Abraham et al. 1999; Sheth et al. 2003; Jogee et al. 2004; Sheth et al. 2008; Cameron et al. 2010), and in dense environments. Dense environments such as clusters can be an important laboratory for studying the co-evolution of bars and their host disks, as there are many physical processes, which are unique to such environments and impact disks and bars. For example, we can study how the cumulative effect of frequent weak galaxy encounters ('harassment', Moore et al. 1996), the effect of the intra-cluster medium (ICM) on galaxies (Gunn & Gott 1972; Larson et al. 1980; Quilis et al. 2000), and the influence of the cluster potential as a whole (e.g., Byrd & Valtonen, 1990; Gnedin, 2003) affect the properties of bars and disks. Theoretical studies exploring these

processes give conflicting predictions. For example, although the numerous tidal encounters in a dense cluster core can induce bars in unbarred disks in the case of a prograde encounter, they can also have little or no effect in terms of inducing a bar (or affecting the strength of an already existing bar) in the case of retrograde encounters (Gerin, Combes, & Athanassoula 1990; Romano-Díaz et al. 2008; Aguerri & González-García 2009). Determining the fraction and properties of barred galaxies in such extreme environments and comparing them to those of galaxies in environments of varying densities, can give clues to the outstanding problems in understanding the formation and growth of bar instabilities in disks, and therefore to understanding disk evolution. In addition, identifying barred disks in cluster environments can provide a lower limit to the fraction of disk systems in clusters.

Quantitative results addressing this issue are only starting to emerge. Several recent studies of non-dwarf galaxies at a range of redshifts from $0.01 < z < 0.4$ (Barazza et al. 2009; Aguerri et al. 2009; M09), find that the optical bar fraction shows at most a modest variation ($\pm 10\%$) between field and intermediate density environments (e.g., moderately rich clusters). But what happens at really high densities (i.e., dense cluster cores)? Some studies (Thompson 1981; Andersen 1996; Barazza et al. 2009) have suggested that, within a galaxy cluster, the bar fraction may be higher in the dense core regions than the outskirts. However, this has remained an open question for cluster cores due to issues such as limited number statistics, projection effects, and uncertainties in cluster membership.

In this paper, we provide anchor results for the densest environment in the local Universe: the central regions of Coma. We conduct two explorations using two different samples. In the first part of this paper (§ 4.3), we focus on the sample of bright ($M_{\rm V} \lesssim -18$) non-dwarf S0 galaxies, which comprise 94% of our sample of bright disk galaxies in the Coma core. We characterize their disk and bar properties and present results on the optical bar fraction for bright S0 galaxies from ellipse fitting and visual classification. We compare with the results of other studies of S0 galaxies in Coma, and less dense clusters (Abell 901/902 and Virgo).

In the second part of this paper (§ 4.4), we take advantage of the exquisite 50 pc resolution of the ACS images to search for bars and other disk features (spiral arms, inclined disks) in the faint, dwarf ($M_{\rm V} > -18$) galaxies of the Coma cluster core. The prevalence or paucity of bar structures in early-type dwarf galaxies can not only provide clues on the evolutionary history of these dwarf systems, but also has implications for the conditions necessary for bar formation and growth in galaxies. Are bar/spiral arm instabilities commonplace for dwarf galaxies? Some early-type dwarfs in clusters are believed to have originated from late-type spirals or dwarf irregulars (e.g., Lin & Faber, 1983; Kormendy, 1985) that have been stripped of their gas by external processes. This is especially true in a cluster setting where environmental processes like ram-pressure stripping and harassment are commonplace. If the progenitor galaxy hosted a bar or spiral arms, these structures may remain after the galaxy has been processed by the cluster environment. In fact, a

number of early-type dwarf galaxies in Virgo have been observed to host disk structure such as a lens, a bar, or spiral arms (e.g., Sandage & Binggeli, 1984; Binggeli & Cameron, 1991; Jerjen et al., 2000; Barazza et al., 2002; Lisker et al., 2006b, 2007; Lisker & Fuchs, 2009) thus supporting the above scenario. Graham et al. (2003) discovered the first two early-type dwarf galaxies with spiral-like structure in the Coma cluster using unsharp masking, concluding that such galaxies may provide the 'missing link' for evolution of faint spiral galaxies into dwarf spheroidals due to cluster processes.

The layout of this paper is as follows: In § 4.2 we describe our dataset and sample selection. Section 4.3 deals with our bright ($M_{\rm V} \lesssim -18$) Coma core sample. In this section we outline our methods for identifying bright S0 galaxies (§ 4.3.1), our methods for identifying bars in these galaxies (§ 4.3.2 and 4.3.3), our results for S0 galaxies in the Coma core (§ 4.3.4–§ 4.3.7), and the implications of these results for bar and disk formation and evolution in dense environments (§ 4.3.8). In § 4.4, we present our investigation of the faint, dwarf galaxies in our Coma core sample. We describe our methods for finding disk features (bar, spiral arms, inclined disk) in these galaxies (§ 4.4.2), as well as our results and discussion for dwarf galaxies in § 4.4.3. We summarize all of our results in § 5.

4.2 Data and Selection of a Cluster Sample

Our data come from the *Hubble Space Telescope* (*HST*) Advanced Camera for Surveys (ACS) Treasury survey of the Coma cluster at $z \sim 0.02$

(Carter et al., 2008). Originally designed to cover a large area of the core and infall region of Coma, the survey remains only $\sim$ 28% complete because of the failure of ACS in 2007. Nevertheless, the available data span 274 arcmin^2, where approximately 75% of the data are within 0.5 Mpc of the cluster center. The data cover approximately 70% of the core region of Coma (assuming $R_{\rm core} \sim 0.2$ Mpc) and are therefore representative of the core and the immediate surroundings, namely the region where the galaxy number density is $\sim$ 10,000 galaxies Mpc^{-3} before it drops sharply as a function of distance from the cluster center (The & White, 1986). This dataset contains thousands of sources down to a limiting magnitude of $I = 26.8$ mag in F814W (AB mag). The ACS point-spread function (PSF) is $\sim 0.1''$, which corresponds to $\sim$ 50 pc at the distance of the Coma cluster[1]. *SExtractor* source catalogs are available as a part of the Coma survey data releases. The second data release (DR2) is described in detail in Hammer et al. (2010). Throughout the paper, $M_{\rm I(814)}$ as well as SDSS g and r magnitudes are given in the AB system, while B and V magnitudes are in the Vega system.

We first use the eyeball catalog of Trentham et al. (in preparation) to select cluster members. In this catalog, galaxies are visually assigned a cluster membership class from 0 to 4. Galaxies with membership class 0 are spectroscopically confirmed members, while galaxies with class 4 are visually deemed to be likely background objects. The intermediate membership classes from 1

[1]We assume in this paper a flat cosmology with $\Omega_M = 1 - \Omega_\Lambda = 0.3$ and H_0 =70 km s^{-1} Mpc^{-1}.

(very probable cluster member) to 3 (plausible cluster member), are assigned based on a visual estimation taking into account both surface brightness and morphology (Trentham et al. in prep). We select objects with apparent magnitude $m_{\mathrm{I(814)}} \leq 24$ (AB mag) and membership class 0 to 3, resulting in a sample of 469 cluster galaxies. For these galaxies, 41% are spectroscopically confirmed members (class 0), while 7%, 27%, and 25% have membership classes 1 to 3, respectively.

We derive B and V magnitudes (in Vega mag) for the Coma galaxies using SDSS g and r (in AB mag). For the bright sample, we use the B, V, g, and r magnitudes (instead of the ACS F814W) for ease of comparison to other studies. In addition, Hammer et al. (2010) find that for bright galaxies ($M_{\mathrm{I(814)}} \leq 17$ AB mag) in the Coma survey, it is more reliable to use the SDSS rather than ACS magnitudes, as the latter may be unreliable for some galaxies with large, diffuse stellar halos. We use the following transformations from Jester et al. (2005) to convert the SDSS g and r (AB) to B and V (Vega)[2]:

$$B = g + 0.39 \times (g - r) + 0.21 \tag{4.1}$$

$$V = g - 0.59 \times (g - r) - 0.01. \tag{4.2}$$

We calculate absolute magnitudes assuming a distance modulus of 35.0 (Carter et al. 2008).

[2]The transformation equation tables can be found at http://www.sdss.org/dr7/algorithms/sdssUBVRITransform.html

In this paper, we explore the optical bar fraction in two regimes: bright, non-dwarf S0 disks (§ 4.3) and faint (dwarf) galaxies (§ 4.4). To separate these two regimes, we apply a magnitude cut of $M_{\mathrm{I(814)}} \leq -18.5$, roughly equivalent to $M_{\mathrm{V}} \lesssim -18$ or $M_{\mathrm{B}} \lesssim -17$ for our sample. We choose a cut at $M_{\mathrm{V}} \sim -18$ because it tends to separate well the regimes where normal and dwarf galaxies dominate on the luminosity functions of clusters (Binggeli et al., 1988; Trentham & Hodgkin, 2002; Mobasher et al., 2003). Luminosity cuts at magnitudes $M_{\mathrm{V}} \sim -18$ are often used to separate dwarf and non-dwarf galaxies in the literature (Matković & Guzmán, 2005; Aguerri et al., 2005; van Zee, 2001; Barazza et al., 2006). This cut gives 52 galaxies brighter than, and 417 galaxies fainter than $M_{\mathrm{V}} = -18$. From the 52 bright galaxies, we discard four galaxies (two are a close/merging pair and two galaxies are partially off the edge of a tile) bringing our initial bright sample to 48 galaxies. We discuss the methods for selecting S0 galaxies from this bright sample in § 4.3.1.

In Fig. 4.1a we show the absolute magnitude $M_{\mathrm{I(814)}}$ distribution for the non-dwarf (bright) and dwarf Coma core samples. Fig. 4.1b shows the central surface brightness μ_0 vs. absolute magnitude $M_{\mathrm{I(814)}}$ distribution of the bright, non-dwarf (black circles) and dwarf (green plus) galaxies.

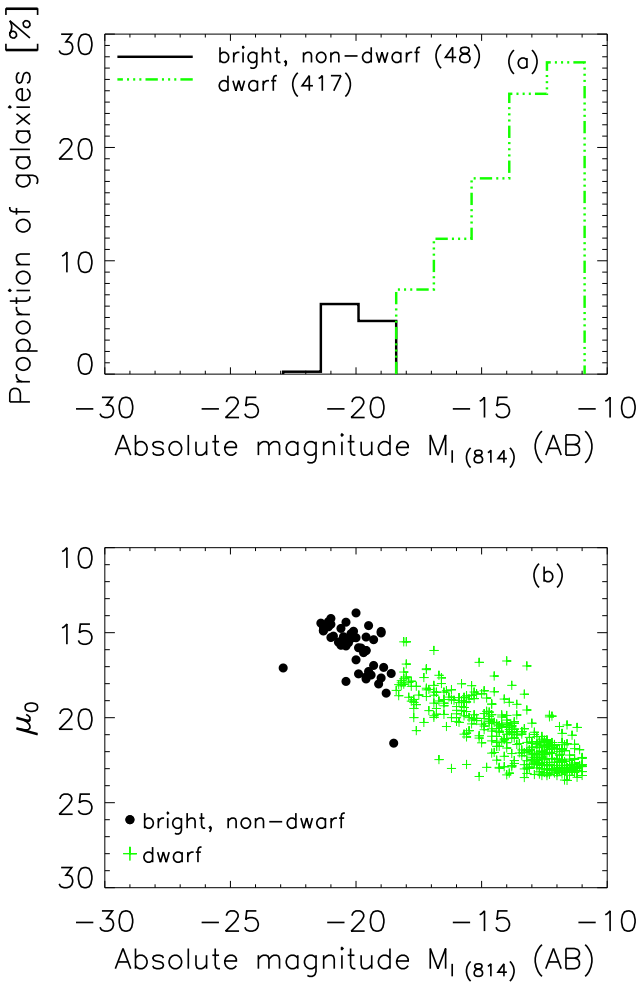

Figure 4.1 **(a)** Absolute magnitude ($M_{\mathrm{I}(814)}$) distribution of the bright, non-dwarf ($M_{\mathrm{V}} \lesssim -18$) and dwarf ($M_{\mathrm{V}} > -18$) galaxies in our Coma core cluster member sample (§ 4.2). Most galaxies are dwarfs with $M_{\mathrm{V}} > -18$. **(b)** Central surface brightness μ_0 vs. absolute magnitude $M_{\mathrm{I}(814)}$ for the bright and dwarf cluster core samples.

4.3 Bars in bright S0 galaxies in the central region of the Coma cluster

4.3.1 Identifying Bright S0 Galaxies

Due to the fact that bars are inherently a disk phenomenon, the bar fraction is traditionally defined as

$$f_{\rm bar} = \frac{N_{\rm bar}}{N_{\rm bar} + N_{\rm unbar}}, \tag{4.3}$$

where $N_{\rm bar}$ and $N_{\rm unbar}$ represent the number of barred and unbarred disk galaxies, respectively. Therefore, from the bright sample of 48 galaxies, we need a sample of disk galaxies (e.g., S0–Im) for analysis. As discussed in § 4.1, recent work has shown that a bar fraction averaged over a wide range in Hubble types gives only limited information. The bar fraction is a strong function of galaxy properties, such as B/T, luminosity, stellar mass, and color. Because our sample is too small to split into fine bins by morphological type, and because most (94%) of bright disk galaxies in our Coma core sample are S0s (see below), *our analysis of bright galaxies in this paper focuses on S0s only.* The goal of our study is to provide the bar fraction for the densest low redshift ($z \sim 0.02$) environment and to serve as a comparison point for studies of barred S0 galaxies in field and intermediate-density environments at different redshifts.

Starting with the bright sample of 48 galaxies, we use visual classification to separate the galaxies into ellipticals, S0s, visually ambiguous E/S0, and spirals. We note that our visually-identified class of 'S0' galaxies includes all Hubble type S0 sub-types from S0$^-$ to S0/a (numerical T-types -3 to 0).

It is fairly easy to separate S0s and ellipticals visually when the S0s host bars. However, unbarred S0s are harder to separate from ellipticals since an unbarred S0 hosts a disk, which is effectively featureless and devoid of tell-tale disk signatures, such as a bar or spiral arms. We find a group of 10 bright galaxies that are *visually* ambiguous E/S0s. For each of these 10 galaxies, we perform multiple component structural decomposition with the GALFIT code (Peng et al., 2002) by fitting the two-dimensional (2D) light distribution taking into account the PSF, following the procedure described in Weinzirl et al. (2009). In brief, we fitted each galaxy with three models: a single-component model, a bulge+disk model, and a bulge+disk+bar model. The single component, bulge, and bar were fitted with Sérsic profiles, while the disk was fitted with an exponential profile (Sérsic $n = 1$). If needed, a point source component was added. For each model, GALFIT finds the optimum solution using the Levenberg-Marquardt algorithm. The goodness of fit is determined iteratively by calculating χ^2. GALFIT continues to adjust the model parameters until the gradient $\delta\chi^2/\chi^2$ is very small (e.g., 10^{-4}) for 10 continuous iterations. Out of the three models (spheroid, bulge+disk, bulge+disk+bar), the best one was selected by considering a number of factors, including the χ^2 values, the strength and spatial distribution of the residuals, and the output parameters (e.g., spheroid, bulge, and disk effective radii). These factors were used to decide whether the galaxy is likely an elliptical or an S0. Examples of the data, model, and residuals for three representative galaxies classified as E, S0, and E/S0 after decomposition are shown in Figure 4.2.

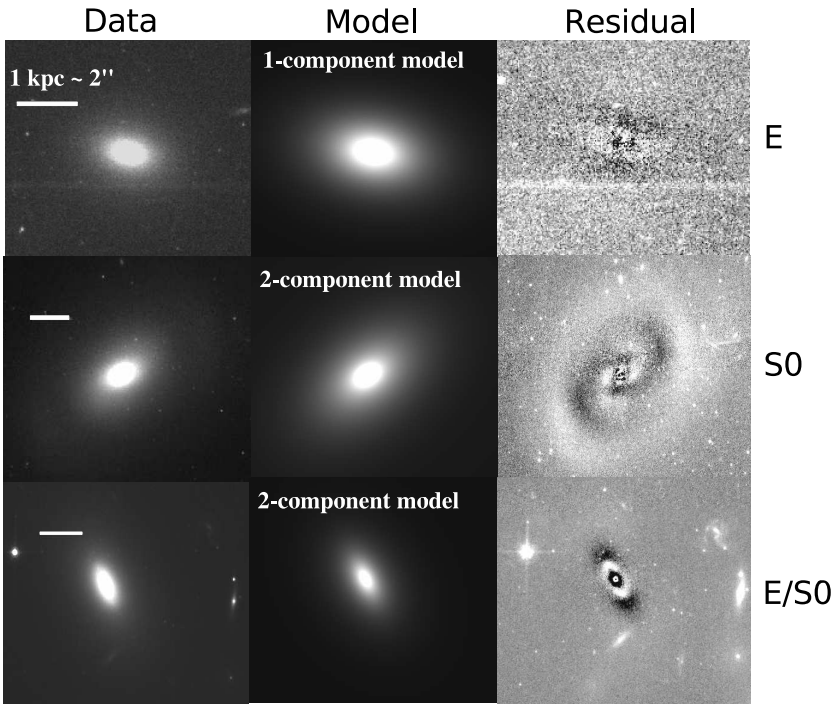

Figure 4.2 Examples of the data (left), GALFIT model (middle), and residual (right) for three of the 10 visually-ambiguous cases where single-component Sérsic fits and bulge+disk decompositions were performed to determine whether the galaxy is an elliptical or S0. The top/middle/bottom rows show examples of galaxies classified as E, S0, and still ambiguous E/S0 respectively, after decomposition (§ 4.3.1). The galaxy in the top row (COMAi125930.268p28115.17) is classified as an elliptical based on the residuals, which are much smaller for the single-component Sérsic fit than for the two-component bulge+disk fit. The galaxy in the second row (COMAi125938.323p275913.84) is classified as an S0 because spiral structure is seen in the residual of the bulge+disk fit, signifying that a disk is present, since spiral arms are inherently disk features (we classify this galaxy as an S0 instead of Sa because the spiral structure is not readily visible by eye on the direct image). The galaxy in the third row (COMAi125950.103p275529.47) is classified as an ambiguous E/S0 because, based on the residuals and other factors (χ^2 and fit parameters), it is still not possible to determine whether this galaxy is more likely to be an elliptical with an inner debris disk or an S0.

Out of the 10 *visually* ambiguous E/S0 galaxies, we find from multi-component decompositions that one is an elliptical, eight are S0s, and one is still ambiguous E/S0. The ambiguous galaxy may be a disk galaxy with complex structure or an elliptical with an inner debris disk. In § 4.3.4 we use this galaxy to estimate the uncertainty in the optical bar fraction by calculating $f_{\rm bar}$ (see Equation 4.1) for the two cases where this galaxy is either included or excluded in the number of unbarred disks ($N_{\rm unbar}$).

The absolute magnitude $M_{\rm I(814)}$ distribution of the bright Coma core sample is shown in Fig. 4.3a. The final morphological breakdown of our bright sample (13 ellipticals, 1 ambiguous E/S0, 32 S0s, and 2 spirals) is shown in Fig 4.3b. It is clear that S0s dominate among the bright disk galaxies in our Coma core sample, which is expected for the central regions of a dense cluster. We find a ratio of E : S0 : Sp of 28% : 68% : 4%. This is at the extreme end of the morphology-density relation found in dense environments by Dressler (1980). Fig. 4.3c shows the distribution of stellar mass for the S0 disk sample as well as all bright ($M_{\rm V} \lesssim -18$) galaxies. Stellar masses are calculated using the relations from Bell et al. (2003) assuming a Kroupa et al. (1993) initial mass function:

$$\frac{M}{M_{\odot}} = v_{\rm lum} \times 10^{-0.628+1.305(B-V)-0.1}, \tag{4.4}$$

where

$$v_{\rm lum} = 10^{-0.4(V-4.82)}. \tag{4.5}$$

Galaxies in our S0 disk sample have stellar masses between $10^{9.5}$ and $10^{11}{\rm M}_{\odot}$. Fig. 4.3d shows a $g-r$ color vs. $M_{\rm r}$ magnitude diagram. Almost all ellipticals

and most disk galaxies fall on the red sequence. We overplot the relation from Blanton et al. (2005) for the break between the red sequence and blue cloud using the equation

$$(g - r) = 0.65 - 0.03(M_{\rm r} + 20). \tag{4.6}$$

We also plot a subsample of the dwarf galaxies ($M_{\rm V} > -18$) for which SDSS data are available ($\sim 30\%$).

We show examples from our final bright S0 sample of 32 galaxies in Figure 4.4. We note that all 32 S0s in the bright sample are spectroscopically confirmed cluster members.

4.3.2 Identification of bars in S0s via ellipse fits

Ellipse fitting is our primary method of detecting bars in the bright S0 sample (e.g., Wozniak et al. 1995, Friedli et al. 1996; Regan et al. 1997; Mulchaey & Regan 1997; Jogee et al. 1999, 2002, 2004; Knapen et al. 2000; Laine et al. 2002; Sheth et al. 2003, 2008; Elmegreen et al. 2004; Menéndez-Delmestre et al. 2007; MJ07; Aguerri et al. 2009). To detect bars through ellipse fitting we use the standard IRAF task $ELLIPSE$ in conjunction with an adaptive wrapper (Jogee et al. 2004), which runs $ELLIPSE$ iteratively on each galaxy until the best fit is found or up to a maximum number of times specified by the user. Ellipses are fit to the galaxy isophotes out to a maximum distance ($a_{\rm disk}$) where the brightness of the isophotes reaches the noise level. We note that the value of $a_{\rm disk}$ depends on the depth of the image,

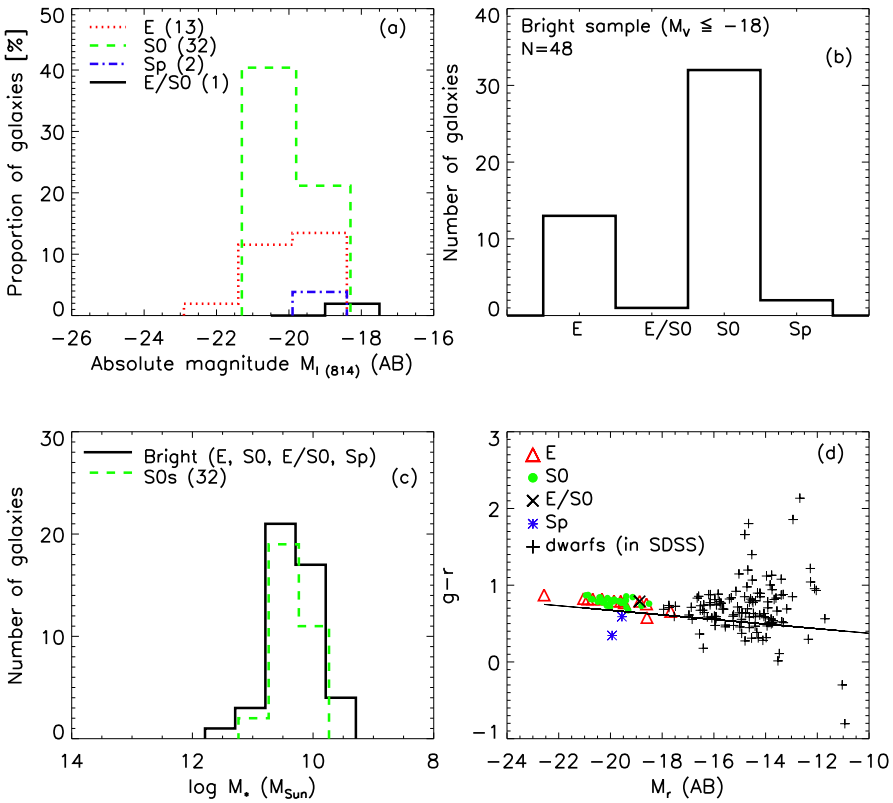

Figure 4.3 **(a)** Absolute magnitude distribution of bright ($M_V \leq -18$) galaxies in our Coma core sample (§ 4.3.1). **(b)** Distribution of morphological types (E, E/S0, S0, Sp) in the bright non-dwarf sample. S0 galaxies (32), comprise 94% of the bright disk galaxies. Morphological types are from visual classification, supplemented with 2D, multi-component decomposition for visually ambiguous cases (§ 4.3.1). **(c)** Stellar mass distribution of the bright galaxies in our Coma core sample, with the S0 galaxies shown in green. The S0s have masses between $10^{9.5}$ and $10^{11} M_\odot$. **(d)** $g-r$ color-magnitude diagram of the bright cluster sample and a subset (30%) of the dwarf sample with available SDSS magnitudes. We overplot the relation from Blanton et al. (2005) for the break between the red sequence and blue cloud. Most elliptical and S0 galaxies lie on the red sequence.

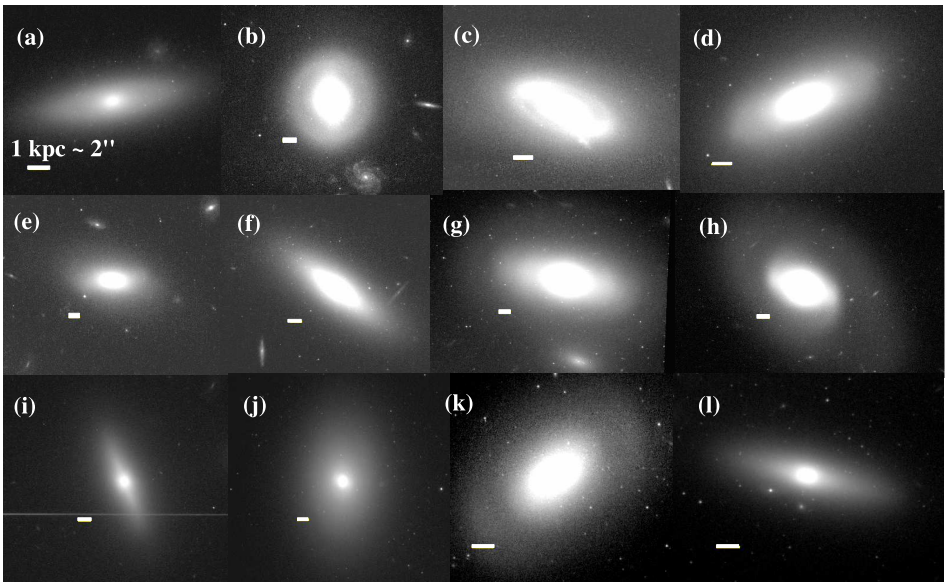

Figure 4.4 Examples of some S0 galaxies from our bright sample (§ 4.3.1). The scale bars show 1 kpc. The galaxies shown are: (a) COMAi125704.336p273133.26, (b) COMAi125710.767p272417.44, (c) COMAi125833.136p272151.77, (d) COMAi125832.060p272722.85, (e) COMAi125928.728p28225.90, (f) COMAi125929.404p275100.51, (g) COMAi125929.956p275723.26, (h) COMAi125930.825p275303.42, (i) COMAi125931.455p28247.62, (j) COMAi125932.789p275900.95, (k) COMAi125938.323p275913.84, (l) COMAi125939.657p275713.86.

as $a_{\rm disk}$ will reach larger values for deeper images. However for the purpose of bar detection, it is only necessary for the radial profile to extend beyond the bar into the more circular region of the disk. We typically set the maximum allowed iterations to 300, however for most galaxies a good fit is achieved in only a few iterations. A good fit is one where an ellipse can be fitted at every isophote out to $a_{\rm disk}$. Residuals characterizing how well each isophote is fitted by its corresponding ellipse are given by the harmonic amplitudes A3, B3, A4, and B4 (e.g., Carter, 1978; Jedrzejewski, 1987; Carter, 1987). For our barred galaxies, we find typical amplitudes of 5–10%. For a detailed discussion on the advantages and drawbacks of using ellipse fitting to characterize bars we refer the reader to MJ07.

Once the galaxies are fitted, we use an interactive visualization tool to display the overlays of the fit on the galaxy image, as well as the radial profiles of surface brightness, ellipticity (e), and position angle (PA). Using the radial profiles of ellipticity (e) and PA, we classify the galaxies as 'highly inclined', 'barred', or 'unbarred'. We discuss these classes in more detail below.

4.3.2.1 Detecting and removing highly inclined galaxies

In studies of bars, it is conventional to exclude highly inclined galaxies as the large inclination precludes accurate structural classification, making it particularly difficult to identify systems as barred or unbarred. We use two ways to identify highly inclined galaxies in the bright S0 sample. The first is via the ellipse fit criteria, where the observed outermost disk isophote (at

$a_{\rm disk}$) has $e > 0.5$, corresponding to $i > 60°$. We find eight galaxies that fit this criterion. This method works well for spirals of intermediate to late Hubble types, but does not capture all highly inclined disks for S0s because for some edge-on or highly inclined S0s, a rounder, thickened outer stellar component can sometimes dilute the outermost isophote so that the outermost ellipticity is below 0.5 although the galaxy is highly inclined.

Therefore, our second method is to visually identify highly-inclined S0s. We visually identify these systems using the criteria that a thinner, high-surface brightness, highly-inclined disk appears embedded in a thick, diffuse stellar component, which could be a mix of thick disk, bulge, and bar stars. A typical example of one of these galaxies is shown in Fig. 4.5. We encounter four such cases, where the galaxy appears visually to be close to edge-on, and is classified as highly inclined. We distinguish these cases from a face-on galaxy with a bar because (1) the thin, highly-inclined disk and the thicker stellar component are always oriented along the same position angle, (2) the thick outer stellar component in these highly-inclined S0 galaxies appears much fainter and more diffuse than a face-on disk, and (3) in three out of these four galaxies, a box or X-shaped bulge is present, suggesting that the galaxy is seen edge-on (e.g., Athanassoula 2005). We therefore exclude from further analysis the 12 highly-inclined systems that we find in the sample.

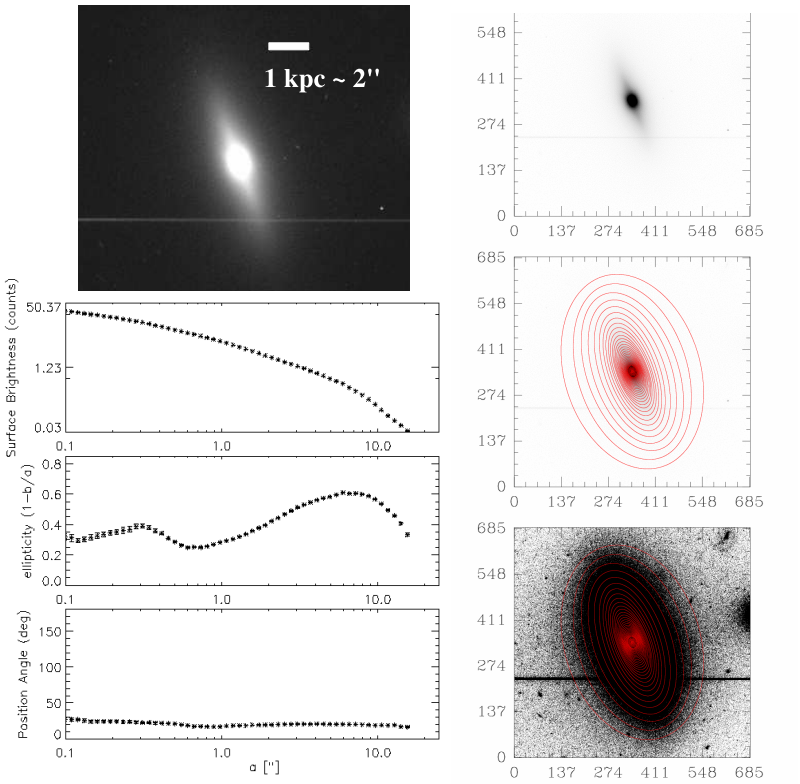

Figure 4.5 Left: *HST* image and radial profiles of surface brightness, e, and PA of a highly-inclined S0 with an outer, diffuse, thickened stellar component (see § 4.3.2.1). Right: the ellipse fits are overlaid onto the galaxy image. The top two panels are shown with a stretch that enhances the thin disk and boxy bulge, while the bottom panel shows the outer disk. The thickened, diffuse, outer stellar component causes the outermost isophotes to have $e \sim 0.4$, which is less than the quantitative inclination cut of $e > 0.5$. Therefore, we classify this galaxy as highly-inclined using visual classification according to the criteria outlined in § 4.3.2.1.

4.3.2.2 Detecting barred galaxies

Traditionally, when ellipse fits are used to identify bars, a galaxy is classified as barred if the radial profiles of the ellipticity and PA fulfill the following requirements: (1) the e rises to a *global* maximum, $e_{\rm bar} > 0.25$, while the PA remains relatively constant (within $\pm 10^{\circ}$), and (2) the e drops by at least 0.1 and the PA changes by more than 10° at the transition between the bar and disk region. An example of a barred S0 galaxy in our sample that meets the traditional criteria is shown in Fig. 4.6.

These criteria will identify primary stellar bars in the vast majority of spirals, particularly those of intermediate to late Hubble types (Sb–Sm). However, they can marginally fail in some galaxies due to a rare set of circumstances, which we describe in detail below. These circumstances are particularly likely to occur in S0s with large bulge-to-disk ratios.

In some S0s, a combination of structural parameters and viewing angle causes the observed (i.e., not deprojected) maximum bar ellipticity ($e_{\rm bar}$; typically measured from the isophote crossing the end of the bar) to become a *local* maximum of the ellipticity radial profile rather than the *global* maximum. In these rare cases, the ellipticity ($e_{\rm disk}$) of the outer disk becomes the *global* maximum in the radial profile of ellipticity. This can happen in the case of a barred galaxy, where all or most of the following conditions are satisfied: (i) The galaxy has a moderate to large inclination (e.g., $i > 50^{\circ}$). This causes the outer circular disk of the galaxy to appear elongated along the line of nodes (LON) in the projected image of the galaxy on the sky, leading to a higher

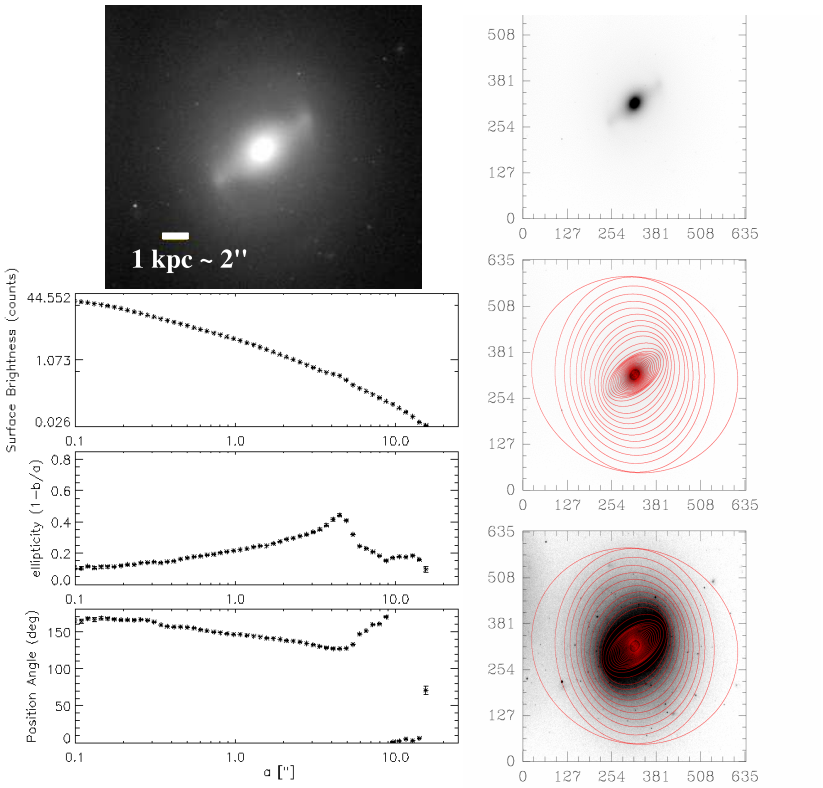

Figure 4.6 Left: *HST* image and radial profiles of surface brightness, e, and PA of a barred cluster galaxy. In this example, the traditional bar signature is evident in the smooth rise of the e to a global maximum of ~ 0.4, while the PA remains relatively constant in the bar region. The e then drops and the PA changes, indicating the transition to the disk region. Right: the ellipse fits are overlaid onto the galaxy image. The top two panels are shown with a stretch that enhances the inner disk and bar regions, while the bottom panel shows the outer disk. See § 4.3.2.2 for details.

measured $e_{\rm disk}$. (ii) A large fraction of the length of the bar lies within a fairly axisymmetric bulge, which is much more luminous than the bar. In this case, the bulge light dilutes the ellipticity of the bar by 'circularizing' the isophote crossing the bar end, thus causing $e_{\rm bar}$, measured from this isophote to be significantly lower than the true ellipticity of the bar. (iii) The bar major axis has a large offset ($\Delta\theta$) with respect to the LON, such that projection effects make the disk appear more elongated, while the bar appears more round. The most extreme example occurs when the bar is perpendicular to the LON (i.e., $\Delta\theta = 90^{\circ}$). Such situations can potentially cause the observed ellipticity of the disk to exceed that of the bar. Thus, a combination of factors (i) to (iii) can cause the measured $e_{\rm bar}$ to fall below $e_{\rm disk}$ so that $e_{\rm bar}$ is a *local* maximum in the e radial profiles. In this case, the bar can still be identified through ellipse-fits if the traditional criterion that the measured maximum bar ellipticity $e_{\rm bar}$ must be a *global* maximum is relaxed, and a *local* maximum be deemed acceptable.

In the case of barred S0s, the conditions (i) to (iii) can be satisfied in a larger fraction of galaxies than for a sample of barred intermediate-to-late Hubble type (Sb–Sm) spirals due to the following reasons. Many barred cluster S0s host bulges that are bright, have large bulge-to-disk light ratios, and encompass a large fraction of the length of the bar. Indeed, among our sample of 20 moderately-inclined cluster S0s, we find three such cases and an example is shown in Fig. 4.7. For this reason, we quote two bar fractions derived through ellipse fits: the first bar fraction ($f_{\rm bar,ES}$), where we use the

strict criteria (1) and (2) above, and the second bar fraction ($f_{\rm bar,ER}$) where for galaxies satisfying (i) to (iii), we relax the criterion that the maximum bar ellipticity must be a *global* maximum (however we still require it to rise above $e = 0.25$). We note that all bars identified with the strict ellipse-fitting criteria ('ES') are also picked up under the relaxed ellipse-fitting criteria ('ER'). We further note that, for the galaxies where the bar is detected only through the relaxed criteria, if the radial profiles of the ellipticity and PA are deprojected (§ 4.3.7), the bar ellipticity $e_{\rm bar}$ does become the global maximum. However, because many large studies of bars do not deproject the radial profiles (e.g., M09), we use the observed radial profiles to detect the bars as described above for ease of comparison.

4.3.3 Identification of bars in S0s via visual classification

In addition to ellipse fitting, we also present the optical bar fraction for bright S0s in Coma from visual classification performed by I.M., S.J., and P.E. This facilitates comparison to other work where bars are identified visually (§ 4.3.5).

A galaxy is classified as 'barred' through visual classification if it has a significant elongated feature extending from the center of the disk with an axial ratio (estimated from the image with $DS9$) < 0.7 and a PA that differs from the PA of the outer disk by at least 10°. A galaxy is classified as 'unbarred' if there is no elongated structure present that fits the above criteria.

All of the bright barred S0s we identify in the Coma sample through

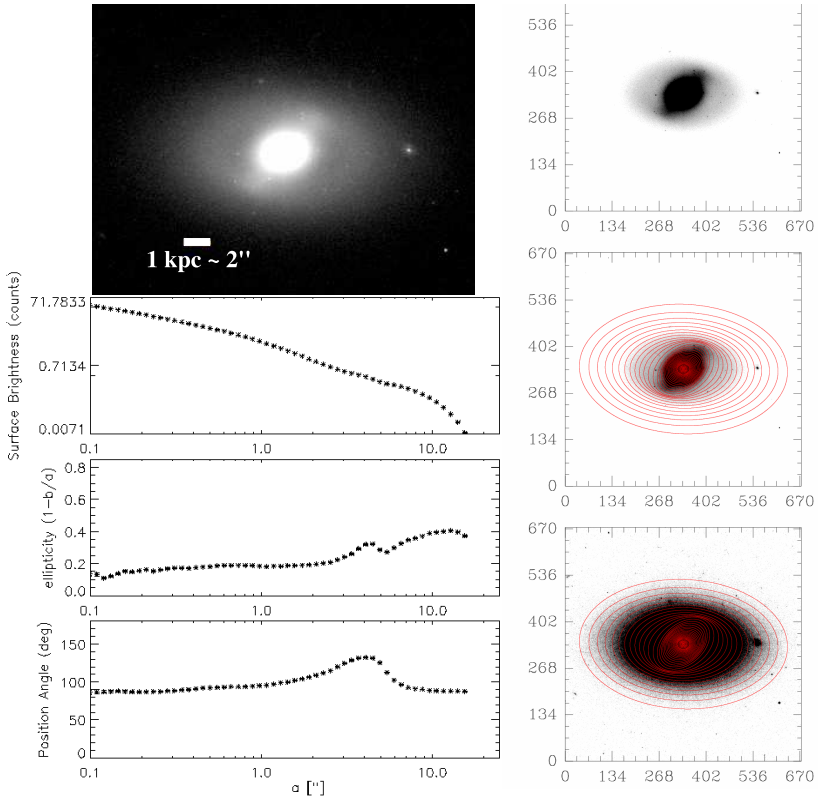

Figure 4.7 The panels are as in Fig. 4.6, but here we show an example of a barred galaxy that does not meet the strict ellipse-fit criterion requiring that $e_{\rm bar}$ is the *global* maximum in the e radial profile. In this case, the observed outer disk ellipticity $e_{\rm disk}$ is higher than $e_{\rm bar}$, making it a *local* maximum in the e radial profile. This happens due to a combination of properties of the galaxy: (1) the galaxy is inclined ($i \sim 51°$) causing the outer disk to be elongated along the line of nodes with a significant ellipticity ($e_{\rm disk} = 0.37$); (2) the stellar bar is significantly offset (by $\sim 45°$) with respect to the line of nodes and hence its intrinsic axial ratio is diluted by projection effects; (3) the stellar bar has a significant fraction of its length inside a very luminous bulge, and the measured bar ellipticity is diluted to lower values than the true $e_{\rm bar}$. Therefore this galaxy is identified as 'barred' through the relaxed ellipse-fitting criteria. We find three such cases among the bright Coma S0 galaxies (see § 4.3.2.2).

ellipse fitting and visual classification are listed in Table 4.1. The methods through which the bar is detected are shown in column (5).

4.3.4 Optical S0 bar fraction in the central region of the Coma cluster

The optical bar fractions for our sample of bright S0 galaxies in the Coma cluster core are presented in Table 4.2.

Using the strict ellipse fitting criteria (§ 4.3.2.2), we find that the optical bar fraction for the bright S0s is $f_{\rm bar,ES} = 50 \pm 11\%$ (10/20). Using the relaxed ellipse fitting criteria, we find $f_{\rm bar,ER} = 65 \pm 11\%$ (13/20). Visual classification gives an optical bar fraction of $60 \pm 11\%$ (12/20). All errors are binomial errors. The barred S0 galaxies identified through ellipse fitting and visual classification are shown in Fig. 4.8.

To correctly derive the bar fraction for S0s in clusters, we need to accurately estimate the number of unbarred S0s ($N_{\rm unbar}$ in Eq. 1). As S0s are devoid of typical disk features such as spiral arms, star-forming rings, etc., it is particularly challenging to *visually* identify all unbarred S0s and separate them from ellipticals. Therefore, in § 4.3.1, we identified S0s through both visual classification and two-dimensional structural decomposition of the images into single-component Sérsic models, bulge+disk models, and bulge+disk+bar models. We found 13 Es, 32 S0s, and one E/S0 case, which still remains ambiguous even after decomposition. This ambiguous E/S0 case is not included in the optical bar fraction in Table 4.2. If it is included as an un-

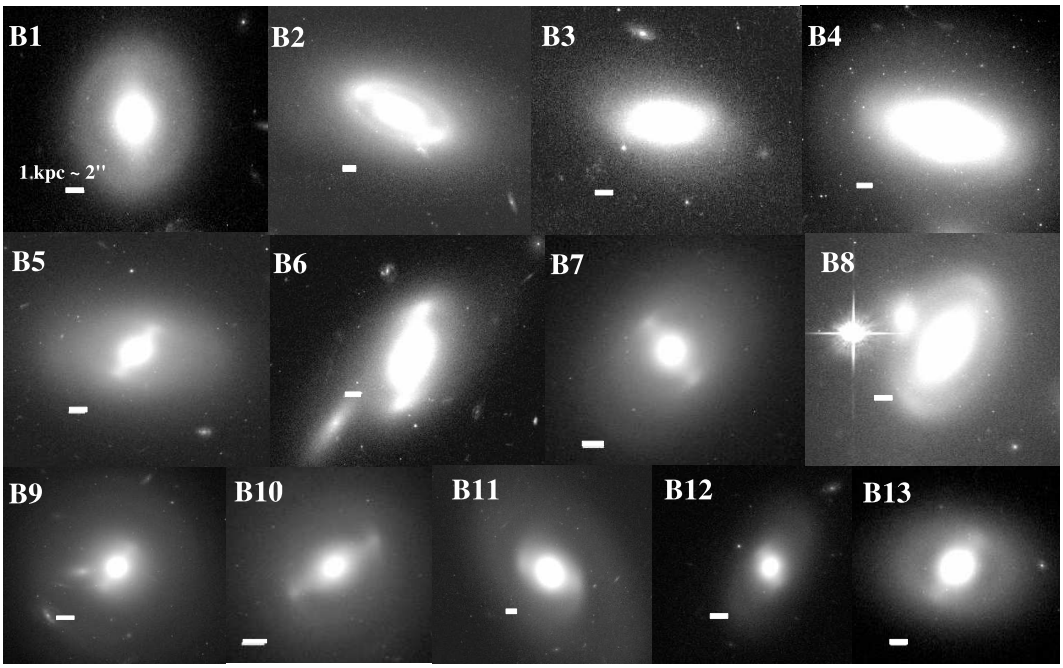

Figure 4.8 Barred bright ($M_V \lesssim -18$) S0 galaxies in the Coma cluster core found through ellipse fits (strict and relaxed criteria) and visual classification (see § 4.3.2 and Table 4.1). All bars identified through the relaxed ellipse fit criteria are also identified by visual classification and vice versa. Bright stars such as the one in B8 are masked during the fitting.

barred S0 in our analysis, the optical bar fractions fall to: $f_{\rm bar,ES} = 48\pm$ 11%, $f_{\rm bar,ER} = 62\pm$ 11%, and 57$\pm$ 11% from visual classification. We therefore estimate that the uncertainties associated with determining the number of unbarred S0s can lead us to overestimate the optical bar fraction by only a small factor of ~ 1.05.

We note that in the field, the bar fraction is lower in the optical than in the NIR by factor of 1.3 (Eskridge et al. 2000; M07) for intermediate (Sab–Sc) Hubble types due to obscuration by gas, dust, and star formation. However in S0s, where there is little gas and dust on large scales, we don't expect the difference between the optical and NIR bar fractions to be significant.

4.3.5 S0 bar fraction across different environments

Due to the fact that different bar detection methods can yield different bar fraction results, it is important to compare studies using the same methods for consistency. In addition, as discussed in § 4.1, the bar fraction depends on host galaxy properties such as Hubble type or B/T (Odewahn 1996; BJM08; Aguerri et al. 2009; M09; Weinzirl et al. 2009; Laurikainen et al. 2009), luminosity (Barazza et al. 2009; M09), stellar mass, and color (Nair & Abraham, 2010b; Cameron et al., 2010). Therefore we use comparison samples that are matched to our Coma sample in Hubble type (S0s), luminosity ($M_{\rm V} \lesssim -18$), color, and method of bar detection. We compare our results for S0s to those of other studies in Coma and lower-density clusters (Abell 901/902 and Virgo).

First, we compare to another study in the very dense environment of

the central regions of the Coma cluster (galaxy number density $n \sim$ 10,000 galaxies/Mpc^3) by T81. T81 uses visual classification on ground-based Kitt Peak National Observatory (KPNO) plates to detect bars in S0s brighter than $M_V = -17.5$ (very similar to our magnitude cutoff of $M_V \sim -18$). Therefore we compare his result to our optical bar fraction from visual classification (§ 4.3.3). Table 4.3 shows that our optical bar fraction from visual classification for S0s (60±11%) in the Coma core is higher than the result (42±7%) that T81 obtained after correcting raw galaxy counts for projection effects[3]. A clue to the reason for this difference comes from our finding that in many S0s in our sample, the bar ellipticity and its overall signature are diluted because the bulge is bright compared to the bar and it is large enough to encompass a large fraction of the bar length. In such cases, as discussed in section § 4.3.2.2, the bar is harder to detect via any method, be it visual classification or ellipse fits, unless the image is of high quality and the classifier has significant expertise. In the case of T81, the visual classification was performed on ground-based optical plates, which are of lower quality than CCD images, making it even more difficult to detect such diluted or/and short bars. It is not possible to directly compare our case-by-case results with T81, as he does not publish the list of galaxies he classifies as barred and does not provide the lengths and ellipticities of the bars. However, we perform two indirect tests to gauge the

[3]This correction is used by T81 to account for the effects of foreground and background objects contaminating the cluster field in the absence of spectroscopic data. Since all bright S0s in our Coma core sample are spectroscopically-confirmed cluster members, we compare to the corrected bar fraction from T81.

impact of missing diluted, weak, and/or short bars. In our sample, seven of the 13 barred S0s have an observed peak bar ellipticity $e_{\rm bar} < 0.4$ (Fig. 4.12). If all of these galaxies were classified as unbarred, the bar fraction would drop to 30%. Alternatively, if the shorter ($a_{\rm bar} < 2$ kpc) bars are excluded, the bar fraction would drop to 45%. These tests suggest that it is likely that the lower optical bar fraction of T81 is due to his missing some of these diluted or/and short bars.

For a comparison to intermediate-density cluster environments, we use the study of M09 for the Abell 901/902 cluster system ($z \sim 0.165$; $n \sim 1000$ galaxies/Mpc^3, see Table 5 in Heiderman et al. 2009). To match our sample, we pick S0 galaxies from the M09 study with $M_{\rm V} \leq -18$, using classifications performed by the members of the STAGES collaboration for the Abell 901/902 cluster system (Gray et al. 2009; see Wolf et al. 2009 for more details). In M09, inclined galaxies were picked as those with outer disk ellipticity $e_{\rm disk} > 0.5$, as traditionally done in bar studies using ellipse fitting. However, since we are only focusing on S0 galaxies (which sometimes have large bulges/diffuse, thick stellar components that can dilute the $e_{\rm disk}$ below 0.5 even for edge-on S0s, as discussed in § 4.3.2.1) we apply the same additional visual criteria outlined in § 4.3.2.1 to the M09 S0 sample to detect and remove highly inclined S0s. Figure 4.9 shows the host galaxy properties of the Abell 901/902 and Coma S0 samples. The two samples are well-matched in mean luminosity, $g - r$ color, and stellar mass, but the Abell 901/902 sample has a tail of galaxies with masses both lower and higher than the Coma core sample, translating,

respectively, into a tail of bluer colors and brighter absolute magnitudes. The Abell 901/902 S0s appear ~ 0.2 mag bluer in $B-V$ color, on average. In M09 bars were detected on optical (HST ACS F606W) images via the strict ellipse-fitting criteria only. We therefore also derive the bar fraction through visual classification and using the 'relaxed' ellipse-fitting criteria for the S0s in the M09 sub-sample in order to derive the corresponding bar fractions for comparison to Coma S0s. As shown in Table 4.3, we find no statistically significant difference in the S0 bar fraction in Abell 901/902 and Coma clusters when detecting bars through visual classification, strict ellipse fit criteria, or relaxed ellipse fit criteria. For instance, from visual classification (Table 4.3, bottom section), the Coma bar fraction (60±11%) is slightly higher than the A901/902 bar fraction (55±5%), but the difference is not statistically significant as the values are consistent within the error bars. Similarly, via the relaxed ellipse fitting criteria (Table 4.3, middle section), the Coma bar fraction is 65±11%, while the A901/902 bar fraction is 48±5%, (barely) consistent within the error bars. A comparison of the bar and disk properties (such as $e_{\rm bar}$ and $a_{\rm bar}/R_{25}$) in Coma and the Abell 901/902 cluster system is discussed in § 4.3.7.

Next, we compare to results in Virgo from Erwin et al. (in preparation; E11). Virgo is the most nearby cluster ($D \sim 20$ Mpc, $z \sim 0.005$) and is representative of a low-density cluster environment ($n \sim 300$ galaxies/Mpc^3 in the core region). We note however, that different environmental tracers paint different pictures in Virgo. While the number density ($n \sim 300$ galaxies/Mpc^3) is lower than that of Abell 901/902 ($n \sim 1000$ galaxies/Mpc^3) or the Coma

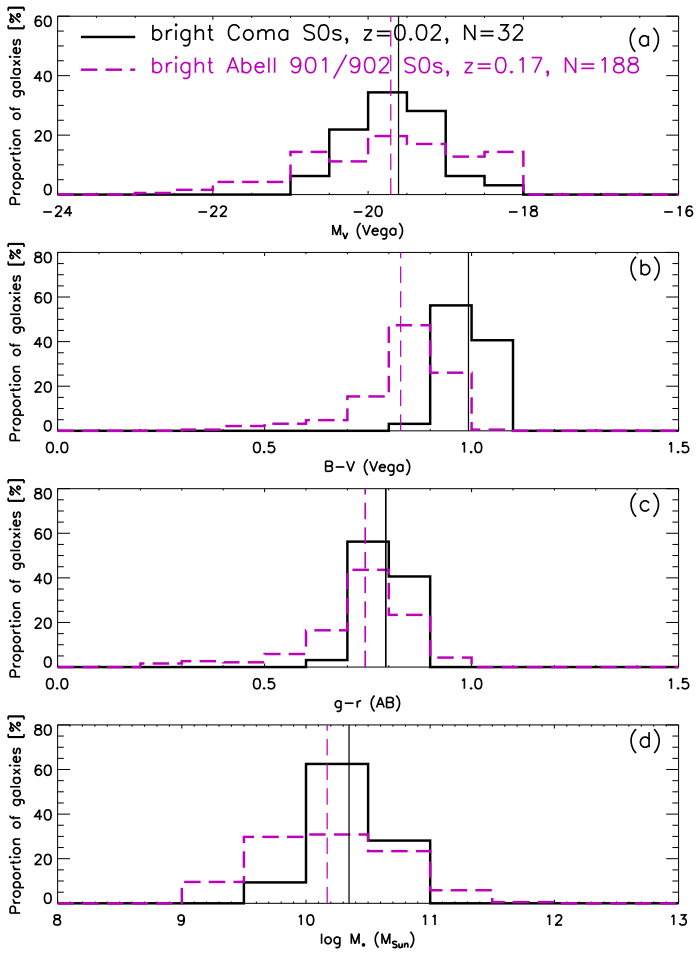

Figure 4.9 The properties of bright S0 galaxies in the Abell 901/902 cluster system (dashed pink lines) and Coma (solid black line). The vertical lines show the mean values for each distribution. The two samples are well-matched in mean luminosity, $g-r$ color, and stellar mass, but the Abell 901/902 galaxies extend to slightly brighter and bluer values. The Abell 901/902 S0s appear ~ 0.2 mag bluer in $B-V$ color, on average.

core ($n \sim$ 10,000 galaxies/Mpc^3), the velocity dispersions in Virgo can be as high as 750 km/s (Binggeli et al. 1987), comparable to those seen in Abell 901/902 and much higher than in groups ($\sim$ 100 km/s; Tago et al. 2008). These properties are relevant for the discussion of our results in § 4.3.8. Our Virgo comparison sample consists of S0 galaxies brighter than $M_{\rm V} = -18$ from E11. Fig. 4.10 shows that the colors of the Virgo S0s are slightly bluer (by $\sim$ 0.1 mag, on average). We compare optical bar fractions derived with all three methods: strict ellipse fitting criteria (ES), relaxed ellipse fitting criteria (ER), and visual classification performed by P.E., I.M., and S.J. according to the criteria outlined in § 4.3.3. Again, we do not find a statistically significant difference in the optical bar fraction (within the errors) for S0s in the Coma core and those in Virgo using any of the three bar-detection methods above (see Table 4.3)[4].

A graphical representation of the trend of the bar fraction for S0s as a function of environment density is shown in Fig. 4.11. We note that Fig. 4.11 shows a hint of an increase in the mean bar fraction toward the dense core of the Coma cluster, however given the error bars, we cannot say whether this trend is significant. A comparison of the bar and disk properties, for S0s in Coma and the Virgo cluster is discussed in § 4.3.7.

We note that to compare to the lowest-density environments (i.e., field

[4]We note that Giordano et al. (2010) quote a much lower bar fraction ($\sim$ 30%) using visual classification for Virgo S0 galaxies. This lower value is likely due to the fact that Giordano et al. 2010 include much fainter galaxies (down to $M_{\rm B} = -15$), use a higher inclination cutoff ($i = 73°$), and a different method for selecting cluster members.

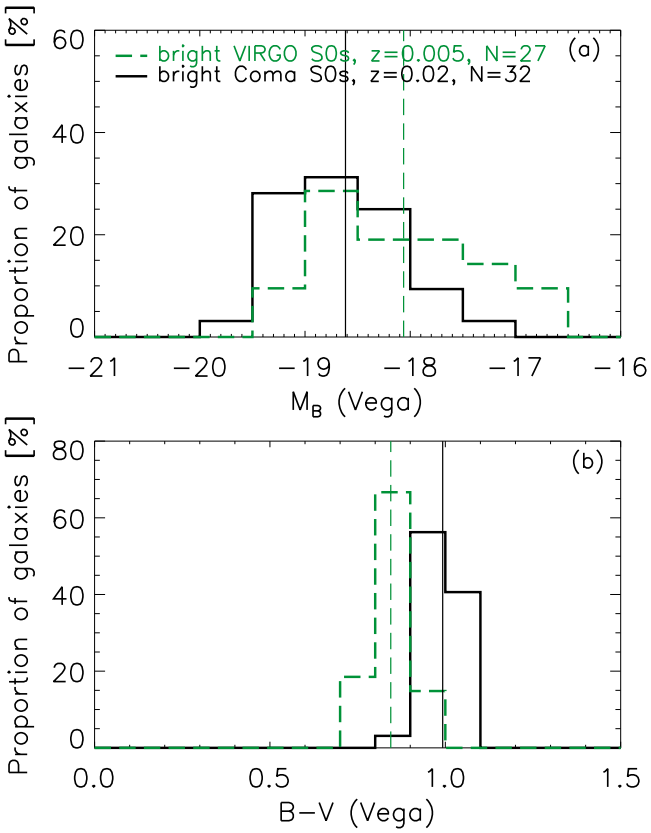

Figure 4.10 The properties of bright S0 galaxies in the Virgo cluster (dashed green line) and Coma (solid black line). The vertical lines show the mean values for each distribution. The two samples are well-matched in mean luminosity. The Virgo S0s are somewhat bluer in $B-V$ color (~ 0.15 mag on average).

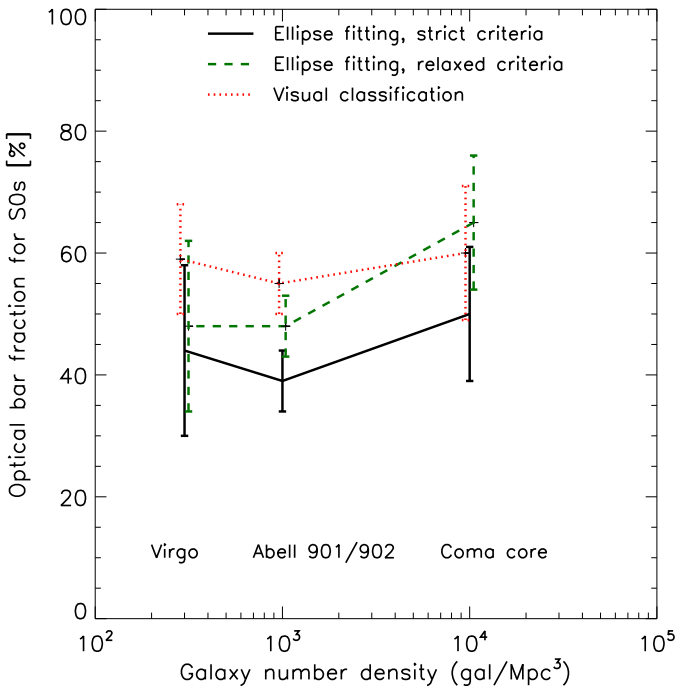

Figure 4.11 The optical bar fraction for S0 galaxies characterized through three methods (ellipse fitting with strict criteria, ellipse fitting with relaxed criteria, and visual classification) as a function of environment density. The different environments probed are the high-density core of Coma ($n \sim$ 10,000 gal/Mpc^3), the intermediate-density Abell 901/902 cluster system ($n \sim$ 1000 gal/Mpc^3), and the low-density Virgo cluster ($n \sim$ 300 gal/Mpc^3; § 4.3.5). The bar fraction for S0s does not show a statistically significant variation across the environments probed, within the error bars.

galaxies), we would ideally like to have a comparison sample where bar detection is done quantitatively via ellipse fits, and where the sample is matched to ours in both Hubble type (S0 galaxies), luminosity ($M_{\rm V} \lesssim -18$), and color. However, there is as of yet no field comparison sample that fulfills all of the above requirements. The two large ellipse fit bar studies of field galaxies (BJM08 and Aguerri et al. 2009) are not adequate because they are mismatched in Hubble type and color (BJM08) or luminosity (Aguerri et al. 2009). Therefore, a comparison with these samples could be misleading, in light of recent results showing that the bar fraction varies non-monotonically with Hubble type, host galaxy luminosity, and color (Nair & Abraham, 2010b). A comparison of the bar fraction derived through visual classification to a matched subset of S0s from the RC3 is complex, because RC3 galaxies are a mix of field and Virgo cluster members. The best candidate for a field comparison is the recently released public catalog by Nair & Abraham (2010a), containing visual morphologies for $\sim$ 14,000 SDSS galaxies. However, such a study is beyond the scope of this paper and therefore we defer this comparison to a later work.

Recently Méndez-Abreu et al. (2010) used the Coma Treasury survey data to analyze the properties of barred galaxies in the Coma cluster (using visual classification to detect bars). They do not select a disk sample but look for bars in all galaxies (including ellipticals and dwarfs). It is problematic and unconventional to quote the bar fraction from a sample of disk galaxies and ellipticals, particularly in the context of studying the bar fraction as a function

of environment, as variations in this bar fraction can then be caused by the fact that the proportion of ellipticals to S0s to spirals changes strongly as a function of environment. For this reason, our study and other studies quote the bar fraction as the fraction of disk galaxies hosting bars. Comparison of our work with the results of Méndez-Abreu et al. (2010) is therefore not straightforward, but nonetheless we attempt a comparison to check whether our findings are consistent. If we include all galaxies from our sample in the magnitude range $-23 \leq M_{\rm r} \leq -14$, to match their sample, we find a total (visual) bar fraction of $7\pm2\%$ (14/188), while Méndez-Abreu et al. (2010) find 9% (secure bars) and 14% (weak/uncertain bars). Although our results are broadly consistent within the uncertainties, there are several further caveats to this comparison. Méndez-Abreu et al. (2010) apply the axial ratio constraint $b/a > 0.5$ to their whole sample, regardless of morphology, while we only apply an inclination cutoff to our bright disk galaxies. In addition to the inclination cutoff, we also exclude S0 galaxies deemed to be highly-inclined/edge-on by eye, since as discussed in § 4.3.2.1, using only the $i > 60^{\circ}$ cut misses highly-inclined and edge-on S0s with a more circular, thickened stellar component. Furthermore, in the process of selecting cluster members, Méndez-Abreu et al. (2010) apply a color cut where they discard all galaxies that have $g - r$ color greater than 0.2 above their fit to the cluster red sequence.

4.3.6 Observed and deprojected properties

In Figure 4.12 we show the observed (solid line) and deprojected (dotted line) distributions of the bar semi-major axis ($a_{\rm bar}$) and bar ellipticity ($e_{\rm bar}$) for the 13 barred S0 galaxies detected through ellipse fitting (using both strict and relaxed criteria). In MJ07, we found that deprojecting the bar semi-major axis and ellipticity for a large sample makes only a very small statistical difference (a factor of 1.2), on average. However, since our Coma core sample is small, we deproject the observed radial profiles of ellipticity and PA and derive deprojected values of $e_{\rm bar}$ and $a_{\rm bar}$. We perform the deprojection using a code developed by Laine et al. (2002) and used previously in Laine et al. (2002), Jogee et al. (2002a,b), and MJ07.

We find an observed mean bar size of 2.5±1 kpc (2.9±1 kpc deprojected; Fig. 4.13) and the mean observed and deprojected bar ellipticity is 0.4±0.1. It is evident that deprojection does not make a large difference in the mean $a_{\rm bar}$ and $e_{\rm bar}$. The observed and deprojected values of $a_{\rm bar}$ and $e_{\rm bar}$ of the three bars detected through the relaxed criteria only are shown as filled and open circles, respectively in Fig. 4.12. These galaxies satisfy the relaxed ellipse fit criteria, where the peak ellipticity of the bar is a local and not a global maximum due to the combination of factors discussed in § 4.3.2.2. After deprojection removes the projection effects, which cause the ellipticity of the disk to be artificially boosted compared to the bar ellipticity, the peak bar ellipticity then becomes a global maximum in these three galaxies. Thus, after deprojection, these three barred galaxies also pass the strict ellipse fit

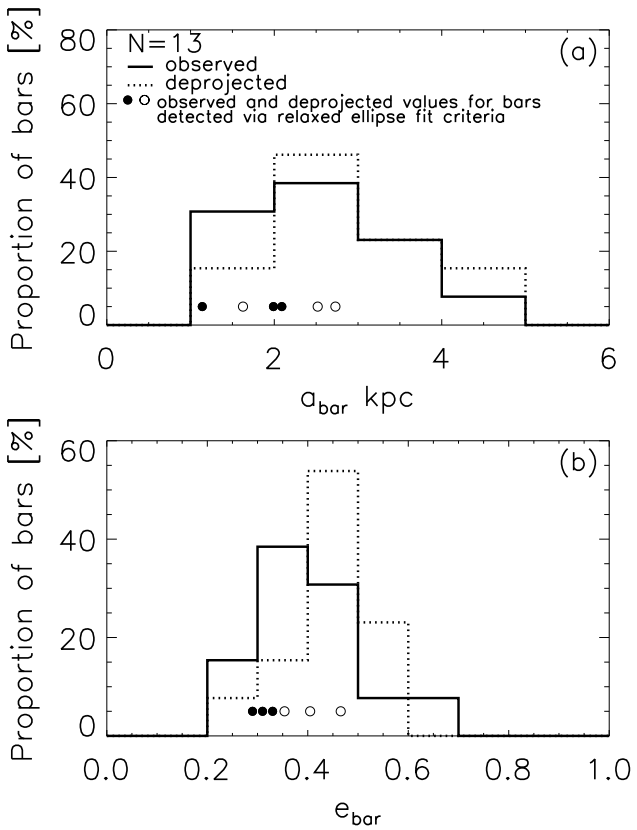

Figure 4.12 Observed (solid line) and deprojected (dotted line) bar size ($a_{\rm bar}$) **(a)** and ellipticity $e_{\rm bar}$ **(b)** distributions for the 13 barred S0 galaxies detected through ellipse fitting (including ones detected through relaxed criteria). The observed and deprojected values for the three bars detected through the ellipse fit relaxed criteria are shown as filled and open circles, respectively (§ 4.3.2.2). The mean observed $a_{\rm bar}$ for our barred S0s (including those detected with relaxed criteria) is 2.5±1 kpc (2.9±1 kpc deprojected), while the mean observed and deprojected $e_{\rm bar}$ is 0.4± 0.1. Most (85%) of bars have an observed $e_{\rm bar} \leq 0.5$. We also note that all extra bars that were detected via the relaxed ellipse fit criteria on the observed images, would be detected via the strict ellipse fit criteria after deprojection. This is due to the fact that the latter removes projection effects, which cause the maximum bar ellipticity $e_{\rm bar}$ to go from a local maximum in the radial profile of ellipticity to a global maximum.

criteria. The observed and deprojected $a_{\rm bar}$ for these galaxies are shorter than average. We note, however, that the bars of the three galaxies that failed to meet the strict ellipse fit criteria before deprojection are not necessarily weak bars. The intrinsic ellipticities $e_{\rm bar}$ of these three bars after deprojection are similar to the mean value of the whole sample (0.4±0.1). This can be understood from the combination of factors discussed in § 4.3.2.2, particularly the relative orientation of the bar with respect to the LON and projection effects.

Fig. 4.13 shows that the mean observed and deprojected bar lengths ($a_{\rm bar}$) in our bright S0 Coma core sample are very similar to those of S0s in the Virgo cluster (E11). We explore the comparison of the bar and disk properties as a function of environment density in more detail below.

4.3.7 Properties of disks and bars in the Coma core

We compare our sample of Coma cluster core S0s to the properties of S0s in less dense environments, namely to those in the intermediate-density Abell 901/902 cluster system ($z \sim 0.165$; M09) and those in the low density Virgo cluster ($z \sim 0.005$; E11).

Figure 4.14 shows the distributions of (a) the galaxy disk R_{25} (the isophotal radius where $\mu_{\rm B}$ reaches 25 mag arcsec^{-2}), (b) bar semi-major axis $a_{\rm bar}$, measured at the peak bar ellipticity $e_{\rm bar}$ for all bars identified through ellipse fitting (ER+ES), (c) the $a_{\rm bar}/R_{25}$ ratio, and (d) peak bar ellipticity $e_{\rm bar}$ for the Coma, Abell 901/902, and Virgo (E11) S0 samples. R_{25} values

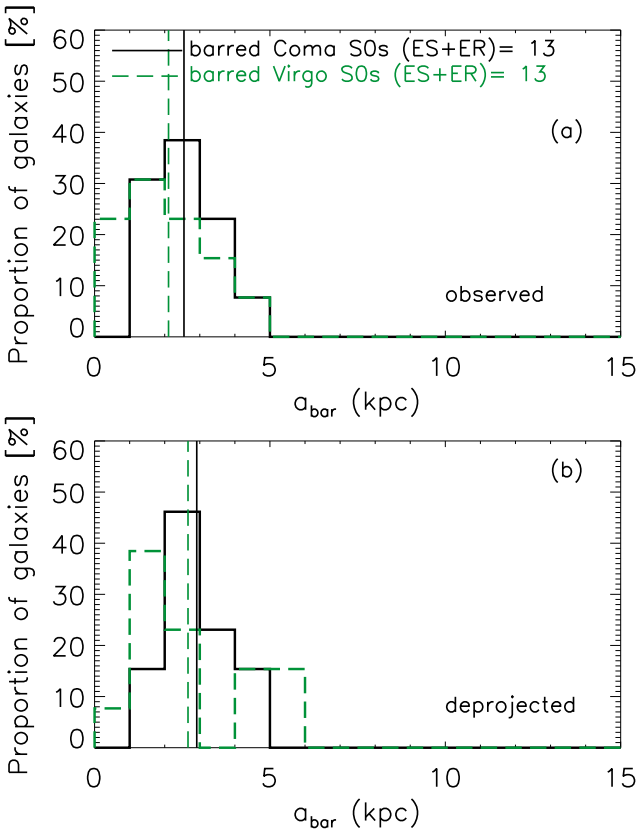

Figure 4.13 Comparison of the observed **(a)** and deprojected **(b)** bar semi-major axis $a_{\rm bar}$ distributions for our sample of barred bright Coma core S0s and those in Virgo from Erwin et al. (in prep.). For both samples, the distributions include barred galaxies detected through the strict ellipse-fitting criteria as well as the relaxed criteria (§ 4.3.2.2). The vertical lines show the mean values for each distribution. We do not find a significant difference in observed and deprojected bar size between Coma and Virgo S0s.

for the E11 Virgo sample are from the RC3. R_{25} for the Coma sample is estimated by ellipse fitting the galaxies on the ACS F475W images, which approximately correspond to SDSS g band. We calibrate the radial profiles of surface brightness to mag/arcsec^2, then convert them from $\sim$ g band (AB) to B mag arcsec^{-2} (Vega) using Equation 4.2. For two galaxies, we could not measure R_{25} radius because a good fit could not be obtained of the outer disk of the galaxy due to the presence of a close companion. For the M09 Abell 901/902 sample, R_{25} is calculated from the absolute $M_{\rm B}$ magnitudes according to

$$log(\frac{R_{25}}{kpc}) = -0.249 \times M_{\rm B} - 4.00, \tag{4.7}$$

from Schneider (2006). This formula is derived from an empirical relation measured for local spirals. To double-check its validity, we use it to calculate R_{25} radii for the Virgo S0s, where we already know R_{25} from RC3. Comparing the calculated values with those from RC3 confirms that the measured values from RC3 do follow the above relation, however it under-predicts the true R_{25} by $\sim$ 1.6 kpc on average. All three samples have similar bar and disk properties, but the bar semi-major axis and disk R_{25} distributions for Abell 901/902 S0s have a tail to larger values. This tail corresponds to the tail of brighter S0s present in the Abell 901/902 sample. The mean values of R_{25} for the Coma, Abell 901/902, and Virgo S0s are 6.5$\pm$1.3 kpc, 5.9$\pm$2.8 kpc, and 5.0$\pm$2.0 kpc, respectively. The Abell 901/902 and Virgo S0s have similar mean $a_{\rm bar}/R_{25}$ ratios of $\sim$ 0.4$\pm$0.16, although the range in values is large ($\sim$ 0.1–0.9). Coma S0s have a slightly lower mean $a_{\rm bar}/R_{25} =$ 0.35$\pm$0.12. An $a_{\rm bar}/R_{25}$ ratio

of $\sim 0.3\pm0.2$ has also been found for field galaxies averaged over all Hubble types (e.g., MJ07, Menendez-Delmestre et al. 2007) and for S0 galaxies (Erwin 2005). We note that the range of $a_{\rm bar}/R_{25}$ spanned by the three samples is quite large ($\sim$ 0.1–0.9), however although our number statistics are small, this range is similar to that found for local field galaxies in MJ07.

The observed bar ellipticities we find for S0s in the Coma cluster as well as those for S0s in Virgo and Abell 901/902 are skewed toward lower values (e.g., mean $e_{\rm bar} \sim$ 0.3–0.4) compared to the bar ellipticities in samples dominated by intermediate- to late-type galaxies (e.g., MJ07; BJM08; mean $e_{\rm bar} \sim$ 0.5–0.7). This difference could be intrinsic (i.e., the bars in S0 galaxies are really less elliptical than those in later Hubble types), or it could be due to the dilution by the bright bulges of the isophotes crossing the end of the bar, where the ellipticity is measured (see § 4.3.2.2). This effect has been demonstrated by (Gadotti, 2008).

4.3.8 Discussion: implications for the evolution of S0 bars and disks as a function of environment density

What do our results imply for the evolution of bars and disks in bright S0 galaxies as a function of environment? We first recapitulate our results. Using three detection methods (traditional ellipse fit criteria, relaxed ellipse fit criteria, and visual classification), we found an optical bar fraction of 50±11%, 65±11%, and 60±11%, respectively for our sample of bright ($M_{\rm V} \lesssim -18$) S0 galaxies in the central region of the Coma cluster (§ 4.3.4). We find that

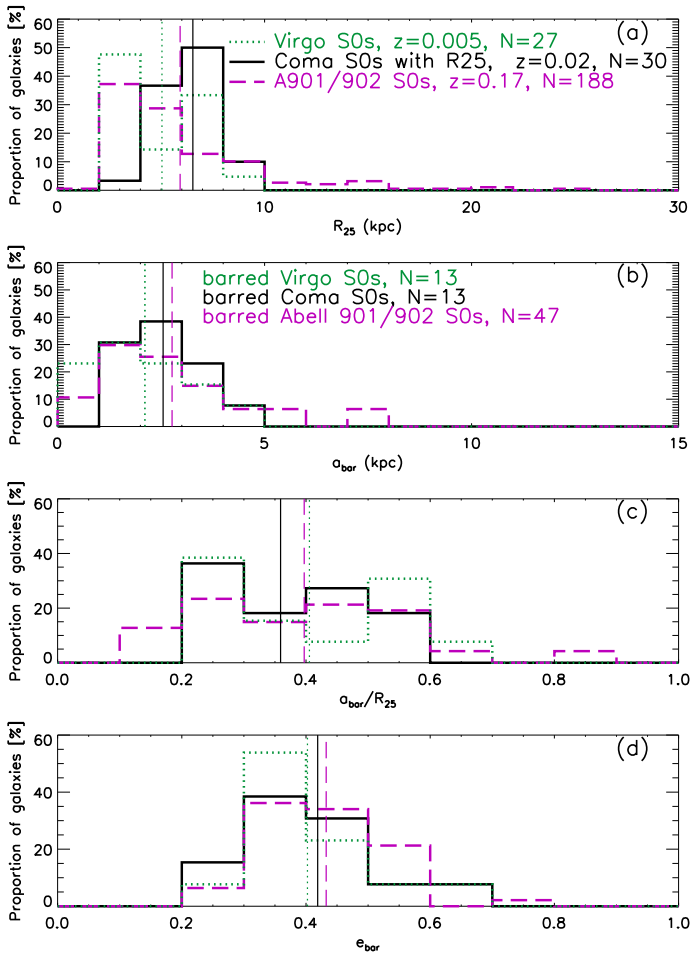

Figure 4.14 Distributions of **(a)** disk R_{25} (the isophotal radius where $\mu_{\rm B}$ reaches 25 mag arcsec^{-2}), **(b)** bar semi-major axis $a_{\rm bar}$, measured at the peak bar ellipticity $e_{\rm bar}$ for all bars identified through ellipse fitting (ER+ES), **(c)** $a_{\rm bar}/R_{25}$ ratio, and **(d)** peak bar ellipticity $e_{\rm bar}$ for the Coma S0 sample (solid black) and the comparison samples of S0s from the intermediate-density cluster system Abell 901/902 (dashed pink) and the low-density Virgo cluster (dotted green). R_{25} values for Coma and Abell 901/902 S0s are derived as described in § 4.3.7, while R_{25} for Virgo galaxies are from the RC3. The vertical lines show the mean values for each distribution. All three samples have similar mean bar and disk properties, but the bar semi-major axis and disk R_{25} distributions for Abell 901/902 S0s have a tail to larger values.

the bar fraction and properties (e.g., $e_{\rm bar}$, $a_{\rm bar}$) *in bright S0 galaxies* derived through all three of the above methods do not show a statistically significant variation (greater than a factor of ~ 1.3) between the dense central regions of Coma ($n \sim 10{,}000$ gal/Mpc^3), the intermediate-density Abell 901/902 clusters at $z \sim 0.165$ ($n \sim 1000$ gal/Mpc^3), and the low-density Virgo cluster ($n \sim 300$gal/Mpc^3; Table 4.3). We note that there is a hint that the mean bar fraction may show a slight increase as a function of environment density toward the dense core of the Coma cluster (Fig. 4.11), however given the error bars, we cannot say whether this trend is significant. Below, we explore what our results may imply for the formation and evolution of bars.

It has long been known that DM halo properties influence bar formation and evolution. At high redshifts (e.g., $z \sim 5$–8), recent theoretical studies of galaxy evolution using cosmological initial conditions find that bars are triggered by the triaxiality of DM halos and the asymmetric DM distribution as a whole (Romano-Díaz et al. 2008; Heller et al. 2007). These early bars are gas rich, and quickly decay. Subsequent bar generations form and are destroyed during the major-merger epoch (e.g., $z \sim 2$–4) due to the rapidly-changing potentials and gas dissipation associated with major mergers (Romano-Díaz et al. 2008). Although DM halos at early times can trigger bar formation due to their triaxiality, this triaxiality is diluted as disks and other central components form. The DM halos become more symmetric, on a timescale that is a function of mass (e.g., Dubinski 1994; Kazantzidis et al. 2004; Heller et al. 2007). By $z \sim 1$ disks have also become more massive and stable. Simulations

find that large-scale stellar bars forming at around this epoch are long-lived (Romano-Díaz et al. 2008; Heller et al. 2007). Interestingly, new observational results find that the bar fraction for the most massive disks ($M_* > 10^{11} M_\odot$) does not change between $z \sim 0.6$ and 0.2 (Cameron et al. 2010). However, the picture is complicated by the fact that for intermediate-mass disk galaxies ($M_* = 10^{10.5}$–$10^{11} M_\odot$), the bar fraction builds up by a factor of two over that redshift range. In addition, at $z \sim 0$, the bar fraction and properties are a non-monotonic function of the host galaxy properties, such as stellar mass, luminosity, color, Hubble type, and SF history (BJM08; M09; Aguerri et al., 2009; Barazza et al., 2009; Weinzirl et al., 2009; Laurikainen et al., 2009; Gadotti, 2011; Nair & Abraham, 2010b).

The picture above does not directly discuss environmental effects. In fact, there are still few theoretical and observational studies addressing this aspect of bar evolution. However, increasingly the emerging picture is suggesting that the frequency and properties of bars do not appear to be a sensitive function of environment (van den Bergh 2002; Aguerri et al. 2009; M09; Barazza et al. 2009; Cameron et al. 2010; although see Giuricin et al. 1993 and Elmegreen et al. 1990).

How do the above results make sense in light of many theoretical studies that show that galaxy interactions can trigger bars in unbarred galaxies (e.g., Noguchi, 1988; Mihos & Hernquist, 1996)? We present a tentative picture below, considering the competing effects present in galaxy clusters. If a disk galaxy is sufficiently dynamically cold (i.e., Toomre $Q \lesssim 1.5$), it is susceptible

to non-axisymmetric $m = 2$ instabilities (e.g., bars) whether spontaneously induced (e.g., Toomre, 1981; Binney & Tremaine, 1987) or tidally induced (e.g., Noguchi, 1988; Hernquist, 1989; Heller & Shlosman, 1994; Mihos & Hernquist, 1996; Jogee, 2006). The effect of the interaction depends on the geometry (i.e., prograde or retrograde encounter), with retrograde encounters having little to no effect on an already existing bar (e.g., Gerin, Combes, & Athanassoula 1990; Steinmetz & Navarro 2002; Romano-Díaz et al. 2008; Aguerri & González-García 2009).

At $z < 1.5$, as clusters assemble and field galaxies fall into the existing cluster potential, let us now ask how the fraction and properties of bars in S0s might be expected to differ from the field environment. In a rich cluster, where the projected galaxy number density (n) and galaxy velocity dispersion (σ) is high, the timescale for close interactions (or collision timescale, $t_{\rm coll}$) will be short. We can estimate this timescale using:

$$t_{\rm coll} = \frac{1}{n\sigma_{\rm gal}A}, \tag{4.8}$$

where n is the galaxy number density, $\sigma_{\rm gal}$ is the galaxy velocity dispersion, and A is the cross-section for close interactions defined as

$$A = \pi f(2r_{\rm gal})^2. \tag{4.9}$$

We assume f is unity, $r_{gal} \sim 10$ kpc. For the Coma core $\sigma_{\rm gal} \sim 900$ km/s, and $n \sim 10{,}000$ gal/Mpc^3 (The & White 1986) giving a short timescale for close interactions $t_{\rm coll} \sim 90$ Myr.

However, although these close galaxy-galaxy interactions are frequent in a rich cluster, the large galaxy velocity dispersions present mean that each single encounter will be a *high speed one*. Unlike single slow, strong encounters, a single high-speed encounter will typically not induce a large amount of tidal damage and not lead to major mergers. As a result, three factors may make it difficult for new bars to be induced in disk galaxies in a cluster. Firstly, single high-speed encounters may not be as effective in inducing bars as slow, strong encounters, because the timescale over which gravitational torques act is short. Secondly, over time, the cumulative effect of many high-speed and weak encounters (galaxy harassment), can tidally heat disks (e.g., Moore et al. 1996; Aguerri & González-García 2009), making such disks dynamically hot (with Toomre $Q > 1.5$), and thus less susceptible to bar instabilities. Finally, in a cluster environment, the accelerated star formation history (e.g., Balogh et al. 2004, Blanton et al. 2005; Hogg et al. 2003) as well as physical processes such as ram pressure stripping (Gunn & Gott 1972; Larson et al. 1980; Quilis et al. 2000) will make S0 disks gas-poor, thus making them less bar-unstable. We therefore speculate that these three factors, namely the predominance of high speed encounters over slow ones, the tidal heating of S0 disks, and the low gas content of S0s in rich clusters, make it difficult for many new bars to be induced in S0 disks as they infall from a field-like to a cluster-like environment. This scenario may explain, at least in part, our findings that there is no strong variation in the optical bar fraction of S0s across the range of low density to high density environments characterized by Coma, Virgo, and Abell 901/902

in our study, as well as claims by other studies that there is no difference in the bar fraction between clusters and the field (van den Bergh 2002, Aguerri et al. 2009, Barazza et al. 2009; M09).

We note that it is possible that in rich clusters, the above effects, particularly the tidal heating, may cause existing bars to weaken. However, this effect is hard to robustly demonstrate observationally as the measured bar ellipticity is diluted by relatively large bulges in S0s (which dominate the disk population in clusters), while in the field, the disk population is dominated by spirals where such a dilution is not as severe (see § 4.3.7).

It is also important to note that the arguments above, which explain why the bar fraction might not be greatly enhanced in rich clusters compared to the field, would lead to a rather different prediction for how the bar fraction in groups would compare to that in the field. In a group, the number density is moderately high ($n \sim 10$) but the galaxy velocity dispersions are typically low ($\sigma \sim 100$; Tago et al. 2008). Therefore slow, strong encounters are expected to be frequent in groups. Such encounters are likely to induce extra bars in disk galaxies compared to the field, particularly given the fact that the disks will not be stripped of their cold gas in groups as they would in rich clusters. In this context, we note that indeed higher bar fractions have been reported for early-type galaxies in binary pairs (Elmegreen et al. 1990) and early-type galaxies that are disturbed/interacting (Varela et al. 2004).

4.4 Bars and disk features in Coma dwarfs

In addition to investigating bars in high-mass galaxies, we also take advantage of the exquisite resolution of the ACS ($\sim$ 50 pc at the distance of Coma) to search for bars and other disk features (e.g., spiral arms, edge-on disks) in the numerous dwarf galaxies in the central regions of the Coma cluster. Are some of these galaxies the remnants of late-type spirals that have gone through processing in a dense cluster environment? In Virgo, some early-type dwarfs are known to host features (e.g., lenses, bars, spiral arms; Sandage & Binggeli, 1984; Binggeli & Cameron, 1991; Jerjen et al., 2000; Barazza et al., 2002; Lisker et al., 2006b, 2007; Lisker & Fuchs, 2009) suggesting the presence of a disk. Not only can such features provide clues to the formation history of these systems, but the presence or absence of bar structures has implications for the conditions necessary for bar formation and growth in galaxies.

4.4.1 Identifying dwarf galaxies

As outlined in § 4.2, we use a magnitude cut at $M_{\mathrm{I}(814)} = -18.5$ (AB mag), (roughly corresponding to $M_{\mathrm{V}} = -18$ Vega mag) to separate dwarf and normal galaxies. A montage of some of the faint, low-mass dwarfs in our Coma core sample is shown in Fig. 4.15. Fig. 4.16a shows the distribution of absolute magnitude $M_{\mathrm{I}(814)}$ of the galaxies in the faint dwarf sample. Fig. 4.16b shows where the dwarf galaxies lie on a plot of the μ_{e} (the surface brightness at R_{e}) vs. absolute magnitude $M_{\mathrm{I}(814)}$. Effective radii and μ_{e} are from Hoyos et al. (2011), derived through single-component Sérsic fits.

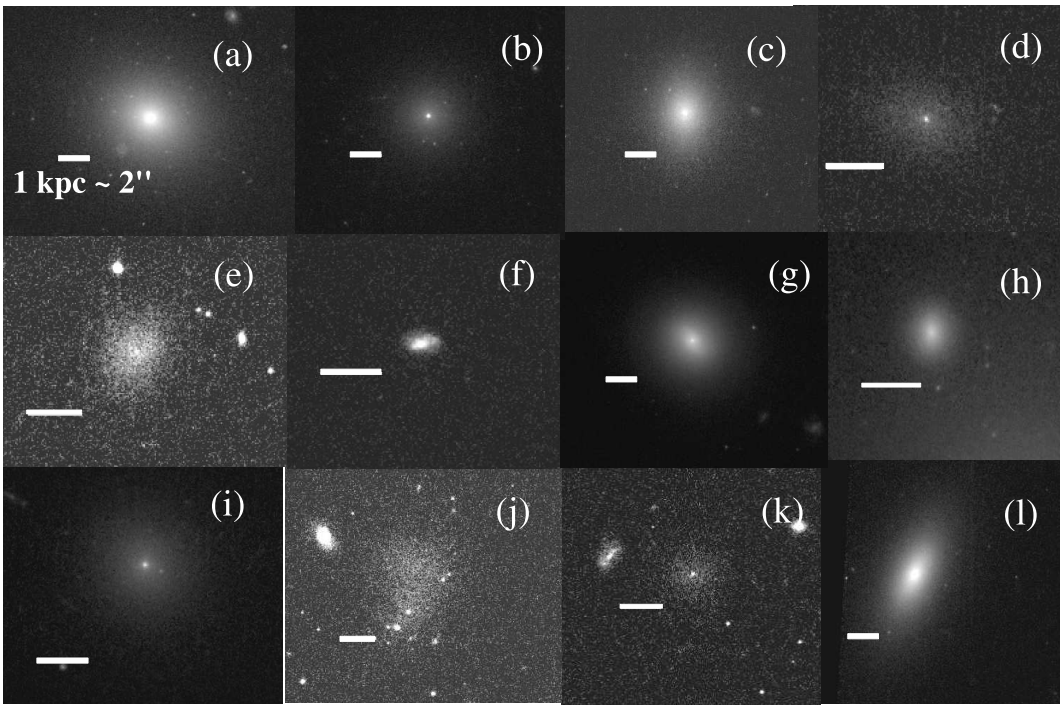

Figure 4.15 Examples of some of the faint, low-mass dwarfs in the Coma core sample. The scale bars are 1 kpc. The galaxies shown are: (a) COMAi13011.143p28354.92, (b) COMAi13025.977p28344.68, (c) COMAi13026.152p28032.02, (d) COMAi13029.853p28400.85, (e) COMAi13030.027p28135.08, (f) COMAi13039.068p28437.52, (g) COMAi13041.192p28242.38, (h) COMAi13047.670p28533.95, (i) COMAi13048.045p28557.42, (j) COMAi13050.590p28356.56, (k) COMAi13052.942p28435.86, (l) COMAi13030.949p28630.18.

Prior to applying the unsharp masking technique (§ 4.4.2) on the dwarf sample, we pick out good candidates through a cut in surface brightness ($\mu_e <$ 25 mag arcsec^{-2}) and radius ($R_{90} > 100$ pc). These cuts remove very low surface-brightness objects, and those where we are unlikely to resolve disk structure. We choose a size cut at $R_{90} > 100$ pc, which is twice the ACS PSF at the distance of Coma. Out of the 417 dwarf galaxies, we find 333 dwarfs that satisfy these criteria. The μ_e vs. $M_{I(814)}$ distribution of these galaxies is plotted with yellow triangles in Fig. 4.16b.

4.4.2 Identifying bars and other disk features in dwarfs

In many dwarf galaxies disk features may not be readily apparent by eye (or traditional quantitative methods such as ellipse fitting) because their amplitude is very low and is overwhelmed by the smooth light from the galaxy. Which method is sensitive enough to detect faint spiral/bar structure in such systems? Jerjen et al. (2000) used residuals from subtracting the azimuthally-averaged light profile of the galaxy from the original image to discover hidden spiral features in IC 3328 with deep VLT observations. They analyzed the spiral structure using Fourier expansion, finding that the amplitude of the spiral is only $\sim$ 3 to 4%. However, upon further analysis of a larger sample of 20 Virgo dwarfs, Barazza et al. (2002) find that some spiral or bar-resembling residuals may be artifacts from the combination of the increasing ellipticity and twisting isophotes (due to triaxiality) present in these galaxies and not actual spiral structure. Fourier decomposition is similarly unsuccessful in

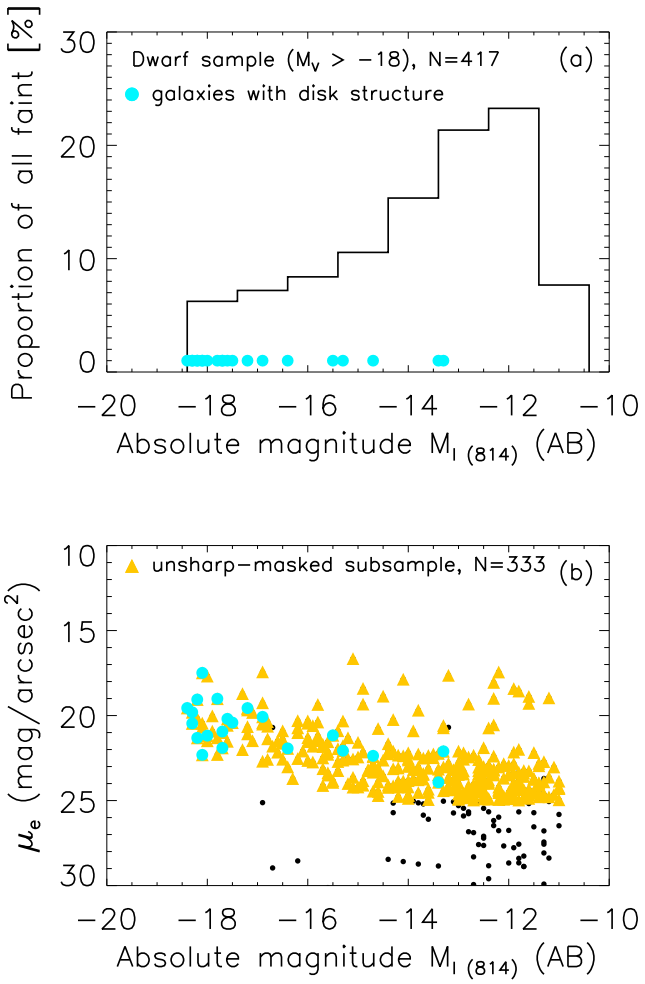

Figure 4.16 **(a)** Absolute magnitude ($M_{\mathrm{I}(814)}$) distribution and **(b)** plot of surface brightness vs. absolute magnitude ($M_{\mathrm{I}(814)}$) of the 417 galaxies in the Coma faint sample. The cyan points show the values for the 21 faint galaxies where we find disk structure (bar, spiral, edge-on disk) through unsharp masking. Most (76%) of the objects where we find disk structure have $M_{\mathrm{I}(814)} \leq -16$.

many galaxies. Barazza et al. (2002) find that a much better method seems to be unsharp masking (e.g., Schweizer & Ford, 1985; Mendez et al., 1989; Buta & Crocker, 1993; Colbert et al., 2001; Erwin & Sparke, 2003). In this method, no assumptions about the light profile/inclination of the galaxy are necessary. Recently, Lisker et al. (2006a) also successfully employed unsharp masking on $\sim$ 470 Virgo dwarfs to look for evidence of bar/spiral structure. Graham et al. (2003) discovered two dwarf galaxies with spiral structure in the Coma cluster using unsharp masking as well as subtracting a symmetrical model to reveal non-symmetrical disk features (one of these galaxies is COMAi125937.988p28003.56 in Table 4.4, while the other is not covered by the Coma ACS Treasury survey). Chilingarian et al. (2008) use unsharp masking to find disk features in dwarf galaxies in Abell 496. We therefore use the unsharp masking method to seek out bar (or spiral) structures in the Coma cluster core dwarf sample.

We perform unsharp masking for the 333 dwarf galaxies that fit the criteria outlined in § 4.4.1. First, we smooth the galaxy images by convolving with a Gaussian using the IRAF task *GAUSS*. Then we divide the original galaxy image by the smoothed image. We choose the Gaussian smoothing kernel size to be $\sim$ 25 pixels, corresponding to $\sim$ 625 pc for our galaxies. We also try a range of smoothing lengths from $\sim$ 15–45 pixels ($\sim$ 375–1125 pc) for a subsample of the galaxies and find no substantial change in the results. A point made by Lisker et al. (2006) is that in some cases, it is desirable to use an elliptical smoothing aperture matched to the outer ellipticity and PA

of the galaxy, in order to avoid spurious detections that resemble an edge-on disk. For this reason, in all cases where we suspect that the galaxy host an inclined/edge-on disk, we also perform the unsharp masking using an elliptical PSF to ensure that the structures found are not spurious detections.

We find bars and/or spiral arms in 13 galaxies out of the 333 dwarfs in the unsharp-masked subsample. An additional eight galaxies show evidence of an inclined disk (or ambiguous inclined disk or bar). The galaxies where we find structure are listed in Table 4.4. Fig. 4.17 shows examples of the residuals due to different types of structures: (a) spiral arms only, (b) bar and spiral arms, (c) inclined disk, (d) bar and/or spiral, (e) ambiguous bar or inclined disk embedded in a stellar halo. The galaxies with disk structure are overplotted as cyan points in Fig. 4.16. Most (76%) of the galaxies where we find disk structure are brighter than $M_{\mathrm{I}(814)} = -16$ (AB mag). We discuss the possible implications of these results below.

4.4.3 Discussion: barred dwarf galaxies in the Coma core

Using visual inspection and unsharp masking we find only 13 galaxies with bars and/or spiral arms in our Coma core dwarf subsample of 333 galaxies with $\mu_{\mathrm{e}} < 25$ mag arcsec^{-2} and $R_{90} > 100$ pc. Does this result imply that faint/dwarf galaxies with disks are very rare within the Coma population, or rather that any existing disks in these galaxies are too dynamically hot to be unstable to disk instabilities?

Studies have long been finding early-type dwarf galaxies with spiral/bar

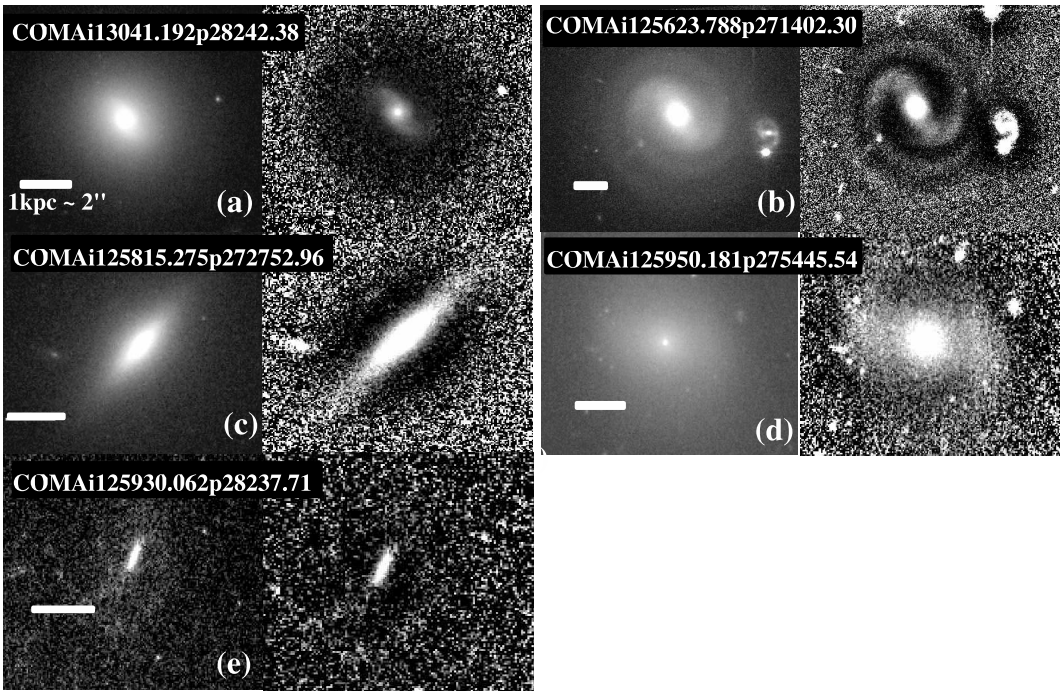

Figure 4.17 Examples of five galaxies from the dwarf ($M_{\rm V} > -18$) sample highlighting the different types of disk structure that we find through unsharp masking: **(a)** spiral arms, **(b)** bar+spiral arms, **(c)** edge-on disks, **(d)** bar and/or spiral structure, and **(e)** ambiguous bar/edge-on disk (§ 4.4.2). We use a Gaussian smoothing kernel size of $\sim$ 25 pixels, corresponding to $\sim$ 625 pc at the distance of Coma. The original *HST* images are shown in the left panels and the corresponding residuals highlighting the disk structure are on the right. The scale bars show 1 kpc.

structure in Virgo and Fornax (e.g., Sandage & Binggeli 1984; Binggeli & Cameron 1991; Jerjen et al. 2000; Barazza et al. 2002; Lisker et al. 2006; Lisker et al. 2007; Lisker & Fuchs 2009). Lisker et al. (2006) search through 476 Virgo early-type dwarfs and find unambiguous stellar disk structure (bar/spiral) in 14 of them, while another 27 have probable or possible disk features. Some authors have speculated that anywhere from 5% to 50% of Virgo early-type dwarfs have disk structure, depending on the magnitude range under scrutiny (Lisker et al. 2006; Lisker & Fuchs 2009).

Approaching the search for disks in early-type dwarfs a different way, Aguerri et al. (2005) investigate a sample of galaxies in Coma with $-18 \leq M_{\rm B} \leq -16$ and classify them into two types dE or dS0 depending on their surface brightness profile. Galaxies whose surface brightness profiles are well fitted by a single Sérsic law are classified as dEs, and those with surface brightness profiles fitted with a Sérsic plus exponential profile are classified as dS0s. Aguerri et al. (2005) find that about 30% of their Coma dwarf sample cannot be fitted well by a single Sérsic law, suggesting that early-type dwarfs with disks may not be scarce in Coma. Graham & Guzmán (2003) found evidence for outer disks in three out of a sample of 18 Coma early-type dwarfs, modeling the surafce brightness profiles using a Sersic function in combination with either a central point source or a resolved central Gaussian component using high-resolution HST images.

While it is still unclear whether all early-type dwarfs with disk structure represent a distinct class of galaxies that are the product of a single formation

mechanism, one plausible scenario is that they are formed through processing of faint, late-type spirals and irregulars in cluster environments (e.g., Kormendy, 1985; Lin & Faber, 1983; Graham et al., 2003; Lisker et al., 2006a). This processing includes the loss of their gas through ram-pressure stripping (e.g., Gunn & Gott 1972) as well as the cumulative effects of harassment in a cluster environment (e.g., Moore et al. 1996). The simulations of Mastropietro et al. (2005) have shown that indeed late-type spirals can be reprocessed into early-type dwarfs through cluster processes (such as harassment), and that these dwarfs do retain their stellar disk structure. On the other hand, observations of a small number of isolated early-type dwarf galaxies (e.g., Fuse, 2008; Hernández-Toledo et al., 2010) argue against cluster transformation processes as the sole explanation for the formation of these objects.

We find evidence of only 13 dwarfs hosting disk instabilities (bar and/or spiral arms) in our unsharp-masked subsample of 333 dwarfs. Our result implies that although it is possible that as many as $\sim 30\%$ of dwarf galaxies in Coma may have a disk component (Aguerri et al. 2005), the majority do not have the necessary conditions to form or maintain bar and spiral instabilities, namely a disk that is dynamically cold. This result is consistent with previous studies, showing a paucity of *thin* disks in lower-luminosity dwarf galaxies (Sánchez-Janssen et al., 2010; Yoachim & Dalcanton, 2006).

4.5 Summary

We use ACS F814W images from the *Hubble Space Telescope* ACS Treasury survey of the Coma cluster at $z \sim 0.02$ to study the fraction and properties of barred galaxies in the central region of Coma, the densest environment in the nearby Universe. The available data span 274 arcmin^2, where approximately 75% of the data are within 0.5 Mpc of the cluster center, and contain thousands of sources down to a limiting magnitude of $I = 26.8$ mag in F814W (AB mag). We initially select 469 cluster members and split the sample with a magnitude cut at $M_{\rm V} \lesssim -18$ (Vega mag). Using this magnitude cut, we investigate two different regimes: (1) the fraction and properties of bright $M_{\rm V} \lesssim -18$ S0 galaxies and (2) the presence of bars and other disk features (e.g., bars and spiral arms) in faint/dwarf galaxies in the Coma core. Our results for the two populations are described below.

(1) For S0 galaxies: We select a sample of 32 bright S0 galaxies based on visual classification supplemented by multi-component decompositions in ambiguous cases (§ 4.3.1). After discarding 12 highly-inclined galaxies, we identify and characterize bars in the remaining 20 moderately-inclined S0s using three methods: ellipse fits where the bar is detected through strict criteria (the peak bar ellipticity $e_{\rm bar}$ is required to be a global maximum in the radial profile of ellipticity); ellipse fits where the bar is detected through relaxed criteria (which do not require the peak bar ellipticity $e_{\rm bar}$ to be a global maximum); and visual classification. We find: The optical bar fraction for our bright S0 sample is: 50± 11%, 65± 11%, and 60± 11% based on ellipse

fits with traditional and relaxed criteria, and visual classification, respectively (Table 4.2).We compare to results from studies in less dense environments (Abell 901/902 and Virgo) and find that the bar fraction, as well as the mean quantitative properties of the S0 bars and disks (e.g., R_{25}, $a_{\rm bar}$, $e_{\rm bar}$) do not show a statistically significant variation, within the error bars, for samples of matched S0s in environment densities ranging from $n \sim 300$ gal/Mpc^3 (Virgo), $n \sim 1000$ gal/Mpc^3 (Abell 901/902), and $n \sim 10{,}000$ gal/Mpc^3 (Coma), with high galaxy velocity dispersions $\sigma \sim 800$ km/s (Table 4.3, Fig. 4.14). We note that there is a hint that the mean bar fraction may show a slight increase as a function of environment density toward the dense core of the Coma cluster (Fig. 4.11), however given the error bars, we cannot say whether this trend is significant. We speculate that the bar fraction among S0s is not dramatically enhanced in rich clusters compared to low density environments because in clusters, where the velocity dispersions are large, high-speed encounters dominate over slow, strong encounters (see § 4.3.8). In addition, S0s in rich clusters are expected to be gas poor and dynamically stable, due to ram pressure stripping, accelerated star formation, and harassment. The combination of these effects precludes an enhancement in the bar fraction for S0 galaxies in cluster environments compared to the field. Our results are in agreement with recent observational studies which find no difference in the fraction of barred galaxies with environment density over all Hubble types.

(2) For faint/dwarf galaxies: We select a sample of 417 galaxies fainter than $M_{\rm I(814)} = -18.5$ (AB mag; § 4.4.1) where we utilize our ~ 50 pc res-

olution to look for disk structures such as bars and spiral arms using visual classification of unsharp-masked images. After applying unsharp masking to a subsample of 333 dwarfs ($\mu_e < 25$ mag arcsec^{-2}, $R_{90} > 100$ pc; § 4.4.2), we find only 13 dwarf galaxies with a bar and/or spiral arms, and an additional eight galaxies where an inclined disk may be present (Fig. 4.17). These results suggest that either disks are not common in these galaxies in the Coma cluster core, or that any disks present are too hot to form instabilities.

Table 4.1. Optically barred bright ($M_{\rm V} \lesssim -18$) S0s.

Bar ID	Galaxy ID	RA	DEC	$M_{\rm I(814)}$ (AB mag)	Bar detection method	$e_{\rm bar}$ obs	$e_{\rm bar}$ dep	$a_{\rm bar}$ obs (kpc)	$a_{\rm bar}$ dep (kpc)
(1)	(2)	(3)	(4)	(5)	(6)	(7)	(8)	(9)	(10)
B1	COMAi125710.767p272417.44	194.29486	27.404846	-20.1	ES, ER, V	0.35	0.26	2.97	2.99
B2	COMAi125833.136p272151.77	194.63806	27.364383	-20.0	ES, ER, V	0.68	0.54	3.19	3.52
B3	COMAi125928.728p28225.90	194.86970	28.040531	-19.7	ES, ER	0.49	0.40	2.26	2.44
B4	COMAi125929.956p275723.26	194.87481	27.956462	-21.1	ES, ER, V	0.47	0.51	4.36	5.04
B5	COMAi125946.775p275825.88	194.94490	27.973856	-20.6	ES, ER, V	0.39	0.70	2.22	2.82
B6	COMAi125956.707p275548.62	194.98628	27.930173	-19.9	ES, ER, V	0.55	0.46	3.42	4.00
B7	COMAi13022.156p28249.08	195.09231	28.046968	-20.6	ES, ER, V	0.37	0.46	1.92	2.23
B8	COMAi13038.731p28052.22	195.16137	28.014507	-20.3	ES, ER, V	0.47	0.31	3.57	3.77
B9	COMAi13042.753p275816.88	195.17814	27.971355	-21.3	ES, ER, V	0.25	0.31	1.46	1.55
B10	COMAi13042.833p275746.98	195.17846	27.963052	-20.3	ES, ER, V	0.43	0.46	2.48	2.64
B11	COMAi125930.825p275303.42	194.87843	27.884283	-21.1	ER, V	0.33	0.35	1.99	2.33
B12	COMAi13017.020p28350.10	195.07092	28.063917	-19.0	ER, V	0.29	0.40	1.14	1.45
B13	COMAi13027.971p275721.54	195.11654	27.955985	-20.1	ER, V	0.31	0.47	2.09	2.79

Note. — (1) Bar ID; (2) Galaxy ID as given in the Coma Treasury survey DR2 (Hammer et al. 2010); (3) RA (J2000); (4) DEC (J2000); (5) $M_{\rm I(850)}$ absolute magnitude in AB mag; (6) Bar detection method: 'ES' - strict ellipse fit criteria (§ 4.3.2.2), 'ER' - relaxed ellipse fit criteria (§ 4.3.2.2), and 'V' - visual classification on direct image (§ 4.3.3; (7) Observed peak bar ellipticity $e_{\rm bar}$; (8) Deprojected peak bar ellipticity; (9) Observed bar semi-major axis $a_{\rm bar}$ measured at $e_{\rm bar}$; (10) Deprojected bar semi-major axis (§ 4.3.7).

Table 4.2. Optical bar fraction for bright ($M_{\rm V} \lesssim -18$) S0s based on different methods.

Method	Unbarred	Barred	$f_{\rm bar,opt}$
Ellipse fit, strict	10	10	50±11%
Ellipse fit, relaxed	7	13	65±11%
Visual classification	8	12	60±11%

Note. — optical bar fraction for the 20 moderately inclined ($i < 60°$) bright ($M_{\rm V} \lesssim -18$) S0 galaxies. Barred galaxies are characterized through: (1) ellipse fitting using the strict criteria (where $e_{\rm bar}$ is required to be a global maximum in the ellipticity profile), (2) ellipse fitting using relaxed criteria ($e_{\rm bar}$ can be a local maximum), and (3) visual classification.

Table 4.3. Optical bar fraction for bright ($M_V \lesssim -18$) S0s in different environments.

Study (1)	Environment (2)	Number density (gal/Mpc^3) (3)	Velocity dispersion (km/s) (4)	S0 f_{bar} for $M_V \lesssim -18$ (5)
Bars identified through ellipse fitting (strict criteria; § 4.3.2.2)				
this work	Coma central region, $z \sim 0.02$	10,000	900[a]	50±11% (10/20)
M09[b]	Abell 901/902 clusters, $z \sim 0.165$	1000	800–1200[c]	39±5% (38/98)
E11	Virgo, $z \sim 0$	300	400–750[d]	44±14% (12/27)
Bars identified through ellipse fitting (relaxed criteria; § 4.3.2.2)				
this work	Coma central region $z \sim 0.02$	10,000	900	65±11% (13/20)
M09[b]	Abell 901/902 clusters, $z \sim 0.165$	1000	800–1200	48±5% (47/98)
E11	Virgo, $z \sim 0$	300	400–750	48±14% (13/27)
Bars identified through visual classification				
this work	Coma central region, $z \sim 0.02$	10,000	900	60±11% (12/20)
T81[e]	Coma central region, $z \sim 0.02$	10,000	900	42±7% (19/45)
M09[b]	Abell 901/902 clusters, $z \sim 0.165$	1000	800–1200	55±5% (54/98)
E11[f]	Virgo, $z \sim 0$	300	400–750	59±9% (16/27)

Note. — T81: Thompson 1981; M09: Marinova et al. 2009; E11: Erwin et al. (in prep.)
(a) The & White (1986)
(b) We use a sub-sample from M09, with the criteria outlined in § 4.3.5.
(c) Heiderman et al. (2009)
(d) Binggeli et al. (1987)
(e) Bar classification is performed on ground-based KPNO plates.
(f) For this paper, visual classification is performed on the E11 sample by P.E., I.M., and S.J. using the criteria outlined in § 4.3.3.

Table 4.4. Galaxies in the faint ($M_V > -18$) sample where we find disk structure through unsharp masking.

Galaxy ID (1)	RA (2)	DEC (3)	Visit (4)	$M_{I(814)}$ (AB) (5)	Structure (6)
COMAi13030.949p28630.18	195.12895	28.10838	02	-17.6	inclined disk
COMAi13041.192p28242.38	195.17163	28.04510	08	-17.8	spiral
COMAi13018.883p28033.55	195.07867	28.00931	09	-18.1	bar
COMAi13013.398p28311.81	195.05583	28.05328	10	-17.7	inclined disk
COMAi13007.727p28051.91	195.03219	28.01441	10	-13.3	inclined disk
COMAi125930.062p28237.71	194.87525	28.04380	13	-13.4	bar/inclined disk
COMAi125904.792p28301.21	194.76997	28.05033	14	-18.3	bar
COMAi125911.545p28033.38	194.79811	28.00927	14	-18.2	inclined disk
COMAi125953.930p275813.76	194.97471	27.97048	18	-16.9	spiral
COMAi125937.988p28003.56	194.90827	28.00098	19	-18.0	bar + spiral
COMAi13035.418p275634.05	195.14758	27.94279	22	-17.7	bar
COMAi13024.823p275535.89	195.10342	27.92663	23	-18.2	bar + spiral
COMAi125950.181p275445.54	194.95909	27.91265	25	-17.5	bar
COMAi125820.533p272546.03	194.58555	27.42945	45	-18.3	spiral
COMAi125815.275p272752.96	194.56364	27.46471	45	-17.2	inclined disk
COMAi125814.969p272744.81	194.56237	27.46244	45	-15.5	bar + spiral
COMAi125825.308p271200.04	194.60545	27.20001	59	-18.4	bar + spiral
COMAi125623.788p271402.30	194.09912	27.23397	63	-18.1	bar + spiral
COMAi125638.099p271304.09	194.15875	27.21780	63	-16.4	bar
COMAi125845.297p274650.75	194.68873	27.78076	75	-15.3	bar/inclined disk
COMAi125845.906p274655.90	194.69126	27.78219	75	-14.7	bar/inclined disk

Note. — (1) Galaxy ID as given in the Coma Treasury survey DR2 (Hammer et al. 2010); (2) RA (J2000); (3) DEC (J2000); (4) *HST* visit number; (5) $M_{I(850)}$ absolute magnitude in AB mag; (6) type of disk structure detected through unsharp masking (see § 4.4.2).

Chapter 5

Summary, Discussion, and Implications

5.1 The importance of stellar bars as a driver of disk galaxy evolution

Evidence is building that since $z \sim 1$ major mergers have played a less important role in galaxy evolution, specifically in building bulges (e.g., Balcells et al., 2003; Laurikainen et al., 2007; Kormendy & Fisher, 2008; Graham & Worley, 2008; Weinzirl et al., 2009) and contributing to the cosmic star formation rate (SFR) density (e.g., Bell et al., 2005; Wolf et al., 2005a; Jogee et al., 2009; Robaina et al., 2009) than have minor mergers, smooth accretion (e.g., Brooks et al., 2009; Kereš et al., 2009; Dekel et al., 2009), and secular processes.

Stellar bars are the most efficient internal driver of evolution in disk galaxies, as they efficiently drive gas inflows and redistribute angular momentum in the baryons and dark matter (DM). As bar instabilities grow and evolve, they exchange angular momentum with other components of the galaxy such as the outer disk, DM halo, and bulge. Gas entering the density enhancement of the bar is subject to shocks (e.g., Regan et al., 1997), causing it to lose rotational support (e.g., Athanassoula, 1992b), and to be funneled radially by the torque of the bar. Inside corotation, the bar drives large gas inflows

to the central region of the galaxy. The resulting central dense gas concentrations ignite powerful starbursts (Schwarz, 1981; Elmegreen, 1994; Hunt & Malkan, 1999; Sakamoto et al., 1999; Jogee, 1999; Jogee et al., 2005; Sheth et al., 2005). In this way, bars are thought to build disky central components (Hohl, 1975; Kormendy, 1979; Combes & Sanders, 1981; Combes et al., 1990; Kormendy, 1993; Jogee, 1999; Jogee et al., 1999, 2005; Athanassoula, 2005), often called pseudobulges (Kormendy, 1993; Kormendy & Kennicutt, 2004). Boxy and peanut-shaped bulges observed in about 20–45% of edge-on galaxies (Shaw, 1987; Kuijken & Merrifield, 1995; Lütticke et al., 2000; Kormendy & Kennicutt, 2004) are related to bars and are the result of the bar being observed end-on (Combes & Sanders, 1981; Athanassoula & Misiriotis, 2002; Athanassoula, 2005; Bureau & Athanassoula, 2005) or caused by the bar vertical buckling instability or resonant heating in a bar observed edge-on (Combes & Sanders, 1981; Pfenniger & Friedli, 1991; Sellwood & Wilkinson, 1993; Berentzen et al., 1998; Athanassoula & Misiriotis, 2002; Athanassoula, 2005; Bureau & Athanassoula, 2005; Martinez-Valpuesta et al., 2006).

In the local universe, evidence for bar-driven secular evolution comes from observations that barred galaxies host larger central gas concentrations than unbarred galaxies (Sakamoto et al., 1999). Additionally, Hunt & Malkan (1999), Hao et al. (2009), and Laurikainen et al. (2004a) find that starburst galaxies have a higher incidence of bars than non-starburst galaxies, as would be expected in scenarios of bar-driven gas inflow to the central regions of galaxies, where the gas piles up and episodes of intense star formation are triggered.

Higher bar fractions have also been reported in Seyfert galaxies compared to non-active galaxies (Knapen et al., 2000; Laine et al., 2002; Laurikainen et al., 2004a, also see Jogee, 2006 and references therein). On the other hand, Hao et al. (2009) finds similar bar fractions for galaxies hosting acive galactic nuclei (AGN) and non-active galaxies, thus the question of whether bars play a role in fueling AGN remains controversial. Finally, metallicity gradients are shallower in barred than unbarred galaxies (Vila-Costas & Edmunds, 1992; Zaritsky et al., 1994; Martin & Roy, 1994; Ellison et al., 2011), suggesting that the bar redistributes material within the galaxy disk.

5.2 Field galaxies at low redshift

5.2.1 Observational results

Prior to a few years ago, most studies investigating the role of bar structures in galaxies focused on the average bar fraction over disks of all Hubble types (Eskridge et al., 2000; Knapen et al., 2000; Hunt & Malkan, 1999; Mulchaey & Regan, 1997; Laine et al., 2002; Laurikainen et al., 2004b; Block et al., 2004), although see Odewahn (1996). In addition, many studies used visual classification to identify and characterize bars, thus giving no quantitative measurements of their properties. As discussed in Chapters 1 and 2, for a long time, the definitive result on the optical bar fraction in the local universe came from visual classification of the galaxies in the RC3. In the RC3, over all disk galaxies (S0–Im), the visual optical bar fraction is 30% for strong bars (SB), and 30% for weak bars (SAB), giving 60% overall.

Recent studies have gone beyond RC3 and visual classification in several ways. First, quantitative methods are being used to reduce the level of subjectivity. Characterizing bars with methods such as ellipse fitting gives distributions of galaxy properties that may be compared objectively across galaxy samples of different environments (Chapters 3 and 4) and redshifts (Chapter 2 and §5.3). Specifically, in Chapter 2 (Marinova & Jogee, 2007), we present the distributions of bar size and strength (as characterized by the bar ellipticity e) for field galaxies in the local Universe of intermediate Hubble types (Sbc-Sc) and with $M_* \gtrsim 10^{10} M_\odot$ (Figs. 5.1 and 5.2). We find that most ($\sim$ 70%) bars have $a_{\rm bar} \leq 5$ kpc, and $\sim$ 50% of them cluster in the range 2 to 5 kpc. Galaxies of lower masses and later Hubble types, have even smaller bars (Kormendy, 1979; Erwin, 2005). Thus our results set constraints on the observability of bars at intermediate redshifts (see §5.3). In Chapters 3 and 4, we compare the quantitative bar and host disk properties of S0 galaxies in environments of different densities (Virgo, Abell 901/902, Coma; Fig. 5.3), finding that these properties remain similar over a range of galaxy number desities spanning over an order of magnitude ($n \sim$ 300–10,000 gal Mpc^{-3}).

Second, evidence is mounting that the bar fraction varies across galaxies of different Hubble types, and depends on the host galaxy properties, such as bulge-to-total ratio (B/T), luminosity, stellar mass, and color at a range of redshifts and environments.

Figure 5.4 summarizes the recent results from quantitative studies on the variation of the optical and NIR bar fraction as a function of Hubble type,

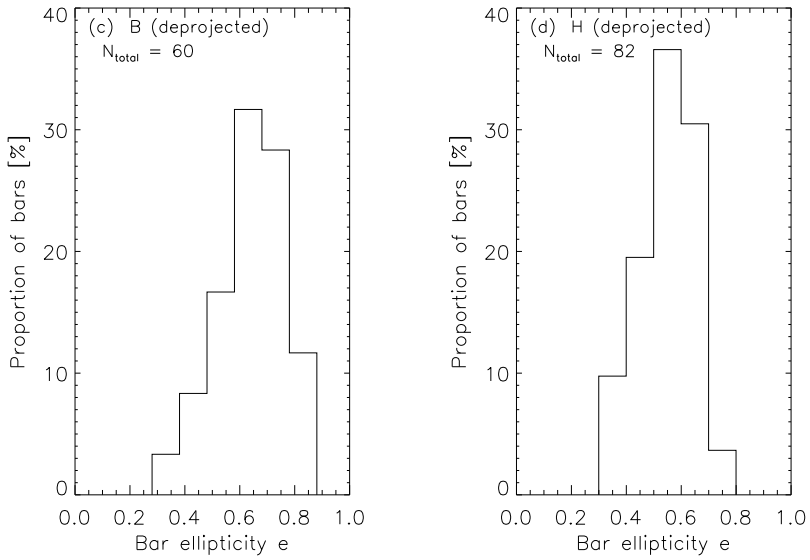

Figure 5.1 The distribution of deprojected bar ellipticity (a proxy for bar strength) for field galaxies in the local Universe with intermediate Hubble types (Sbc-Sc) and with $M_*\gtrsim 10^{10} M_\odot$ in the optical and NIR (Chapter 2; MJ07). Only a few bars ($\sim 10\%$) are very weak with $e_{\rm bar}$ between 0.25–0.40, while the majority of bars ($\sim 70\%$) seem to have moderate to high ellipticities, with $e_{\rm bar}$ between 0.50 to 0.75.

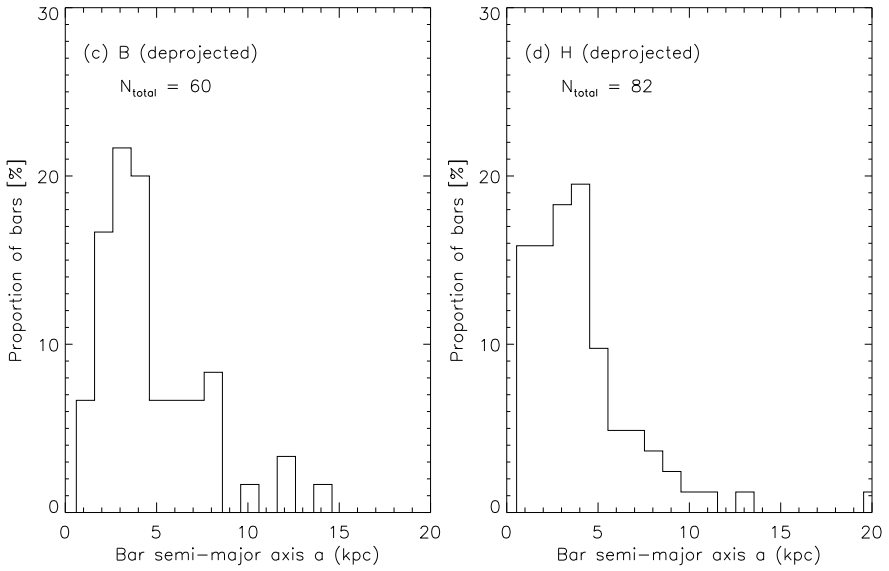

Figure 5.2 Distributions of deprojected bar sizes ($a_{\rm bar}$) for field galaxies in the local Universe with intermediate Hubble types (Sbc-Sc) and with $M_*\gtrsim10^{10}M_\odot$ in the optical and NIR (Chapter 2; MJ07). Most ($\sim$ 70%) bars have $a_{\rm bar} \leq 5$ kpc, and $\sim$ 50% of them cluster in the range 2 to 5 kpc, putting constraints on the observability of bars at intermediate redshifts (see §5.3).

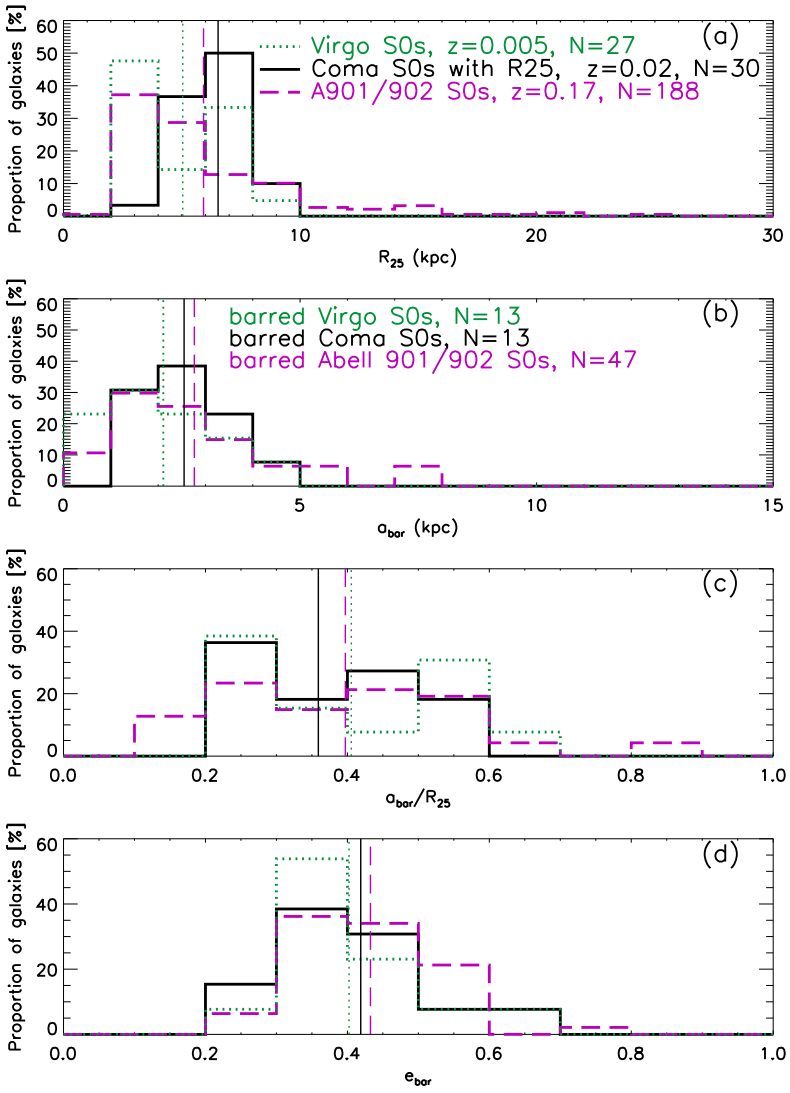

Figure 5.3 Comparisons of quantitative properties of bars and their host disks for S0 galaxies across clusters of different number density (Virgo - $n \sim 300$ gal/Mpc^3, Abell 901/902 - $n \sim 1000$ gal/Mpc^3, and the core of Coma - $n \sim 10{,}000$ gal/Mpc^3). We find that the bars and disks of S0s have similar size distributions, and the bars have similar strength distributions even though the number density of the three clusters differs by over an order of magnitude.

primarily for field galaxies in the local Universe. The contributions from work done towards this thesis are shown as the four open and filled stars.

In MJ07 (Chapter 2), we use ellipse-fitting to quantify the bar fraction and properties for a sample of $\sim$ 180 field galaxies in the local Universe. Our sample consists primarily of intermediate Hubble type galaxies (e.g., Sab–Scd). For such systems, we find that the optical bar fraction is 44$\pm$ 7% (filled blue star in Fig. 5.4). This result is in agreement with Reese et al. (2007), who find 47% in the I band using Fourier decomposition (open blue square in Fig. 5.4). Both studies find an optical bar fraction that is lower than the canonical RC3 value due to two factors, as discussed in detail in Chapter 2: (1) the bar fraction quoted from RC3 is an average over a wider range of Hubble types, and (2) the visual classification in the RC3 uses indirect, somewhat subjective indicators to detect bars (e.g., the shape of dust lanes and spiral arms) rather than quantitative criteria based on the light directly from the bar feature. As a result, systems classified in RC3 from optical images to be weakly barred (SAB), turn out at NIR wavelengths to be a mixed bag of truly barred and unbarred galaxies. We also find that there is a large overlap in bar ellipticity ($e_{\rm bar}$) between types 'SB' and 'SAB'.

In MJ07 (Chapter 2), we also quantify the bar fraction in the NIR, using H-band images. We find that for intermediate-Hubble type galaxies (e.g., Sbc–Sc), the bar fraction increases from 44% to 60$\pm$ 7% in the NIR (filled red star in Fig. 5.4). This is caused by the decrease in obscuration from dust and patchy star formation when looking in the NIR bands. Our results are consistent

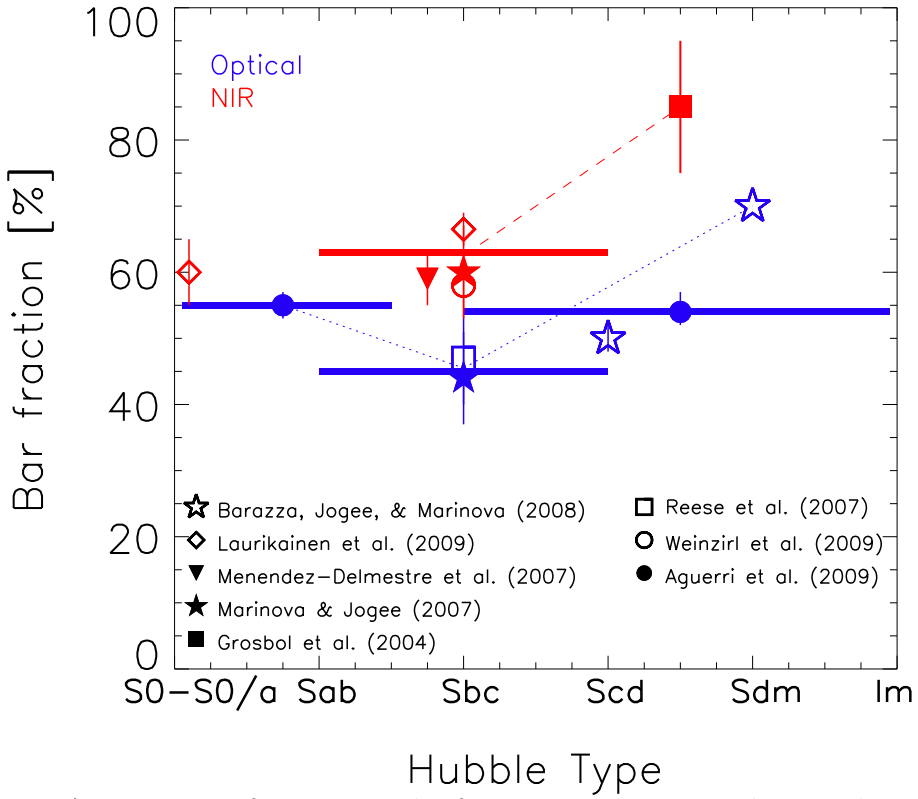

Figure 5.4 A summary of recent results from quantitative studies on the variation of the optical and NIR bar fraction (including both strong and weak bars) as a function of Hubble type, primarily for galaxies in field-like (low density) environments in the local Universe. The contributions from work done towards this thesis are shown as the four open and filled stars. The horizontal lines show the main range of Hubble types over which the results of specific studies apply. The horizontal red line shows the approximate range of Hubble types for all NIR studies for samples dominated by intermediate Hubble type galaxies (MJ07; Menendez-Delmestre et al., 2007; Laurikainen et al. 2009; Weinzirl et al. 2009). The filled red square shows the NIR bar fraction for a small sample ($N = 13$) of Scd-Sd galaxies from Grosbøl et al. (2004). For BJM08 (open blue stars), where Hubble type classifications are unavailable, only the approximate mean of the Hubble type of the sample galaxies is shown. Our work and the results from other studies shown in this figure suggest that the bar fraction rises sharply from galaxies of intermediate Hubble types (Sbc) to late Hubble types (Sd/Sm), a robust trend that is also confirmed in Figure 5.5. It is unclear whether the bar fraction rises from intermediate Hubble types (Sbc) toward early Hubble types (Sa and S0/a), since fewer independent data points exist in this regime.

with other studies using ellipse fits (Menéndez-Delmestre et al., 2007, Fig. 5.4, filled red triangle), and bulge-disk-bar decomposition (Laurikainen et al., 2009; Weinzirl et al., 2009, Fig. 5.4, red diamond and red open circle, respectively).

Fig. 5.4 shows that moving from intermediate to late Hubble types (e.g., Sc–Sdm), the optical bar fraction rises from $\sim$ 45% to $\sim$ 70%. This result was first shown using quantitative methods in BJM08 (also see Odewahn, 1996 conference proceedings). In BJM08, we analyze a sample of $\sim$ 2000 disk galaxies, selected via color cut, from the SDSS with z =0.01–0.03. Although standard Hubble types are not used in this study, the significant rise of the bar fraction is seen going from galaxies that host prominent bulges (e.g., intermediate Hubble types), to those that appear disk-dominated (e.g., late Hubble types such as Scd–Sd; Fig. 5.4, blue open stars). A similar trend is seen with galaxy color, where the bar fraction rises for bluer galaxies in the sample. The rise in the optical bar fraction for late Hubble types was subsequently confirmed by the quantitative study of Aguerri et al. (2009, Fig. 5.4, filled blue circles), as well as the much larger, *visual* study of Nair & Abraham (2010b), as shown in Fig. 5.5.

In the NIR, the filled red square shows the bar fraction from Fourier decomposition for a small sample (N = 13) of Scd-Sd galaxies by Grosbøl et al. (2004), confirming the upward rise of the fraction of barred disks from intermediate to lat-type galaxies.

Moving from intermediate Hubble types (Sb) to early Hubble types (S0-Sa), the trend of the bar fraction is less well established due to the difficulty in

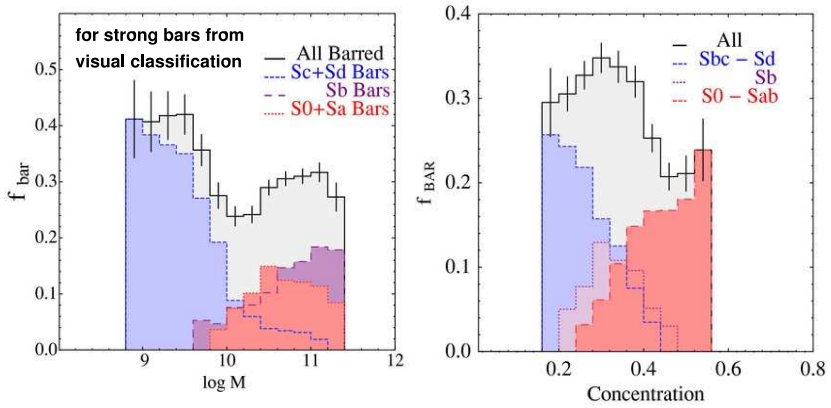

Figure 5.5 We reproduce Figures 1(c) and 5(b) from Nair & Abraham (2010b), showing the non-monotonic variation of the optical bar fraction for field galaxies in the local Universe as a function of Hubble type and stellar mass (left), and Hubble type and central concentration (right). Bar classifications in Nair & Abraham (2010b) are performed through visual classification and the bar fraction shown is only for strong, SB-type bars. Whether galaxies are separated according to stellar mass (left) or light concentration (right), this figure shows that the optical fraction of strong bars rises sharply from galaxies of intermediate Hubble types (Sb) to late Hubble types (Sd), consistent with the similar trend shown in Fig. 5.4. A rise toward early Hubble types (S0-Sa) is also seen if galaxies are separated in terms of light concentration (right), but is not evident in stellar mass. As a function of stellar mass, the bar faction seems to be bimodal, being high/low at low/high stellar masses.

separating unbarred S0 and ellipticals (Chapter 4) and the lack of independent data points. Laurikainen et al. (2009) use two-dimensional bulge-disk-bar decomposition to investigate the NIR bar fraction in a sample containing 82 S0 galaxies and 18 S0/a galaxies. Taken together, the bar fraction in these early types (S0-S0/a) is 60±5% (red diamond, Fig. 5.4). Aguerri et al. (2009) report an optical bar fraction of 55% for early-type spirals (S0/a-Sab), which is similar to or slightly higher than the optical bar fraction ($\sim$ 45%) for intermediate Hubble types Sbc-Sc (MJ07; Reese et al. 2007). At best, the result of Aguerri et al. (2009) suggests only a modest rise of the bar fraction from intermediate (e.g., Sb) to early-type galaxies (S0/a-Sab).

Because many galaxy properties vary across Hubble type, it is not straightforward to identify the main driver of the trends seen in Fig. 5.4. Therefore, studies are now looking directly at the dependence of the bar fraction on specific host galaxy properties such as luminosity, B/T, stellar mass (M_*), and color. Figure 5.6 shows how these disk galaxy properties vary as a function of Hubble type from a sample of 1384 disk galaxies (S0–Im) in the RC3 with $cz > 1000$ km/s, Hubble stage -2 to 11, and morphological classification error < 1. The absolute B magnitude (Figure 5.6a) is calculated from the total B magnitude $B_{\rm T}$. Stellar masses are calculated using the relations from Bell et al. (2003) assuming a Kroupa et al. (1993) initial mass function:

$$\frac{M}{M_\odot} = v_{\rm lum} \times 10^{-0.628+1.305(B-V)-0.1}, \tag{5.1}$$

where

$$v_{\rm lum} = 10^{-0.4(V-4.82)}. \tag{5.2}$$

The orange points show the mean values for each Hubble type. The leftmost large orange circle shows the mean values for $S0^0$–S0/a Hubble types grouped together. It is evident that absolute B magnitude M_B, stellar mass M_*, and $B-V$ color all decrease with Hubble type for late-type galaxies Sc–Sm. For early Hubble types (S0–Sb), these properties remain mostly constant.

In BJM08 we find that the optical bar fraction increases (by a factor of ~ 1.5) in disk-dominated galaxies with large r_e/R_{24} (a measure of the B/D ratio). In M09 (Chapter 3 and see §5.4 below), we find the interesting result that the bar fraction exhibits a *non-monotonic* trend with galaxy properties for galaxies in the Abell 901/902 cluster system at $z \sim 0.165$. *Specifically, we find that at a given morphology, the optical bar fraction is higher for more luminous galaxies. In addition, at a constant luminosity, the bar fraction is higher for galaxies with low B/T.* The recent, very large ($\sim$ 14,000 galaxies) *visual* study of Nair & Abraham (2010b) confirms our results (Fig. 5.5), extends them to galaxies in the field, and sheds more light on the non-monotonic trend we find in Chapter 3. Nair & Abraham (2010b) find that the bar fraction is a strong function of stellar mass, with a minimum at $M_* = 10^{10.2} M_\odot$ (roughly corresponding to the mean mass of Scd galaxies, Fig. 5.6b), and increasing towards lower-mass (late-type, bluer, more disk-dominated), while exhibiting only a modest rise for higher-mass (earlier-type, redder, more bulge-dominated) galaxies, mimicking the trend shown in Fig. 5.4 (see Fig. 5.5). The results in Fig. 5.4, along with those of Nair & Abraham (2010b) explain the disparate results seen in some recent studies, showing that different trends

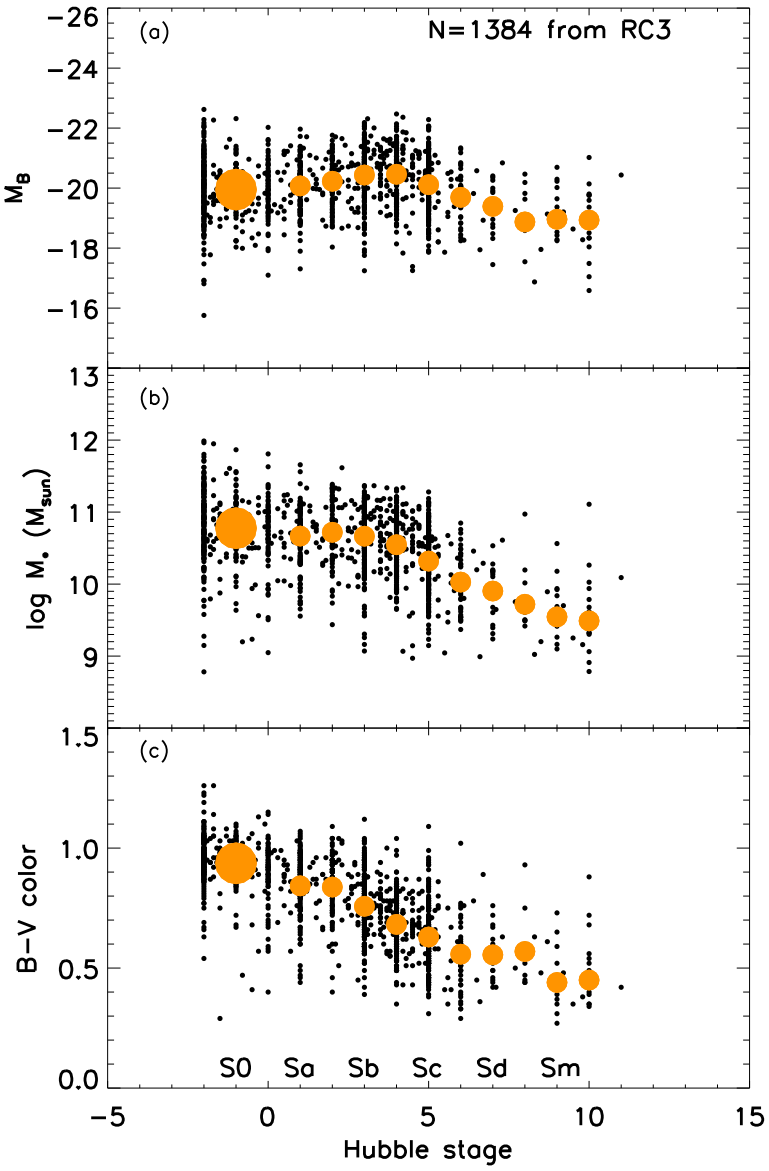

Figure 5.6 Galaxy properties as a function of Hubble type from a sample of 1384 disk galaxies (S0–Im) from the RC3 with $cz > 1000$ km/s, Hubble stage -2 to 11, and morphological classification error < 1. The orange points show the mean values for each Hubble type. The leftmost large orange circle shows the mean values for $S0^0$–S0/a Hubble types grouped together. It is evident that **(a)** absolute B magnitude M_B, **(b)** stellar mass M_*, and **(c)** $B-V$ color all decrease with Hubble type for Sc–Sm. For early Hubble types (S0–Sb), these properties remain mostly constant.

in the bar fraction as a function of galaxy properties can be obtained depending on the morphological mix of galaxies in the sample. For a sample dominated by late-type galaxies, one will find that the bar fraction rises for bluer, more disk-dominated, less luminous (massive) objects (e.g., BJM08, Aguerri et al., 2009). For samples dominated by intermediate Hubble types (Sab–Sc), with few galaxies of very early type (e.g., S0–Sa) or very late type (e.g., Scd–Sd), one will find no (or a very weak) trend with galaxy properties (e.g., Eskridge et al. 2000; Buta et al. 2005; MJ07). Finally, for a sample dominated by early-type galaxies, one may find that the bar fraction rises for redder, more bulge-dominated galaxies (e.g., Masters et al., 2011; Sheth et al., 2008), or see no trend as a function of mass (Nair & Abraham, 2010b, Fig. 5.5, left).

In addition to the bar fraction, the properties of bars (such as size and strength) also depend on the host galaxy characteristics. Lower luminosity galaxies of type Sb or later, host smaller bars both in absolute and normalized terms, independent of the bar size characterization method (Kormendy, 1979; Martin, 1995; Erwin, 2005; Gadotti, 2011). Interestingly, Gadotti (2011) also finds that in the correlation between normalized bar size and B/T, bars with different ellipticities follow parallel tracks, suggesting that although bars may form with varying normalized sizes and strengths in galaxies of different Hubble types, they evolve similarly. Elmegreen & Elmegreen (1985) find that bars in early-type galaxies have slowly-decreasing surface brightness profiles (called 'flat' bars), whereas bars in late-type galaxies have exponentially-

decreasing surface brightness profiles (called 'exponential' bars). We return to these points in §5.2.2.

Our main results are summarized below, giving the trends that need to be explained by theoretical models (see §5.2.2)

1. *Bar fraction as a function of Hubble type (Fig. 5.4)*: The bar fraction for strong and weak bars rises sharply from galaxies of intermediate Hubble types (Sbc) to late Hubble types (Sd/Sm) – a robust trend also confirmed in Fig.5.5 when galaxies are separated by light concentration (point 2) or stellar mass (point 3 below). The bar fraction may remain flat or show a modest rise from intermediate Hubble types (Sbc) toward early Hubble types (Sa and S0/a), but fewer independent data points exist in this regime.

   A number of factors vary along the Hubble sequence, such as stellar mass, dark matter fraction (e.g., Persic et al., 1996), cold gas fraction (e.g., Young & Scoville, 1991), and bulge-to-disk ratio (e.g., Laurikainen et al., 2007; Weinzirl et al., 2009; Graham & Worley, 2008). In §5.2.2, we discuss which may be the main factors driving the bar evolution.

2. *Bar fraction as a function of Hubble type, light concentration, and stellar mass (Fig. 5.5):* Results for the bar fraction as a function of light concentration and stellar mass are only available for strong bars from the visual study of (Nair & Abraham, 2010b, Fig. 5.5):
   a) As a function of stellar mass (Fig. 5.5, left), the visual optical fraction

of strong bars is high at low stellar masses ($M_* \leq 10^{10} M_\odot$) and drops at higher masses.

b) As a function of light concentration (Fig. 5.5, right), which is a rough measure of the bulge to disk light ratio, the visual fraction of strong bars is high for low concentration (< 0.4) but drops sharply at higher concentration.

c) Whether galaxies are separated according to stellar mass (Fig. 5.5, left) or light concentration (Fig. 5.5, right), the visual optical fraction of strong bars rises sharply from galaxies of intermediate Hubble types (Sb) to late Hubble types (Sc-Sd), consistent with the similar trend shown in Fig. 5.4. A rise toward early Hubble types (S0-Sa) is only seen if galaxies are separated in terms of light concentration (Fig. 5.5, right), however as a function of mass, the bar fraction remains flat at high masses for early types (S0-Sa).

d) Within the late types (Sc-Sd) the visual optical fraction of strong bars falls as concentration rises, while among the early types (S0-Sa) the reverse behavior is seen. We return to this point in § 5.2.2.

3. In addition to (1) and (2), the properties of bars such as size and strength also correlate with galaxy properties. Bars are longer (normalized to disk size) and stronger in early-type galaxies, and galaxies with larger B/T (Kormendy, 1979; Martin, 1995; Erwin, 2005; Gadotti, 2011). Additionally, bars in early-type galaxies have slowly-decreasing ('flat') surface brightness profiles, while bars in late-type galaxies have exponentially-

decreasing surface brightness profiles (Elmegreen & Elmegreen, 1985).

5.2.2 Theoretical models

What do these results tell us about the internal evolution of disks in the context of theoretical studies? Are there different mechanisms of bar formation and evolution at play for different mass regimes (and Hubble types)? The formation, evolution, and dynamics of bars are governed by complex processes that are not fully understood. Various models and mechanisms have been proposed by theoretical studies, however there is no one comprehensive model to date that can predict the observed fraction of bars in the local Universe. We summarize below some of the main factors (F1–F6), which influence bar formation, growth, and destruction. In §5.2.3, we discuss which of these factors are consistent with the observational results in §5.2.1.

F1: Dynamically cold disk

A disk that is dynamically cold is more susceptible to gravitational instabilities than a disk that is dynamically hot. The Toomre Q parameter (Toomre, 1964, 1981) defined below, is often used to roughly gauge the susceptibility of an axisymmetric disk to gravitational instabilities:

$$Q = \frac{\alpha \sigma \kappa}{3.36 G \Sigma} \tag{5.3}$$

Here σ is the velocity dispersion of the stars, Σ is the mass surface density of the disk, κ is the epicyclic frequency, and G is the gravitational constant. For an infinitely thin gaseous disk, $\alpha = 1$, but this value is larger for disks of

finite thickness (Larson, 1985). A differentially rotating stellar disk is subject to dynamical instabilities if $Q \lesssim 1$. A galaxy disk where both gas and stars are present is more unstable than a purely gaseous or purely stellar disk (Jog & Solomon, 1984; Elmegreen, 1995), so Q may be higher (~ 1.5) and still allow for the onset of instabilities. Therefore, gas-rich disks with lower stellar velocity dispersions will be much more susceptible to gravitational instabilities such as bars, than dynamically 'hot' disks with high stellar σ.

In practice, it is hard to rely on Q in detail to gauge the susceptibility of a disk to bar instabilities for several reasons. Strictly speaking, Q applies to axisymmetric instabilities. In general, however, a disk with very high Q ($>> 1$) will not be bar-unstable. On the other hand, moderate Q values (1 to 2) provide favorable conditions for many bar-triggering mechanisms such as the classical bar instability amplified through the swing amplifier mechanism (F2, Binney & Tremaine, 1987) or tidal triggering of bars (F5).

F2: Classical bar instability amplified by swing amplifier

Once a dynamical instability like a stellar bar is formed in a disk, it can be maintained through swing amplification in the presence of a feedback loop (e.g., Toomre, 1981). Swing amplification of a density wave occurs when the wave swings from leading to trailing, due to a temporary quasi-match between the epicyclic motion of the star at frequency κ, and the maximum rotation rate of the unwinding spiral arm. This leads to an enhancement of the gravitational force of the arm on the stellar orbit, as well as an enhancement of the star's gravitational effect on the density wave. This enhances the surface density

of the wave, and the cumulative effect is an amplification of the instability (e.g., Binney & Tremaine, 1987). For strong swing amplification the Toomre Q must be ≤ 3 and $X \leq 3$, where X is a parameter that governs the behavior of the density wave at the resonances (e.g., Goldreich & Tremaine, 1978; Binney & Tremaine, 1987). The swing amplification mechanism is only effective in maintaining a bar instability if a feedback loop exists to keep converting trailing waves into leading waves. One such loop can be produced by the propagation of the density wave through the center of the galaxy in the absence of an inner Lindblad resonance (ILR). The presence of an ILR is dictated by the density distribution in the central regions of the galaxy; in general, in galaxies without a large increase in central mass concentration (e.g., galaxies of low B/T or bulgeless galaxies) an ILR is absent, while galaxies with large central mass concentrations tend to host one or more ILRs.

F3: Angular momentum exchange between the bar and DM, disk and bulge

The bar grows and evolves through angular momentum exchange with the outer disk and DM halo (e.g., Sellwood, 1981; Athanassoula et al., 1983; Weinberg, 1985; Berentzen et al., 1998; Athanassoula & Misiriotis, 2002; Martinez-Valpuesta et al., 2006; Berentzen et al., 2007; Villa-Vargas et al., 2009), and perhaps the galaxy bulge (Athanassoula & Misiriotis, 2002; Athanassoula, 2003). The angular momentum exchange happens at the resonances, and is dictated by the mass and velocity dispersion of the material present. Studies show that the strength (and length) of the bar, as well as its pattern speed, are set by this angular momentum exchange (e.g., Athanassoula, 2003; Martinez-

Valpuesta et al., 2006; Villa-Vargas et al., 2009), which in turn depends on the mass distribution and velocity dispersion in the disk and spheroidal components.

The DM halo has been clearly established in theoretical studies as an effective angular momentum sink based on many simulations. The DM halo extends to large radii, encompassing the outer Lindblad resonance (OLR) and corotation (CR), which play an important role in angular momentum transfer (e.g., Martinez-Valpuesta et al., 2006; Villa-Vargas et al., 2009). However the importance of the bulge component as an angular momentum sink is controversial and is still an area of active study (Athanassoula & Misiriotis, 2002; Villa-Vargas et al., 2009; Saha et al., 2011, see §5.2.3).

F4: Interaction of bar and DM

There are multiple ways in which the DM halo can influence bar formation and growth. The DM mass fraction within the disk radius, as well as the concentration of the DM halo, its shape, and the presence of substructure are all important factors.

In F3 above we discuss how the DM halo acts as an angular momentum sink for the bar, facilitating its growth. The efficient transfer of angular momentum depends on the mass and velocity dispersion of the DM component at the resonances where this exchange takes place. Simulations find that in disks where the DM halos are more centrally concentrated (higher DM fraction within the disk radius), bars can grow longer and stronger (e.g., Athanassoula & Misiriotis, 2002).

Dubinski et al. (2008) finds that bars can be triggered through interactions with dark satellites, present as part of the substructure in the DM halos of galaxies. This mechanism is likely to play a bigger role for less massive, late-type galaxies, due to the higher likelihood that dark halos of similar masses will exist in the vicinity of such low-mass disks. In contrast, due to the mass function of galaxies, it is much less likely for a massive disk galaxy to interact with a halo of similar mass.

If the DM halo is triaxial, it can trigger a bar in the galaxy disk. Simulations find that this mechanism triggers the first generation of bars at early epochs ($z \sim 5$; Heller et al., 2007; Romano-Díaz et al., 2008). However, DM halos are predicted to become more symmetric with time, on a timescale that is a function of mass, as disks and other central components form (e.g., Kazantzidis et al., 2004; Heller et al., 2007). We note that Dubinski & Chakrabarty (2009) find bars may still be triggered in a galaxy where the *outer* DM halo remains triaxial and tumbles slowly even after the inner DM halo becomes axisymmetric and coupled to the disk.

F5: Tidal triggering of bars

Tidal interactions can induce bars in a dynamically cold disk (with moderate Q, see F1 above; Noguchi, 1987; Elmegreen et al., 1990; Gerin et al., 1990; Elmegreen et al., 1991; Hernquist & Mihos, 1995; Dubinski et al., 2008; Romano-Díaz et al., 2008; Aguerri et al., 2009). However, the triggering of bars through tidal interactions depends on the geometry of the interaction as well as the mass distribution of the various galaxy components. For example,

although tidal encounters can induce bars in unbarred disks in the case of a prograde encounter, they can also have little or no effect in terms of inducing a bar (or affecting the strength of an already existing bar) in the case of retrograde encounters (Gerin, Combes, & Athanassoula 1990; Romano-Díaz et al. 2008; Aguerri & González-García 2009). In addition, lower-mass galaxies may be more susceptible to bar triggering by satellites due to the arguments outlined in F4.

F6: Bar weakening and destruction

Recent simulations suggest that bar destruction by central mass concentrations (CMCs) is difficult in the present-day, as the types of very massive, dense CMCs (with masses $> 10\%$ of the disk mass in the inner few hundred parsec) necessary to destroy a bar (e.g., Athanassoula, 2005; Shen & Sellwood, 2004; Martinez-Valpuesta et al., 2006; Debattista et al., 2006) are not common in present-day galaxies (see Chapter 2). However, bar destruction by CMCs may have been important in the past ($z > 1$) when disks were not very massive. Simulations show that the CMC can weaken or destroy bars due to the introduction of chaotic orbits in the central regions (**?**Berentzen et al., 2007). One can also make the following intutitive argument for weakly barred potentials where the epicyclic approximation applies. As the CMC grows, $\Omega - \kappa/2$ increases sharply towards the central regions. The large variation in $\Omega - \kappa/2$ makes it more difficult for the self-gravity of the bar to keep the stellar orbits precessing together at the pattern speed of the bar, thus disrupting its structure (e.g., Kormendy & Kennicutt, 2004).

The gas content of disks also influences the robustness and evolution of the bar (e.g, Shlosman & Noguchi, 1993; Berentzen et al., 1998; Bournaud & Combes, 2002; Bournaud et al., 2005; Debattista et al., 2006; Berentzen et al., 2007; Villa-Vargas et al., 2010). In simulations, the gas may weaken or destroy a bar in two ways: it may build a CMC, which could heat the stars in the central regions of the disk, thus disrupting the bar orbits (e.g. Berentzen et al., 2007), or the gas may lose angular momentum to the stars in the bar, thus weakening or destroying it (e.g. Bournaud et al., 2005). The efficiency of the second mechanism (the transfer of angular momentum from the inflowing gas to the stars in the bar) for bar destruction remains controversial. While Bournaud et al. (2005) claim that this is the main mechanism for bar destruction in their simulations, Berentzen et al. (2007) perform detailed tests of this scenario and show that the bar remains unaffected. Instead, the gaseous CMC that forms in the central regions of the galaxy damps the buckling instability of the bar and inhibits its subsequent secular growth (Berentzen et al., 2007).

Finally, it is possible that some bars are more susceptible by destruction or weakening by CMCs than others. Athanassoula 2005 finds that 'flat' bars are more robust, while 'exponential' bars are more easily destroyed by a CMC with a mass equal to a few percent of the disk mass.

5.2.3 Theory confronts observations

In this section, we attempt to explain the observational results in §5.2.1 within the framework of the theoretical mechanisms F1–F6 discussed in §5.2.3.

(1) The high bar fraction in galaxies of late Hubble types (Scd and later)
Galaxies of late Hubble types (Scd and later) have lower stellar mass (Fig. 5.6), higher DM fraction (Persic et al., 1996) and concentration (Kormendy & Freeman, 2004), higher gas fraction (Young & Scoville, 1991), and lower bulge-to-disk (B/D) ratio (Laurikainen et al., 2007; Graham & Worley, 2008; Weinzirl et al., 2009) than galaxies of intermediate or early Hubble types. This has several consequences:

- A high fraction of cold gas will act to make the disk generally susceptible to gravitational instabilities and bar formation (F1 in §5.2.2). Although it is not known at present which mechanism of bar formation and growth is dominant in late-type galaxies, a dynamically cold disk with moderate Q favors most bar growth mechanisms, including the classical bar instability via the swing amplifier (F2 in §5.2.2) and tidal triggering of bars (F5 in §5.2.2).

- We expect that tidal triggering of bars will be more effective for galaxies of lower stellar mass (F5 in §5.2.2). As discussed in §5.2.2, based on the mass function of galaxies, whereby low-mass galaxies are much more numerous than high-mass galaxies, a low-mass galaxy is much more likely to interact with satellites of similar mass. In contrast, such an interaction is less likely for higher mass galaxies, where interactions with low-mass satellites will have a less dramatic effect.

- Triggering of bars via interactions with the DM substructure and shape

(F4; Heller et al., 2007; Dubinski et al., 2008; Romano-Díaz et al., 2008) is also facilitated by the high DM fraction and low stellar masses expected in late-type systems.

- The high DM fraction and/or concentration (Kormendy & Freeman, 2004) in low-mass, late-type galaxies (with up to 85% of the mass within the disk optical radius being dominated by DM; Persic et al., 1996), is expected to facilitate the angular momentum transfer from the bar to the DM halo - a mechanism important for bar growth (see F3 in §5.2.2).

Thus, all of the above factors present in late-type galaxies (Scd and later) make such systems very conducive to bar formation and growth, predicting a high bar fraction, as observed (§5.2.1, Fig. 5.4).

(2) The fall in bar fraction from galaxies of late Hubble types to intermediate Hubble types

Several factors might be at play to produce the fall in bar fraction from galaxies of late Hubble types (Scd and later) to intermediate Hubble types (Sb; §5.2.1, Figs. 5.4 and 5.5):

- Galaxies of intermediate Hubble types (Sb) tend to have significantly higher stellar masses (Fig. 5.6b) and lower DM fraction (e.g., Persic et al. 1996) than late Hubble types (Scd and later). For example, the mean stellar mass for Sb galaxies is $\sim 5{\times}10^{10} M_{\odot}$, while the mean stellar mass for Sd galaxies is $\sim 5{\times}10^{9} M_{\odot}$ (Fig. 5.6b). Persic et al. (1996) find that

in the brightest spirals (e.g., Sa-Sbc, Fig. 5.6a), the DM comprises about 15% of the mass within the disk optical radius, whereas for the faintest spirals (e.g., Scd, Fig. 5.6a), the DM can make up $\sim 85\%$ of the mass within the disk optical radius. The higher stellar mass and lower DM fraction are both expected to reduce the effectiveness of tidal triggering of bars via the DM substructure (F4) or through the tidal triggering of bars by external satellites (F5), based on the arguments presented in §5.2.2.

- The detailed variation of B/T as a function of Hubble type from Sd to Sb galaxies is unclear due to the fact that published values in the literature tend to overestimate the true B/T in barred systems if the bar is not included in the structural decomposition (as shown by Laurikainen et al. 2007; Graham & Worley 2008; Weinzirl et al. 2009). Recent work by Weinzirl et al. (2009) shows that the majority of massive spirals, many of which have intermediate Hubble type, tend to have lower B/T than originally reported in studies such as Simien & de Vaucouleurs (1986). Nonetheless, on average galaxies of intermediate Hubble types (Sb) tend to have higher B/T than Scd and later types (Laurikainen et al., 2007; Weinzirl et al., 2009). One consequence of the larger B/T and central mass concentration of intermediate-type galaxies, is that they will develop one or more ILRs, which may limit bar formation through the classical bar instability and swing amplifier, by cutting off the swing amplifier feedback loop (F2; §5.2.2). However, it is important

to note that the swing amplification mechanism *cannot* be the main factor controlling the formation and growth of bars, since in a significant number of early-type galaxies (e.g., S0s) bars and large bulges coexist. In addition, there is no evidence (Fig. 5.4) of any sharp decline in the bar fraction when going from Sb/Sbc galaxies with intermediate bulge-to-disk ratios to bulge-dominated S0/Sas.

- One should also note that the total gas fraction is lower in galaxies of intermediate Hubble types (Sb) than late Hubble types (Scd and later), varying from 0.4± 0.2 for Scd galaxies to $0.08^{+0.17}_{-0.06}$ (Young & Scoville, 1991). However, it is unclear whether this decline in the gas fraction makes the disk dynamically hot enough to suppress the efficiency of bar formation either by tidal triggering or the classical bar instability. In simulations, galaxies with gas fractions of $< 3\%$ easily form bars (e.g., Berentzen et al. 2007). Furthermore, the disks in Sb galaxies are often actively star-forming, suggesting that at least locally, the gas is susceptible to gravitational instabilities.

Thus, in summary, the higher stellar mass, and lower DM fraction in intermediate Hubble types (Sb-Sc) compared to late Hubble types (Scd and later), can contribute to the lower bar fraction in the former group. It is unclear whether the lower gas fraction in intermediate Hubble types compared to late types plays a significant role.

One should also bear in mind that the formation and evolution of bars

in galaxies should ideally be placed in a hierarchical framework, whereby we consider the assembly process of the galaxy bulge and disk, as well as the concurrent growth of the bars. This broad picture is complex and uncertain due to many factors. The bulge and disk can grow through a combination of mechanisms such as major mergers (e.g., Steinmetz & Navarro, 2002), minor mergers, smooth accretion (e.g., Brooks et al., 2009; Kereš et al., 2009; Dekel et al., 2009), and/or internal secular processes such as bar-driven gas inflow (Kormendy & Kennicutt, 2004). The effect of these mechanisms on bar growth during the epochs of galaxy assembly is unclear, as simulations are only starting to explore bar growth in a cosmological context (Curir et al. 2006, 2007, 2008; Heller et al. 2007; Romano-Diaz et al. 2008). They show that bars at early epochs ($z \sim 5$) can be destroyed and reformed multiple times, while bars formed around ($z \sim 1$) remain robust to the present day (Heller et al. 2007; Romano-Diaz et al. 2008). Further, recent observations show that the bar fraction for intermediate-mass disk galaxies ($M_* = 10^{10.5}$–$10^{11} M_\odot$) builds up by a factor of two over $z \sim$0.6–0.2 (Cameron et al. 2010). In addition, as discussed above, the bar fraction and properties show a complex dependence on the host galaxy properties, such as stellar mass, luminosity, color, and Hubble type (BJM08; M09; Aguerri et al. 2009; Barazza et al. 2009; Weinzirl et al. 2009; Laurikainen et al. 2009; Gadotti 2010; Nair & Abraham 2010b), which vary as a function of redshift during the epochs of galaxy formation.

(3) Does the bar fraction rise from galaxies of intermediate Hubble types to early Hubble types?

While the bar fraction rises significantly for galaxies of late Hubble types (e.g., Scd and later; Figs.5.4, 5.5), it is less well established how the bar fraction varies between intermediate (Sb-Sc) and early (S0-Sa) Hubble types. This is in part due to the fact that it is challenging to obtain an accurate bar fraction for S0 galaxies, which are difficult to distinguish from ellipticals in the absence of a bar (Chapter 4). In addition, bars are more difficult to identify in S0 galaxies due to the dilution of the bar signature by the large bulges present in these systems (Chapter 4).

Laurikainen et al. (2009) investigate the bar fraction in a large number of early-type galaxies from the NIR S0 survey (NIRSOS; Laurikainen et al. 2005) using 2D bulge-disk-bar decompositions. The sample analyzed in Laurikainen et al. (2009) contains 82 S0 galaxies and 18 S0/a galaxies. Taken together, the bar fraction in these early types (S0-S0/a) is 60±5% (Fig. 5.4, red diamond). In the optical, Aguerri et al. (2009) find a bar fraction of 55% for S0/a–Sb galaxies, similar to or slightly higher than that in intermediate Hubble types ($\sim$ 45%; MJ07, Reese et al. 2007). This result suggests that the bar fraction remains roughly constant from intermediate to early Hubble types, or shows a moderate rise at best. Although Nair & Abraham (2010b) do not show the variation of the bar fraction as a function of Hubble type, Fig. 5.5, left panel, shows that the bar fraction remains fairly flat at high masses ($M_* > 10^{10} M_\odot$), covering the range from early types (S0–Sa) to intermediate types (Sb-Sc).

In summary, a few observational studies show hints that the bar fraction

may rise from intermediate Hubble types (Sb-Sc) toward early Hubble types (S0-Sa), however this trend is less dramatic and less well-established than that observed toward late-type (Scd and later) galaxies. However, it has been well established that bars tend to be longer (normalized to disk size) and stronger in early-type galaxies (Kormendy, 1979; Martin, 1995; Erwin, 2005; Gadotti, 2011) and in galaxies with larger B/T (Gadotti, 2011).

If the bar fraction does indeed rise from intermediate Hubble types to early-types, explaining the driver of this trend is a challenge for theoretical models.

As discussed in point (2) above, the factors F1 to F6 contributing to bar formation and growth, predict the observed drop in the bar fraction from late types (Scd and later) to intermediate Hubble types (Sb), as the latter have a higher stellar mass, lower DM fraction, and higher B/T. However, as we go from intermediate to early types, we would expect the bar fraction to either stay similar (if bar formation has already saturated) or to drop.

One possibility that might explain a potential growth in the fraction and strength of bars in early types is suggested by the N-body simulations of Athanassoula & Misiriotis (2002) and Athanassoula (2003). Their simulations show that in galaxies where the disk mass dominates the DM mass within the radius of the disk (e.g., early Hubble types), the models with the heaviest bulges are the most favorable to bar growth because the bar can shed large amounts of angular momentum to the bulge component at the ILR. We note, however that these simulations may not be representative of real early-type

galaxies for two reasons. Firstly, the B/D ratio of 0.6 assumed in the simulations of Athanassoula & Misiriotis (2002) and Athanassoula (2003) is at the very high extreme of the range found observationally for S0/a–Sb galaxies through 2-D bulge-disk-bar decomposition (0.3–0.5; Weinzirl et al. 2009). Secondly, it is unclear whether the bulge and halos are accurately modeled in the simulations where the effect of the large bulge is investigated (I. Shlosman, private communication). More recent simulations, (Villa-Vargas et al., 2009), with lower B/D ratios do not see evidence of angular momentum transfer from the bar to the bulge component, however the resolution in these simulations is too low to properly resolve the bulge.

From an observational perspective, if the bar is shedding angular momentum to the bulge component in early-type galaxies, one would expect that these bulges will have a significant amount of rotation. There are few observational results to adequately assess this effect. Some early work, (Kormendy, 1982b), shows evidence of faster rotation in the bulges of barred S0 galaxies than in those of unbarred galaxies, however interpretation of this result is complicated by low number statistics, and incomplete sampling of the full parameter space.

Therefore, the question of the growth and evolution of early-type galaxies is still an area of active research both observationally and theoretically (e.g., Villa-Vargas et al. 2009, 2010; Saha et al. 2011). Higher-resolution simulations, wich resolve the bulge region, spanning a wider range of parameter space, are needed, to shed more light on this question.

5.3 Barred galaxies at intermediate redshifts

Naturally, as the importance of stellar bars as probes of galaxy evolution came to light, the next step was to attempt to study stellar bars at higher redshifts. Do the same proportion of galaxies at $z \sim 1$ host bars as at $z \sim 0$? Can we observationally constrain bar evolution over cosmic times?

The first studies to attempt to answer these questions were those of van den Bergh et al. (1996) and Abraham et al. (1999). van den Bergh et al. (1996) used visual classification to characterize galaxies in the whole Hubble Deep Field (HDF) sample, without applying magnitude cuts. Abraham et al. (1999) also utilized the HDF, but looked for bars by fitting ellipses to two chosen isophotes for each galaxy (generally the isophote at 85% of the maximum flux to probe the bar region, and at 1% of the maximum flux to probe the outer disk). Both studies report a dramatic decline in the fraction of barred spirals with redshift in the HDF, and in particular the results of Abraham et al. (1999) show over an order of magnitude decline in the fraction of strong ($e > 0.4$) bars (Fig. 5.7), with the fraction declining from 29±10% over $z \sim 0.2$–0.7 to 0% at $z \sim 0.7$–1. Sheth et al. (2003) find four large barred galaxies (with mean semi-major axis $\sim$ 12 kpc) among 95 spirals at $z >$0.7 using ellipse fitting on Near-Infrared Camera and Multi-Object Spectrometer (NICMOS3) images. Due to the large NICMOS3 PSF ($\sim 0.3''$, corresponding to $\sim$ 2.4 kpc at $z \sim 1$) they can only detect very large bars, and argue that there is no evidence that bars are more scarce at intermediate redshifts.

The above studies were based on very small samples with WFPC2 or

NICMOS3 whose field of view (FOV) were small (150″ with WFPC2 and 51″ with NICMOS3), and additionally the coarse NICMOS3 PSF only enabled the very largest bars to be reliably detected. Such studies could therefore not robustly determine the bar fraction at intermediate redshifts. As of 2003, the advent of the optical Advanced Camera for Surveys (ACS), with the simultaneously large FOV ($\sim 3'$) of the wide field camera (WFC) and sharp PSF (typically 0.095″ in drizzled combined images in the F814W filter, corresponding to $\sim$ 800pc at $z \sim 1$), allowed a dramatic improvement in the study of bars at intermediate redshifts. Large galaxy surveys like Tadpole (Elmegreen et al., 2004), GEMS (Rix et al. 2004), GOODS (Giavalisco et al. 2004) started to allow samples of several thousand galaxies to be studied.

Elmegreen et al. (2004) argue for a constant optical bar fraction out to $z \sim 1$ in the Tadpole field for a sample of $\sim$ 180 galaxies, using high-resolution (PSF$\sim$ 0.1″) *HST* ACS images. Using three disk selection techniques (Sersic cuts, rest-frame color cuts, and concentration indices), Jogee et al. (2004) find that the rest-frame optical bar fraction for strong ($e > 0.4$) bars ranges from 36$\pm$ 6% to 24$\pm$ 4% from $z \sim 0.2$–1, only allowing for a modest factor of 1.2 to 2 decline. In a recent very large study ($N \sim 2000$ face-on spirals) of the COSMOS field, Sheth et al. (2008) claim that the optical bar fraction shows a decline by a factor of $\sim$ 3 (all bars) or $\sim$ 2 (strong bars with $e > 0.4$) from $z \sim 0.2$–0.84.

Figs. 5.7 and 5.8 show that when comparing bars at high and low redshift, it is better to work explicitly with strong ($e > 0.4$) bars than with all

bars, as the former are more reliably recovered at higher redshifts. Additionally, strong bars have a larger impact on galaxy evolution. In Fig. 5.7, which focuses on strong ($e > 0.4$) bars, one can see that the optical fraction of *strong ($e > 0.4$)* bars over $z \sim 0.2$ to 1.0 from Jogee et al. (2004) is similar to those subsequently reported using the much larger sample of ~ 2000 spirals (Sheth et al., 2008) in the COSMOS survey. In contrast, Fig. 5.8 shows that for studies including both strong and weak bars, there is a wide range of results even at $z < 0.5$. For example at $z = 0.2$, Elmegreen et al. (2004) reports a bar fraction (all bars) of 36% vs. 70% found by Sheth et al. (2008). This difference is likely caused by Elmegreen et al. (2004) detecting mostly the strong bars in their study, even though they do not explicitly perform a cut in ellipticity.

How does the optical fraction of strong ($e > 0.4$) bars vary with redshift? Fig. 5.7 shows that the *raw measured* optical fraction of strong ($e > 0.4$) bars declines by a factor of ~ 1.5 to 2.0 (Jogee et al., 2004) or ~ 2–3 (Sheth et al., 2008) from $z = 0.2$ to 1, but it does not decline by an order of magnitude, as previously implied by the study of Abraham et al. (1999), where no bars with $e > 0.4$ are identified at $z \sim 0.7$ to 1. Furthermore, the points plotted in Fig. 5.7 are *raw* data points, which are not corrected for redshift-dependent systematic effects. All known systematic effects, and in particular the decreasing spatial resolution and the increasing obscuration of bars by star formation and dust at $z \sim 0.2$ to 1.0, will cause the *raw* measured optical bar fraction to be lower at higher redshift. We discuss these two effects in more detail below.

The first systematic effect impacting the detectability of bars is caused

by the decreasing spatial resolution at higher redshifts. Criteria for robustly detecting and characterizing the bar via ellipse fit require a detection of the smooth rise in ellipticity along the bar region, as well as the drop of ellipticity in the disk region (e.g., Knapen et al., 2000; Jogee et al., 2004; Marinova & Jogee, 2007). Thus, only bars with semi-major axis $a_{\rm bar} \geq 2.5$ times the PSF can be robustly characterized using ellipse fitting. Consequently, primary bars with $a_{\rm bar} > 1.5$ kpc require a minimum PSF of 600 pc for robust characterization. Since the ACS PSF ($0.1''$ in drizzled frames) increases from 300 to 800 pc from $z \sim 0.2$ to 1.0, we expect to begin missing bars with $a_{\rm bar}$ in the range of 1.5 to 2.0 kpc at $z > 0.5$. Locally, most primary stellar bars in spirals of intermediate to early Hubble types have $a_{\rm bar} \leq 5$ kpc (Erwin, 2005; Marinova & Jogee, 2007; Barazza et al., 2008). In fact, we find that $\sim 26\%$ of bars at $z \sim 0$ have $a_{\rm bar} < 2$ kpc (MJ07). Therefore, decreasing spatial resolution alone can artificially lower the measured optical bar fraction by a factor of 1.3 by $z \sim 1$ (MJ07).

The second systematic effect at play is the increasing obscuration of bars in optical images at higher redshifts. The obscuration of bars by star formation and dust can mask bars at optical wavelengths: even at $z \sim 0$ this causes a factor of 1.3 loss in optically-visible bars (e.g., Eskridge et al., 2000; MJ07), and this loss factor X is very likely to increase with redshift over the interval $z \sim 0$ to 1, where the SFR density rises by a factor of 4 to 10 (e.g., Lilly et al., 1996; Le Floc'h et al., 2005; Jogee et al., 2009) The amount by which X increases with redshift is presently unknown.

In summary, a large part of the observed factor of $\sim$ 2–3 decline in the *raw measured* optical fraction of strong ($e > 0.4$) bars over $z \sim 0.2$–1.0 is likely due to an artificial loss of bars caused by redshift-dependent systematic effects, such as decreasing spatial resolution and increasing obscuration by star formation and dust of bars in optical images at higher redshifts.

Our results from MJ07 and the above arguments imply that in order to best constrain the evolution of the bar fraction at intermediate redshifts, James Webb Space Telescope (JWST) imaging will be necessary. The Near Infrared Camera (NIRcam) on JWST will resolve the issue of the obscuration of bars by dust and star formation at optical wavelengths. Specifically, the NIRcam PSF of $\sim 0.08''$ at the wavelength range between 0.6 to 5 μ, will be capable of resolving primary bars with $a_{\rm bar} \sim 1.6$ kpc out to $z \sim 1$ and those with $a_{\rm bar} > 2.5$ kpc out to $z \sim 2$ *in the rest-frame NIR*. In contrast, current NIR imagers such as the Wide Field Camera 3 (WFC3) on the *HST* can only resolve bars with $a_{\rm bar} > 2.5$ kpc out to $z \sim 0.7$ in the rest-frame NIR.

Interestingly, comparison of the bar fraction at $z \sim 0$ to that at intermediate redshifts may be complicated by one further factor: the dependence of results on stellar mass. Using the COSMOS sample, Cameron et al. (2010) explore this issue in more detail for galaxies with $i < 45°$, $R_{\rm e} > 2.2$ kpc, and for strong bars with $e > 0.4$. They find that the optical bar fraction for disk galaxies with intermediate masses ($M_* = 10^{10.5}$–$10^{11} M_\odot$) build up their bar fraction by a factor of two from $z = 0.6$ to $z = 0.2$. In contrast, the highest-mass disks ($M_* > 10^{11} M_\odot$) seem to have a constant bar fraction over this

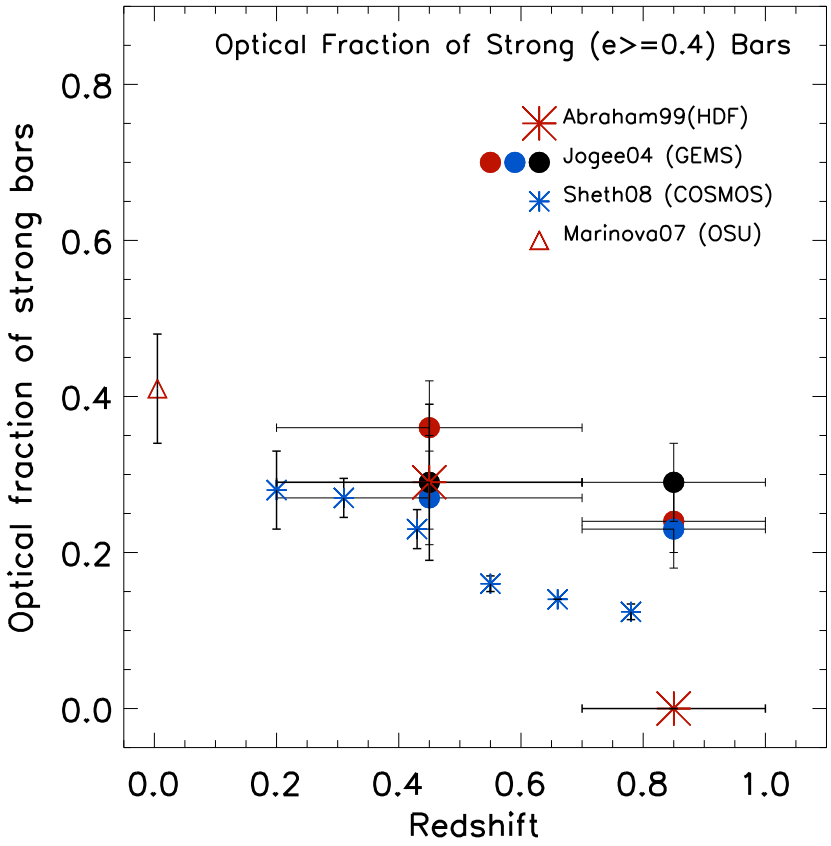

Figure 5.7 The rest-frame optical fraction of strong ($e > 0.4$) bars as a function of redshift is shown for the studies of Abraham et al. (1999); Jogee et al. (2004); Sheth et al. (2008) at intermediate redshifts, and MJ07 at $z \sim 0$. Abraham et al. (1999) finds a dramatic decline in the fraction of strong bars from 29±10% over $z \sim 0.2$–0.7 to 0% at $z \sim 0.7$–1. In contrast, using three disk selection techniques (Sersic cuts, rest-frame color cuts, and concentration indices), Jogee et al. (2004) find that the rest-frame optical bar fraction for strong ($e > 0.4$) bars ranges from (36±6%) to (24±4%) from $z \sim 0.2$ to 1, only allowing for a modest factor of ~ 1.5 to 2 decline. The results of Sheth et al. (2008) show a modest decline in the bar fraction by a factor of ~ 2. [Figure courtesy S. Jogee, based on data points published in the literature.]

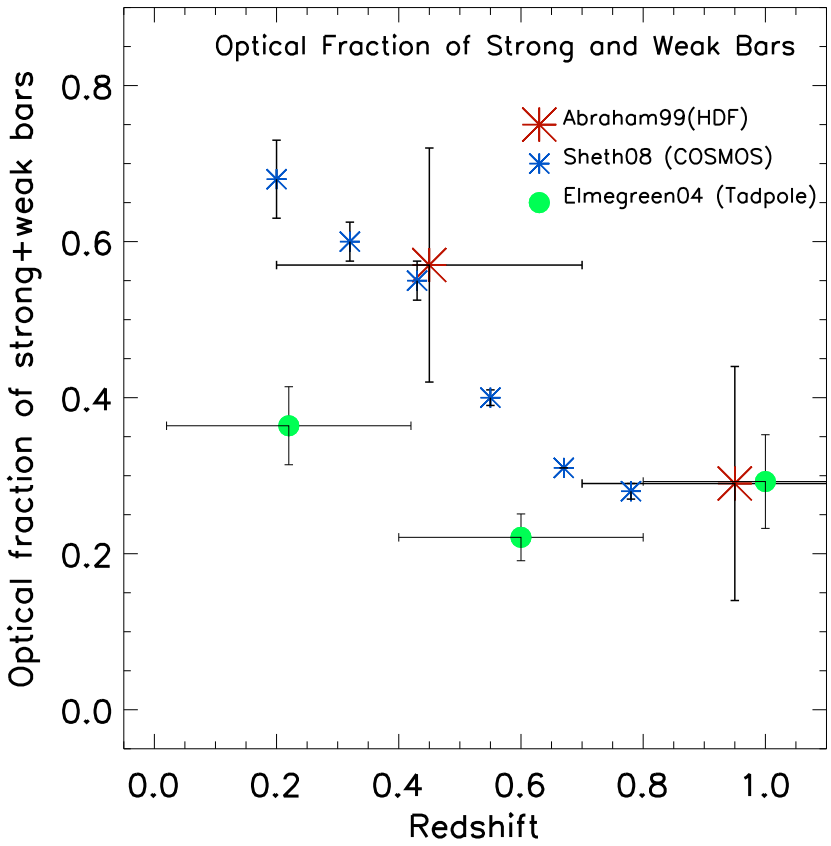

Figure 5.8 The rest-frame optical fraction all bars (strong and weak). Sheth et al. (2008) finds that the total bar fraction decreases by a factor of ~ 3 over z $\sim$0.2–0.8, while Elmegreen et al. (2004) finds a constant bar fraction out to $z \sim 1$. [Figure courtesy S. Jogee, based on data points published in the literature.]

redshift range. Cameron et al. (2010) find that this trend persists when comparing to a complementary low-redshift ($z \sim 0.02$–0.04) sample drawn from the SDSS. This result suggests that by $z \sim 0.6$, the most massive disk galaxies are already mature and stable enough to form and sustain bar instabilities, and have assembled into the Hubble types we see today. The bar fraction variation along galaxies of different Hubble types may then be increasingly set since $z \lesssim 1$ by the properties of the host galaxy, such as stellar mass, dark matter fraction, bulge-to-disk ratio, gas fraction, etc. (see §5.2.3).

Although theoretical studies of bars have only recently started investigating how bar formation and evolution takes place in a cosmological context, results are in broad qualitative agreement with the emerging observational perspective outlined above. In simulations of galaxy evolution at high redshifts (e.g., $z \sim 5$–8) using cosmological initial conditions, bars are triggered by the triaxiality of DM halos and the asymmetric DM distribution as a whole (Romano-Díaz et al. 2008; Heller et al. 2007). However, these early bars are not long-lived, and decay and reform until the more quiescent epochs at $z \lesssim 2$ when major mergers are no longer frequent, the DM halo triaxiality is diluted (e.g., Dubinski 1994; Kazantzidis et al. 2004; Heller et al. 2007), and disks have become more massive and stable. Specifically, Heller et al. (2007) find that large-scale bars formed at later times ($z < 1$) after the active epochs of disk growth persist to the present day. This is in qualitative agreement with the observational picture that the more massive, more mature disks at $z \sim 1$ have already formed long-lived bars, while this happens at later times for less-

massive disks (Cameron et al., 2010), which are still in the process of assembly. However, we note that the galaxies studied in the simulations of Heller et al. (2007) are roughly an order of magnitude less massive $M_* \sim 10^{10} M_\odot$ than the massive galaxies observed in Cameron et al. (2010), which have $M_* \sim 10^{11} M_\odot$.

5.4 Barred galaxies in clusters at low redshift

Prior to this thesis, results on the evolution of the fraction and properties of barred disks in dense environments were sparse. Early studies produced puzzling results. Kumai et al. (1986) find no difference in the fraction of barred galaxies between cluster and field environments, using visual classifications of Uppsala General Catalog galaxies. Thompson (1981) reports twice as many barred S0 galaxies in the core of Coma than in the outer regions, but the results are compromised by uncertainties in cluster membership and classifications performed on ground-based B-band optical plates. In contrast, Andersen (1996) reports no difference in the distribution of barred and unbarred S0s between the core and outer regions of the Virgo cluster. In addition, several studies have shown an excess of barred early-type disk galaxies (e.g., S0/Sa) in binary pairs (Kumai et al., 1986; Elmegreen et al., 1990; Varela et al., 2004). Furthermore, at the time of these studies, the complex relationship of the bar fraction with galaxy properties (§ 5.2) was still unknown, and therefore not taken into account when analyzing and interpreting the results.

In M09 (Chapter 3) and M11 (Chapter 4), we undertake some of the most comprehensive, quantitative studies of barred disks in dense environ-

ments, by deriving the optical bar fraction and properties in the Abell 901/902 supercluster system at $z \sim 0.165$, and the core of the Coma cluster at $z \sim 0.02$, the densest environment in the local Universe.

In M09 (Chapter 3), we use ellipse-fitting on ACS F606W images to identify and characterize the properties of bars in the Abell 901/902 cluster system at $z \sim 0.165$. In addition, we use visual classification to characterize secondary morphological parameters such as the prominence of the bulge and whether the galaxy appears clumpy or smooth. *Within the Abell 901/902 cluster system*, at intermediate densities (e.g., $\log\Sigma_{10}$=1.7–2.3, where Σ_{10} is defined as the galaxy number density in $(Mpc/h)^{-2}$, calculated by finding the radius enclosing the 10 nearest neighbors to a galaxy), we find that the bar fraction is not strongly dependent on environment as function of distance from the cluster center (within a factor of $\sim$ 1.3; Fig. 5.9).

We compare the results for Abell 901/902 to those for field samples, specifically MJ07 (Chapter 2) and Aguerri et al. (2009), where bar identification and characterization was also performed through ellipse-fitting. Given the dependence of the bar fraction on galaxy properties (§ 5.2), we compare to galaxy subsamples with similar morphological properties (e.g., Hubble type, luminosity). We find that for bright ($M_{\rm V} \leq -20$), early Hubble types, *the optical bar fraction in the Abell 901/2 clusters is comparable within a factor of $\sim$ 1.3 to that of field galaxies at lower redshifts ($z \sim$ 0–0.04).*

In M11 (Chapter 4), we characterize the optical bar fraction in S0 galaxies with $M_{\rm V} \lesssim -18$ (using *HST* ACS F814W images) in the central re-

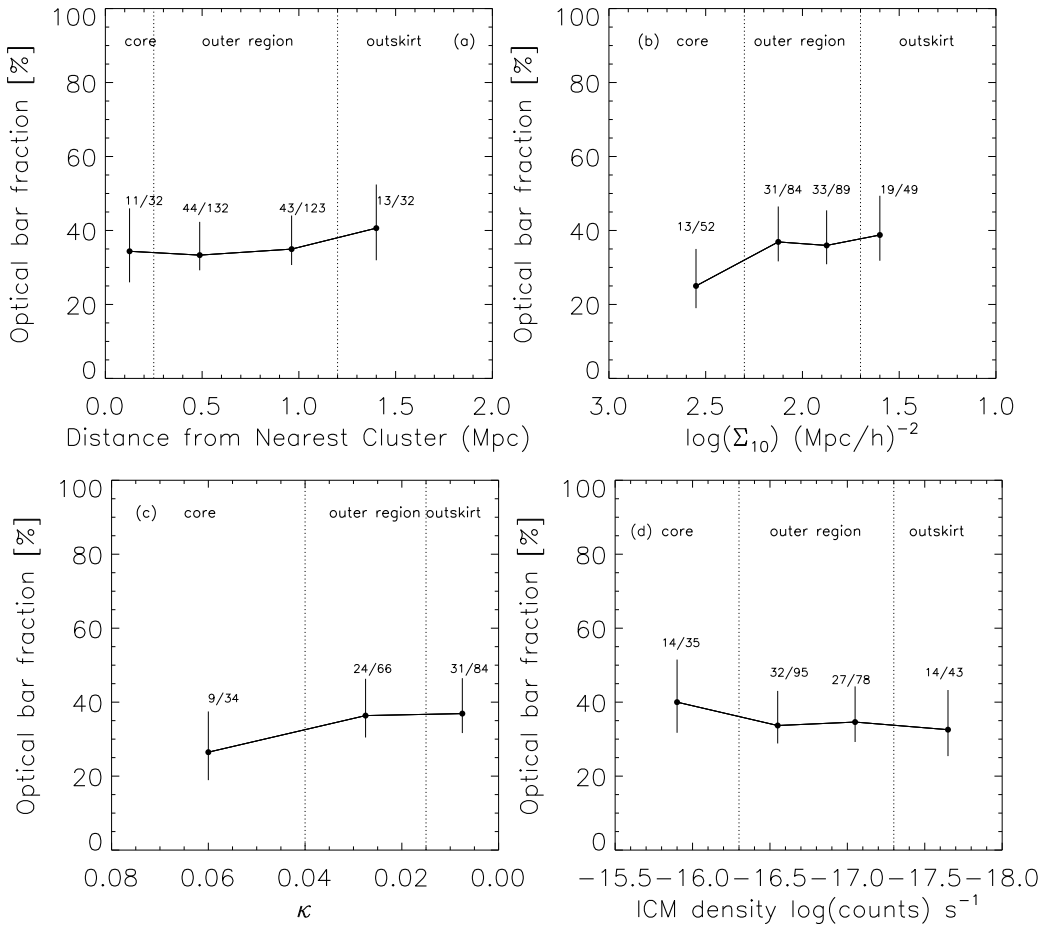

Figure 5.9 The fraction of barred galaxies a function of: (a) distance from nearest cluster center, (b) logΣ_{10}, (c) κ, and (d) ICM density in the Abell 901/902 cluster system (Chapter 3; M09). The vertical dashed lines denote the core radius at 0.25 Mpc and the virial radius at 1.2 Mpc. We find that between the core and the virial radius of the cluster ($R \sim 0.25$ to 1.2 Mpc), the optical bar fraction does not depend strongly on the local environment density tracers (κ, Σ_{10}, and ICM density), and varies at most by a factor of ~ 1.3, allowed by the error bars.

gions of the Coma cluster at $z \sim 0.02$. Due to the potential dilution of the bar signature by light from a relatively large, bright bulge, we take special care in deriving the bar fraction for these S0 galaxies, using three methods: ellipse fitting with strict criteria, ellipse fitting with relaxed criteria, and visual classification (see § 4.3.2.2). We compare our results in the Coma core ($n \sim$ 10,000 gal Mpc^{-3}) to those in less dense clusters (Abell 901/902 with $n \sim 1000$ gal Mpc^{-3}, and Virgo with $n \sim 300$ gal Mpc^{-3}). *Once the samples are matched as well as possible in absolute magnitude, color, and detection method, we find no statistically significant difference (within the error bars of ±10%) in the optical bar fraction for S0s across environments spanning two orders of magnitude in number density ($n \sim$ 300 to 10,000 gal Mpc^{-3}).* This result is presented in Fig. 5.10. We note that Fig. 5.10 shows a hint of an increase in the mean bar fraction toward the dense core of the Coma cluster, however given the error bars, we cannot say whether this trend is significant.

Taken together, the results in M09 (Chapter 2) and M11 (Chapter 3) reveal that the optical bar fraction does not show a statistically significant variation (within the error bars of ±10%) with environment density for bright, early-type disk galaxies between intermediate-density clusters and the field (M09), and specifically for S0s over two orders of magnitude in cluster galaxy number density ($n \sim$ 300 to 10,000 gal Mpc^{-3}; M11). Our results are consistent with concurrent and subsequent studies, who also do not find a variation in the bar fraction with environment density at low (van den Bergh, 2002; Aguerri et al., 2009) and intermediate (Barazza et al., 2009; Cameron et al., 2010)

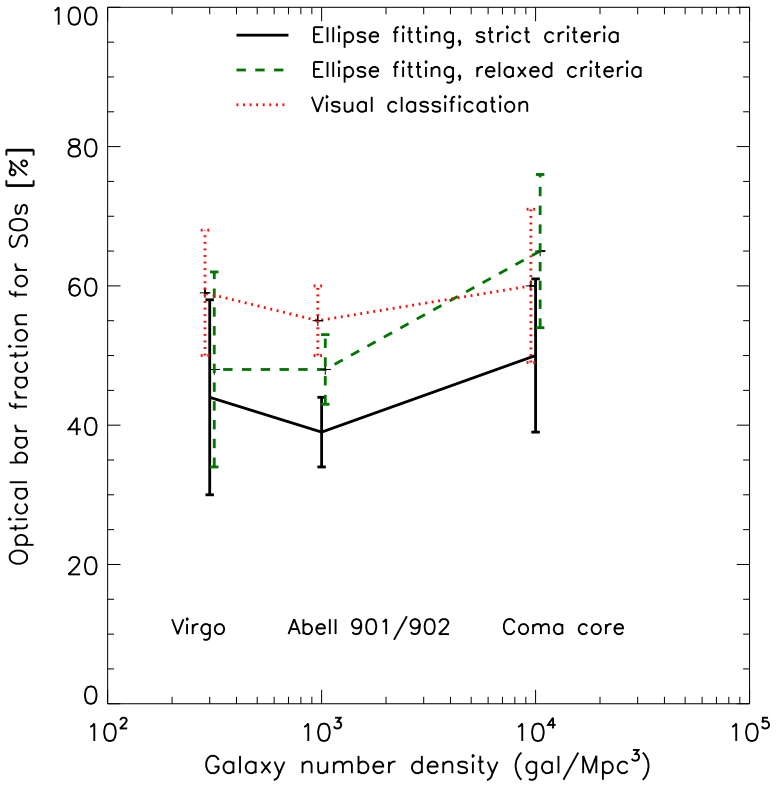

Figure 5.10 The optical bar fraction for bright ($M_{\rm V} \lesssim -18$) S0 galaxies as a function of environment density, characterized through three different methods: ellipse fitting with strict criteria, ellipse fitting with relaxed criteria, and visual classification (see Chapter 4). The different environments probed are the high-density core of Coma ($n \sim$ 10,000 gal/Mpc^3), the intermediate-density Abell 901/902 cluster system ($n \sim$ 1000 gal/Mpc^3), and the low-density Virgo cluster ($n \sim$ 300 gal/Mpc^3). The bar fraction for S0s does not show a statistically significant variation across the environments probed, within the error bars.

redshifts.

What can these results tell us about the competing effects of cluster environments (e.g., harassment, interactions with the ICM) on disk galaxies? As discussed in § 5.3, theoretical studies of bar formation and evolution in a cosmological context (Heller et al., 2007) as well as recent observational results (Cameron et al., 2010), suggest that the bar fraction is set at early times ($z \sim 1$), especially for massive disks. Our results in M09 (Chapter 2) and M11 (Chapter 3) show that the bar fraction (at least for bright, early-type disk galaxies) is not significantly enhanced in cluster environments (Fig. 5.10), in agreement with other observational studies (van den Bergh, 2002; Aguerri et al., 2009; Barazza et al., 2009; Cameron et al., 2010). How do these results make sense in light of many theoretical studies that show that galaxy interactions can trigger bars in unbarred galaxies (e.g., Noguchi, 1988; Mihos & Hernquist, 1996)? Below, we consider the competing effects present in galaxy clusters to speculate why this may be the case.

First, we consider the types of encounters taking place in galaxy clusters. In a rich cluster, where the projected galaxy number density (n) and galaxy velocity dispersion (σ) is high, the timescale for close interactions (or collision timescale, $t_{\rm coll}$) will be short. We can estimate this timescale using:

$$t_{\rm coll} = \frac{1}{n\sigma_{\rm gal}A}, \tag{5.4}$$

where n is the galaxy number density, $\sigma_{\rm gal}$ is the galaxy velocity dispersion,

and A is the cross-section for close interactions defined as

$$A = \pi f (2r_{\rm gal})^2. \tag{5.5}$$

We assume f (the gravitational focusing factor) is unity, $r_{gal} \sim 10$ kpc. For the Coma core $\sigma_{\rm gal} \sim 900$ km/s, and $n \sim 10{,}000$ gal/Mpc^3 (The & White 1986) giving a short timescale for close interactions $t_{\rm coll} \sim 90$ Myr.

However, although these close galaxy-galaxy interactions are frequent in a rich cluster, the large galaxy velocity dispersions present ($\sigma \sim 900$ km/s for Coma, 800–1200 km/s for Abell 901/902, and 400–750 km/s for Virgo) mean that each single encounter will be a *high speed one*. Unlike single slow, strong encounters, a single high-speed encounter will typically not induce a large amount of tidal damage and not lead to major mergers. Single high-speed encounters may not be as effective in inducing bars as slow, strong encounters, because the timescale over which gravitational torques act is short.

Second, simulations show that not all galaxy interactions will necessarily induce a bar. In fact, whether this happens depends on the geometry of the encounter; bars are favored in prograde interactions, but not in retrograde ones, which also have little or no effect on an already existing bar (e.g., Gerin et al., 1990; Steinmetz & Navarro, 2002; Romano-Díaz et al., 2008; Aguerri & González-García, 2009). In addition, the effect of an interaction on disk stability may also depend on the specific properties of the galaxies, such as the DM halo-to-disk ratio (Gerin et al., 1990).

Finally, in cluster environments, many processes combine to make galax-

ies more dynamically hot (i.e., with large Toomre Q), which makes them more stable to bar formation (§5.2). The cumulative effect of many high-speed and weak encounters (galaxy harassment), can tidally heat disks (Moore et al., 1996; Aguerri & González-García, 2009). Further, the accelerated star formation history in cluster environments (e.g., Balogh et al., 2004; Blanton et al., 2005; Hogg et al., 2003) as well as physical processes such as ram pressure stripping (Gunn & Gott, 1972; Larson et al., 1980; Quilis et al., 2000) will make S0 disks gas-poor, thus making them less bar-unstable.

We therefore speculate that the predominance of high speed encounters over slow ones, the tidal heating of S0 disks, and the low gas content of S0s in rich clusters, make it difficult for many new bars to be induced in S0 disks, which form in clusters through the transformation of spirals infalling into the cluster environment.

It is also important to note that the arguments above, which explain why the bar fraction might not be greatly enhanced in rich clusters compared to the field, would lead to a rather different prediction for how the bar fraction in groups would compare to that in the field. In a group, the number density is moderately high ($n \sim 10$) but the galaxy velocity dispersions are typically low ($\sigma \sim 100$; Tago et al., 2008). Therefore slow, strong encounters are expected to be frequent in groups. Such encounters are likely to induce extra bars in disk galaxies compared to the field, particularly given the fact that the disks will not be stripped of their cold gas in groups as they would in rich clusters. In this context, we note that indeed higher bar fractions have been reported

for early-type galaxies in binary pairs (Elmegreen et al., 1990) and early-type galaxies with close companions (Varela et al., 2004).

5.5 Next steps in the field

While much has been unraveled in recent years about the evolution of bars and their host disks, there is ample opportunity for new progress. The availability of large galaxy surveys like the SDSS, and those conducted with the *HST* ACS and WFC3, as well as upcoming new instruments such as the VIRUS-P integral field spectrometer (IFU Hill et al., 2008), will enable future studies to tackle some interesting open issues.

1. *The complex dependence of the bar fraction on galaxy properties in the local Universe:*

   Studies are just starting to explore the interesting picture that is emerging in Fig. 5.4, and its implications for galaxy evolution. One of the largest studies to date is that of Nair & Abraham (2010b). However, this study uses only visual classification and thus cannot provide interesting results on the quantitative properties of bars and disks. The next step is to combine quantitative methods, such as bulge-disk-bar decompositions (e.g., Weinzirl et al., 2009; Gadotti, 2011) with large samples like the one studied in Nair & Abraham (2010b). Such a study could shed more light on the physics behind the trends in the bar fraction observed, by quantitatively constraining the relationships between galaxy

components (bulge, bar, disk) in a sample comprised of a statistically significant number of galaxies at a wide range of morphological types. It would also allow for the much-needed step of moving beyond the Hubble classification (which works well only for low-redshift field galaxies) and investigating the multi-dimensional parameter space where galaxy properties such as the bulge-to-disk ratio, luminosity, and gas content can be studied independently rather than assumed to be a priori correlated.

2. *Spatially-resolved spectroscopic studies of individual galaxies:*
   New state-of-the art instruments such as VIRUS-P (Hill et al., 2008), will offer a detailed view into the inner workings of barred disks. Such studies can greatly advance the field by: (1) testing theoretical predictions on gas kinematics in barred disks, (2) quantifying the gas inflow that bars are driving, and perhaps connecting this to measures of bar strength (such as ellipticity, or the bar torque $Q_{\rm b}$), (3) characterizing the star-formation environment along bars and determining whether the strength of the shocks on the leading edges of bars can inhibit star formation, and (4) determining the stellar populations and chemical gradients in barred galaxies and comparing the ages of various galaxy components (bulge, bar, disk, ring) in barred and unbarred galaxies of various Hubble types. In the past, studying galaxies in such detail has been an extremely time-consuming undertaking using regular slit spectroscopy or Fabry-Perot methods (e.g., Regan et al., 1997, for NGC 1530). However, the advent of IFUs such as VIRUS-P with its large field of view ($110''$) combined

with adequate spatial resolution ($\sim 4''$) is ideally suited to greatly expand observational results addressing all of the above issues.

Several barred galaxies have been observed with VIRUS-P as part of the VENGA survey (Blanc et al., 2010). While the analysis of the VIRUS-P IFU data was not initially part of this thesis, we nonetheless started a preliminary analysis and pilot study of the barred galaxy NGC 2903. Some early results are shown in Fig. 5.11. In Fig. 5.11, the stellar bar is evident in the 2MASS H-band image, along with the beginning of the spiral arms at the end of the bar. In the left panel, the overplotted contours show the $H\alpha$ velocity field from VIRUS-P. The $H\alpha$ velocity field deviates from the spider diagram for pure circular motion, indicative of non-circular streaming along the bar. In the right panel, we overplot the $H\alpha$ flux from VIRUS-P. As expected, the ionized gas is offset toward the leading edges of the bar in a spiral pattern due to the presence of the '$x2'$ orbits perpendicular to the bar major axis (Athanassoula, 1992b).

3. *Evolution of the fraction and properties of bars as a function of redshift:* As outlined in §5.3, many open questions remain regarding the evolution of barred disks at intermediate redshifts. The main area of opportunity within the next decade will be to characterize the fraction of barred galaxies in the *rest-frame NIR* out to $z \sim 1$ and beyond, seeing bars that were previously obscured by dust and gas at optical wavelengths. These results would provide valuable constraints for theoretical studies attempting to investigate galaxy evolution in a cosmological context.

As outlined in §5.3, the NIRcam PSF of $\sim 0.08''$ at the wavelength range between 0.6 to 5 μ, will be capable of resolving primary bars with $a_{\rm bar} \sim 1.6$ kpc out to $z \sim 1$ and those with $a_{\rm bar} > 2.5$ kpc out to $z \sim 2$ *in the rest-frame NIR*. In contrast, currently available NIR imagers such as the Wide Field Camera 3 (WFC3) on the *HST* can only resolve bars with $a_{\rm bar} > 2.5$ kpc out to $z \sim 0.7$ in the rest-frame NIR, thus missing a significant fraction (at least 33%) of barred disks at intermediate redshifts.

Another question of fundamental importance is to determine the impact that bars have on the *young* galaxies at these epochs, when the Universe was about half its present age. As outlined in Chapter 1, for local galaxies, observations show that bars drive central starbursts and may build central components such as pseudobulges. How do bars relate to the disk growth, central mass concentration, bulge-to-disk ratio, SF activity, and morphology of their hosts at intermediate redshifts? Is there evidence that bars are driving secular evolution across the Hubble sequence over the last 9 Gyr? The current resolution of instruments such as *Spitzer* at 24 μ is $\sim 6''$, corresponding to ~ 40 kpc at $z \sim 0.5$. This precludes a study investigating the role of bars in inducing circumnuclear starbursts in galaxies at intermediate redshifts. Future instruments, such as the Mid-Infra Red Imager (MIRI) planned for JWST, might make such a study possible, by resolving the central few kiloparsecs of galaxies at rest-frame infrared wavelengths (up to 24 μ) at intermediate redshifts,

where its PSF of $\sim 0.2''$ corresponds to ~ 1.3 kpc at $z \sim 0.5$.

4. *Evolution of barred disks in dense environments:*

   While we have made important first steps in characterizing the fraction and properties of barred disks in clusters (Chapter 3, Chapter 4), this aspect of the field is still in its infancy. Important next steps include comparing the results from M11 (Chapter 4) to a fully-matched field sample (in terms of galaxy properties, as well as bar detection method), establishing more cluster environment data points, which are necessary to solidify the results and to make possible a detailed exploration of the bar fraction and properties as a function of environment density for various galaxy morphologies. In addition, there as yet do not exist any detailed, quantitative studies focusing on barred disks in group environments. These studies are necessary to test the interesting predictions for groups outlined in §5.4, namely that barred disks in such environments should be much more common than in both field and dense cluster environments.

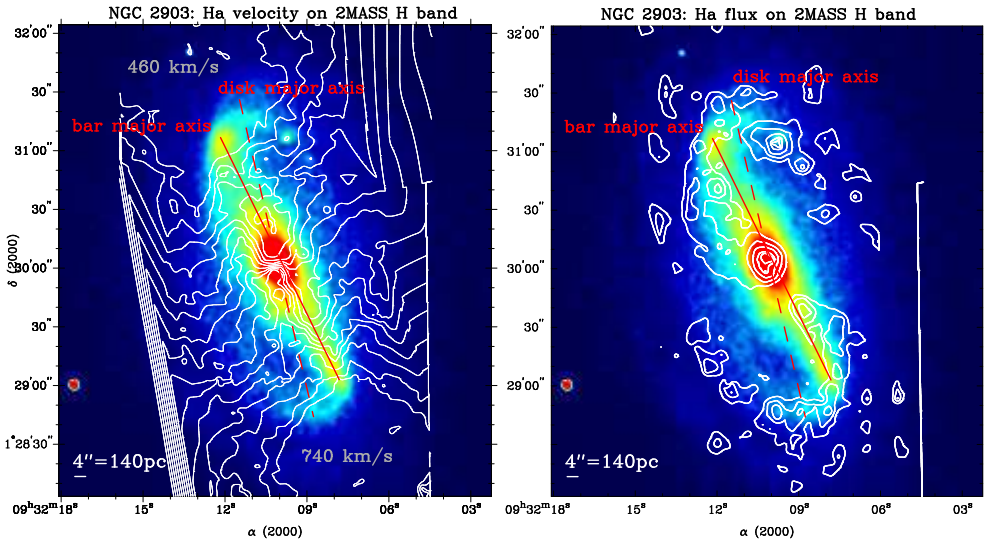

Figure 5.11 *Left:* The $H\alpha$ velocity field (from VIRUS-P) overlaid onto the H-band image of NGC 2903 from 2MASS. The latter shows the stellar bar with the beginning of spiral arms at the end of the bar. The diagonal red line denotes the bar major axis. The $H\alpha$ velocity field deviates from the spider diagram for pure circular motion. The deviations are indicative of non-circular streaming motions along the bar, and possibly of shocks on the leading edges of the bar. *Right:* The $H\alpha$ flux (from VIRUS-P) on the H-band image of NGC 2903. The ionized gas is offset toward the leading edges of the bar in a spiral pattern due to the presence of '$x2$' orbits perpendicular to the bar major axis (Athanassoula, 1992b).

Appendix

Appendix 1

Methodology

In Chapters 2, 3, and 4, we outline the methods we use to identify disks and bars. These chapters describe three different studies, focusing on galaxies at different epochs and environments, using data at optical and near infra-red (NIR) wavelengths. In this Appendix, we summarize the essential methods and concepts for bar identification.

There are four main methods to identify bars: visual classification, ellipse fits on observed and deprojected images, the $Q_{\rm b}$ method, and bulge-disk-bar decompositions. In this thesis, we use ellipse fits, supplemented with checks from visual classification and bulge-disk-bar decomposition.

1.1 Visual classification

In early studies, as well as in the RC3, bars were detected and characterized through visual classification (Chapter 1). While visual classification has its advantages and was an invaluable first step, it did not provide quantitative properties of bars or an objective measure of the frequency of barred galaxies in the local universe. Such measures from quantitative methods are necessary for objective comparisons with results at higher redshifts or across

environments. We note that results from bar studies relying primarily on visual classification must be considered with caution. Visual classification can give bar fractions both higher and lower than quantitative methods, depending on the criteria used to identify bars and the expertise of the classifier. For example, the visual *optical* bar fraction from the RC3 for local galaxies ($\sim$ 60%) is higher than that found from quantitative studies ($\sim$ 45%; MJ07; Barazza, Jogee, & Marinova, 2008, hereafter BJM08; Reese et al., 2007) because expert morphologists used subtle secondary tracers (e.g., dust lanes) to classify galaxies as barred, whereas the stellar bar itself is only clearly revealed in *near infra-red (NIR)* images. In contrast, in studies such as the one based on Galaxy Zoo (Masters et al., 2011), where the galaxy classifications are performed by volunteers from the general public, only the strong, large, obvious bars are detected (Barazza, F., private communication; Masters et al., 2011), leading to a much lower value for the optical bar fraction.

1.2 Ellipse fits

Athanassoula et al. (1990) showed that bars can be well-fitted with generalized ellipses. This allows for the quantitative measurement of the axis ratio of the bar (specifically the maximum ellipticity) as well as its length. The axis ratio of the bar, along with its mass, are related to the gravitational potential and therefore the 'strength' of the bar (Athanassoula, 1992a). Once measured, the bar strength (as characterized by the axis ratio) can be related to other properties seen in galaxies, such as the host morphology or the pres-

ence of central starbursts. Many studies have employed this method (e.g., Knapen et al., 1995; Wozniak et al., 1995; Friedli et al., 1996; Regan et al., 1997; Mulchaey & Regan, 1997; Jogee, 1999; Jogee et al., 1999, 2002a,b, 2004; Knapen et al., 2000; Laine et al., 2002; Sheth et al., 2003; Elmegreen et al., 2004; Menéndez-Delmestre et al., 2007; Sheth et al., 2008) due to the fact that it is direct, requires the least amount of assumptions, and can be set up to work efficiently on large samples (e.g., Jogee et al., 2004; Marinova & Jogee, 2007; Sheth et al., 2008).

Therefore, we adopt the widely used method of isophotal ellipse fitting for detecting and characterizing bars in this thesis. Detecting and characterizing a bar with ellipse fits involves the following steps. We use the standard IRAF task $ELLIPSE$ in conjunction with an adaptive wrapper (Jogee et al., 2004), which runs $ELLIPSE$ iteratively on each galaxy until the best fit is found or up to a maximum number of times specified by the user. Ellipses are fit to the galaxy isophotes out to a maximum distance ($a_{\rm disk}$) where the brightness of the isophotes reaches the noise level. We note that the value of $a_{\rm disk}$ depends on the depth of the image, as $a_{\rm disk}$ will reach larger values for deeper images. However for the purpose of bar detection, it is only necessary for the radial profile to extend beyond the bar into the more circular region of the disk. We typically set the maximum allowed iterations to 300, however for most galaxies a good fit is achieved in only a few iterations. A good fit is one where an ellipse can be fitted at every isophote out to $a_{\rm disk}$.

Once the galaxies are fitted, we use an interactive visualization tool to

display the overlays of the fit on the galaxy image, as well as the radial profiles of surface brightness, ellipticity (e), and position angle (PA). Examples of the overlays and radial profiles are shown in Figs. 2.2, 2.4, and 2.5. Using the radial profiles of ellipticity (e) and PA, we classify the galaxies as 'highly inclined', 'barred', or 'unbarred'. Following convention, galaxies with outer disk $e > 0.5$ (corresponding to $i > 60°$) are deemed 'highly inclined' and discarded from further analysis, due to the fact that it is difficult to systematically identify such galaxies as barred or unbarred (Fig. 2.2). A galaxy is classified as barred if the radial variation of ellipticity and PA follows the behavior that is expected based on the dominant orbits of a barred potential. Specifically, the following conditions must be satisfied before a galaxy is deemed to be barred: (1) The ellipticity, e, increases steadily to a global maximum, $e_{\rm bar}$, greater than 0.25, while the PA value remains constant (within $\pm 10°$). This criterion is based on the fact that the main bar-supporting orbits, namely the 'x_1' family of orbits, can be modeled by concentric ellipses with a constant PA as a function of radius in the bar region (Athanassoula, 1992a). The requirement that the PA must remain constant in the bar region is important for excluding other spurious elliptical features that may mimic a bar signature in their ellipticity profile. (2) Then, at the transition from the bar to the disk region, the ellipticity, e, must drop by at least 0.1, and the PA usually changes. This criterion is justified by the fact that we expect a transition from the highly eccentric x_1 orbits near the bar end to the more circular orbits in the disk. We also note that the drop in ellipticity by 0.1 at the transition from bar to disk has been

shown to work well in identifying bars (e.g., Knapen et al., 2000; Laine et al., 2002; Jogee et al., 2002a,b, 2004). Figure 2.5 shows an example of the overlays and radial profiles of e and PA on the barred galaxy NGC 4643.

This method can be applied on both projected and deprojected images, as well as on the analytically-deprojected radial profiles of e and PA. In MJ07 (Chapter 2), we find good agreement between ellipse-fitting the deprojected image and simply deprojecting the radial profiles analytically for the same galaxy (see Fig. 2.7). In addition, we find that deprojection does not have a statistically significant impact on the results for the bar fraction and properties, especially for the moderately large sample ($N \sim 100$ galaxies) in MJ07.

The ellipse fitting method is very reliable at detecting bars in the vast majority of galaxies, but we note that in our study of S0 galaxies in the Coma cluster, we find that for galaxies with large, bright bulges (such as those in S0s in the Coma cluster), the strict ellipse fit criteria for bar detection outlined above may miss bars in some cases (Chapter 4). Specifically, this is more likely to happen when the bar is relatively short, and the bulge is relatively large and bright, while the galaxy has a significant inclination ($i \gtrsim 50^\circ$). Then, the dilution of the bar isophotes by the rounder isophotes of the bulge along with projection effects can combine to make the peak bar ellipticity a *local* instead of *global* maximum in the radial profile of ellipticity (with the disk ellipticity then being the global maximum). In this case, the bar can still be identified via the ellipse fit radial profiles, if the strict ellipse fit criteria are relaxed so

that a *local* maximum for the peak bar ellipticity is acceptable. An example of a galaxy where this happens is shown in Fig. 4.7. We note that if the radial profiles of ellipticity and PA for such galaxies are deprojected (or the ellipse fits are performed on deprojected images), the bar ellipticity does indeed become the *global* maximum and the bar can be detected using the strict ellipse fit criteria as well (M11; Chapter 4).

1.3 Other methods

Other quantitative methods have also been employed in recent years, such as the $Q_{\rm b}$ method (which attempts to measure the torque exerted by the bar; Block et al., 2002; Buta et al., 2003, 2005), bulge-disk-bar decomposition (e.g., Laurikainen et al., 2007, 2009; Weinzirl et al., 2009; Gadotti, 2011), and Fourier decomposition (Reese et al., 2007). In Chapter 2 (MJ07) we discuss in more detail the disadvantages and advantages of these quantitative methods of analyzing barred galaxies. We note that our results in MJ07 (Chapter 2) are in excellent agreement with those of Weinzirl et al. (2009), who used bulge-disk-bar decomposition on the same sample of galaxies.

Bibliography

Abazajian, K., Adelman-McCarthy, J. K., Agüeros, M. A., Allam, S. S., Anderson, K., Anderson, S. F., Annis, J., Bahcall, N. A., Baldry, I. K., Bastian, S., Berlind, A., Bernardi, M., Blanton, M. R., Bochanski, Jr., J. J., Boroski, W. N., Briggs, J. W., Brinkmann, J., Brunner, R. J., Budavári, T., Carey, L. N., Carliles, S., Castander, F. J., Connolly, A. J., Csabai, I., Doi, M., Dong, F., Eisenstein, D. J., Evans, M. L., Fan, X., Finkbeiner, D. P., Friedman, S. D., Frieman, J. A., Fukugita, M., Gal, R. R., Gillespie, B., Glazebrook, K., Gray, J., Grebel, E. K., Gunn, J. E., Gurbani, V. K., Hall, P. B., Hamabe, M., Harris, F. H., Harris, H. C., Harvanek, M., Heckman, T. M., Hendry, J. S., Hennessy, G. S., Hindsley, R. B., Hogan, C. J., Hogg, D. W., Holmgren, D. J., Ichikawa, S.-i., Ichikawa, T., Ivezić, Ž., Jester, S., Johnston, D. E., Jorgensen, A. M., Kent, S. M., Kleinman, S. J., Knapp, G. R., Kniazev, A. Y., Kron, R. G., Krzesinski, J., Kunszt, P. Z., Kuropatkin, N., Lamb, D. Q., Lampeitl, H., Lee, B. C., Leger, R. F., Li, N., Lin, H., Loh, Y.-S., Long, D. C., Loveday, J., Lupton, R. H., Malik, T., Margon, B., Matsubara, T., McGehee, P. M., McKay, T. A., Meiksin, A., Munn, J. A., Nakajima, R., Nash, T., Neilsen, Jr., E. H., Newberg, H. J., Newman, P. R., Nichol, R. C., Nicinski, T., Nieto-Santisteban, M., Nitta, A., Okamura, S., O'Mullane, W., Ostriker, J. P., Owen, R., Padmanabhan, N., Peoples, J., Pier, J. R., Pope, A. C., Quinn, T. R., Richards, G. T., Rich-

mond, M. W., Rix, H.-W., Rockosi, C. M., Schlegel, D. J., Schneider, D. P., Scranton, R., Sekiguchi, M., Seljak, U., Sergey, G., Sesar, B., Sheldon, E., Shimasaku, K., Siegmund, W. A., Silvestri, N. M., Smith, J. A., Smolčić, V., Snedden, S. A., Stebbins, A., Stoughton, C., Strauss, M. A., SubbaRao, M., Szalay, A. S., Szapudi, I., Szkody, P., Szokoly, G. P., Tegmark, M., Teodoro, L., Thakar, A. R., Tremonti, C., Tucker, D. L., Uomoto, A., Vanden Berk, D. E., Vandenberg, J., Vogeley, M. S., Voges, W., Vogt, N. P., Walkowicz, L. M., Wang, S.-i., Weinberg, D. H., West, A. A., White, S. D. M., Wilhite, B. C., Xu, Y., Yanny, B., Yasuda, N., Yip, C.-W., Yocum, D. R., York, D. G., Zehavi, I., Zibetti, S., & Zucker, D. B. 2004, AJ, 128, 502

Abraham, R. G. & Merrifield, M. R. 2000, AJ, 120, 2835

Abraham, R. G., Merrifield, M. R., Ellis, R. S., Tanvir, N. R., & Brinchmann, J. 1999, MNRAS, 308, 569

Aguerri, J. A. L., Debattista, V. P., & Corsini, E. M. 2003, MNRAS, 338, 465

Aguerri, J. A. L. & González-García, A. C. 2009, A&A, 494, 891

Aguerri, J. A. L., Iglesias-Páramo, J., Vílchez, J. M., Muñoz-Tuñón, C., & Sánchez-Janssen, R. 2005, AJ, 130, 475

Aguerri, J. A. L., Méndez-Abreu, J., & Corsini, E. M. 2009, A&A, 495, 491

Andersen, V. 1996, AJ, 111, 1805

Athanassoula, E. 1992a, MNRAS, 259, 328

—. 1992b, MNRAS, 259, 345

—. 2002, ApJ, 569, L83

—. 2003, MNRAS, 341, 1179

—. 2005, MNRAS, 358, 1477

Athanassoula, E., Bienayme, O., Martinet, L., & Pfenniger, D. 1983, A&A, 127, 349

Athanassoula, E. & Bosma, A. 1985, ARA&A, 23, 147

Athanassoula, E. & Misiriotis, A. 2002, MNRAS, 330, 35

Athanassoula, E., Morin, S., Wozniak, H., Puy, D., Pierce, M. J., Lombard, J., & Bosma, A. 1990, MNRAS, 245, 130

Balcells, M., Graham, A. W., Domínguez-Palmero, L., & Peletier, R. F. 2003, ApJ, 582, L79

Ball, R., Sargent, A. I., Scoville, N. Z., Lo, K. Y., & Scott, S. L. 1985, ApJ, 298, L21

Balogh, M., Eke, V., Miller, C., Lewis, I., Bower, R., Couch, W., Nichol, R., Bland-Hawthorn, J., Baldry, I. K., Baugh, C., Bridges, T., Cannon, R., Cole, S., Colless, M., Collins, C., Cross, N., Dalton, G., de Propris, R., Driver, S. P., Efstathiou, G., Ellis, R. S., Frenk, C. S., Glazebrook, K., Gomez, P., Gray, A., Hawkins, E., Jackson, C., Lahav, O., Lumsden,

S., Maddox, S., Madgwick, D., Norberg, P., Peacock, J. A., Percival, W., Peterson, B. A., Sutherland, W., & Taylor, K. 2004, MNRAS, 348, 1355

Balogh, M. L., Navarro, J. F., & Morris, S. L. 2000, ApJ, 540, 113

Barazza, F. D., Binggeli, B., & Jerjen, H. 2002, A&A, 391, 823

Barazza, F. D., Jablonka, P., Desai, V., Jogee, S., Aragón-Salamanca, A., De Lucia, G., Saglia, R. P., Halliday, C., Poggianti, B. M., Dalcanton, J. J., Rudnick, G., Milvang-Jensen, B., Noll, S., Simard, L., Clowe, D. I., Pelló, R., White, S. D. M., & Zaritsky, D. 2009, A&A, 497, 713

Barazza, F. D., Jogee, S., & Marinova, I. 2008, ApJ, 675, 1194

Barazza, F. D., Jogee, S., Rix, H.-W., Barden, M., Bell, E. F., Caldwell, J. A. R., McIntosh, D. H., Meisenheimer, K., Peng, C. Y., & Wolf, C. 2006, ApJ, 643, 162

Barden, M., Rix, H.-W., Somerville, R. S., Bell, E. F., Häußler, B., Peng, C. Y., Borch, A., Beckwith, S. V. W., Caldwell, J. A. R., Heymans, C., Jahnke, K., Jogee, S., McIntosh, D. H., Meisenheimer, K., Sánchez, S. F., Wisotzki, L., & Wolf, C. 2005, ApJ, 635, 959

Bell, E. F., McIntosh, D. H., Barden, M., Wolf, C., Caldwell, J. A. R., Rix, H.-W., Beckwith, S. V. W., Borch, A., Häussler, B., Jahnke, K., Jogee, S., Meisenheimer, K., Peng, C., Sanchez, S. F., Somerville, R. S., & Wisotzki, L. 2004, ApJ, 600, L11

Bell, E. F., McIntosh, D. H., Katz, N., & Weinberg, M. D. 2003, ApJS, 149, 289

Bell, E. F., Papovich, C., Wolf, C., Le Floc'h, E., Caldwell, J. A. R., Barden, M., Egami, E., McIntosh, D. H., Meisenheimer, K., Pérez-González, P. G., Rieke, G. H., Rieke, M. J., Rigby, J. R., & Rix, H.-W. 2005, ApJ, 625, 23

Bell, E. F., Phleps, S., Somerville, R. S., Wolf, C., Borch, A., & Meisenheimer, K. 2006, ApJ, 652, 270

Berentzen, I., Heller, C. H., Shlosman, I., & Fricke, K. J. 1998, MNRAS, 300, 49

Berentzen, I. & Shlosman, I. 2006, ApJ, 648, 807

Berentzen, I., Shlosman, I., & Jogee, S. 2006, ApJ, 637, 582

Berentzen, I., Shlosman, I., Martinez-Valpuesta, I., & Heller, C. H. 2007, ApJ, 666, 189

Binggeli, B. & Cameron, L. M. 1991, A&A, 252, 27

Binggeli, B., Sandage, A., & Tammann, G. A. 1988, ARA&A, 26, 509

Binney, J. & Tremaine, S. 1987, Galactic dynamics, ed. Binney, J. & Tremaine, S.

Blanc, G. A., Gebhardt, K., Heiderman, A., Evans, II, N. J., Jogee, S., van den Bosch, R., Marinova, I., Weinzirl, T., Yoachim, P., Drory, N., Fabricius, M., Fisher, D., Hao, L., MacQueen, P. J., Shen, J., Hill, G. J., &

Kormendy, J. 2010, in Astronomical Society of the Pacific Conference Series, Vol. 432, New Horizons in Astronomy: Frank N. Bash Symposium 2009, ed. L. M. Stanford, J. D. Green, L. Hao, & Y. Mao, 180–+

Blanton, M. R., Lupton, R. H., Schlegel, D. J., Strauss, M. A., Brinkmann, J., Fukugita, M., & Loveday, J. 2005, ApJ, 631, 208

Block, D. L., Bertin, G., Stockton, A., Grosbol, P., Moorwood, A. F. M., & Peletier, R. F. 1994, A&A, 288, 365

Block, D. L., Bournaud, F., Combes, F., Puerari, I., & Buta, R. 2002, A&A, 394, L35

Block, D. L., Buta, R., Knapen, J. H., Elmegreen, D. M., Elmegreen, B. G., & Puerari, I. 2004, AJ, 128, 183

Borch, A., Meisenheimer, K., Bell, E. F., Rix, H.-W., Wolf, C., Dye, S., Kleinheinrich, M., Kovacs, Z., & Wisotzki, L. 2006, A&A, 453, 869

Bournaud, F. & Combes, F. 2002, A&A, 392, 83

Bournaud, F., Combes, F., & Semelin, B. 2005, MNRAS, 364, L18

Brooks, A. M., Governato, F., Quinn, T., Brook, C. B., & Wadsley, J. 2009, ApJ, 694, 396

Burbidge, E. M., Burbidge, G. R., & Prendergast, K. H. 1962, ApJ, 136, 119

Bureau, M. & Athanassoula, E. 2005, ApJ, 626, 159

Buta, R., Block, D. L., & Knapen, J. H. 2003, AJ, 126, 1148

Buta, R. & Crocker, D. A. 1993, AJ, 106, 939

Buta, R., Vasylyev, S., Salo, H., & Laurikainen, E. 2005, AJ, 130, 506

Byrd, G. & Valtonen, M. 1990, ApJ, 350, 89

Cameron, E., Carollo, C. M., Oesch, P., Aller, M. C., Bschorr, T., Cerulo, P., Aussel, H., Capak, P., Le Floc'h, E., Ilbert, O., Kneib, J.-P., Koekemoer, A., Leauthaud, A., Lilly, S. J., Massey, R., McCracken, H. J., Rhodes, J., Salvato, M., Sanders, D. B., Scoville, N., Sheth, K., Taniguchi, Y., & Thompson, D. 2010, MNRAS, 409, 346

Carter, D. 1978, MNRAS, 182, 797

—. 1987, ApJ, 312, 514

Carter, D., Goudfrooij, P., Mobasher, B., Ferguson, H. C., Puzia, T. H., Aguerri, A. L., Balcells, M., Batcheldor, D., Bridges, T. J., Davies, J. I., Erwin, P., Graham, A. W., Guzmán, R., Hammer, D., Hornschemeier, A., Hoyos, C., Hudson, M. J., Huxor, A., Jogee, S., Komiyama, Y., Lotz, J., Lucey, J. R., Marzke, R. O., Merritt, D., Miller, B. W., Miller, N. A., Mouhcine, M., Okamura, S., Peletier, R. F., Phillipps, S., Poggianti, B. M., Sharples, R. M., Smith, R. J., Trentham, N., Tully, R. B., Valentijn, E., & Verdoes Kleijn, G. 2008, ApJS, 176, 424

Chilingarian, I. V., Cayatte, V., Durret, F., Adami, C., Balkowski, C., Chemin, L., Laganá, T. F., & Prugniel, P. 2008, A&A, 486, 85

Colbert, J. W., Mulchaey, J. S., & Zabludoff, A. I. 2001, AJ, 121, 808

Combes, F., Debbasch, F., Friedli, D., & Pfenniger, D. 1990, A&A, 233, 82

Combes, F. & Gerin, M. 1985, A&A, 150, 327

Combes, F. & Sanders, R. H. 1981, A&A, 96, 164

Contopoulos, G. & Grosbol, P. 1989, A&A Rev., 1, 261

Contopoulos, G. & Papayannopoulos, T. 1980, A&A, 92, 33

Curir, A., Mazzei, P., & Murante, G. 2006, A&A, 447, 453

Das, M. & Jog, C. J. 1995, ApJ, 451, 167

de Vaucouleurs, G. & de Vaucouleurs, A. 1963, AJ, 68, 278

—. 1964, Reference catalogue of bright galaxies, ed. de Vaucouleurs, G. & de Vaucouleurs, A.

de Vaucouleurs, G., de Vaucouleurs, A., Corwin, Jr., H. G., Buta, R. J., Paturel, G., & Fouqué, P. 1991, Third Reference Catalogue of Bright Galaxies. Volume I: Explanations and references. Volume II: Data for galaxies between 0^h and 12^h. Volume III: Data for galaxies between 12^h and 24^h., ed. de Vaucouleurs, G., de Vaucouleurs, A., Corwin, H. G., Jr., Buta, R. J., Paturel, G., & Fouqué, P.

Debattista, V. P., Corsini, E. M., & Aguerri, J. A. L. 2002, MNRAS, 332, 65

Debattista, V. P., Mayer, L., Carollo, C. M., Moore, B., Wadsley, J., & Quinn, T. 2006, ApJ, 645, 209

Debattista, V. P. & Sellwood, J. A. 1998, ApJ, 493, L5+

—. 2000, ApJ, 543, 704

Dekel, A., Birnboim, Y., Engel, G., Freundlich, J., Goerdt, T., Mumcuoglu, M., Neistein, E., Pichon, C., Teyssier, R., & Zinger, E. 2009, Nature, 457, 451

Dressler, A. 1980, ApJ, 236, 351

Dubinski, J. 1994, ApJ, 431, 617

Dubinski, J. & Chakrabarty, D. 2009, ApJ, 703, 2068

Dubinski, J., Gauthier, J.-R., Widrow, L., & Nickerson, S. 2008, in Astronomical Society of the Pacific Conference Series, Vol. 396, Formation and Evolution of Galaxy Disks, ed. J. G. Funes & E. M. Corsini, 321–+

Ellison, S. L., Patton, D. R., Nair, P., Simard, L., Mendel, J. T., McConnachie, A. W., & Scudder, J. M. 2011, ArXiv e-prints

Elmegreen, B. G. 1979, ApJ, 231, 372

—. 1994, ApJ, 425, L73

—. 1995, MNRAS, 275, 944

Elmegreen, B. G. & Elmegreen, D. M. 1985, ApJ, 288, 438

Elmegreen, B. G., Elmegreen, D. M., Chromey, F. R., Hasselbacher, D. A., & Bissell, B. A. 1996, AJ, 111, 2233

Elmegreen, B. G., Elmegreen, D. M., & Hirst, A. C. 2004, ApJ, 612, 191

Elmegreen, D. M. & Elmegreen, B. G. 1980, AJ, 85, 1325

Elmegreen, D. M., Elmegreen, B. G., & Bellin, A. D. 1990, ApJ, 364, 415

Elmegreen, D. M., Sundin, M., Sundelius, B., & Elmegreen, B. 1991, A&A, 244, 52

Englmaier, P. & Shlosman, I. 2004, ApJ, 617, L115

Erwin, P. 2004, A&A, 415, 941

—. 2005, MNRAS, 364, 283

Erwin, P. & Sparke, L. S. 2003, ApJS, 146, 299

Eskridge, P. B., Frogel, J. A., Pogge, R. W., Quillen, A. C., Berlind, A. A., Davies, R. L., DePoy, D. L., Gilbert, K. M., Houdashelt, M. L., Kuchinski, L. E., Ramírez, S. V., Sellgren, K., Stutz, A., Terndrup, D. M., & Tiede, G. P. 2002, ApJS, 143, 73

Eskridge, P. B., Frogel, J. A., Pogge, R. W., Quillen, A. C., Davies, R. L., DePoy, D. L., Houdashelt, M. L., Kuchinski, L. E., Ramírez, S. V., Sellgren, K., Terndrup, D. M., & Tiede, G. P. 2000, AJ, 119, 536

Fisher, D. B. 2006, ApJ, 642, L17

Friedli, D., Wozniak, H., Rieke, M., Martinet, L., & Bratschi, P. 1996, A&AS, 118, 461

Fuse, C. R. 2008, PhD thesis, Texas Christian University

Gadotti, D. A. 2008, MNRAS, 384, 420

—. 2011, MNRAS, 888

Gerin, M., Combes, F., & Athanassoula, E. 1990, A&A, 230, 37

Giavalisco, M., Ferguson, H. C., Koekemoer, A. M., Dickinson, M., Alexander, D. M., Bauer, F. E., Bergeron, J., Biagetti, C., Brandt, W. N., Casertano, S., Cesarsky, C., Chatzichristou, E., Conselice, C., Cristiani, S., Da Costa, L., Dahlen, T., de Mello, D., Eisenhardt, P., Erben, T., Fall, S. M., Fassnacht, C., Fosbury, R., Fruchter, A., Gardner, J. P., Grogin, N., Hook, R. N., Hornschemeier, A. E., Idzi, R., Jogee, S., Kretchmer, C., Laidler, V., Lee, K. S., Livio, M., Lucas, R., Madau, P., Mobasher, B., Moustakas, L. A., Nonino, M., Padovani, P., Papovich, C., Park, Y., Ravindranath, S., Renzini, A., Richardson, M., Riess, A., Rosati, P., Schirmer, M., Schreier, E., Somerville, R. S., Spinrad, H., Stern, D., Stiavelli, M., Strolger, L., Urry, C. M., Vandame, B., Williams, R., & Wolf, C. 2004, ApJ, 600, L93

Gilmour, R., Gray, M. E., Almaini, O., Best, P., Wolf, C., Meisenheimer, K., Papovich, C., & Bell, E. 2007, MNRAS, 380, 1467

Giordano, L., Tran, K.-V. H., Moore, B., & Saintonge, A. 2010, ArXiv e-prints

Gnedin, O. Y. 2003, ApJ, 589, 752

Goldreich, P. & Tremaine, S. 1978, ApJ, 222, 850

Graham, A. W. & Guzmán, R. 2003, AJ, 125, 2936

Graham, A. W., Jerjen, H., & Guzmán, R. 2003, AJ, 126, 1787

Graham, A. W. & Worley, C. C. 2008, MNRAS, 388, 1708

Gray, M. E., Taylor, A. N., Meisenheimer, K., Dye, S., Wolf, C., & Thommes, E. 2002, ApJ, 568, 141

Gray, M. E., Wolf, C., Barden, M., Peng, C. Y., Häußler, B., Bell, E. F., McIntosh, D. H., Guo, Y., Caldwell, J. A. R., Bacon, D., Balogh, M., Barazza, F. D., Böhm, A., Heymans, C., Jahnke, K., Jogee, S., van Kampen, E., Lane, K., Meisenheimer, K., Sánchez, S. F., Taylor, A., Wisotzki, L., Zheng, X., Green, D. A., Beswick, R. J., Saikia, D. J., Gilmour, R., Johnson, B. D., & Papovich, C. 2009, MNRAS, 393, 1275

Grosbøl, P., Patsis, P. A., & Pompei, E. 2004, A&A, 423, 849

Gunn, J. E. & Gott, III, J. R. 1972, ApJ, 176, 1

Hammer, D., Verdoes Kleijn, G., Hoyos, C., den Brok, M., Balcells, M., Ferguson, H. C., Goudfrooij, P., Carter, D., Guzmán, R., Peletier, R. F., Smith, R. J., Graham, A. W., Trentham, N., Peng, E., Puzia, T. H., Lucey, J. R., Jogee, S., Aguerri, A. L., Batcheldor, D., Bridges, T. J., Chiboucas, K., Davies, J. I., del Burgo, C., Erwin, P., Hornschemeier, A., Hudson, M. J., Huxor, A., Jenkins, L., Karick, A., Khosroshahi, H., Kourkchi, E., Komiyama, Y., Lotz, J., Marzke, R. O., Marinova, I., Matkovic, A., Merritt, D., Miller, B. W., Miller, N. A., Mobasher, B., Mouhcine, M., Okamura, S., Percival, S., Phillipps, S., Poggianti, B. M., Price, J., Sharples, R. M., Tully, R. B., & Valentijn, E. 2010, ApJS, 191, 143

Hao, L., Jogee, S., Barazza, F. D., Marinova, I., & Shen, J. 2009, in Astronomical Society of the Pacific Conference Series, Vol. 419, Galaxy Evolution: Emerging Insights and Future Challenges, ed. S. Jogee, I. Marinova, L. Hao, & G. A. Blanc, 402–+

Hasan, H. & Norman, C. 1990, ApJ, 361, 69

Hasan, H., Pfenniger, D., & Norman, C. 1993, ApJ, 409, 91

Heiderman, A., Jogee, S., Marinova, I., van Kampen, E., Barden, M., Peng, C. Y., Heymans, C., Gray, M. E., Bell, E. F., Bacon, D., Balogh, M., Barazza, F. D., Böhm, A., Caldwell, J. A. R., Häußler, B., Jahnke, K., Lane, K., McIntosh, D. H., Meisenheimer, K., Sánchez, S. F., Somerville, R. S., Taylor, A., Wisotzki, L., Wolf, C., & Zheng, X. 2009, ApJ, 705, 1433

Heller, C., Shlosman, I., & Englmaier, P. 2001, ApJ, 553, 661

Heller, C. H. & Shlosman, I. 1994, ApJ, 424, 84

—. 1996, ApJ, 471, 143

Heller, C. H., Shlosman, I., & Athanassoula, E. 2007, ApJ, 671, 226

Hernández-Toledo, H. M., Vázquez-Mata, J. A., Martínez-Vázquez, L. A., Choi, Y.-Y., & Park, C. 2010, AJ, 139, 2525

Hernquist, L. 1989, Nature, 340, 687

Hernquist, L. & Mihos, J. C. 1995, ApJ, 448, 41

Heymans, C., Gray, M. E., Peng, C. Y., van Waerbeke, L., Bell, E. F., Wolf, C., Bacon, D., Balogh, M., Barazza, F. D., Barden, M., Böhm, A., Caldwell, J. A. R., Häußler, B., Jahnke, K., Jogee, S., van Kampen, E., Lane, K., McIntosh, D. H., Meisenheimer, K., Mellier, Y., Sánchez, S. F., Taylor, A. N., Wisotzki, L., & Zheng, X. 2008, MNRAS, 385, 1431

Hill, G. J., MacQueen, P. J., Smith, M. P., Tufts, J. R., Roth, M. M., Kelz, A., Adams, J. J., Drory, N., Grupp, F., Barnes, S. I., Blanc, G. A., Murphy, J. D., Altmann, W., Wesley, G. L., Segura, P. R., Good, J. M., Booth, J. A., Bauer, S.-M., Popow, E., Goertz, J. A., Edmonston, R. D., & Wilkinson, C. P. 2008, in Society of Photo-Optical Instrumentation Engineers (SPIE) Conference Series, Vol. 7014, Society of Photo-Optical Instrumentation Engineers (SPIE) Conference Series

Hogg, D. W., Blanton, M. R., Eisenstein, D. J., Gunn, J. E., Schlegel, D. J., Zehavi, I., Bahcall, N. A., Brinkmann, J., Csabai, I., Schneider, D. P., Weinberg, D. H., & York, D. G. 2003, ApJ, 585, L5

Hohl, F. 1975, in IAU Symposium, Vol. 69, Dynamics of the Solar Systems, ed. A. Hayli, 349–+

Hoyos, C., den Brok, M., Kleijn, G. V., Carter, D., Balcells, M., Guzmán, R., Peletier, R., Ferguson, H. C., Goudfrooij, P., Graham, A. W., Hammer, D., Karick, A. M., Lucey, J. R., Matković, A., Merritt, D., Mouhcine, M., & Valentijn, E. 2011, MNRAS, 411, 2439

Huang, J. H., Gu, Q. S., Su, H. J., Hawarden, T. G., Liao, X. H., & Wu, G. X. 1996, A&A, 313, 13

Hubble, E. P. 1926, ApJ, 63, 236

—. 1929, ApJ, 69, 103

—. 1936, Realm of the Nebulae, ed. Hubble, E. P.

Hunt, L. K. & Malkan, M. A. 1999, ApJ, 516, 660

Jedrzejewski, R. I. 1987, MNRAS, 226, 747

Jerjen, H., Binggeli, B., & Freeman, K. C. 2000, AJ, 119, 593

Jog, C. J. & Solomon, P. M. 1984, ApJ, 276, 127

Jogee, S. 1999, PhD thesis, California Institute of Technology

Jogee, S. 2006, in Lecture Notes in Physics, Berlin Springer Verlag, Vol. 693, Physics of Active Galactic Nuclei at all Scales, ed. D. Alloin, 143–+

Jogee, S., Barazza, F. D., Rix, H.-W., Shlosman, I., Barden, M., Wolf, C., Davies, J., Heyer, I., Beckwith, S. V. W., Bell, E. F., Borch, A., Caldwell, J. A. R., Conselice, C. J., Dahlen, T., Häussler, B., Heymans, C., Jahnke, K., Knapen, J. H., Laine, S., Lubell, G. M., Mobasher, B., McIntosh, D. H., Meisenheimer, K., Peng, C. Y., Ravindranath, S., Sanchez, S. F., Somerville, R. S., & Wisotzki, L. 2004, ApJ, 615, L105

Jogee, S., Kenney, J. D. P., & Smith, B. J. 1999, ApJ, 526, 665

Jogee, S., Knapen, J. H., Laine, S., Shlosman, I., Scoville, N. Z., & Englmaier, P. 2002a, ApJ, 570, L55

Jogee, S., Miller, S. H., Penner, K., Skelton, R. E., Conselice, C. J., Somerville, R. S., Bell, E. F., Zheng, X. Z., Rix, H.-W., Robaina, A. R., Barazza, F. D., Barden, M., Borch, A., Beckwith, S. V. W., Caldwell, J. A. R., Peng, C. Y., Heymans, C., McIntosh, D. H., Häußler, B., Jahnke, K., Meisenheimer, K., Sanchez, S. F., Wisotzki, L., Wolf, C., & Papovich, C. 2009, ApJ, 697, 1971

Jogee, S., Scoville, N., & Kenney, J. D. P. 2005, ApJ, 630, 837

Jogee, S., Shlosman, I., Laine, S., Englmaier, P., Knapen, J. H., Scoville, N., & Wilson, C. D. 2002b, ApJ, 575, 156

Kassin, S. A., de Jong, R. S., & Weiner, B. J. 2006, ApJ, 643, 804

Kazantzidis, S., Kravtsov, A. V., Zentner, A. R., Allgood, B., Nagai, D., & Moore, B. 2004, ApJ, 611, L73

Kenney, J. D. P., Scoville, N. Z., & Wilson, C. D. 1991, ApJ, 366, 432

Kereš, D., Katz, N., Fardal, M., Davé, R., & Weinberg, D. H. 2009, MNRAS, 395, 160

Knapen, J. H., Beckman, J. E., Shlosman, I., Peletier, R. F., Heller, C. H., & de Jong, R. S. 1995, ApJ, 443, L73

Knapen, J. H., Mazzuca, L. M., Böker, T., Shlosman, I., Colina, L., Combes, F., & Axon, D. J. 2006, A&A, 448, 489

Knapen, J. H., Shlosman, I., & Peletier, R. F. 2000, ApJ, 529, 93

Koopmann, R. A. & Kenney, J. D. P. 1998, ApJ, 497, L75+

Koribalski, B., Dettmar, R.-J., Mebold, U., & Wielebinski, R. 1996, A&A, 315, 71

Kormendy, J. 1977, ApJ, 214, 359

—. 1979, ApJ, 227, 714

Kormendy, J. 1982a, in Saas-Fee Advanced Course 12: Morphology and Dynamics of Galaxies, ed. L. Martinet & M. Mayor, 113–288

—. 1982b, ApJ, 257, 75

—. 1985, ApJ, 295, 73

Kormendy, J. 1993, in IAU Symposium, Vol. 153, Galactic Bulges, ed. H. Dejonghe & H. J. Habing, 209–+

Kormendy, J. & Fisher, D. B. 2008, in Astronomical Society of the Pacific Conference Series, Vol. 396, Formation and Evolution of Galaxy Disks, ed. J. G. Funes & E. M. Corsini, 297–+

Kormendy, J. & Freeman, K. C. 2004, in IAU Symposium, Vol. 220, Dark Matter in Galaxies, ed. S. Ryder, D. Pisano, M. Walker, & K. Freeman, 377–+

Kormendy, J. & Kennicutt, Jr., R. C. 2004, ARA&A, 42, 603

Kormendy, J. & Norman, C. A. 1979, ApJ, 233, 539

Kroupa, P., Tout, C. A., & Gilmore, G. 1993, MNRAS, 262, 545

Kuijken, K. & Merrifield, M. R. 1995, ApJ, 443, L13

Kumai, Y., Taniguchi, Y., & Ishii, H. 1986, MNRAS, 223, 139

Laine, S., Kenney, J. D. P., Yun, M. S., & Gottesman, S. T. 1999, ApJ, 511, 709

Laine, S., Shlosman, I., & Heller, C. H. 1998, MNRAS, 297, 1052

Laine, S., Shlosman, I., Knapen, J. H., & Peletier, R. F. 2002, ApJ, 567, 97

Larson, R. B. 1985, MNRAS, 214, 379

Larson, R. B., Tinsley, B. M., & Caldwell, C. N. 1980, ApJ, 237, 692

Laurikainen, E., Salo, H., & Buta, R. 2004a, ApJ, 607, 103

—. 2005, MNRAS, 362, 1319

Laurikainen, E., Salo, H., Buta, R., & Knapen, J. H. 2007, MNRAS, 381, 401

—. 2009, ApJ, 692, L34

Laurikainen, E., Salo, H., Buta, R., & Vasylyev, S. 2004b, MNRAS, 355, 1251

Laurikainen, E., Salo, H., & Rautiainen, P. 2002, MNRAS, 331, 880

Le Floc'h, E., Papovich, C., Dole, H., Bell, E. F., Lagache, G., Rieke, G. H., Egami, E., Pérez-González, P. G., Alonso-Herrero, A., Rieke, M. J., Blaylock, M., Engelbracht, C. W., Gordon, K. D., Hines, D. C., Misselt, K. A., Morrison, J. E., & Mould, J. 2005, ApJ, 632, 169

Lilly, S. J., Le Fevre, O., Hammer, F., & Crampton, D. 1996, ApJ, 460, L1+

Lin, D. N. C. & Faber, S. M. 1983, ApJ, 266, L21

Lisker, T., Debattista, V. P., Ferreras, I., & Erwin, P. 2006a, MNRAS, 370, 477

Lisker, T. & Fuchs, B. 2009, A&A, 501, 429

Lisker, T., Grebel, E. K., & Binggeli, B. 2006b, AJ, 132, 497

Lisker, T., Grebel, E. K., Binggeli, B., & Glatt, K. 2007, ApJ, 660, 1186

López-Sanjuan, C., Balcells, M., Pérez-González, P. G., Barro, G., García-Dabó, C. E., Gallego, J., & Zamorano, J. 2010, ApJ, 710, 1170

Lord, S. D., Strom, S. E., & Young, J. S. 1987, in NASA Conference Publication, Vol. 2466, NASA Conference Publication, ed. C. J. Lonsdale Persson, 303–307

Lütticke, R., Dettmar, R.-J., & Pohlen, M. 2000, A&AS, 145, 405

Marinova, I. & Jogee, S. 2007, ApJ, 659, 1176

Martin, P. 1995, AJ, 109, 2428

Martin, P. & Friedli, D. 1997, A&A, 326, 449

Martin, P. & Roy, J.-R. 1994, ApJ, 424, 599

—. 1995, ApJ, 445, 161

Martinez-Valpuesta, I. & Shlosman, I. 2004, ApJ, 613, L29

Martinez-Valpuesta, I., Shlosman, I., & Heller, C. 2006, ApJ, 637, 214

Masters, K. L., Nichol, R. C., Hoyle, B., Lintott, C., Bamford, S. P., Edmondson, E. M., Fortson, L., Keel, W. C., Schawinski, K., Smith, A. M., & Thomas, D. 2011, MNRAS, 411, 2026

Mastropietro, C., Moore, B., Mayer, L., Debattista, V. P., Piffaretti, R., & Stadel, J. 2005, MNRAS, 364, 607

Matković, A. & Guzmán, R. 2005, MNRAS, 362, 289

Mendez, M., Orsatti, A. M., & Forte, J. C. 1989, ApJ, 338, 136

Méndez-Abreu, J., Sánchez-Janssen, R., & Aguerri, J. A. L. 2010, ApJ, 711, L61

Menéndez-Delmestre, K., Sheth, K., Schinnerer, E., Jarrett, T. H., & Scoville, N. Z. 2007, ApJ, 657, 790

Merrifield, M. R. & Kuijken, K. 1995, MNRAS, 274, 933

Mihos, J. C. & Hernquist, L. 1996, ApJ, 464, 641

Miller, R. H. & Smith, B. F. 1979, ApJ, 227, 785

Mobasher, B., Colless, M., Carter, D., Poggianti, B. M., Bridges, T. J., Kranz, K., Komiyama, Y., Kashikawa, N., Yagi, M., & Okamura, S. 2003, ApJ, 587, 605

Moellenhoff, C., Matthias, M., & Gerhard, O. E. 1995, A&A, 301, 359

Moore, B., Katz, N., Lake, G., Dressler, A., & Oemler, A. 1996, Nature, 379, 613

Mulchaey, J. S. & Regan, M. W. 1997, ApJ, 482, L135+

Mundell, C. G. & Shone, D. L. 1999, MNRAS, 304, 475

Nair, P. B. & Abraham, R. G. 2010a, ApJS, 186, 427

—. 2010b, ApJ, 714, L260

Noguchi, M. 1987, MNRAS, 228, 635

—. 1988, A&A, 203, 259

Odewahn, S. C. 1996, in Astronomical Society of the Pacific Conference Series, Vol. 91, IAU Colloq. 157: Barred Galaxies, ed. R. Buta, D. A. Crocker, & B. G. Elmegreen, 30–+

O'Neill, J. K. & Dubinski, J. 2003, MNRAS, 346, 251

Ostriker, J. P. & Peebles, P. J. E. 1973, ApJ, 186, 467

Peeples, M. S. & Martini, P. 2006, ApJ, 652, 1097

Peng, C. Y., Ho, L. C., Impey, C. D., & Rix, H.-W. 2002, AJ, 124, 266

Persic, M., Salucci, P., & Stel, F. 1996, MNRAS, 281, 27

Pfenniger, D. & Friedli, D. 1991, A&A, 252, 75

Pfenniger, D. & Norman, C. 1990, ApJ, 363, 391

Quilis, V., Moore, B., & Bower, R. 2000, Science, 288, 1617

Quillen, A. C., Frogel, J. A., Kenney, J. D. P., Pogge, R. W., & Depoy, D. L. 1995, ApJ, 441, 549

Ravindranath, S., Ferguson, H. C., Conselice, C., Giavalisco, M., Dickinson, M., Chatzichristou, E., de Mello, D., Fall, S. M., Gardner, J. P., Grogin,

N. A., Hornschemeier, A., Jogee, S., Koekemoer, A., Kretchmer, C., Livio, M., Mobasher, B., & Somerville, R. 2004, ApJ, 604, L9

Reese, A. S., Williams, T. B., Sellwood, J. A., Barnes, E. I., & Powell, B. A. 2007, AJ, 133, 2846

Regan, M. W. & Teuben, P. 2003, ApJ, 582, 723

Regan, M. W., Vogel, S. N., & Teuben, P. J. 1997, ApJ, 482, L143+

Rix, H.-W., Barden, M., Beckwith, S. V. W., Bell, E. F., Borch, A., Caldwell, J. A. R., Häussler, B., Jahnke, K., Jogee, S., McIntosh, D. H., Meisenheimer, K., Peng, C. Y., Sanchez, S. F., Somerville, R. S., Wisotzki, L., & Wolf, C. 2004, ApJS, 152, 163

Robaina, A. R., Bell, E. F., Skelton, R. E., McIntosh, D. H., Somerville, R. S., Zheng, X., Rix, H.-W., Bacon, D., Balogh, M., Barazza, F. D., Barden, M., Böhm, A., Caldwell, J. A. R., Gallazzi, A., Gray, M. E., Häussler, B., Heymans, C., Jahnke, K., Jogee, S., van Kampen, E., Lane, K., Meisenheimer, K., Papovich, C., Peng, C. Y., Sánchez, S. F., Skibba, R., Taylor, A., Wisotzki, L., & Wolf, C. 2009, ApJ, 704, 324

Roberts, W. W. 1969, ApJ, 158, 123

Romano-Díaz, E., Shlosman, I., Heller, C., & Hoffman, Y. 2008, ApJ, 687, L13

Saha, K., Martinez-Valpuesta, I., & Gerhard, O. 2011, ArXiv e-prints

Sakamoto, K., Okumura, S. K., Ishizuki, S., & Scoville, N. Z. 1999, ApJ, 525, 691

Sánchez-Janssen, R., Méndez-Abreu, J., & Aguerri, J. A. L. 2010, MNRAS, 406, L65

Sandage, A. & Binggeli, B. 1984, AJ, 89, 919

Schneider, P. 2006, Extragalactic Astronomy and Cosmology, ed. Schneider, P.

Schwarz, M. P. 1981, ApJ, 247, 77

Schweizer, F. & Ford, Jr., W. K. 1985, in Lecture Notes in Physics, Berlin Springer Verlag, Vol. 232, New Aspects of Galaxy Photometry, ed. J.-L. Nieto, 145–+

Scoville, N., Abraham, R. G., Aussel, H., Barnes, J. E., Benson, A., Blain, A. W., Calzetti, D., Comastri, A., Capak, P., Carilli, C., Carlstrom, J. E., Carollo, C. M., Colbert, J., Daddi, E., Ellis, R. S., Elvis, M., Ewald, S. P., Fall, M., Franceschini, A., Giavalisco, M., Green, W., Griffiths, R. E., Guzzo, L., Hasinger, G., Impey, C., Kneib, J.-P., Koda, J., Koekemoer, A., Lefevre, O., Lilly, S., Liu, C. T., McCracken, H. J., Massey, R., Mellier, Y., Miyazaki, S., Mobasher, B., Mould, J., Norman, C., Refregier, A., Renzini, A., Rhodes, J., Rich, M., Sanders, D. B., Schiminovich, D., Schinnerer, E., Scodeggio, M., Sheth, K., Shopbell, P. L., Taniguchi, Y., Tyson, N. D., Urry, C. M.,

Van Waerbeke, L., Vettolani, P., White, S. D. M., & Yan, L. 2007, ApJS, 172, 38

Scoville, N. Z., Matthews, K., Carico, D. P., & Sanders, D. B. 1988, ApJ, 327, L61

Sellwood, J. A. 1981, A&A, 99, 362

Sellwood, J. A. & Debattista, V. P. 2006, ApJ, 639, 868

Sellwood, J. A. & Wilkinson, A. 1993, Reports on Progress in Physics, 56, 173

Shaw, M. A. 1987, MNRAS, 229, 691

Shen, J. & Sellwood, J. A. 2004, ApJ, 604, 614

Sheth, K., Elmegreen, D. M., Elmegreen, B. G., Capak, P., Abraham, R. G., Athanassoula, E., Ellis, R. S., Mobasher, B., Salvato, M., Schinnerer, E., Scoville, N. Z., Spalsbury, L., Strubbe, L., Carollo, M., Rich, M., & West, A. A. 2008, ApJ, 675, 1141

Sheth, K., Regan, M. W., Scoville, N. Z., & Strubbe, L. E. 2003, ApJ, 592, L13

Sheth, K., Vogel, S. N., Regan, M. W., Thornley, M. D., & Teuben, P. J. 2005, ApJ, 632, 217

Shlosman, I., Frank, J., & Begelman, M. C. 1989, Nature, 338, 45

Shlosman, I. & Heller, C. H. 2002, ApJ, 565, 921

Shlosman, I. & Noguchi, M. 1993, ApJ, 414, 474

Shlosman, I., Peletier, R. F., & Knapen, J. H. 2000, ApJ, 535, L83

Simien, F. & de Vaucouleurs, G. 1986, ApJ, 302, 564

Sparke, L. S. & Sellwood, J. A. 1987, MNRAS, 225, 653

Steinmetz, M. & Navarro, J. F. 2002, New Astronomy, 7, 155

Tago, E., Einasto, J., Saar, E., Tempel, E., Einasto, M., Vennik, J., & Müller, V. 2008, A&A, 479, 927

The, L. S. & White, S. D. M. 1986, AJ, 92, 1248

Thompson, L. A. 1981, ApJ, 244, L43

Toomre, A. 1964, ApJ, 139, 1217

Toomre, A. 1981, in Structure and Evolution of Normal Galaxies, ed. S. M. Fall & D. Lynden-Bell, 111–136

Tran, H. D., Sirianni, M., Ford, H. C., Illingworth, G. D., Clampin, M., Hartig, G., Becker, R. H., White, R. L., Bartko, F., Benítez, N., Blakeslee, J. P., Bouwens, R., Broadhurst, T. J., Brown, R., Burrows, C., Cheng, E., Cross, N., Feldman, P. D., Franx, M., Golimowski, D. A., Gronwall, C., Infante, L., Kimble, R. A., Krist, J., Lesser, M., Magee, D., Martel, A. R., McCann, W. J., Meurer, G. R., Miley, G., Postman, M., Rosati, P., Sparks, W. B., & Tsvetanov, Z. 2003, ApJ, 585, 750

Trentham, N. & Hodgkin, S. 2002, MNRAS, 333, 423

Tully, R. B. 1988, Nearby galaxies catalog, ed. Tully, R. B.

van Albada, G. D. & Roberts, Jr., W. W. 1981, ApJ, 246, 740

van den Bergh, S. 2002, AJ, 124, 782

van den Bergh, S., Abraham, R. G., Ellis, R. S., Tanvir, N. R., Santiago, B. X., & Glazebrook, K. G. 1996, AJ, 112, 359

van den Bosch, F. C., Aquino, D., Yang, X., Mo, H. J., Pasquali, A., McIntosh, D. H., Weinmann, S. M., & Kang, X. 2008, MNRAS, 387, 79

van Zee, L. 2001, AJ, 121, 2003

Varela, J., Moles, M., Márquez, I., Galletta, G., Masegosa, J., & Bettoni, D. 2004, A&A, 420, 873

Vila-Costas, M. B. & Edmunds, M. G. 1992, MNRAS, 259, 121

Villa-Vargas, J., Shlosman, I., & Heller, C. 2009, ApJ, 707, 218

—. 2010, ApJ, 719, 1470

Weinberg, M. D. 1985, MNRAS, 213, 451

Weiner, B. J., Williams, T. B., van Gorkom, J. H., & Sellwood, J. A. 2001, ApJ, 546, 916

Weinzirl, T., Jogee, S., Khochfar, S., Burkert, A., & Kormendy, J. 2009, ApJ, 696, 411

White, S. D. M., Clowe, D. I., Simard, L., Rudnick, G., De Lucia, G., Aragón-Salamanca, A., Bender, R., Best, P., Bremer, M., Charlot, S., Dalcanton, J., Dantel, M., Desai, V., Fort, B., Halliday, C., Jablonka, P., Kauffmann, G., Mellier, Y., Milvang-Jensen, B., Pelló, R., Poggianti, B., Poirier, S., Rottgering, H., Saglia, R., Schneider, P., & Zaritsky, D. 2005, A&A, 444, 365

Whyte, L. F., Abraham, R. G., Merrifield, M. R., Eskridge, P. B., Frogel, J. A., & Pogge, R. W. 2002, MNRAS, 336, 1281

Wolf, C., Aragón-Salamanca, A., Balogh, M., Barden, M., Bell, E. F., Gray, M. E., Peng, C. Y., Bacon, D., Barazza, F. D., Böhm, A., Caldwell, J. A. R., Gallazzi, A., Häußler, B., Heymans, C., Jahnke, K., Jogee, S., van Kampen, E., Lane, K., McIntosh, D. H., Meisenheimer, K., Papovich, C., Sánchez, S. F., Taylor, A., Wisotzki, L., & Zheng, X. 2009, MNRAS, 393, 1302

Wolf, C., Bell, E. F., McIntosh, D. H., Rix, H.-W., Barden, M., Beckwith, S. V. W., Borch, A., Caldwell, J. A. R., Häussler, B., Heymans, C., Jahnke, K., Jogee, S., Meisenheimer, K., Peng, C. Y., Sánchez, S. F., Somerville, R. S., & Wisotzki, L. 2005a, ApJ, 630, 771

Wolf, C., Gray, M. E., & Meisenheimer, K. 2005b, A&A, 443, 435

Wolf, C., Meisenheimer, K., Kleinheinrich, M., Borch, A., Dye, S., Gray, M., Wisotzki, L., Bell, E. F., Rix, H.-W., Cimatti, A., Hasinger, G., & Szokoly, G. 2004, A&A, 421, 913

Wozniak, H., Friedli, D., Martinet, L., Martin, P., & Bratschi, P. 1995, A&AS, 111, 115

Yoachim, P. & Dalcanton, J. J. 2006, AJ, 131, 226

Young, J. S. & Scoville, N. Z. 1991, ARA&A, 29, 581

Zaritsky, D., Kennicutt, Jr., R. C., & Huchra, J. P. 1994, ApJ, 420, 87

Zheng, X. Z., Hammer, F., Flores, H., Assémat, F., & Rawat, A. 2005, A&A, 435, 507

Zurita, A., Relaño, M., Beckman, J. E., & Knapen, J. H. 2004, A&A, 413, 73

Vita

Irina Marinova was born on March 23, 1983 to parents Lilia and Stoil Marinovi in Botevgrad, Bulgaria. After moving to the US in 1993, Irina attended the University of Illinois, receiving a Bachelors of Science in Physics with high departmental honors in 2005. During her time at Illinois, Irina worked with Prof. Susan Lamb through the Research Experience for Undergraduates (REU) program, investigating the formation of tidal dwarf galaxies using numerical simulations. In May of 2005, Irina moved to Austin to pursue graduate studies in Astronomy at the University of Texas with Prof. Shardha Jogee. During her time at UT, Irina studied the fraction and properties of barred disk galaxies in field and cluster environments. In addition to doing research, she also volunteered her time to numerous education and outreach projects, such as helping with the McDonald Observatory teacher workshops, Project Astro, and putting together an activity for high-school students using the web-based Galaxy Cosmos Explorer Tool (GCET). In the future, Irina hopes to pursue a career in science education and public outreach.

Permanent address: marinova@astro.as.utexas.edu

This dissertation was typeset with LaTeX[†] by the author.

[†]LaTeX is a document preparation system developed by Leslie Lamport as a special version of Donald Knuth's TeX Program.